INTERACTIONS BETWEEN PLASMA AND MATERIAL SURFACES FOR STERILIZATION AND IMPURITY ADSORPTION

By

Madeline Ann Mackinder

A DISSERTATION

Submitted to
Michigan State University
in partial fulfillment of the requirements
for the degree of

Chemical Engineering – Doctor of Philosophy

2022

ABSTRACT

INTERACTIONS BETWEEN PLASMA AND MATERIAL SURFACES FOR STERILIZATION AND IMPURITY ADSORPTION

By

Madeline Ann Mackinder

As the worldwide population increases, maintaining a standard of public health becomes more critical. Two major concerns in this area are nosocomial infections (NI) and water contamination. Current processes in sterilization and water treatment have limitations that could be overcome using plasma techniques. The unique characteristics of plasma make it a promising alternative for energy-intensive processes. This work investigated the characteristics of plasma that have the greatest impact on sterilization and the reactivation of activated carbon. Previous studies have researched the physical and chemical surface properties of biochar but have not been able to establish an efficient process to activate biochar with desired characteristics. Plasma treatment would offer a way to etch the surface of biochar and specifically functionalize the surface. Successfully activating biochar would increase its adsorption ability and enable its use for water treatment. This project aims to harness these plasma properties and use plasmas to address three important topics related to public health: sterilization of surfaces, modulating commercial activated carbon (AC), and activations of biochar.

Cold plasma sterilization offers an efficient way to sterilize medical components and instruments without the risk of deformation to heat-sensitive materials. This paper reports the use of magnetized plasma to realize low-temperature sterilization. A radio frequency dielectric barrier discharge was created in a quartz tube using a mixture of argon and oxygen gas. Glass slides inoculated with a uniform amount of Escherichia coli were exposed to the plasma afterglow at different pressures with and without a magnetic field. A global model was developed to evaluate the magnetically enhanced dielectric barrier discharges and predict species densities. Optical emission spectroscopy identified the plasma species present and validated the model. The magnetic field significantly promoted the intensity of the plasma and the sterilization efficiency. A process gas

pressure of 100 mTorr presented the most effective treatment with a sterilization time less than one minute and sample temperature below 32 °C.

The effects of O2 plasma on the adsorption capacity of activated carbon (AC) was investigated by varying treatment times. Transmission electron microscopy (TEM), X-ray photoelectron spectroscopy (XPS), Fourier transform infrared spectroscopy (FTIR), and Zeta potential were used to characterize the surface properties of the AC. The carbon was then applied to remove methylene blue (MB) from an aqueous solution. The adsorption kinetics and isotherm were also studied. Results showed that pseudo-second-order kinetics was the most suitable model for describing the adsorption of MB onto AC. Equilibrium data were well fitted to the Freundlich and Langmuir isotherm models. The highest adsorption capacity resulted from 4 minutes of O_2 plasma treatment. This work shows that activation of AC by plasma can open the micropore and increase the effectiveness of chemical removal.

Biochar was activated using a combination of O_2 plasma and KOH. The adsorption capacity was investigated for different O_2 plasma treatment times, KOH concentrations, and treatment temperatures. The adsorption capacity of methylene blue (MB) by the plasma activated biochar was evaluated. The adsorption kinetics and isotherm were also investigated. Results showed pseudo-second-order kinetics was the most suitable model for describing the adsorption of MB onto biochar. Both the Freundlich and Langmuir isotherm models fit the equilibrium data. The highest adsorption capacity resulted from 10% KOH + 300 °C for 5 minutes. This work shows that activation of biochar by plasma can improve adsorption capacity.

The plasma treated AC and the plasma activated biochar were applied to the removal of PFOA. It was demonstrated that plasma treatment can improve PFOA adsorption. The negative surface charge was shown to negatively impact PFOA adsorption which aligns with the hypothesis that PFOA would preferentially adsorb onto more positive surfaces due to its anionic state in water.

To Tom. For your love and patience

ACKNOWLEDGEMENTS

I would like to express my deepest gratitude to my advisor Dr. Qi Hua Fan for his exceptional guidance and continuous support. His trust, encouragement, and enthusiasm enabled me to grow as a scientist and researcher. His kindness and confidence allowed me to pursue various projects and expand my knowledge. He provided insightful discussions and suggestions. Without him, this accomplishment would not be possible. He is my best role model as a scientist, mentor, and teacher. I will forever be grateful for the unparalleled kindness and compassion he has shown me during my time as his student, and I hope to reflect the values he taught me every day. Thank you for taking a chance and welcoming me into your group. My life is fundamentally changed for the better.

I would also like to extend my sincerest thanks to my committee: Dr. Scott Calabrese Barton, Dr. Andre Lee, and Dr. Daniel Woldring, whose knowledge, expertise, and guidance were invaluable to the success of my research and growth as a researcher. I would also like to thank Dr. Xanthippi Chatzistavrou for her advice and support. All of you provided unlimited support and always made time to discuss questions, give career advice, and provide new perspectives. I am forever grateful.

I would additionally like to extend my thanks to members of Plasma Sources and Processing Lab: Dr. Maheshwar Shrestha, Dr. Keliang Wang, Dr. Bocong Zheng, as well as fellow graduate students Young Kim, Al-Ahsan Talukder, Vanessa Maldonado, and Thanh Tran. Thank you especially to Dr. Keliang Wang for your willingness to teach me and for always being available to give assistance. Thank you for making me feel welcome. Your insight and mentorship have been invaluable. I would also like to thank Dr. Cory Rusinek for his instrumental role in beginning my graduate school journey. I would like to recognize the contributions of Dr. Per Askland and Dr. Anthony Schilmiller.

Thank you, to the wonderful friends, I made during this journey: Young Kim, Adam Marsh, JoAnn Ballor, Brad Luzenski, Tom Mittelbrun, and Rachael Zarger. You made this arduous journey better. I would have never gotten through this without the laughter we shared and the unconditional

support.

Thank you to my best friend Jacqueline Scholz, who always listened, made time to visit, and kept me grounded. You made sure I recognized the positive even when it seemed impossible. Thank you to Jacklyn Lynch for being one of my best friends and being my voice of reason. You inspire me every day to keep moving forward. Thank you to my best friend and name twin Madalyn Majors. Your sarcasm and wit always make me laugh. You are my role model for what a woman in the field of engineering can do. Thank you all for loving and always believing in me.

Thank you to my amazing and brilliant husband Tom Lindsey. You have been by my side throughout this journey. Your unconditional belief, love, and support enabled me to flourish and thrive. Thank you for late nights editing and listening to my presentations even when you do not understand what I am talking about. Thank you for celebrating every little success and letting me lean on you with every setback. I will love you forever and always.

Last, but never least, I would like to thank my family, all of whom have provided me with love and support. My parents Dr. Robert Mackinder and Mrs. Ann Mackinder, who have been a source of unconditional love. Thank you for believing in me. Thank you to my wonderful brothers Jacob Mackinder and James Mackinder for always putting a smile on my face. To my aunt Melissa Mackinder for being my staunchest cheerleader. To my grandfather, Mr. Robert Mackinder for always making sure I know I am loved and reminding me that I can accomplish whatever I set my mind to. Thank you especially to my grandmother Mrs. Lois Mackinder, who was taken too soon. I feel your unceasing belief in me and love every day. Thank you for always being proud of me.

TABLE OF CONTENTS

LIST OF TABLES

LIST OF FIGURES

KEY TO ABBREVIATIONS

AC	Activated carbon
BET	Brunauer-Emmett-Teller
CFU	Colony forming units
D-value	Decimal reduction time
DNA	Deoxyribonucleic acid
EtO	Ethylene oxide
FTIR	Fourier-transformed infrared spectroscopy
GAC	Granular activated carbon
IUPAC	International Union of Pure and Applied Chemistry
KOH	Potassium hydroxide
LC-MS	Liquid chromatography-mass spectroscopy
MB	Methylene blue
NI	Nosocomial infections
PAC	Powdered activated carbon
PFAS	Perfluoroalkyl substances
PFOA	Perfluorooctanoic acid
PFOS	Perfluorooctanesulfonic acid
ppb	Parts per billion
ppm	Parts per million
OES	Optical emission spectrum
RNA	Ribonucleic acid
ROS	Reactive oxygen species
SAL	Sterility assurance level
sccm	Standard cubic centimeters per minute
SEM	Scanning electron microscopy

TEM	Transmission electron microscopy
UV	Ultra-violet
UV-Vis	Ultraviolet/visible light spectroscopy
wt%	Weight%
XPS	X-ray photoelectron spectroscopy

CHAPTER 1

INTRODUCTION

1.1 Plasma as an Alternative for Energy-Intensive Processes

With the expansion of world population, industrialization, and environmental changes, a large scope of threats to public health have emerged [1, 2]. Two major concerns are nosocomial infections (NI) and water contamination.

NI, hospital-acquired infections, are responsible for a large number of deaths and post-surgical complications every year [2–4]. The risk for NI are increased due to crowded hospital conditions, frequent transfers of patients, and areas where immunocompromised patients are grouped together [2–4]. In fact, most NI are caused by common microorganisms that would normally cause mild or no disease in a healthy person [2–4]. Susceptible areas (e.g. wounds, respiratory tract, urinary tract) become infected when microorganisms are introduced to the body through contaminated objects [2–4]. Many of these infections could be avoided by efficient sterilization techniques.

Modern sterilization methods include using autoclave or high heat (> 350 °C), ethylene oxide gas, hydrogen peroxide gas plasma, and radiation [3, 5, 6]. Sterilization by heat or autoclaving is not a viable option for heat-sensitive materials, thus requiring alternative methods of sterilization [6]. Ethylene oxide is a viable candidate (for heat sensitive materials), but requires special equipment to be used safely given its toxicity and flammability [6]. Furthermore, surfaces treated with ethylene oxide require an airing time before they are safe to handle due to the toxic byproducts generated by the ethylene oxide [7]. The use of hydrogen peroxide gas plasma can overcome these concerns as it generates a diffusion and plasma phase, thus making it a "partial" plasma sterilization technique

[5, 8, 9]. Challenges remain as the use of hydrogen peroxide requires long processing and ventilation times [7]. Using gamma rays for radiation sterilization requires sophisticated operator protection and a specialized site [6].

The various limitations of conventional sterilization techniques have led to investigations of plasma sterilization. Plasma is a quasi-neutral ionized gas consisting of electrons, ions, excited species, neutral molecules and atoms [10, 11]. When energetic electrons collide with the background gas, they can create biochemically active species: gas ions (e.g. O_2^+), atoms (e.g. O), and excited species (e.g. O^*, O_2^*) [12]. Current literature agrees that these reactive species and ions play a large role in sterilization and destroy or inactive microorganisms by three mechanisms by which plasma sterilizes a surface: ultra-violet (UV) irradiation of genetic material, chemical reactions with the plasma species, and plasma ion sputtering [13].

Previous studies have shown that reactive species and ions created in plasmas play a key role in sterilization. Therefore, increasing plasma density causes more surface reactions [12, 14]. This work seeks to understand how the plasma density affects the sterilization efficiency. On the other hand, an increased plasma density generally leads to large heating load to the sample surface due to the bombardment of the charged particles created in the plasma. To mitigate the risk of damage associated with heating, this work also studies the effects of a magnetic field on the confinement of plasma, i.e., energetic electrons. Understanding plasma properties and plasma interactions with materials is critical to exploring new processes for material modification and engineering.

Toxic chemicals in industrial wastewater pose a significant threat to public health and the environment [15–17]. These pollutants vary in structure, chemical stability, and composition, making it difficult for a single treatment to be used. Many are resistant to degradation and cannot be effectively treated using conventional methods such as chemical oxidation, membrane treatment,

and photodegradation [15, 16, 18]. Therefore, a simple and effective universal treatment is needed.

Tetramethylthionine chlorine, also known as methylene blue (MB), is a cationic dye frequently found in industrial wastewater due to its widespread use in manufacturing, biology, and medicine [15, 19–21]. While MB is not life-threatening in low doses, long-term MB exposure can cause various responses including vomiting, anemia, hypertension, cyanosis, and jaundice [20–22]. Therefore, it is necessary to effectively treat and remove MB before wastewater is introduced into the environment.

Various methods have been applied to remove MB. Ion-exchange resins remove chemicals via electrostatic interactions or van der Waals forces. These resins are designed to attract ions of the opposite charge. This poses a problem when trying to remove chemicals with opposing charges. Reverse osmosis and nanofiltration are used for treating drinking water in large scales but are expensive. The membranes become fouled and deteriorated There is also a problem with fouling and deterioration of the membranes used that require their own treatment or disposal.

Electrochemical methods are based on electrochemical oxidation, which may form a toxic by-product. Recent investigations show adsorption by AC to be an attractive method to remove harmful chemicals from wastewater and is cost-effective for treating large volumes [23]. Activated carbon is a versatile and effective adsorbent due to its high porosity, large surface area, and surface functional groups [16, 19]. The adsorption properties of AC can be further enhanced by chemical activation.

Conventional techniques for chemical activation of carbon are complex, time-consuming, and expensive [24]. Additionally, these techniques mainly include the addition of elements that could leach from the activated carbon adding to pollution [24]. Plasma treatment offers an alternative form of activated without these concerns. Plasma processing produces energetic electrons,

ions, and radicals that can increase the active functional groups on the surface of carbon and improve pore structure without toxic chemicals [24]. Plasma also offers the ability to generate specific chemical species and functional surface groups through the use of appropriate plasma gases, which allows the AC to be tailored for specific purposes.

Recent investigations show adsorption by activated carbon (AC) to be an attractive method to remove a multitude of harmful chemicals from large volumes of wastewater [23]. However, many as-derived ACs exhibit adsorption capacities inferior to that estimated from their surface area [25, 26]. A likely reason for this discrepancy is that some micropores are not accessible to impurities [25, 26]. A customary practice is to integrate a high-temperature (e.g. 900 °C) activation stage in combination with the use of large amounts of reactive chemicals to create mesopores and micropores. Plasma can improve pore structure at relatively low temperatures because the energetic electrons, ions, and radicals within plasma provide intensive localized heating. Plasma also offers the ability to generate specific chemical species and functional surface groups using appropriate plasma gases, which allows the AC to be tailored for specific pollutants.

Although AC is a versatile and effective adsorbent due to its high porosity, large surface area, and surface functional groups, it is traditionally produced from coal [16, 19, 27]. Production of AC from coal is expensive, non-renewable, and energy-intensive [27]. Problems with access to potable water are expected to increase in the coming years due to population growth and environmental factors [28]. More effective, renewable, and low-cost methods of water treatments that do not further endanger the environment or the global population are needed [28].

To address these limitations, this work studies plasma activation of biochar formed from renewable lignocellulosic material. Biochar is porous carbon derived from biomass pyrolysis, the thermal degradation of organic matter in an oxygen-poor environment [29–32]. The organic

materials used to create biochar include agricultural wastes, providing a sustainable alternative to coal without compromising current agricultural production [33]. Raw biochar has very poor adsorption capacity, therefore biochar requires chemical activation to compete with commercial AC [29, 31, 34]. Previous studies have investigated the physical and chemical surface properties of biochar but have not been able to establish an efficient process to activate biochar with desired characteristics. Conventional chemical activation techniques are complex, time-consuming, and expensive. Plasma treatment does not require high external heat, making it a more energy efficient processing method. This work aims to establish a plasma treatment that effectively activates biochar both at low temperatures and reduced processing times from hours to minutes. Additionally, the use of plasma improves pore structure through etching and offers the ability to generate functional surface groups using appropriate plasma gases, which allows the biochar to be tailored for specific purposes.

A group of chemicals that have been garnering attention are per- and polyfluoroalkyl substances (PFAS). PFAS are a group of environmentally persistent man-made chemical that have been used in industries world-wide and have been made in the United States since the 1950s [35–39]. Many industrial and consumer products contain PFAS which include non-stick coatings, firefighting foam, and food packaging [36, 38, 40].

The unique characteristics of plasma make it a promising alternative for energy-intensive processes. This project studies plasma-surface interactions in three different areas concerning public health: sterilization of surfaces, the re-activation of commercial activated carbon (AC), functionalizing surfaces, and chemical activations of biochar. This work is made of 4 sections as following:

Section I Cold plasma sterilization offers an efficient way to sterilize medical components and instruments. This paper reports using a magnetized plasma to realize low-temperature sterilization. A radio frequency dielectric barrier discharge is created in a quartz tube using a mixture of argon and oxygen gas. A uniform amount of *Escherichia coli* is applied onto glass slides and exposed to the plasma afterglow at different pressures with and without a magnetic field. Optical emission spectroscopy is used to identify the plasma species present. The magnetic field significantly promotes the intensity of the plasma and the sterilization efficiency. A process gas pressure of 100 mTorr presents the most effective treatment with a sterilization time less than one minute and sample temperature below 32 °C.

Section II The effects of O_2 plasma treatment on the adsorption capacity of activated carbon (AC) were investigated by varying the plasma treatment times. The surface properties of the AC were characterized by transmission electron microscopy (TEM), X-ray photoelectron spectroscopy (XPS), Fourier transform infrared spectroscopy (FTIR), and Zeta potential. The carbon was then applied to remove methylene blue (MB) from an aqueous solution. The adsorption kinetics and isotherm were also studied. Results showed that pseudo-second-order kinetics was the most suitable model for describing the adsorption of MB onto AC. Equilibrium data were well fitted to the Freundlich and Langmuir isotherm models. The highest adsorption capacity resulted from 4 minutes of O_2 plasma treatment. The 4-minute plasma treated AC had the best adsorption capacity for MB at 0.467 mg/mg. This work shows that activation of AC by plasma can open the micropore and increase the effectiveness of chemical removal.

Section III The combination of O_2 plasma and KOH were used to activate biochar. The effects of O_2 plasma treatment, KOH concentration, and treatment temperature on the adsorption capacity of biochar were investigated. The biochar was activated using various concentrations

of KOH. The plasma activated biochar was applied to remove methylene blue (MB) from an aqueous solution. The adsorption kinetics and isotherm were also investigated. Results showed pseudo-second-order kinetics was the most suitable model for describing the adsorption of MB onto biochar. Both the Freundlich and Langmuir isotherm models fit the equilibrium data. The highest adsorption capacity resulted from 10% KOH + 300 °C for 5 minutes. The maximum adsorption capacity was MB, 0.460 ± 0.008 mg/mg. This work shows that activation of biochar by plasma can improve adsorption capacity.

Section IV It was demonstrated that plasma treatment can improve PFOA adsorption. However, the exact mechanism remains unclear. The negative surface charge was shown to negatively impact PFOA adsorption which aligns with the hypothesis that PFOA would preferentially adsorb onto more positive surfaces due to its anionic state in water. Future studies should focus on elucidation of the exact PFOA adsorption mechanisms to AC and biochar. Additionally, pore volume distribution should be investigated using BET and imaging (TEM).

CHAPTER 2

BACKGROUND

2.1 Plasma basics

Matter exists in four natural states: solids, liquids, gases, and plasmas, **Figure 2.1**. Each phase differs in bond strength holding their particles together [41, 42]. The strength of these binding forces decreases in order from solid, liquid, and gas. Random kinetic energy (thermal energy) of its atoms or molecules and interparticle binding forces determines the state of matter [41].

When a solid or liquid is heated, its atoms or molecules gain thermal kinetic energy [41, 42]. As temperature increases, molecules become more energetic and are able to overcome the binding potential energy leading to a phase transition [41–43]. Plasma, the fourth state of matter, is an ionized gas, which refers to the process of free electrons converting neutral atoms or molecules to ions [10, 41, 43, 44]. Plasmas are created when ample energy is supplied to a gas causing the formation of charged particles [10, 41, 43, 44]. This energy knocks electrons free from atoms producing free electrons and ions. Plasma is generated using either thermal energy, adiabatic compression, energetic beams, or electric fields [44]. Raising the temperature of a substance until the required ionization is achieved can produce a plasma [41, 42, 44]. In nature, many plasmas are produced this way, but it is uncommon in the laboratory [41]. The application of an electric field is the gold standard for generating and maintaining low-temperature plasma(s) in the laboratory [41, 44].

Plasma is electrically conductive due to the free electric charges (electrons and ions) [41, 43–46]. Applying an electric field to a neutral gas accelerates stray electrons and ions present within

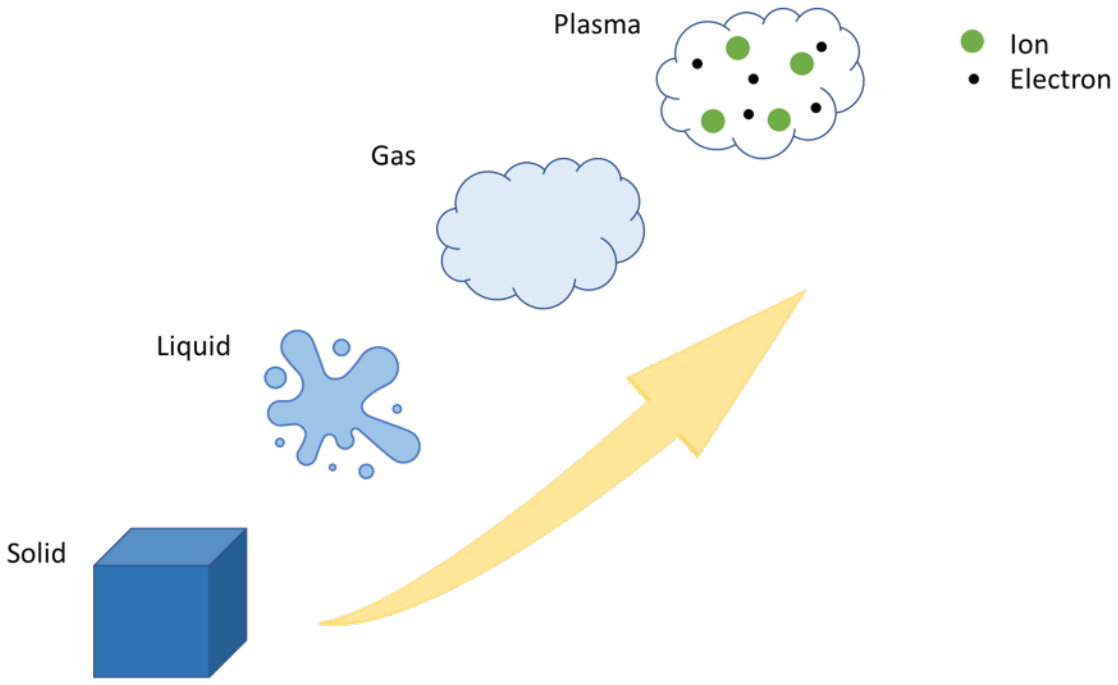

Figure 2.1 States of matter with increasing energy.

the gas [41, 43–46]. The electric field not only accelerates these free charged particles but also generates new charged particles due to collisions with other particles or with the surfaces of electrodes [41, 43–46]. This produces an avalanche of charged particles that is ultimately balanced by charge carrier losses, generating a steady-state plasma [41, 43–46]. Applying an electric field transfers energy more efficiently to the much lighter electrons than to the heavier ions, and electrons lose only a small portion of that energy after colliding with the heavy ion [41, 43–46]. Due to their extremely low mass, electrons cannot transfer much of their thermal energy as heat [41, 43–46]. Because the transfer of energy from electrons to heavy particles is slow, the electron temperature in plasma is usually higher than the ion temperature [41, 43–46]. A subdivision can be made between plasmas that are in thermal equilibrium and those that are not.

2.2 Thermal Equilibrium vs. Non-thermal Equilibrium

Thermal equilibrium implies that all of the species (ions, electrons, neutrals) have the same temperature [41, 43–46]. Thermal plasmas require high temperatures (> 4000 K) and examples of such are stars and fusion plasmas [41, 43–46]. Generally, thermal plasmas are described as being in 'local thermal equilibrium', implying that the temperatures of all plasma species are the same in a localized area within the plasma [41, 43–47]. Overtime, as electrons collide with heavy particles they can equilibrate their temperatures (Joule heating) and local thermal equilibrium can be assumed [41, 43–47]. Local thermal equilibrium is achieved when the electron number density is sufficiently high (> 10^{23} m^3) leading to a high frequency of elastic collisions between electrons and heavy species [41, 43–46]. Conversely, in non-local thermal equilibrium plasma the different plasma species are not the same temperature. In non-local thermal equilibrium plasma the electrons are characterized by much higher temperatures then the heavy particles [41, 43–46]. Electrons can only transfer small amounts of kinetic energy in elastic collisions to the ions [41, 43–46]. Electron temperature (T_e) is the highest in the system, far surpassing the temperatures of heavy neutrals (T_0) and ions (T_i) [43]. In steady state the electron temperature will be much higher than ion and neutral temperatures, therefore, electrons are mainly responsible for local deviations from neutrality. In most non-thermal plasmas the gas temperature is close to room temperature, whereas the T_e is about 1 eV (~10,000 K) [43].

Gas discharge plasmas, lab generated plasmas, can also be differentiated into local thermal equilibrium and non-local thermal equilibrium plasmas. This distinction is related to high pressure instead of high temperature[41, 43–46]. At high pressure there are more collisions which leads to efficient energy exchange between the species and, therefore, equal temperatures [41, 43–46].

In recent years, gas discharge plasmas have gained attention due to the ability to easily modify their parameters to suit specific purposes [46]. **Figure 2.2**, shows some of the range of plasma phenomena [49].

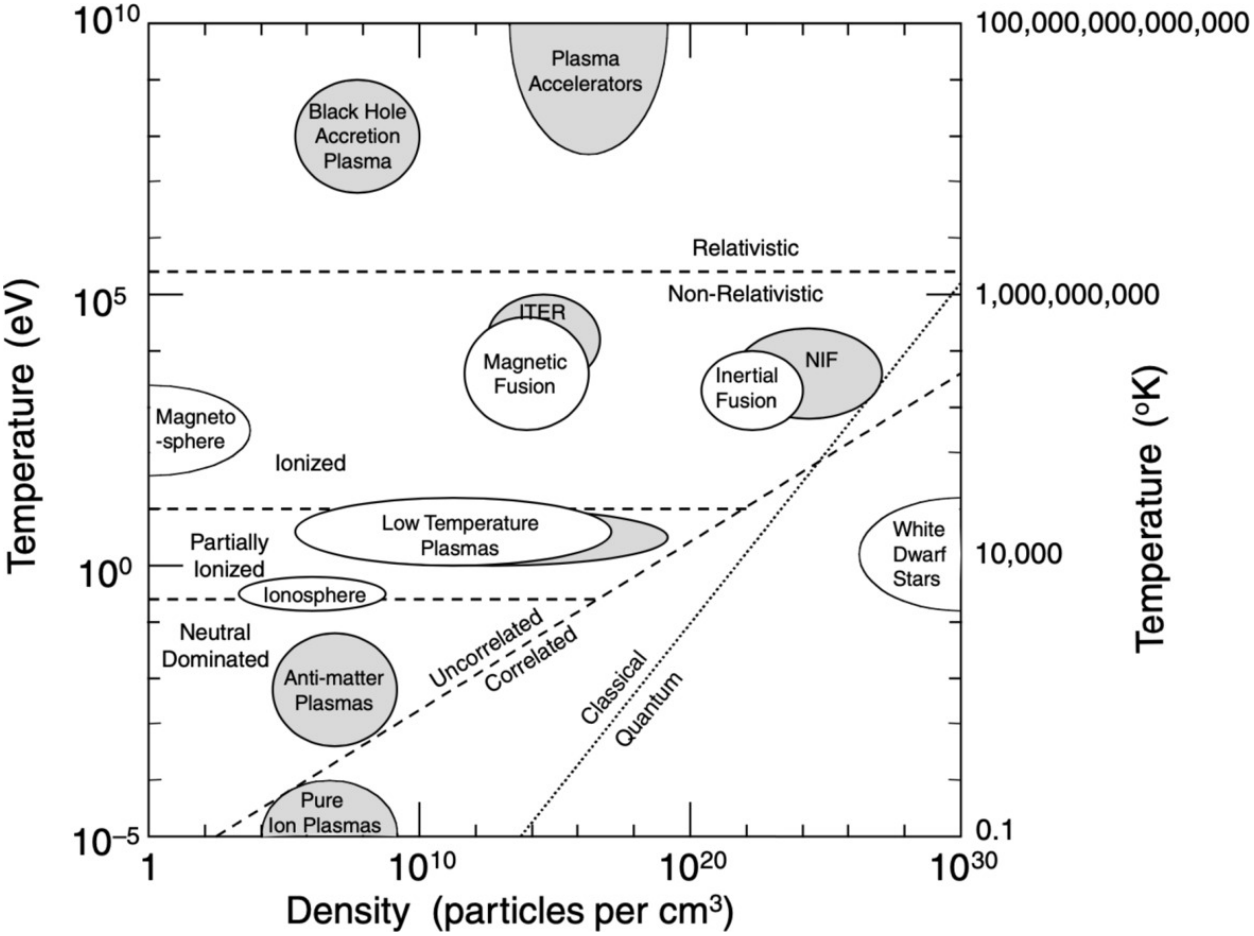

Figure 2.2 Range of plasma phenomena in regard to density and temperature [49]. © Copyright 2021 Elsevier.

Local thermal equilibrium discharges are typically used for applications where heat is desirable, due to their high temperatures (i.e. welding, cutting, spraying) [46]. Conversely, non- local thermal equilibrium discharges are used for applications where heat is not desirable (i.e. etching, deposition) [46]. The heavy particle temperature is low (usually not higher than room temperature), but the electron temperature is much higher because they are light and easily accelerated by the electric field [46]. The high electron temperature leads to inelastic electron

collisions [41, 43–46]. These inelastic collisions (e.g. electron impact ionization) sustain the plasma as well as create a chemically rich environment [41, 43–46]. Ionization and chemical processes in these plasma are directly determined by electron temperature, and are not so sensitive to thermal processes and the temperature of the gas [43].

2.3 Low-temperature Plasma

The main characteristics of plasmas are determined by the electron temperature (T_e) and the electron density (n_e) and are divided into categories according to temperature and pressure. A plot depicting where various plasmas lie in pressure-temperature space is shown in Figure 2.2. If the gas temperature is below 1 eV (~10,000 °C) , the plasma is considered low-temperature or non-thermal [12, 48]. Low-temperature plasmas, mostly generated under low-pressure (> 0.1 Torr) or vacuum conditions, are characterized by their non-equilibrium nature. In low-temperature plasmas, the electron temperature (e.g., a few eV) is much higher than the ion temperature (e.g., 0.06 eV) and neutral particle temperature (e.g., 0.03 eV). Therefore, low-temperature plasmas are particularly attractive for sterilization and surface modification where heat sensitive materials are involved [9, 12, 48].

Low-temperature plasmas are nonequilibrium in nature [50]. Electrons present in the plasma are far from equilibrium with neutrals and ions [50]. Nonequilibrium of electrons can be caused by: large spatial gradients, strong electric fields, fast temporal variations, and collisions with neutral particles [50]. The dominance of electron collisions with neutrals especially inelastic collisions, over Coulomb interactions ensures a non-Maxwellian electron distribution function (EDF) in weakly ionized plasmas [50]. As plasmas are heated, they become less collisional.

The difference in temperature between electrons and neutral particles in collisional weakly

ionized plasma is proportional to the square of the ratio of the electric field (E) and to the pressure (p) [43]. Because of this, the temperatures of electrons and neutrals only approach each other when the values of E/p are small, which is a basic requirement for local thermodynamic equilibrium in plasma [43]. Local thermal equilibrium plasma follows the laws of equilibrium thermodynamics and is characterized by a single temperature for all species at each point of space [43, 47].

2.4 Degree of ionization

Applying sufficient kinetic energy allows the atoms in the gas to overcome their ionizing potential, generating a plasma [10]. The degree of ionization (Eq. 2.1) is described by the ratio of electron density (N_e) divided by the sum of the density of electrons and the density of neutral molecules (N_n) [10, 43]:

$$\text{Degree of ionization} = \frac{N_e}{N_e + N_n} \tag{2.1}$$

Plasma can be characterized as weakly ionized or strongly ionized. This distinction is made based on the type of particle interactions. When the ionization degree is low, the plasma is weakly ionized, so the charge-neutral interactions dominate over the Coulomb interactions [41, 43]. Strongly ionized plasmas occur when the degree of ionization increases so that the Coulomb interactions become dominant [41, 43]. A fully ionized plasma has a degree of ionization close to unity and all particles are subjected to Coulomb interactions [41, 43].

Low-temperature plasmas are weakly ionized because the degree of ionization is less than 10^{-4} [10]. A low degree of ionization coincides with a low-density plasma. In a low density plasma, the neutral molecules surpass the electrostatic interactions of the charged molecules [10, 41, 43]. The plasma effects are impeded because charged particles have a higher probability of colliding with the neutral particles than other charged particles [10, 41, 43]. Conversely, as the degree of

ionization increases, electrostatic interactions take over [10, 41, 43]. An important research topic in low-temperature plasma is to promote the plasma density or ionization efficiency.

2.5 Alternating Current vs. Direct Current Excitation

In gas discharges, two ways to apply an electric field are by direct current and alternating current discharges. Direct current discharges generate plasma in a closed vessel with fixed internal electrodes [44, 46]. The active electrode (cathode) has a high negative potential relative to the ground anode, leading to sputtering of the cathode surface [44, 46]. When a potential difference is applied, the electric field accelerates the electrons from a cathode to an anode, causing them to gain energy and collide with other particles. Inelastic collisions lead to excitation and ionization [44, 46]. The excitation collisions followed by de-excitation emit radiation and are responsible for the 'glow' discharge [44, 46]. The ionization collisions give rise to new ions and electrons [44, 46]. The ions are accelerated by the electric field toward the cathode, where the ion bombardment of the surface causes the emission of secondary electrons [44, 46]. Ion bombardment can cause physical sputtering of the cathode surface [44, 46]. Sputtering is the release of atoms of the cathode material due to the ion bombardment, and occurs at sufficiently high voltages [44, 46]. The electrodes may eventually erode, or they will accumulate positive or negative charges until the discharge is extinguished [44, 46]. This buildup of charge can be overcome by using alternating current, so that each electrode will act alternately as the cathode and anode [44, 46].

Alternating current discharges commonly operate at a radio frequency of 13.56 MHz [44, 46, 51]. The alternating electric field accelerates electrons, which gain sufficient energy to cause an ionization avalanche [44, 51]. When the applied voltage is positive, the electrons will be accelerated toward the electrode [44, 46, 51]. In the case of capacitively coupled plasma, as is used in this work,

the radio frequency voltage is applied across two parallel metal plates, generating an oscillating electric field between them [42, 44, 46, 51]. The heavier ions respond only to time-averaged electric fields. Sheaths form next to the electrodes to keep the plasma neutral [44, 46, 51]. These sheaths provide an electric field perpendicular to the electrode surface and repel fast moving electrons while also accelerating ions [44, 46, 51].

The use of radio frequency discharge plasma is advantageous because electrodes can remain outside of an insulated chamber (dielectric barrier), eradicating the risk of reactions between the gas and electrodes as in direct current discharges [44]. Plasma created through a dielectric barrier discharge, as shown in **Figure 2.3**, is generated by two electrodes separated by a dielectric barrier such as a quartz tube [31, 44, 52]. The standard frequency for radio frequency sources is 13.56 MHz [44, 51]. A carrier gas runs between the electrodes while still separated from them by the dielectric barrier [31, 44, 52]. One electrode is a high voltage electrode while the other one is grounded [31, 44, 52]. Radio frequency discharge plasma can operate in a wide range of pressures with the addition of a magnetic field, modulating the plasma properties (e.g. plasma density and electron temperature) [44]. Dielectric barrier discharge has numerous applications such as: sterilization, surface treatment, and bacterial inactivation.

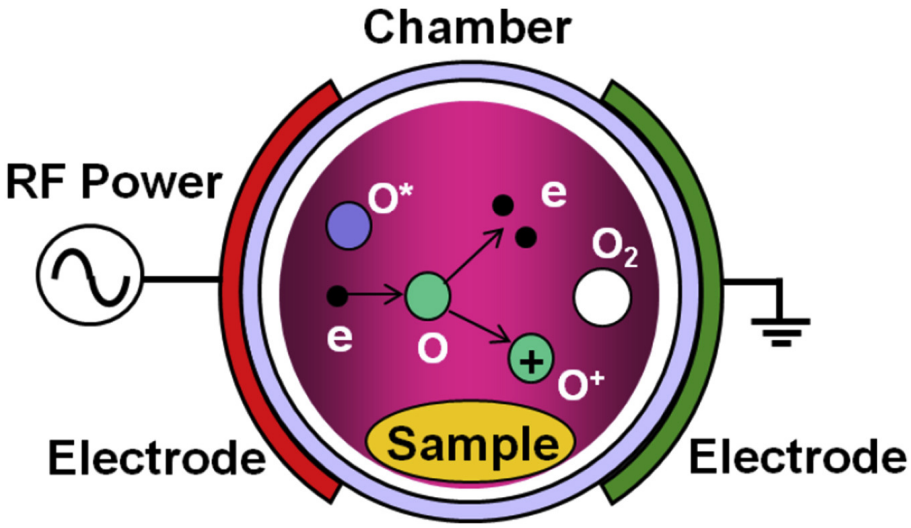

Figure 2.3 The dielectric barrier discharge excited by radio frequency power [31]. © Copyright 2015 Elsevier.

2.6 Plasma properties

2.6.1 Quasi-neutrality

Plasmas are considered to be quasi-neutral, meaning that the net electric charge is zero because the concentrations of positively charged and negatively charged particles are balanced [10, 41, 43]. Fundamentally, plasma tends to remain electrically neutral [10, 41, 43]. Within plasma, microscopic areas of charge separation resulting in small changes in neutrality may occur, but there is no net charge over a macroscopic region [10, 41, 43]. Electrons are then pulled back to their original positions by the resultant electric fields [10, 41, 43]. Due to their inertia, the electrons which are pulled back oscillate about the initially charged region [10, 41, 43]. The high frequency of this oscillation preserves quasi-neutrality on a time-average basis [10, 41, 43]. Naturally occurring changes in plasma neutrality can only occur over distances in which disturbances to electrical neutrality can be restored [10, 41, 43, 47]. Thus, the number densities of electrons (n_e) and ions

(n_i) with charge state Z are locally balanced, i.e. [53]:

$$n_e \simeq Zn_i \tag{2.2}$$

2.6.2 Collective Properties of Plasma

The behavior of plasmas differs from that of solids and ordinary fluids because plasma properties depend on the collective effects of particle interactions [41]. Collective effects are responsible for the abundance of physical phenomena in plasma [41]. Each charged particle within the plasma interacts simultaneously with surrounding charged particles due to the long range effects of electromagnetic forces [41, 53]. Therefore, the macroscopic field usually dominates over microscopic fluctuations, and a net charge imbalance $\rho = e(Zn_i - n_e)$, will immediately produce an electrostatic field according to Gauss's law [53]:

$$\nabla \cdot \mathbf{E} = {}^{\rho}/_{\varepsilon_0} \tag{2.3}$$

Similarly, the same set of charges will give rise to a current density $J = e(Zn_i\upsilon_i - n_e\upsilon_e)$, inducing a magnetic field according to Ampere's law [53]:

$$\nabla \times \mathbf{B} = \mu_0\mathbf{J} \tag{2.4}$$

It is these internally driven electric and magnetic fields that largely determine the dynamics of the plasma, including its response to externally applied fields [53].

The motion and basic particle interactions are electromagnetic; the behavior of the particles

is governed by their own internal fields and by externally applied fields [41]. For our purposes quantum effects are negligible [41].

2.6.3 Debye shielding

The Debye length (λ_D) is a length parameter characterizing the plasma quasi-neutrality and depends equally on the plasma's temperature and density [10, 41, 43, 53, 54]. It represents the characteristic distance of charge separation and plasma polarization [10, 41, 43]. The Debye length is the maximum distance over which plasma can support departures from macroscopic neutrality [10, 41, 43]. This is because within this length, charged particles are able to move freely to neutralize any regions of excess space charge in response to Coulomb forces that appear [10, 41, 43]. In other words, the Debye length is the distance over which balance is obtained between thermal particle energy, and the electrostatic potential energy resulting from any charge separation [10, 41, 43, 47, 54].

The Debye length can also be considered a measure of how far the electrostatic effect of an individual charged particle can be felt. In a plasma, the charged particles arrange in such a way so that mobile charge carriers (e.g. electrons) shield electrostatic fields within a distance of the Debye length (λ_D) [10, 41, 43, 54, 55]. This shielding results from the collective effects of plasma particles. The Debye length is directly proportional to the square root of the temperature (T) and inversely proportional to the square root of the electron number density (n_e). The Debye length is defined mathematically as [10, 41, 43, 54, 55]:

$$\lambda_D = \left(\frac{\varepsilon_o k T_e}{n_e \, e^2} \right)^{\frac{1}{2}} \tag{2.5}$$

In this equation, ε_0 is the permittivity of free space, k is the Boltzmann constant (1×10^{-23} J/K), T_e is the electron temperature, n_e is the electron density, and e is the charge of an electron.

In order for a plasma to exist the physical dimensions of the system be large compared to λ_D [10, 41, 43, 54, 55]. If this criterion is not met then there is not adequate space for the collective shielding effect, and the charged particles will not exhibit plasma behavior. Therefore, a first criterion for the definition of plasma is $L \gg \lambda_D$, where L is a characteristic dimension of plasma [10, 41, 43, 54, 55].

The Debye length can also be considered as a measure of the distance over which fluctuating electric potentials may appear in a plasma [10, 41, 43, 54, 55]. A Debye sphere is a sphere within the plasma whose radius is equal to λ_D. Charged particles within the Debye sphere effectively screen outside electrostatic fields. Consequently, each charge only interacts collectively with the charges that lie inside its Debye sphere [10, 41, 43, 54, 55]. The effects of a single charge on other charges residing outside of the sphere is effectively negligible. The number of electrons N_D within a Debye sphere is given by [10, 41, 43, 54, 55]:

$$N_D = \frac{4}{3}\pi n_e \lambda_D^3 \tag{2.6}$$

The Debye shielding (**Figure 2.4**) effect is characteristic of all plasmas. This leads to a second condition to determine if there is a plasma: there must be sufficient electron density (n_e) within the sphere to produce shielding [10, 41, 43, 54, 55]:

$$N_D \sim n_e \lambda_D^3 \gg 1 \tag{2.7}$$

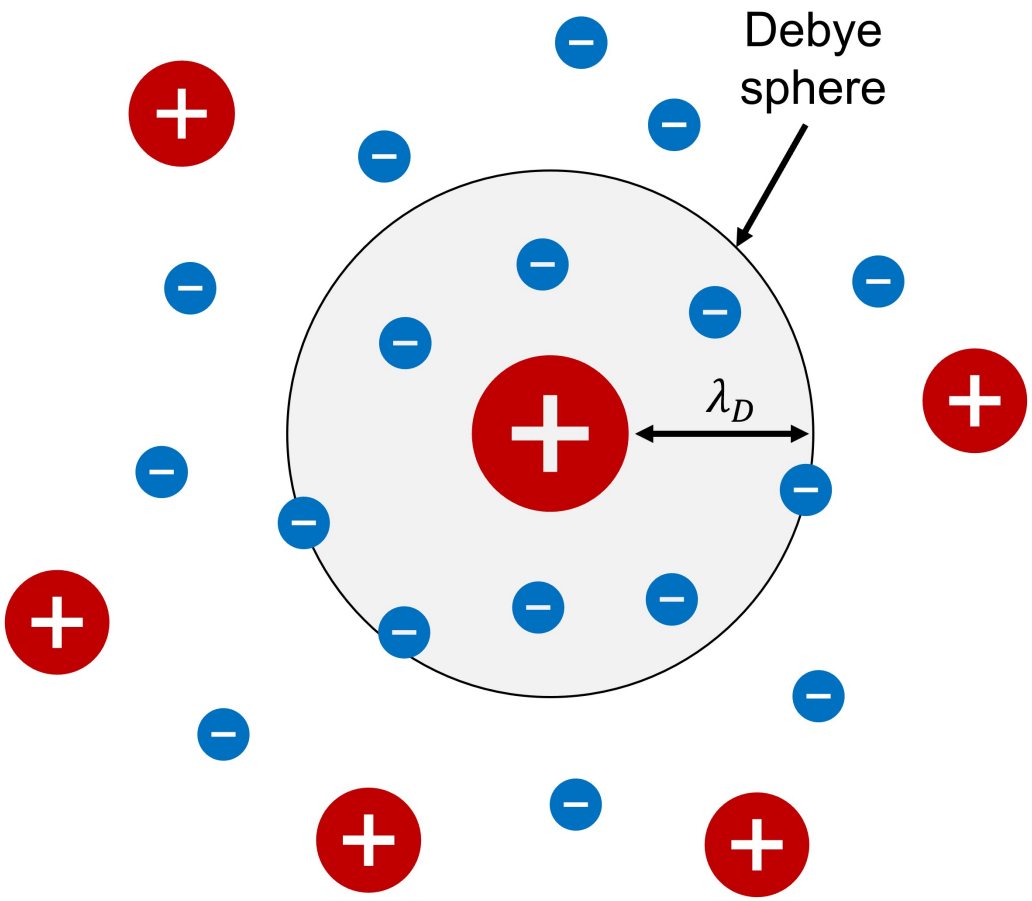

Figure 2.4 Representation of Debye shielding of a charged sphere in a plasma.

This indicates that the average distance between electrons, $\overline{r} \sim n^{\frac{-1}{3}}$, must be much smaller than λ_D [41, 55]. The quantity defined by [10, 41, 43, 54, 55]:

$$g = \frac{1}{n_e \lambda_D^3} = \frac{1}{N_D} \tag{2.8}$$

This is known as the plasma parameter and the condition:

$$g \ll 1 \tag{2.9}$$

is called the plasma approximation. It is necessary that $g \ll 1$ to ensure that dominance of collective

effects over particle collisions, thus becoming a plasma [41, 43, 53–55].

The plasma parameter may also be obtained using potential energy. The average potential energy of interaction between two charges within in plasma is $U \sim \frac{q^2}{\overline{r}}$ [55]. The mean distance of closest approach:

$$r_c \equiv \frac{e^2}{4\pi\epsilon_0 T} \tag{2.10}$$

Balancing the one-dimensional thermal energy of a particle with the repulsive electrostatic potential of a binary pair gives [55]:

$$\frac{1}{2}mv_t^2 = \frac{e^2}{4\pi\epsilon_0 r_c} \tag{2.11}$$

If the ratio of $\overline{r}/r_c$ is small then the charge particles are dominated by the electrostatic field of another particle and their kinetic energies are small compared to the interaction potential energies [55]. The electron density is low, and the Debye radius is large resulting in greater deviations from quasi-neutrality. These plasmas are termed 'strongly coupled'. Conversely, if the ratio is large then strong electrostatic interactions are relatively rare. In this instance, the diffusion of electrons and ions is ambipolar, where the charged particles move at the same rate in opposite directions [43, 55]. Electron density is high, and the Debye radius is small. A high electron density decreases the distance between electrons to be smaller than the Debye length [10, 41, 43]. Such plasmas are termed 'weakly coupled' and a typical particle is influenced by all of the other particles within its Debye sphere. This very rarely causes any sudden change in its motion, thus, the plasma is quasi-neutral [43, 55].

The average kinetic energy of a plasma particle is only T, so that [55]:

$$\frac{U}{K} \sim \frac{q^2 n^{\frac{1}{3}}}{T} \sim \frac{1}{n^{\frac{2}{3}} r_D^2} = g^{\frac{2}{3}} \tag{2.12}$$

Therefore, if $g \ll 1$ then the average potential energy is substantially smaller than the average kinetic energy of a particle [55]. It can be seen that the case $\Lambda \ll 1$, in which the Debye sphere is sparsely populated, corresponds to a strongly coupled plasma. Likewise, the case $\Lambda \gg 1$, in which the Debye sphere is densely populated, corresponds to a weakly coupled plasma [10, 41, 43, 55].

2.6.4 Plasma Frequency

The stability of its macroscopic charge neutrality is an important plasma property [10, 41, 43]. When plasma is disturbed from equilibrium, the resulting internal space charge fields give rise to collective particle motions to reestablish charge neutrality [10, 41, 43]. This happens due to local charge separation resulting in an electric field, which exerts a force on the electrons and ions [10, 41, 43]. The internal electric field acts to reduce the charge separation by collectively accelerating the electrons back to their initial position to restore charge neutrality [10, 41, 43]. However, their inertia carries them past their neutral position, and an electric field is produced in the opposite direction [10, 41, 43]. Because these oscillations are high-frequency oscillations, the larger mass of the ions makes them unable to follow the motion of the electrons [10, 41, 43]. This sequence is repeated resulting in fast collective oscillation of electrons about the heavy ions [10, 41, 43]. Plasma macroscopic charge neutrality is preserved on a time-average basis [10, 41, 43]. The angular frequency of these oscillations is called the plasma frequency and is given

by [10, 41, 43]:

$$\omega_p = \left(\frac{n_e e^2}{m_e \varepsilon_o}\right)^{\frac{1}{2}} \tag{2.13}$$

Collisions between electrons an neutral particles can dampen these oscillations [10, 41, 43]. Plasma oscillations can only develop if the mean free time τ between collisions is long enough compared to the oscillation period [10, 41, 43]:

$$\omega_p \tau \gg 1 \tag{2.14}$$

2.6.5 Plasma Sheaths

While plasmas as a whole are quasi-neutral, their boundary layer is not. Plasmas develop boundary layers or sheaths at the interface between a plasma and a solid (i.e. chamber wall, electrode, substrate, probe) [42, 44, 46, 51, 56]. This Debye sheath is a layer in plasma that has a high density of positive ions, hence an overall positive charge, that balances an opposite negative charge on the surface of a material with which it is in contact. As previously discussed, electron thermal velocity $(eT_e/m)^{1/2}$ is at least 100 times the ion thermal velocity $(eT_i/M)^{1/2}$ because $m/M \ll 1$ and $T_e \gtrsim T_i$ (given in volts) [42, 56]. On a short timescale the fast-moving electrons are not confined and near the walls may escape and be lost to the walls, resulting in charging the surface negative relative to the bulk plasma [42, 44, 46, 51, 56]. The positive ions left in the plasma at the boundary leads to a potential profile $\Phi(x)$ that is positive within the plasma and falls sharply to zero near both walls [42, 44, 46, 51, 56]. This acts as a confining potential for electrons. The force acting on the electrons is directed into the plasma; this reflects electrons traveling toward the walls back into the plasma [42]. Conversely, ions entering the sheaths are accelerated into the walls, as

shown in **Figure 2.5** [42].

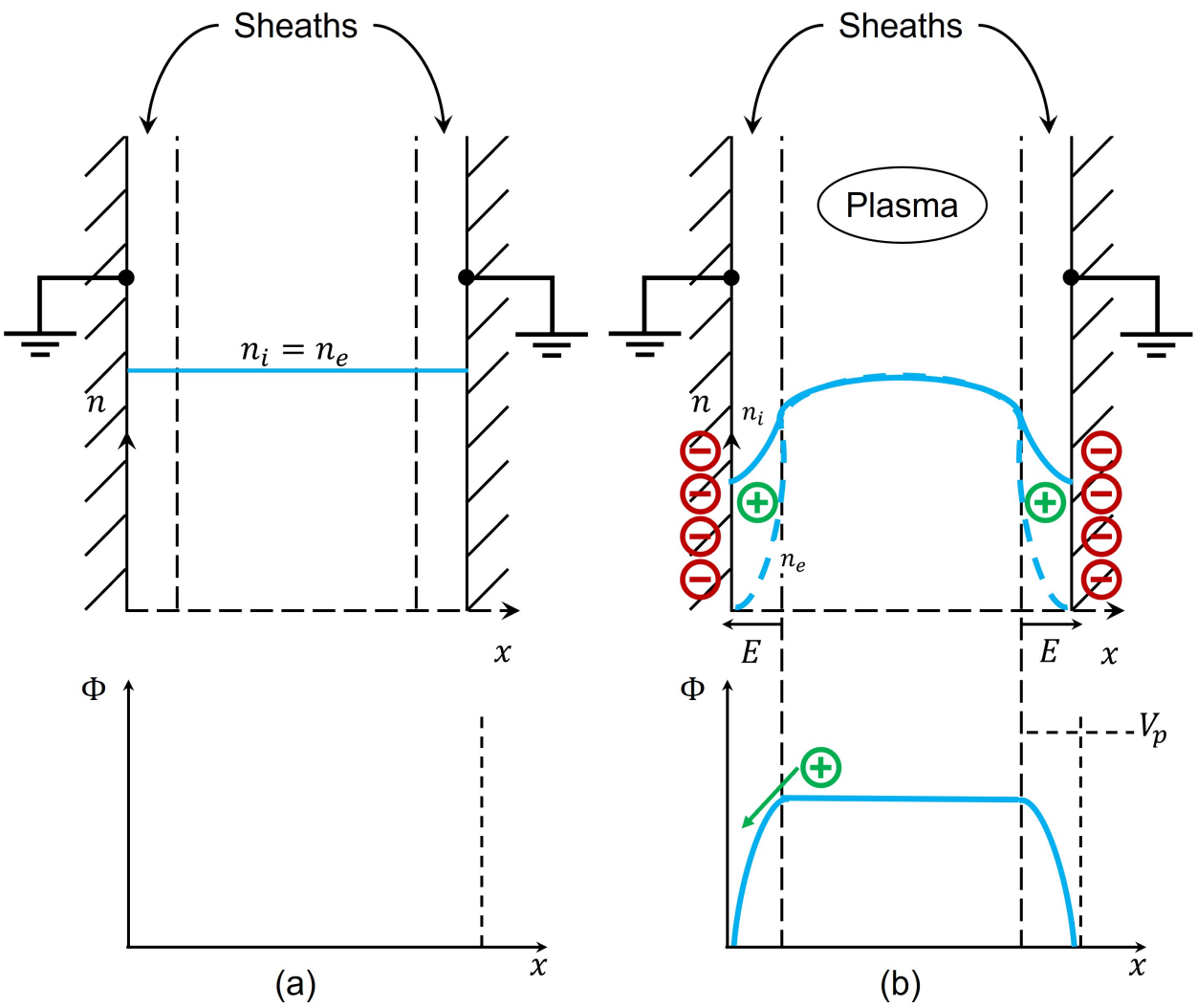

Figure 2.5 The formation of plasma sheaths: (a) initial electron and ion densities and potential, (b) electron and ion densities, electric field, and potential after the formation of plasma sheaths [54].

2.6.6 Interactions in Plasma

Plasma conductivity is governed by electron density (n_e) and frequency of electron-neutral collisions (ν_{en}) [43]. The electron density can be calculated and the frequency of electron-neutral

collisions is proportional to pressure and can be found numerically for specific gases [43]. There are two types of interactions in plasma: charge-charge and charge-neutral [41]. The electrostatic force of a charged particle will govern its interaction with other charged particles (two like electric charges repel while opposite charges attract) [41]. This electrostatic force, or Coulomb force, between two charged particles is inversely proportional to the square of the distance separating them [41]. This is shown by Coulomb's law:

$$|F| = K\frac{|q_1 q_2|}{r^2} \tag{2.15}$$

Here, K is Coulomb's constant ($\approx 8.988 \times 10^9\ N \cdot m^2 \cdot C^{-2}$), q_1 and q_2 are the magnitudes of the charges, and r^2 is the distance. Along with electrostatic forces, a magnetic field associated with moving charged particles will produce a force on other moving charged particles [41]. For charged and neutral particle interactions, if the charged particle travels close enough its electric field will distort the neutral particle's electron cloud [41]. When the distance between the centers of the interacting particles is sufficiently small the perturbation of the orbital electrons can induce electric dipole moments [41].

2.7 Collisional Plasma

The physiochemical properties of plasma are governed by the microscopic elementary processes, atomic and molecular collisions [57]. Plasma is chemically active due to the charged particles present. Therefore, the nature of the parent neutral gas also influences plasma properties because it dictates what type of species may be present [57]. For instance, the formation of negative ions in electronegative gases, such as molecular oxygen, can modify the equilibrium of charged

particles. The large negative ions introduce additional time scales and alter the quasi-neutrality equation of the plasma [57]. In general, plasmas can be considered to be either collisional or collisionless. Collisionless plasmas are thus named because collisions between plasma particles are so infrequent that their effects on plasma dynamics are negligible [10, 43, 58]. Most of the plasma in near-Earth environment, such as the ionosphere, can be treated as collisionless [10, 43, 58]. The majority of technological applications utilize collisional plasmas, which are plasmas in which collisions occur at a high enough frequency as to effect plasma behavior [10, 43, 58].

Collisional plasmas are further divided into two classes, fully and partially ionized. Fully ionized plasmas consist of only electrons and ions, whereas, partially or weakly ionized plasmas contain a large number of neutral particles [10, 54]. In weakly ionized plasmas, most collisions occur between electrons and neutrals. Conversely, in fully ionized plasmas the dominant collision process is between charged particles [10, 54].

In weakly ionized plasma neutral particles impede the motion of charged particles. When an electron collides with a neutral atom, depending on the rebound angle, it may lose a portion or all of its momentum [10, 54]. When particles collide energy and momentum must be conserved [42, 57, 58]. Through these collisions, electrons can transfer energy to other neutral particles which results in many different processes such as ionization, excitation, and dissociation. Three specific types of collisions are elastic, inelastic, and superelastic [42, 43, 57, 58].

2.8 Elementary Plasma Processes

In order to accurately describe the reactions occurring within plasma we must first understand the motion of the particles. A diverse range of phenomena may occur when two particles collide. For example, one of both particles may alter their energy or momentum, neutral particles

may become ionized and vice versa [54]. Electrons are the first to receive energy from electric fields due to their low mass and high mobility [43]. Electrons are the primary energy carriers in plasma and can transfer this energy to other particles via collisions [43]. If the energy carried by the electron is sufficient, the collision, and subsequent transfer of energy, may result in a reaction. Electrons colliding with atoms result primarily in elastic scattering and inelastic processes such as ionization. Although, other plasma-chemical processes such as dissociation may also result from electrons transferring energy to other plasma particles [43, 54]. The main outcomes for ions colliding with atoms are elastic scattering and resonant charge transfer. There are numerous other important processes that occur in molecular gases including dissociation, dissociative recombination, processes involving negative ions (i.e. attachment, detachment, and positive-negative ion charge transfer), and processes involving excitation of molecular vibrations and rotations [43, 54].

2.8.1 Collisions and Fundamental Parameters

Electrons transfer energy to other plasma particles through collisions, and if energy transferred is sufficient, a reaction or plasma-chemical process may result. The rates of these plasma-chemical processes depends upon the number of electrons possessing ample energy to initiate them. Electrons within plasma possess a variety of energy levels, and this distribution can be described by the electron energy distribution function, $f(\varepsilon)$, which is the probability density for an electron to have the energy ε [43]. This energy is in the form of thermal kinetic energy $\varepsilon = \frac{1}{2}m\upsilon^2 = \frac{3}{2}kT$ [42, 43].

The electron energy distribution function depends on plasma conditions such as gas composition and electric field. It can vary from the equilibrium distribution. Commonly the electron energy distribution function is determined primarily by the electron temperature T_e and can be

described by the Maxwell-Boltzmann distribution function [41, 43]:

$$f(\varepsilon) = 2\sqrt{\frac{\varepsilon}{\pi\,(kT_e)^3}}e^{\left(\frac{-\varepsilon}{kT_e}\right)} \tag{2.16}$$

where k is the Boltzmann constant, and when temperature is given in electron volts (eV) then $k = 1$ and can be omitted [43]. The mean electron energy in this case is proportional to the electron temperature as follows [43]:

$$\langle\varepsilon\rangle = \int_0^\infty \varepsilon f(\varepsilon)\,d\varepsilon = \frac{3}{2}T_e \tag{2.17}$$

These elementary processes are governed by the cross section, mean free path, interaction frequency, reaction rate, and reaction rate coefficient [43, 54, 58]. The most fundamental characteristic is the cross section. The cross section is the circular area σ, centered on one particle, in which the center of another particle must be in order for an elementary process to occur [43, 54, 58]. This distance between the center of the two reactant molecules must be less than the sum of their radii. Consider two colliding particles to be hard elastic spheres with radii r_A and r_B, their collisional cross section is equal to [10, 43, 54, 58]:

$$\sigma = \pi\,(r_A + r_B)^2 = \pi r_{AB}^2 \tag{2.18}$$

The interaction radius and cross section can exceed the geometric size of a particle because of long-distance forces acting between electric charges and dipoles.

The mean free path λ describes the average distance a particle travels before having a collision [10, 43, 54]. The mean free path of one particle "A" will travel before colliding or

interacting with particle "B" can be calculated as:

$$\lambda = \frac{1}{n_B \sigma} \tag{2.19}$$

where n_b is the number density (concentration) of the B particles. The interaction or collision frequency, ν, is the number of collisions per second that an incident particle has with the target population [10, 43, 54, 58]. Therefore, the interaction frequency of particle A colliding with B can be defined as the ratio of their relative velocity υ to the mean free path λ:

$$\nu_A = n_B \sigma \upsilon \equiv \tau^{-1} \tag{2.20}$$

where the inverse of the collision frequency, τ, is the mean time between interactions and is calculated as [54]:

$$\tau = \frac{\lambda}{\upsilon} \tag{2.21}$$

The rate constant, K, is the collision frequency per until density [54]:

$$K = \sigma \upsilon \tag{2.22}$$

A range of particle velocities results in different collision frequencies, therefore, an average of particle collisional velocity is needed [10]. Considering the velocity distribution function $f(v)$ and dependence of the cross section σ on the particle's velocity, the interaction frequency of particle

A with another particle B can be defined as:

$$\nu_A = n_B \int f(\upsilon)\sigma(\upsilon)\upsilon \, d\upsilon = \langle \sigma\upsilon \rangle n_B \tag{2.23}$$

The reaction rate, w, is defined as the number of elementary processes which take place per unit volume per unit time [43, 54]. To calculate the reaction rate for biomolecular processes, the number densities and interaction frequency of the colliding partners are multiplied together [43, 54]. Therefore, for the process A+B, the reaction rate can be calculated using the interaction frequency of partner A with partner B, ν_A, and the number density of particles A, n_A:

$$w_{A+B} = \nu_A n_A = \langle \sigma\upsilon \rangle n_A n_B \tag{2.24}$$

The factor $\langle \sigma\upsilon \rangle$ is the reaction rate coefficient, k, which can be calculated using the velocity distribution function and the cross sections of the colliding particles [43]. The reaction rate coefficient for a bimolecular reaction can be calculated as:

$$k_{A+B} = \int f(\upsilon)\sigma(\upsilon)\upsilon \, d\upsilon = \langle \sigma\upsilon \rangle \tag{2.25}$$

The reaction rate coefficient includes information on the energy distribution functions and depends on temperatures or mean energies of the collision partners, whereas the reaction cross section, σ, is generally a function of velocity [43, 54].

2.8.2 Elastic and Inelastic Collisions

Elementary processes that occur within plasma can generally be subdivided into three

classes: elastic, inelastic, and super-elastic [42, 43, 57, 58]. Collisions conserve energy and momentum, alternatively, the total momentum and energy of the colliding particles before and after collision are equal [42, 57, 58]. Electrons and fully stripped ions only possess kinetic energy, whereas atoms and partially stripped ions are influenced by changes in potential energy due to internal energy level structures. The changes in potential energy can result in excitation, de-excitation, or ionization [42, 57, 58]. The sum of the kinetic and potential energy, or total energy, is conserved in a collision [42, 57, 58].

Elastic collisions are those in which the internal energies of the particles do not change, momentum is redistributed, and the total kinetic energy is unchanged [42, 43, 57, 58]. Although the total kinetic energy is conserved in elastic processes, the kinetic energy is generally exchanged between particles and results in geometric scattering [42, 43, 57, 58].

$$e^-_{fast} + A_{slow} \rightarrow e^-_{less\ fast} + A_{less\ slow}$$

During inelastic collisions energy is transferred from the kinetic energy of colliding particles into internal energy [42, 43, 57, 58]. During inelastic collisions, momentum is redistributed between particles, but a small amount of the initial kinetic energy is transferred to internal energy in one or more of the particles causing excited states or ions to form (i.e. excitation and ionization) [42, 43, 57, 58]. Thus, there is less kinetic energy than before, and the sum of kinetic energies is not conserved.

$$\begin{aligned} e^-_{fast} + A &\rightarrow e^-_{slower} + A^* \\ &\rightarrow e^-_{slower} + A^+ + e^- \end{aligned}$$

Finally, in super-elastic collisions there is more kinetic energy after the collisions because

while momentum is conserved, the internal energy in particles entering into a collision is transferred to kinetic energy [42, 43, 57, 58]. This usually occurs when an excited atom is de-excited by a collision, increasing the sum of kinetic energy [42, 43, 57, 58].

$$A^*_{slow} + B_{slow} \rightarrow A_{faster} + B_{faster}$$

2.8.3 Elastic Collisions

Lighter particles (m) (i.e., electrons) cannot lose much energy elastically to heavy particles (M) [58]. The most that can be lost is a fraction $2m/M$ [58]. However, substantial changes in momentum can occur [58]. A moving particle striking elastically a stationary one of equal mass head-on can transfer all of its kinetic energy [58]. Lighter particles can lose almost all their kinetic energy through inelastic collisions with heavier objects [58]. No more than half of a particles kinetic energy can be lost when two particles of equal mass collide inelastically [58]. Long-range Coulomb forces may dominate binary collisions in which at least one particle is charged [58].

2.8.3.1 Coulomb Collisions

Elastic collisions between charged particles (electron-electron, electron-ion, and ion-ion) due to their electric fields are called Coulomb collisions [43, 54, 57, 59]. Charged particles moving through plasma experience the Coulomb electric field of the charged particles in their vicinity [43, 57, 59]:

$$\mathbf{E}(\mathbf{r}) = \frac{q}{4\pi\epsilon_0}\frac{r}{r^3} \tag{2.26}$$

The Coulomb potential energy of an electron in an atom of atomic number Z is [60]:

$$U(r) = \frac{Zq_1q_2}{4\pi\epsilon_0 r} \tag{2.27}$$

where r is the distance of the electron from the nucleus and ϵ_0 is the vacuum permittivity.

Because the Coulomb force is inversely proportional to the squared distance between the spheres ($1/r^2$) is a long-range interaction [41]. The charged particle undergoes a continuous deflection due to the simultaneous Coulomb interactions with many particles, of which the closest encounters have the largest deflections [41, 43, 54, 57, 59]. The multiple Coulomb interactions can be thought of as many simultaneous binary interactions. Their cross sections are high with respect to those of collisions with neutral partners, but they are much less frequent in discharges with low degrees of ionization [43]. The frequency of Coulomb collisions depends on the ionization degree of the plasma. Coulomb collisions are dominant in plasmas that are considered fully ionized with an ionization degree of > 0.01 [57].

Consider the potential energy of interaction for a collision between two perfectly elastic hard spheres with radii R_1 and R_2 [41]:

$$U(r) = 0 \text{ for } r > R_1 + R_2 \tag{2.28a}$$

$$= \infty \text{ for } r < R_1 + R_2 \tag{2.28b}$$

In terms of the impact parameter, $b = 4\pi\epsilon_0 r$, which is the minimum distance of approach if there were no interaction, when $b > R_1 + R_2$ there is no interaction [41, 43]. However, when $b < R_1 + R_2$ the particles collide. Because the spheres are impenetrable, we have $r > R_1 + R_2$ and

an interparticle potential energy function equal to zero, $U(r) = 0$. After colliding with the bounded electron at rest, the ionizing electron is scattered along the angle χ which is given by [41, 57]:

$$\chi = \pi - 2 \int_{r_m}^{\infty} \frac{b}{r^2} \left[1 - \frac{b^2}{r^2} \right]^{\frac{1}{2}} dr \tag{2.29}$$

where $r_m = R_1 + R_2$ is the distance of closest approach. This integral can be solved further by defining a new variable $y = b/r$ and write (Equation 2.29) in the form:

$$\chi = \pi - 2 \int_{0}^{b/r_m} \left(1 - y^2 \right)^{-1/2} dy \tag{2.30}$$

which gives

$$\chi = \pi - 2 \sin^{-1}(b/r_m) \tag{2.31}$$

The Coulomb logarithm $\ln \Lambda$ is a fundamental quantity in basic plasma physics. It quantifies the dominance of small-angle scattering in a weakly coupled plasma [61]:

$$\Lambda = \lambda_D / b_{min} \tag{2.32}$$

where λ_D is the debye length, the effective maximum impact parameter for two-body scattering, and b_{min} is the characteristic length to be determined [61]. Most frequent Coulomb deflections result in a small deviation of the particle path before it encounters another free charge. To produce an effective 90 ° scattering and momentum transfer, many such glancing collisions must be accumulated. In classical scattering theory $b_{min} = b_0$, where b_0 is the impact parameter for 90 ° scattering between

two particles [41, 61]:

$$b_0 = \frac{q_1 q_2}{4\pi\epsilon_0 \mu \upsilon^2} \tag{2.33}$$

where q_1 and q_2 are the charges of particles 1 and 2 respectively, μ is the reduced mass ($\mu = \frac{m_1 m_2}{m_1+m_2}$), and υ is the relative velocity. The quantity μ is the reduced mass, which is very similar to the electron mass because the mass of the nucleus is much larger than the mass of an electron, so $1/\mu = 1/m_e$ and in most work the reduced mass can be replaced by m_e [60].

The cross sections of Coulomb collisions are strongly dependent on the kinetic energy of the colliding particles. If we assume two particles with the same charge and, for simplicity, one of the particles is at rest, a scattering even takes place if the Coulomb interaction energy ($U \sim q^2/b$, where b is the impact parameter) is about the kinetic energy ε of a moving particle [43]. Then, the impact parameter ($b \sim q^2/\varepsilon$) and the reaction cross section σ can be estimated as πb^2 giving the equation:

$$\sigma(\varepsilon) \approx \pi \frac{q^4}{(4\pi\varepsilon_0\varepsilon)^2} \tag{2.34}$$

2.8.3.2 Polarization Scattering

Electron-electron scattering cross sections at room temperature at about 1000 times greater than those at an electron temperature of 1 eV, which is typically for electric discharges. Similar considerations for charged particle scattering on neutral molecules having a permanent dipole moment (potential energy $U \sim 1/r^2$) and induced dipole moment (potential energy $U \sim 1/r^4$) give, respectively, $\sigma(\varepsilon) \sim 1/\varepsilon$ and $\sigma(\varepsilon) \sim 1/\varepsilon^{1/2}$ [43, 54].

Elastic collisions are significant energy transfer processes within plasma [54]. For an elastic collision of a projectile mass m_1 and velocity υ_1 with a stationary target mass m_2, the conservation

of momentum along and perpendicular to υ_1 and the conservation of energy can be written in the laboratory system as:

$$m_1\upsilon_1 = m_1\upsilon_1^{'}\cos\theta_1 + m_2\upsilon_2^{'}\cos\theta_2 \tag{2.35}$$

$$0 = m_1\upsilon_1^{'}\sin\theta_1 - m_2\upsilon_2^{'}\sin\theta_2 \tag{2.36}$$

$$\frac{1}{2}m_1\upsilon_1^{'2} = \frac{1}{2}m_1\upsilon_1^{'2} + \frac{1}{2}m_2\upsilon_2^{'2} \tag{2.37}$$

where the primes denote the values after collisions. We can eliminate $\upsilon_1^{'}$ and θ_1 and solve the system to obtain:

$$\frac{1}{2}m_2\upsilon_2^{'2} = \frac{1}{2}m_1\upsilon_1^2\frac{4m_1m_2}{(m_1+m_2)^2}\cos^2\theta_2 \tag{2.38}$$

Since the initial energy of the projectile is $\frac{1}{2}m_1\upsilon_1^2$ and the energy gained by the target is $\frac{1}{2}m_2\upsilon_2^{'2}$, the fraction of energy lost by projectile in the laboratory system when averaged over the differential scattering cross section, the average loss is:

$$\zeta_L = \frac{4m_1m_2}{(m_1+m+2)^2}\cos^2\theta_2 \tag{2.39}$$

Elastic collisions can only transfer kinetic energy. The average fraction γ of kinetic energy, transferred from one particle of mass m (electron mass) to another of mass M (atom mass), is equal to [43, 54]:

$$\gamma = \frac{2mM}{(m+M)^2} \tag{2.40}$$

In elastic collisions of electrons and heavy neutrals or ions, the mass of the electron is much smaller than the neutral or ion $m \ll M$, and therefore, $\gamma = 2m/M$, so the fraction of energy transferred is minimal ($\gamma \sim 10^{-4}$) [42, 43, 54]. Thus, electrons transfer little energy due to elastic

collisions with heavy particles, leading to $T_e \gg T_i$ in a typical discharge [54]. This small fraction of energy transfer is why direct impact ionization due to a collision of an incident electron with a valence electron of an atom dominates, as electron-electron collisions allow significant energy transfer. Conversely, if $m = M$, then $\gamma = 1/2$, leading to strong elastic energy exchange among heavy particles and therefore to a common temperature [42].

Neutral particles in plasma may result from the non-ionized fraction of the parent gas or from plasma-chemical processes such as electron-induced dissociation and chemical reactions in the plasma. Because neutrals are low temperature in most plasmas, the energy transfer can normally be neglected. Then, the hard sphere approximation for their collisions is appropriate as discussed previously.

2.8.4 Inelastic Collisions of Electrons

Atoms consist of a heavy positive nucleus with one or more electrons bound to it. Classically, electrons move in orbits with radii set by the balance between the inward electrostatic (Coulomb potential) and outward centrifugal forces (angular momentum) [42, 60]. Each electron atomic orbital is defined by four quantum numbers: n, l, ml, and ms. Electrons in an atom are arranged in energy levels, or shells, around the nucleus. The principal quantum number n determines the energy of the electron, and all the orbitals of a given value n belong to the same shell [42, 60]. The farther the shell is from the nucleus, the more electrons it can hold, and the higher the energies of those electrons [42, 60]. These shells are further divided into subshells, based on angular momentum and the shape of the region of space they occupy. The quantum numbers l and ml specify the angular momentum and its component in a particular direction [42, 60]. The number of subshells is equal to the shell number. Within each subshell, electrons are grouped into atomic orbitals, regions of

space within an atom where the specific electrons are most likely to be found. Each orbital can hold two electrons with opposite spin of which the direction is specified by *ms* [42, 60].

The ionization energy, I, of an atom is the minimum energy required to remove an electron from the ground state. The ground state is the state of lowest energy for that electron and it is the energy level it normally occupies [42, 60]. These electrons are the valence electrons, which are those that occupy the last subshell, and determine the collisional and other behavior of atoms [42, 60]. A second electron may be removed from the atom as well, and the minimum energy needed to remove the second electron from the singly charge cation would be called the second ionization energy, I_2. The standard enthalpy of ionization, $\Delta_{ion}H^{\Theta}$ is the energy that must be supplied to remove an electron from an atom and is related to the ionization energy [60]:

$$\Delta_{ion}H^{\Theta} = I + \frac{5}{2}RT \tag{2.41}$$

Mechanisms of ionization can vary with different plasma-chemical systems. The ionization processes in plasma are primarily due to electron impact, although they may also be produced by high energy photons in the UV spectrum [57]. The main volume ionization process stem from high-energy impacts between electrons and ions [58]. Hence, an electron with kinetic energy greater than eV_i for a specific species can ionize that species [58].

$$e^-_{fast} + A \rightarrow A^+ + e^-_{slow} + e^-_{slow}$$

This inelastic collision between an electron and neutral atom is electron impact ionization. It occurs when the valence electron of a neutral atom or molecule interacts with free plasma

electrons possessing kinetic energy greater than the ionization energy [54, 57]. This endothermic process produces a secondary electron and an ion. Direct ionization of atoms or molecules from the ground state is important in plasmas where electric fields are high and concentration of excited neutrals is moderate [57]. In stepwise ionization previously excited atoms or molecules require lower energy from electron for ionization. It is important in collision-dominated local thermal equilibrium plasmas where concentration of highly excited neutral particles is high [54, 57]. In dissociative ionization by electron impact the molecule is separated into its constituents. This takes place when the electron energy is much higher than the ionization potential to break the molecule. Non-dissociative ionization by electron impact simply ionizes the molecule, resulting in a vibrationally excited molecule remaining after electron removal [57, 62].

Numerous electron collision processes exist and are shown in **Table 2.1**. The five types of ionization are: direct ionization by electron impact, stepwise ionization, non-dissociative ionization, and dissociative ionization [43]. The processes of electron excitation, attachment, and recombination will be briefly discussed as well.

Table 2.1 Prominent electron collisions in plasmas for energy exchange (1–4), ion production (5–8), charged particle losses (9–11) and involving negative ions (12–14). The neutral atom is A, its excited state is A* and A+ represents the corresponding single charged ion. The molecules or diatomic gases are indicated as AB [57].

Electron collision processes		
Scheme	**Process**	**Macroscopic effect**
$e^- + A^+ \rightarrow e^- + A^+$	Coulomb collision between electron and ions	Transport and energy transfer in highly ionized plasmas
$e^- + A \rightarrow e^- + A$	Elastic collision between electron and neutral atoms	Electron transport and diffusion. Electron mobility
$e^- + A \rightarrow e^- + A^*$	Excitation of neutrals by electron impact	Multiplication of metastable neutral atoms
$e^- + AB \rightarrow e^- + AB^*$	Vibrational/rotational excitation	Energy transfer to vibrational/ rotational levels of moleccules
$e^- + A \rightarrow 2e^- + A^+$	Electron impact ionization	Multiplication of ion and electrons from the ground state
$e^- + A^* \rightarrow 2e^- + A^+$	Multistep/stepwise ionization	Ionization of neutral atoms from an excited state
$e^- + AB \rightarrow 2e^- + A + B^+$	Dissociative ionization	Production of atomic ions from molecules
$e^- + AB \rightarrow 2e^- + AB^+$	Non-dissociative ionization	Production of positively charged molecules
$2e^- + A^+ \rightarrow e^- + A^*$	Three-body recombination	Relevant in dense highly ionized plasmas
$e^- + A^+ \rightarrow A + h\nu$	Radiative recombination	Relevant in dense highly ionized plasmas
$e^- + AB^+ \rightarrow A + B^*$	Dissociative recombination	Important in weakly ionized molecular plasmas
$e^- + AB \rightarrow A + B^-$	Dissociative attachment	Production of negative ions in molecular gases
$e^- + A + B \rightarrow AB^-$	Three-body attachment	Production of negative ions in molecular gases
$e^- + A^- \rightarrow 2e^- + A$	Detachment by electron impact	Loss of negative ions in electronegative gases

2.8.4.1 Direct Impact Ionization by Electron

Direct ionization occurs when an electron with energy greater or equal to the ionization energy collides with a neutral atom or molecule [43, 63]. An electron possessing high enough energy ε, can ionize a neutral, unexcited atom, or molecule by interacting with a valence electron of that atom [43, 63].

$$e^- + A \rightarrow A^+ + e^- + e^-$$

The energy of the electron must be adequate to provide ionization in one collision, meaning the energy transferred $\Delta\varepsilon$ to the valence electron surpasses the ionization potential I [43, 63]. This process is called direct ionization by electron impact. Direct ionization is most important in cold or non-thermal plasmas where electric fields and therefore electron energies are relatively high, but the excitation level of neutral species is comparatively low [43, 63]. While in-depth analysis of elementary processes requires quantum mechanics, a classical approximation can be made to gain a physical understanding. Beginning with the Rutherford formula (Equation 2.42), it is assumed that the valence electron is at rest and the interaction with the atom is neglected. The Rutherford formula defines the differential cross section of the incident electron scattering with energy transfer $\Delta\varepsilon$ to the valence electron as [43, 63]:

$$d\sigma_i = \frac{1}{(4\pi\epsilon_0)^2}\frac{\pi e^4}{\varepsilon(\Delta\varepsilon)^2}d(\Delta\varepsilon) \tag{2.42}$$

Direct ionization occurs when the transferred energy surpasses the ionization potential, $\Delta\varepsilon \geq I$. Integrating the Rutherford formula over $\Delta\varepsilon \geq I$, where the ionization potential I is the minimum necessary energy transfer for ionization, to the maximum energy transfer E gives

an expression for the ionization cross section by direct electron impact, known as the Thomson formula (Equation 2.43) [43, 63]:

$$\sigma_i = \frac{1}{(4\pi\epsilon_0)^2}\frac{\pi e^4}{\varepsilon}\left(\frac{1}{I} - \frac{1}{\varepsilon}\right) \tag{2.43}$$

In general, the Thomson formula should be multiplied by the number of valence electrons, Z_v. The cross section shrinks ($\sigma_1 \sim 1/\varepsilon$) as the electron energies increase, $\varepsilon \gg I$, and reaches a maximum when $\varepsilon = 2I$ [43, 63]:

$$\sigma_i^{max} = \frac{1}{(4\pi\epsilon_0)^2}\frac{\pi e^4}{4I^2} \tag{2.44}$$

Taking into account the kinetic energy of the valence electron, ε_v [43, 63]:

$$\sigma_i = \frac{1}{(4\pi\epsilon_0)^2}\frac{\pi e^4}{\varepsilon}\left(\frac{1}{\varepsilon} - \frac{1}{I} + \frac{2\varepsilon_v}{3}\left(\frac{1}{I^2} - \frac{1}{\varepsilon^2}\right)\right) \tag{2.45}$$

If we assume the valence electron is at rest $\varepsilon_v = 0$, the Thomson formula (Equation 2.45) agrees with Equation 2.44. Another variation of the Thomson formula (Equation 2.45) can be obtained assuming a Coulomb interaction of the valence electron with the rest of the atom and taking $\varepsilon_v = I$ [43, 63]:

$$\sigma_i = \frac{1}{(4\pi\epsilon_0)^2}\frac{\pi e^4}{\varepsilon}\left(\frac{5}{3I} - \frac{1}{\varepsilon} - \frac{2I}{3\varepsilon^2}\right) \tag{2.46}$$

Combining all modifications of the Thomson formula using the generalized function $f(\varepsilon/I)$ for all atoms [43, 63]:

$$\sigma_i = \frac{1}{(4\pi\epsilon_0)^2}\frac{\pi e^2}{I^2}Z_v f\left(\frac{\varepsilon}{I}\right) \tag{2.47}$$

where Z_v represents the number of valence electrons in an atom. The generalized function can be

written as [43, 63]:

$$f\left(x = \frac{\varepsilon}{I}\right) = \frac{1}{x} - \frac{1}{x^2} \tag{2.48}$$

The generalized function best agrees with experimental data for different atoms and molecules when [43, 63]:

$$\frac{10(x-1)}{\pi(x+0.5)(x+8)} < f(x) < \frac{10(x-1)}{\pi x(x+8)} \tag{2.49}$$

The total cross section diverges due to the long range of Coulomb potential. Therefore, the cross section for all events with a scattering angle > 90 ° can be used as an estimation of a total cross section for significant deflections:

$$\sigma_{90} = \frac{\pi}{4} b^2 \tag{2.50}$$

Integration of the cross section, $\sigma_i(\varepsilon)$, over the electron energy distribution function will calculate the ionization rate coefficient $k_i(T_e)$ [43]:

$$k_i(T_e) = \sqrt{\frac{8T_e}{\pi m}} \sigma_0 e^{\left(-\frac{1}{T_e}\right)} \tag{2.51}$$

where the cross section $\sigma_0 = Z_v \pi e^4 / I^2 (4\pi\epsilon_0)^2$ is about the geometric atomic cross section [42, 43].

2.8.4.2 Stepwise Ionization and Three-body Recombination

Stepwise ionization includes multiple steps to provide adequate ionization energy. First, electron-neutral collisions create excited species. However, these collisions lack the energy to ionize. Then a final collision occurs with a relatively low-energy electron, triggering the ionization

event [43]. If the electronic excitation is great enough, stepwise ionization can be significantly faster than direct ionization due to a higher probability of collision with excited neutrals compared to free plasma electrons. This is because when $T_e \ll I$, the probability of obtaining high ionization energy is much lower for free electrons than for excited atoms and molecules [43].

In thermodynamic equilibrium, the mechanism of neutralization of positive ions is three-body recombination [43, 57]. Three-body recombination proceeds through a set of excited states. A free electron receives the released excess energy from the formation of molecular ions. An intermediate excited state is created which is the inverse of stepwise ionization [43, 57, 63]. Recombination of electrons and ions is important in high density plasmas.

$$2e + A^+ \rightarrow e + A^*$$

Generally, these processes are comprised of a series of two body reactions in which the third body absorbs the excess reaction energy [54].

2.8.4.3 Franck-Condon Principle and Non-dissociative Ionization

When the electron energy does not greatly exceed the ionization potential of a molecule the process is called non-dissociative ionization by direct electron impact [43]:

$$e + AB \rightarrow AB^+ + e + e$$

Molecular vibration is the fastest internal motion of atoms within molecules. Typical periods for molecular vibration are between $\sim 10^{-14}$-10^{-13} s [43, 64, 65]. This is still much longer than

interaction times between electrons and molecules within plasma, which is $a_0/\upsilon_e \sim 10^{-16}$-$10^{-15}$ s, where a_0 is the atomic unit of length and υ_e is the mean electron velocity [43, 64, 65]. Therefore, many electron excitation processes induced by electron impact are faster than all other atomic motions inside the molecules, and the atoms can be considered stationary during the process of electron transition [43, 60, 64, 65]. This is known as the Franck-Condon principle.

According to the Franck-Condon principle, when a molecule undergoes an electronic transition from one electron energy state to another, from normal state to excited state, the electronic transition on an energy (y) versus internuclear distance (x) plot is vertical [64]. It is assumed that there are no changes in the nuclear coordinates during an electronic transitions, therefore, the most probable vibronic transitions are vertical because the time (> 3 x 10^{-14} s) required for an electronic transition is negligibly small compared to the period of nuclear vibration [65]. After the electronic transition occurs, the electron density is rapidly built up in new regions of the molecule and lost from others [60]. The previously stationary nuclei responds to the new force by beginning to vibrate and swing back and forth from the original separation. Looking at the quantum mechanical description of the Franck-Condon principle refines this picture. The molecule is in the lowest vibrational state of its lowest electronic state before excitation; the most probable nuclei location being at their equilibrium separation. When the transition occurs, the molecule is excited to a new state. During excitation the nuclear geometry remains constant so the transition may be thought of being up a straight vertical line cutting through several vibrational levels of the upper electronic state [60]. The most probable vibrational state for the termination of the transition will be one where the separation is the same as the equilibrium separation [60]. Vibrationally excited ions are formed as a result of non-dissociative ionization. Electronic transitions are most probable with low kinetic energies of the nuclei. Possible exceptions to this principle are the lowest vibration

levels [65].

2.8.4.4 Dissociative Ionization

Electron impact dissociation plays a central role in the chemistry of low-pressure reactive discharges [43, 54]. Electronically excited molecules may undergo dissociation, which is the breaking of bonds. If the collision excites the molecule into a state containing more energy than the separated components, exceeding the binding energy, dissociation occurs [54].

$$e + AB \rightarrow A + B + e$$

Dissociative ionization occurs when the electron energy significantly exceeds the ionization potential [43, 54].

$$e + AB \rightarrow A + B^{+} + 2e$$

The molecular ion AB^{+} is formed at a higher threshold energy than that of ionization, and dissociates into fast, positively charged ions and neutrals.

Polar dissociation generates negative ions without electron capture [42].

$$e + AB \rightarrow A^{+} + B^{-} + e$$

Positive ions are formed together with negative ions. The threshold energy is extremely high due to the process including both ionization and dissociation.

2.8.4.5 Recombination

Endothermic ionization processes produce positive ions and electrons. Their counterpart, electron-ion recombination collisions of charged particles, results in their mutual neutralization. Recombination collisions are exothermic processes in which the energy released corresponds to the ionization potential [57].

In molecular gases, the fastest electron neutralization is dissociative recombination and is important in weakly ionized plasmas [57].

$$e + AB^{+} \rightarrow A + B^{*}$$

An electron collision may also break apart an electron-ion pair and produce fast excited neutral fragments. Dissociative recombination occurs when the collision excites the AB atom to the bound excited state AB^{*}. Because the electron is captured, it is unable to carry away part of the reaction energy [42]. Thus, it cannot dissociate to ground states of A and B because the potential energy of AB^{+} is greater than that of AB.

2.8.4.6 Electron Attachment

A negative ion is formed when an electron collides with a neutral gas atom or molecule and becomes attached [58]. This process is dependent on the energy of the electron and the nature of the gas [58]. For example the negative halogen ions and O^{-}, O_2^{-}, NO_2^{-}, NO_3^{-}, OH^{-}, and H^{-} are

easily formed, but not N^-, N_2^-, or negative ions of the rare gases [58]. In the attachment

$$A + e^- \rightarrow A^- + h\nu$$

$$AB^* + e^- \rightarrow A^- + B$$

the energy liberated is any internal energy plus kinetic energy plus the binding energy, E_a (about 1.5 eV for O, 4 eV for F, Cl and 0.7 for H; the molecules of oxygen and the halogens have binding energies around 0.5 eV) [58]. Negative ions can also be destroyed by collisions with atoms, electrons, or photons [58].

In electronegative gases, electrons may also be lost through the formation of negative ions in electron attachment. Attachment processes form ions by capturing electrons [57]. Dissociative electron attachment produces negative ions and neutrals.

$$e + AB \rightarrow A + B^-$$

Negative ions are formed when electrons attach to other plasma particles [43, 57]. Attachment of more than one electron to form a multi-charged negative ion is impossible in the gas phase because of electric repulsion. Similar to positive ions, negative ions are heavy particles and so gain energy through collisions, not electric fields [43]. Negative ions have energy distribution functions similar to that of the positive ions, one that is close to Maxwell- Boltzmann distribution. Their temperatures are also close to the temperature of the neutral gas [43].

This process is important in discharges containing atoms with positive electron affinities due to the threshold energy of production of negative ions being lower than for pure dissociation [42]. The collisional excitation of the molecule from ground state to a repulsive AB^- state due to

attachment, leads to autodetachment or dissociation.

Excess energy may be emitted to stabilize the formation of a negative ion during electron attachment. Thus, a negative ion can be formed in the process of radiative attachment [42, 43].

$$e + M \rightarrow (M^-)^* \rightarrow M^- + h\omega$$

However, the probability of this process is extremely low: 10^{-5}-10^{-7}.

2.8.5 Excitation

During an inelastic collision a fraction of the initial electron kinetic energy is transferred and causes the internal state of the target particle to change [57]. One result of an inelastic collision is electron impact excitation. This occurs when a high energy electron collides with a heavy particle and a bounded electron can jump to an excited state [57].

$$e^- + A \rightarrow e^- + A^*$$

$$e^- + AB \rightarrow e^- + AB^*$$

Gas atoms may also absorb energy through photons and become excited through a process called photo-excitation [58].

These excited states of atoms or molecules usually have a short life before returning to ground state [57]. Sometimes a metastable state is formed with a longer lifetime that can eventually lose its energy by collisions.

2.8.6 Collisions of Ions and Molecules

Ion-atom collisions are most frequent in weakly ionized plasmas, some of which are listed in **Table 2.2** [57]. These encounters within plasma influence the transport of ions and, in turn, its displacement [63]. Unlike electrons, heavy particles such as ions and neutrals are not effective at producing ionization events. Collisions of heavy particles are unable to provide ionization even if their kinetic energy is sufficient. This is because their velocities are much lower than those of the electron orbital velocity in the atom and heavy particles are usually only able to transfer a small fraction $\sim 2m_e/m_i$ of the ion/neutral kinetic energy to valence electrons [43, 57]. Excitation and ionization of atoms by heavy particle and ion collisions is less efficient than electron impact ionization because their interaction frequency is low, and will not be discussed further [57]. However, charge transfer is possible in ion and molecule collisions. Charge, in the form of one or more electrons, can be transferred from an atom or molecule to an ion, creating an excited state, which may deexcite by releasing electromagnetic radiation [66]. The ion-neutral processes that will be discussed are elastic ion-atom collisions, charge exchange processes, Penning ionization, and associative ionization.

Table 2.2 Prominent ion-neutral collisions in plasmas involving momentum and energy exchange. The neutral atom is A, its metastable state or excited state is A* and A+ represents the corresponding single charged ion. The molecules or diatomic gases are indicated as AB [57].

Electron collision processes		
Scheme	**Process**	**Macroscopic effect**
$A^+ + A^+ \rightarrow A^+ + A^+$	Coulomb collision between ions	Transport of ions energy thermalization
$A^+ + A \rightarrow A^+ + A$	Elastic collision between ion and neutral atoms	Transport of ions, diffusion and thermalization energy
$A + B^+ \rightarrow A^+ + B$	Resonant and/or non-resonant charge exchange	Ion transport, diffusion and thermalization energy
$A + B^* \rightarrow A^* + B$	Transfer of excitation	Diffusion of metastable atoms
$A + h\nu \rightarrow A^*$	Radiative excitation	Production of metastable atoms
$A^+ + A \rightarrow 2A^+ + e^-$	Ion impact ionization	Production of ions
$A^* + B \rightarrow A + B^+ + e^-$	Penning ionization	Production of ions in gas mixtures
$A + B^* \rightarrow AB^+ + e^-$	Associative ionization	Production of molecular ions in diatomic or gas mixtures
$A + h\nu \rightarrow A^+ + e^-$	Photoionization	Production of ions
$A^- + B^+ \rightarrow A + B^*$	Ion-ion recombination	Loss of negative ions in electronegative gases

2.8.6.1 Elastic Collisions: Coulomb and Polarized Scattering

The primary collisional processes in weakly ionized plasmas are between charged and neutral particles. Long-range Coulomb collisions require a high degree of ionization (>0.01) [57]. Coulomb collisions have already been addressed in **Section 2.8.3.1** and will not be discussed further here. At lower energies for electrons, the dominant process is relatively short-range polarization scattering [54]. These elastic collisions result in both particles being scattered by the strong electric field produced due to the close approach of the ion. When a charged particle approaches a neutral atom, the electron cloud of the neutral atom polarizes [43, 57]. If the neutral atom has no permanent dipole moment itself, the electric field E of the charged particle induces a dipole moment, p_m [43]:

$$p_m = \alpha \epsilon_0 E = \alpha \frac{e}{4\pi r^2} \tag{2.52}$$

In this equation, r is the distance between the particles, and α is the polarizability of a neutral atom or molecule which is numerically about the volume of the atom or molecule [43].

This means that the electric field of the charged particle distorts the negative cloud of electrons around the positive atomic nuclei in a direction opposite the field [41, 43, 54]. The slight charge separation renders one side of the atom slightly positive and the opposite side slightly negative [43].

The strong radial dependence of this potential causes the trajectory of the charged particle to spiral into the neutral when the impact parameter is below a certain impact parameter p_L. The situation where the charged particle is captured by the neutral is called Langevin capture.

The Langevin capture cross section is defined as [41, 43, 54]:

$$\sigma_L = \pi p_L^2 \sqrt{\frac{\pi \alpha q_1^2}{\epsilon_0 \mu}} \frac{1}{\upsilon_r} \tag{2.53}$$

where υ_r is the relative velocity of the collision partners before the collision. The Langevin capture of electrons is a mechanism for the formation of negative ions, and only occurs in gases with high electron affinity.

2.8.6.2 Resonant Charge Transfer

When a positive ion collides with a neutral atom, a valence electron may be captured, resulting in a transfer of the electron from the atom to the ion [42, 43]. Generally, during this charge exchange, the energy level into which the electron is captured is not equal to that from which it was released [42, 43]. This energy defect, ΔW, may be positive or negative. If $\Delta W \neq 0$, the kinetic energy of the colliding particles is not conserved [42, 43].

$$A^+ + B_{at\ rest} \rightarrow A + B^+_{at\ rest}$$

Charge transfer may occur in the classical over the barrier model or due to resonant tunneling as depicted in **Figure 2.6**.

Charge transfer occurs in two steps; the electron is released from B and then it is captured by A^+. The potential energy of a B electron in a level n with a center-to-center separation of $a_A B$ is given by [54]:

$$W_{nB} = -\frac{U_{iB}}{n^2} - \frac{e^2}{4\pi\epsilon_0 a_{AB}} \tag{2.54}$$

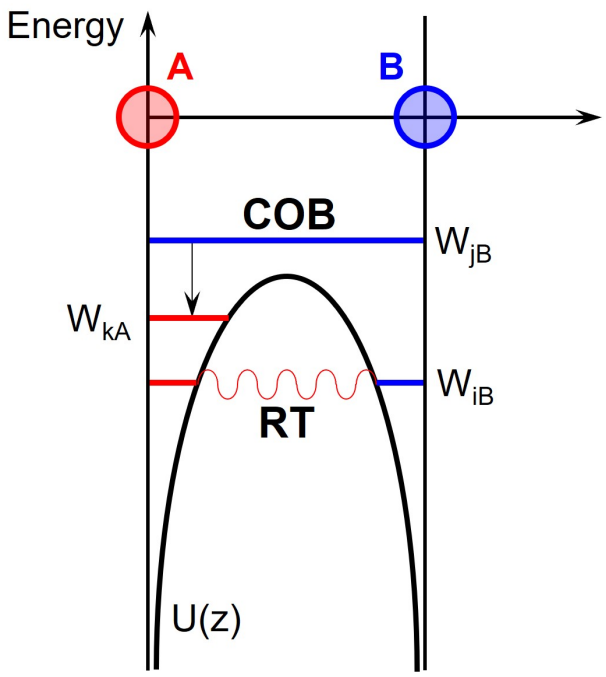

Figure 2.6 Charge transfer from B to A in the classical over-the-barrier model (COB) and due to resonant tunneling (RT).

where in the first term, U_{iB} is the potential energy of B in level $n = 1$. The second term describes the interaction with the ion. In other words, the electrostatic energy due to charge A^+. The released electron obtains the potential energy in the Coulomb fields of the A^+ and B^+ ions [54]:

$$U(z) = -\frac{e^2}{4\pi\epsilon_0 z} - \frac{e^2}{4\pi\epsilon_0 |a_{AB-z}|} \tag{2.55}$$

where z is the distance from the center of A^+ toward B. From this equation (Equation 2.55), the maximum of $U(z)$ between A^+ and B^+, at $z = a_{AB}/2$, results in [54]:

$$U_{max} = -\frac{e^2}{\pi\epsilon_0 a_{AB}} \tag{2.56}$$

This shows that the potential barrier decreases when the collision partner approaches. The classical

condition for electron release is given by $\Delta W_{AB} > U_{max}$, which results in a maximum distance at which the release takes place [54]:

$$a_{AB,r} = -\frac{3e^2n^2}{4\pi\epsilon_0 U_{iB}} \tag{2.57}$$

Assuming ion velocity is low compared to the orbital velocities of the electrons, as is the case for non-thermal plasmas, there is sufficient time for the transfer of the released electron to the ion, provided there is a free level below the releasing level of B. Therefore, the cross section may be estimated from the release only, resulting in [42, 54]:

$$\sigma_{COB} = \pi a_{AB,r}^2 = 9\pi \left(\frac{e^2n^2}{4\pi\epsilon_0 U_{iB}}\right)^2 \tag{2.58}$$

This is the classical "over-the-barrier" model.

Another possibility is the resonant charge transfer by tunneling between identical species, i.e. $A = B$. This is because if the neutral particle and ion are from the same atom a charge transfer can occur without any defect. This process is said to be resonant [42, 43]. The capture is only energetically possible if [54]:

$$\frac{1}{2}m_A + \upsilon_A^2 \geq \Delta W_{AB} \tag{2.59}$$

The cross section can be approximated by:

$$\sigma_{RT} = \frac{1}{U_i}\left(C_1 - C_2 \ln(\upsilon_+)\right)^2 \tag{2.60}$$

where U_i is the ionization potential and the constants $C_1 = 1.58 \cdot 10^{-7}$ and $C_2 = 7.24 \cdot 10^{-8}$ [42]. The cross section decreases with the ion velocity υ_+ and the tunneling probability increases with

interaction time. Resonant tunneling dominates the charge exchange in atomic gases.

$$A_{slow} + A^{+}_{fast} \rightarrow A_{fast} + A^{+}_{slow}$$

Resonant charge transfer acts as an elastic collision because kinetic energy is conserved [54]. Cross-sections are large at low energies and therefore, resonant charge transfer is an important process in weakly ionized plasmas. The large cross-section causes the particles to be practically undeflected after the charge transfer leading to an effective scattering angle for the ion and momentum transfer for every collision [54].

Charge transfer processes between negative ions and neutrals are important in electronegative discharges such as oxygen discharges [54]. The charge transfer cross section between O_2 molecules is resonant if the molecules have the same, or very close vibrational and rotational states after a collision.

2.8.6.3 Penning Ionization

Metastables (long-lived excited states) can be valuable sources of ionization among species where the ionization energy of species B is less than the excitation energy of species A [58].

$$A + B^{*} \rightarrow A^{+} + B + e^{-}$$

When the electron excitation energy of a metastable atom B^{*} surpasses or is equal to the ionization potential of another atom A, the collision between the two may result in ionization of the second atom [57]. Hence, the ionization event arises through the formation of intermediate

metastable molecules. This is called Penning Ionization and can also follow the collision of two metastable atoms.

$$2A^* \rightarrow A + A^+ + e$$

Penning ionization is important in electric discharges of reactive gases doped with noble gases [57, 58, 63].

2.8.6.4 Associative Ionization

Associative ionization is the reverse process to dissociative recombination. If the total electronic excitation energy of the colliding particles is not enough, ionization is still possible when heavy particles stick to each other and form a molecular ion [43, 57].

$$A + B^* \rightarrow AB^+ + e$$

In order to proceed at thermal energies, the sum of the excitation energy of metastable B^* and the dissociation energy of AB^+ must exceed the ionization potential of atom A [43, 54, 57]. If the bound ground state of AB^+ is lower than the bound state of AB^*, unstable AB^* may decay to the ground state of AB^+ by electron emission.

CHAPTER 3

PLASMA STERILIZATION

3.1 Introduction

Sterilization is defined as a physical or chemical process that exterminates or inactivates microorganisms [5]. The worldwide accepted definition for medical devices to be considered sterile is the security assurance level (SAL) [67]. The SAL is a statistical parameter that refers to the probability of one surviving viable microorganism after sterilization [67]. The accepted SAL for medical devices is required to be below 10^{-6}, meaning a probability of 1 in 1,000,000 [67].

Sterilization plays a major role in health-care facilities to prevent the spread of disease. Current sterilization methods include using autoclave or heat, ethylene oxide gas, hydrogen peroxide gas plasma, and radiation [5, 6]. However, these sterilization methods have their limitations.

Autoclave sterilization exposes microbes to saturated water vapor under high pressure and high temperature in an enclosed chamber. The standard temperature and pressure of an autoclave are 250 °C and 15-20 psi on an hour-long cycle [68, 69]. High temperatures disrupt the lipid membranes and denature proteins and nucleic acids (DNA, RNA) in microorganisms, leading to their death [70]. Steam vapor during heating has detrimental effects on metal objects in the form of rust and corrosion. Although using an autoclave or heat is the most popular method for sterilization, it is not advisable for heat-sensitive materials because they may become disfigured [6, 69].

Ethylene oxide (EtO) has been used as a sterilant for heat-sensitive materials since the 1950s, but it presents a risk in its toxicity [6]. Ethylene oxide is an alkylating agent that kills microorganisms by inactivating their proteins, DNA, and RNA. This prevents normal cellular

metabolism and replication, rendering the microorganism nonviable [70, 71]. Surfaces treated with EtO require an airing time before they are safe to handle [7]. Ethylene oxide exposure represents an occupational hazard and can cause respiratory problems, blurred vision, dizziness, nausea, headaches, and convulsions [5, 72]. It is also linked to more serious health concerns like leukemia [72]. The Occupational Safety and Health Administration regulates acceptable vapor levels of EtO exposure to one part EtO, per million parts of air (1 ppm) measured as an 8-hour time-weighted average [72]. After use, the chamber must be flushed with inert gas for 8-12 hours to remove all traces of EtO [69]. This process though effective, is costly and laborious.

Hydrogen peroxide is also used as a sterilant. Hydrogen peroxide inactivates microorganisms through oxidation [70]. It can be converted into extremely reactive hydroxyl radicals (OH), which attack and break down membrane lipids, DNA, and other essential cell components to inactivate bacteria [70]. The process is typically at higher temperatures than ambient, but not as high as autoclave sterilization [7]. The use of hydrogen peroxide also requires a long processing time (4-40 hours). Chemicals may impregnate certain materials and long ventilation times are required before they can be utilized [7].

Gamma rays have been used in radiation sterilization [6]. Gamma rays are high energy photons with no mass or charge that are emitted by a ^{60}Co source [70]. They kill microorganisms by attacking the DNA causing a variety of lesions in DNA including: single- and double-strand breaks, DNA-protein cross-links, oxidized bases and abasic sites [73]. Misrepair of DNA damage can lead to cell death. Sterilization can be conducted at, or close to ambient temperature [7]. Despite the lower temperature, gamma rays can still damage the materials. Gamma radiation is recognized as a potent carcinogen requiring protection for the operators and special site to perform it [6, 73]. Plasma sterilization presents an option that is low temperature, efficient, and non-toxic.

The existing hydrogen peroxide gas plasma process is 'partially' plasma sterilization [9]. This process includes two phases: a diffusion phase and a plasma phase [5, 8, 9]. First, the sterilization chamber is evacuated, and hydrogen peroxide solution is injected from a cassette and is vaporized in the sterilization chamber. The hydrogen peroxide vapor diffuses through the chamber and initiates the inactivation of microorganisms on all the surfaces exposed to the sterilant. Second, a gas plasma is created in the chamber. The residual hydrogen peroxide is then broken apart by the plasma, which aids in the removal of hydrogen peroxide residuals from the sterilizer load to make the contents safe for handling and use. Hence, the hydrogen peroxide plasma treatment is a direct gas plasma sterilization.

In the past 15 years, low-temperature pure gas plasma sterilization has attracted great interest because of the unique characteristics of plasmas. Plasma is quasi-neutral ionized gas, known as the fourth state of matter. A large numbers of gas ions (e.g., O_2^+), atoms (e.g., O), and excited species (e.g., O^*, O_2^*) can be created in a plasma. These gas species are highly reactive and can effectively destroy or inactivate bacteria. Current literature agrees that there are three mechanisms by which plasma sterilizes a surface: ultra-violet (UV) irradiation of genetic material, chemical reactions with the plasma species, and plasma ion sputtering [13].

The use of plasma as an effective sterilization treatment was theorized by Basaran et al. in 2008, which elucidated the importance of selecting the appropriate gas to generate the proper anti-microbial species [74]. They studied SF_6 and air (atmospheric) gas plasma treatments to investigate their sterilization efficacy against *Aspergillus parasiticus*. Fluorine atoms in SF_6 plasma were found to be the primary etching species, which acted as the dominant sterilization mechanism; whereas the use of air gas plasma generated anti-microbial oxygen species, which was the dominant sterilization mechanism [74]. They found that the SF_6 treatment required 15 minutes of treatment for a 6-log

reduction, but after 10 days of storage, the plasma treated nuts had a renewal of fungal growth [74].

Hury et al. 1998, compared the efficiency of multiple plasmas for the killing of *Bacillus subtilis* spores. The plasmas they compared pure Ar plasma to multiple oxygen-based plasmas: O_2, H_2O_2, and CO_2 [75]. Organic molecules, those found in living things like bacteria, are primarily made of C, O, H, and N. An effective plasma treatment for the elimination of bacteria must be able to target and react with these elements. For example, on its own carbon is non-volatile, so it must form a volatile compound with another element in order to be etched [75]. Reactive gas plasmas can form these volatile compounds because atoms and molecules are always present [75]. Thus, in the study done by Hury et al. the oxygen-based plasmas were shown to be much more efficient and it was hypothesized that the oxygen-based plasmas sterilized bacteria by slow combustion with oxygen atoms or radicals [75].

Cvelbar et al. 2007, further demonstrated that oxygen plasma was effective for etching and oxidation by studying the optical emission spectra (OES). When microorganisms are treated with oxygen plasma, they are assaulted by oxygen species. These oxygen species, especially reactive oxygen radicals, irreparably damage the cell by either etching the outer membrane or diffusing through the inner membrane which causes damage to the membrane, DNA, and proteins by oxidation [6, 76, 77]. When micro-organisms undergo plasma treatment they are assaulted by the oxygen radicals causing damage that the cell cannot repair [77]. This process, called etching, happens due to the oxygen species being adsorbed onto the surface of the bacteria to react and form volatile compounds. The capability of the atomic oxygen species to oxidize is essential to their ability to sterilize [77].

A study by Yang et al. 2009, looked at the sterilization mechanisms of argon plasma on the bacteria *Pseudomonas aeruginosa*. Using scanning electron microscopy (SEM) they found that

after treatment, cells were eroded and their proteins and nucleic acid had leaked out [78]. The argon plasma bombarded the surface, which caused etching and cell membranes to rupture [78]. The electrons and ions in the plasma discharge etched the cell walls or membranes of the bacteria, causing protein leakage [78].

Previous studies have shown that the reactive species and ions created in plasmas play the largest role in sterilization. Hence, a high plasma density is expected to promote the sterilization efficiency. One aspect of this work is to understand the effects of plasma density on sterilization efficiency under different gas pressures, which directly affect plasma density. On the other hand, an increased plasma density usually leads to large heating load to the working piece surface due to the bombardment of the charged particles created in the plasma. Hence, another aspect of this work is to reduce the heating load to the sample surface by integrating a magnetic field to confine the plasma. This research combines plasma modeling with optical emission spectroscopy to verify the effects of a magnetic field on the concentrations of plasma species. Subsequently, the sterilization efficiency and temperature with the use of a magnetized plasma are determined. The plasma modeling also helps to predict the reactive species that play an essential role in sterilization.

3.2 After-glow Region for Sterilization

In typical plasma discharges, the direct area, where there is direct contact with the discharge plasma, is used for treatment. This could be between the electrodes (gas discharge), the vessel in direct contact with plasma source, or the flame of a plasma torch [7]. When the discharge takes place in a flowing gas, some species produced in the direct area are carried further down the vessel, and an afterglow (indirect) is obtained [7, 79].

Plasma sterilization has been studied in both the direct and afterglow regions. The afterglow

contains relatively few charged particles compared to the direct glow region. Thus, it is essentially comprised of neutrals, radicals, and molecules, some of which are in an excited state [79]. Species of interest in the afterglow are short-lived particles like atoms (O and N), and excited molecules.

The use of low gas temperature plasma presents an alternative for sterilization of heat-sensitive medical devices such as endoscopes and catheters [77, 79, 80]. There are multiple advantages off using the afterglow over the direct region for sterilization purposes. Besides lower gas temperature when operated with high enough gas flow, the treated surface is less likely to be altered by impact of the charged particles accelerated within the plasma sheath. Under direct discharges the charged particle density is higher [80]. In non-dielectric devices, the electric field of the discharge may cause thermal damage due to local heating. The afterglow can fill large volumes at lower costs compared to other discharges. Finally, the neutral species play a role in sterilization, therefore, it is not essential to use the direct area [80]. Moreau et al. 2000, studied the influence of operating parameters of a microwave discharge on using the afterglow to inactivate *Bacillus subtilis* spores [80]. They found the gas flow rate played an important in their microwave system. This enabled rapid transport of short-lived active species to all parts of the object being treated. Although successful, it took 40 minutes to achieve total inactivation and the power was 100 W [80]. Moisan et al. 2013, investigated the sterilization of medical devices in the flowing afterglow of a N_2-O_2 discharge [7]. They identified metastable-state molecules (O_2 ($^1\Delta_g$)) in the afterglow as playing a prominent role in the inactivation. However, the sterility criteria was not met until after 60 mins at 2450 MHz [7]. Overall, sterilization time is usually shorter in the direct discharge than in its afterglow [79].

We hope to show that the implementation of a magnetic field with a dielectric barrier discharge will increase the efficiency of the plasma and the sterilization capabilities of the afterglow

region by increasing number densities and neutral species.

3.3 Reactive Oxygen Species Effects on Cells

In cold plasma discharges, reactive species are generated through various collisional pathways, such as electron impact ionization, excitation, and dissociation. Molecular oxygen is weakly reactive even though it has two unpaired electrons because they are in different molecular orbitals and have a parallel spin [81]. Oxygen preferentially accepts electrons. Oxygen based plasmas are excellent sources of reactive oxygen species (ROS), which can be atomic and molecular radicals, such as atomic oxygen (O), ozone (O_3) and hydroxyl (OH), etc. Other active species such as O_2 in the metastable singlet state may be present in oxygen-based discharges [79]. Particles in metastable energy states have a very long lifetime because they cannot emit photons though an electric-dipole transition. Under most experimental conditions, metastable species de-excite through collisions, transferring their energy to other particles. This will eventually initiate chemical reactions in the gas phase of the plasma or on surfaces exposed to it. The types of reactions were discussed in **Ch.2**. The ROS have a direct impact on the cells of microorganisms by (i) damaging DNA or RNA, (ii) lipid peroxidation, and (iii) oxidation of proteins (**Figure 3.1**) [81–84].

ROS cause physio-chemical changes in DNA affecting the interpretation and transmission of genetic information. ROS reacts with the nitrogenous bases and deoxyribose in DNA causing oxidative reactions which can lead to mutations, apoptosis, carcinogenesis. ROS may also instigate DNA fragmentation due to forced rupture of nucleosomes (fundamental structures for the organization of DNA within chromosomes), which ultimately causes problems in the compaction and coiling of DNA within chromatin [81]. Chromatin is a complex of DNA and proteins that forms chromosomes and is integral in regulation of gene transcription. It has been found that alterations

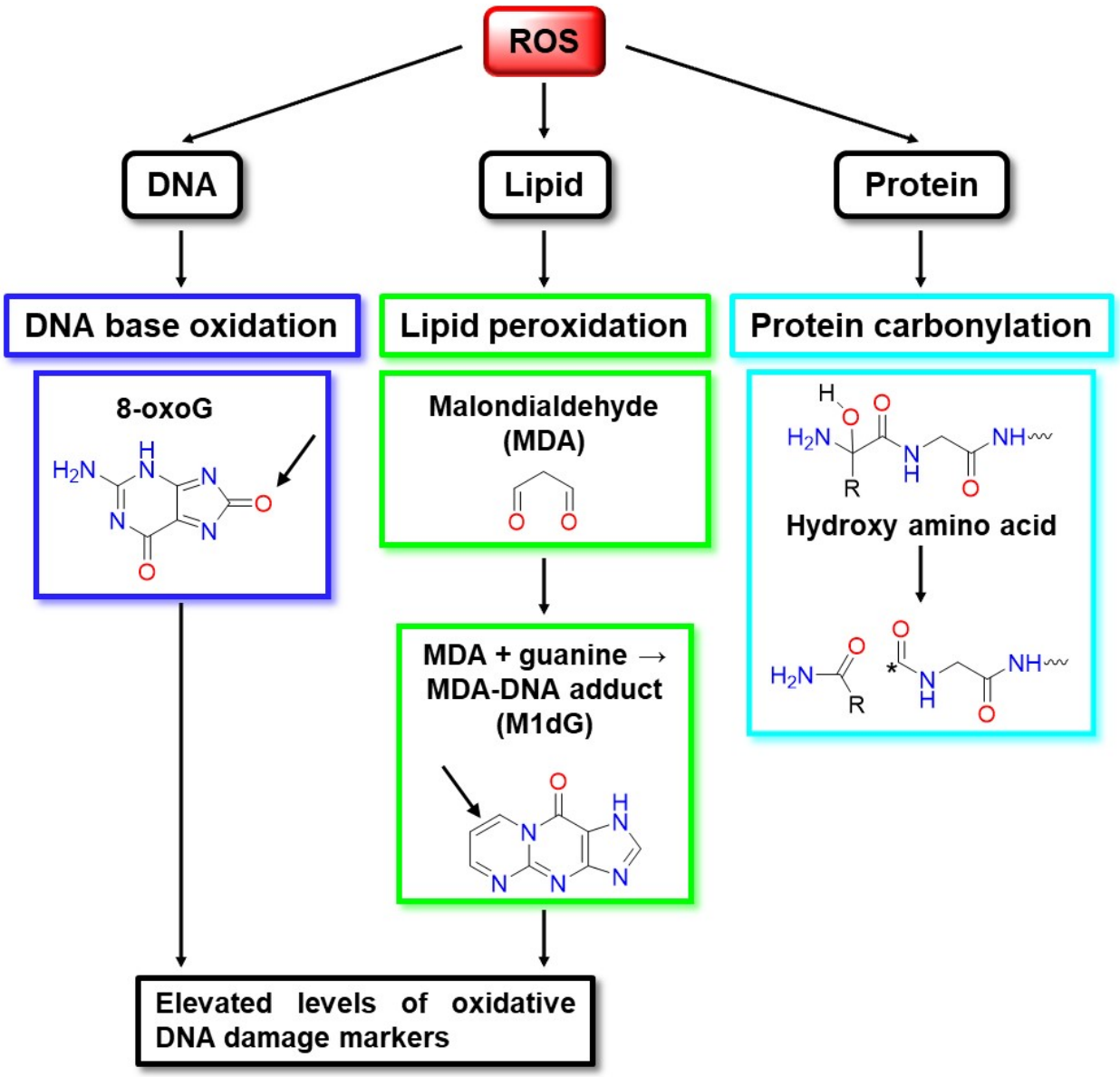

Figure 3.1 ROS reactions with DNA, lipids, and proteins [81].

in chromatin organization can strongly affect mutation rates [81, 85].

Hydroxyl radicals are one of the most reactive and electrophilic of the ROS. The $^{\bullet}OH$ can cause the formation of 8-oxo-7,8-dihydroguanine (8-oxoG) from guanine (G), among other oxidative products. Guanine is the most easily oxidized of the nucleic acid bases because it has the lowest ionization potential among the DNA bases. The reduction potential of 8-oxo-dG is even lower than that of guanosine (RNA nucleoside) so it can be further oxidized creating secondary

oxidation products [81]. Unlike other oxidized bases, 8-oxoG does not inhibit nucleic acid synthesis, instead it induces alternate base mispairing [81, 86–88]. When a mispairing occurs during DNA replication, a base substitution can result. Similarly, 8-oxoG mispairing in RNA synthesis may induce errors in gene expression [86].

During replication DNA that contains 8-oxo-dG, adenine (A) is most often incorporated across from the lesion. This is problematic because within DNA adenine (A) always pairs with thymine (T) and cytosine (C) always pairs with guanine (G) due to the ability of each base pair to form hydrogen bonds. Following replication, the 8-oxo-dG is excised during the repair process and a thymine (T) is incorporated in its place, ultimately causing a G to T transversion mutation [87]. The hydroxyl radical causes strand breaks, which are initiated by abstraction of a deoxyribose hydron atom, especially from thymine and guanosine [81, 88, 89].

Hydroxyl radical reactions with DNA include addition of double bonds to DNA bases and abstraction of an H atom from the methyl group of thymine and each of the C-H bonds of 2'deoxyribose [88]. Addition to the double bonds of DNA bases (C5-C6 double bond of pyrimidines) brings about C5-OH and C6-OH adduct radicals. The redox properties of these adduct radicals differ, with C5-OH radicals being reducing and C6-OH adduct radicals oxidizing [88]. These pyrimidine radicals yield several products by numerous mechanisms.

Moreover, ROS may cause DNA strand breakage through free radical attack on the DNA sugar phosphate backbone [81]. Severe DNA damage that cannot be repaired triggers apoptosis.

ROS attack the outer membranes of the cell. These outer membranes are made of a lipid bilayer which is a polar membrane made up of two layers of lipid molecules. The most abundant membrane lipids are phospholipids [90]. These phospholipids have a hydrophilic phosphate head and two hydrophobic tails containing fatty acid chains. One tail usually has one or more cis-double

bonds making it unsaturated. The cis-double bounds in the unsaturated fatty acids produce kinks in the hydrocarbon chains making them more difficult to pack together. This gives the membrane more fluidity allowing and allows it to remain fluid at lower temperatures. The fluidity also allows the transport of biochemical by-products across the membrane [91]. The cis-double bonds produce kinks in the hydrocarbon chains making them more difficult to pack together. This allows the membrane to remain fluid at lower temperatures. Unsaturated fatty acids that make up cellular membranes are susceptible to hydroxyl radical attacks. This can compromise membrane function so that it is no longer an efficient barrier against the transport of ions and polar molecules into and out of the cell [91]. Proteins embedded in the lipid bilayer also regulate the passage of various compounds. The chains of amino acids that make up proteins are susceptible to oxidation in a radical-rich environment.

A number of ROS can be formed by the sequential reduction of oxygen through the addition of electrons. Examples of which are shown in **Figure 3.2**.

ROS are naturally present in organisms and participate in redox signaling pathways essential to cell function. However, they are also involved in harmful processes such as aging, carcinogenesis, and neurodegenerative disease [84]. The reactive superoxide anion ($O_2^{\bullet -}$) is a negatively charged radical formed through a single electron donation to oxygen [83, 92, 93]. The superoxide anion ($O_2^{\bullet -}$) may be formed under circumstances where the oxygen molecule is partially reduced by receiving a single electron. Due to its charge, $O_2^{\bullet -}$ cannot easily cross cell membranes. Thus, $O_2^{\bullet -}$ and a hydrogen ion may form a hydroperoxyl radical [92, 93].

$$O^{\bullet -} + H^{+} \rightarrow HO_2^{\bullet}$$

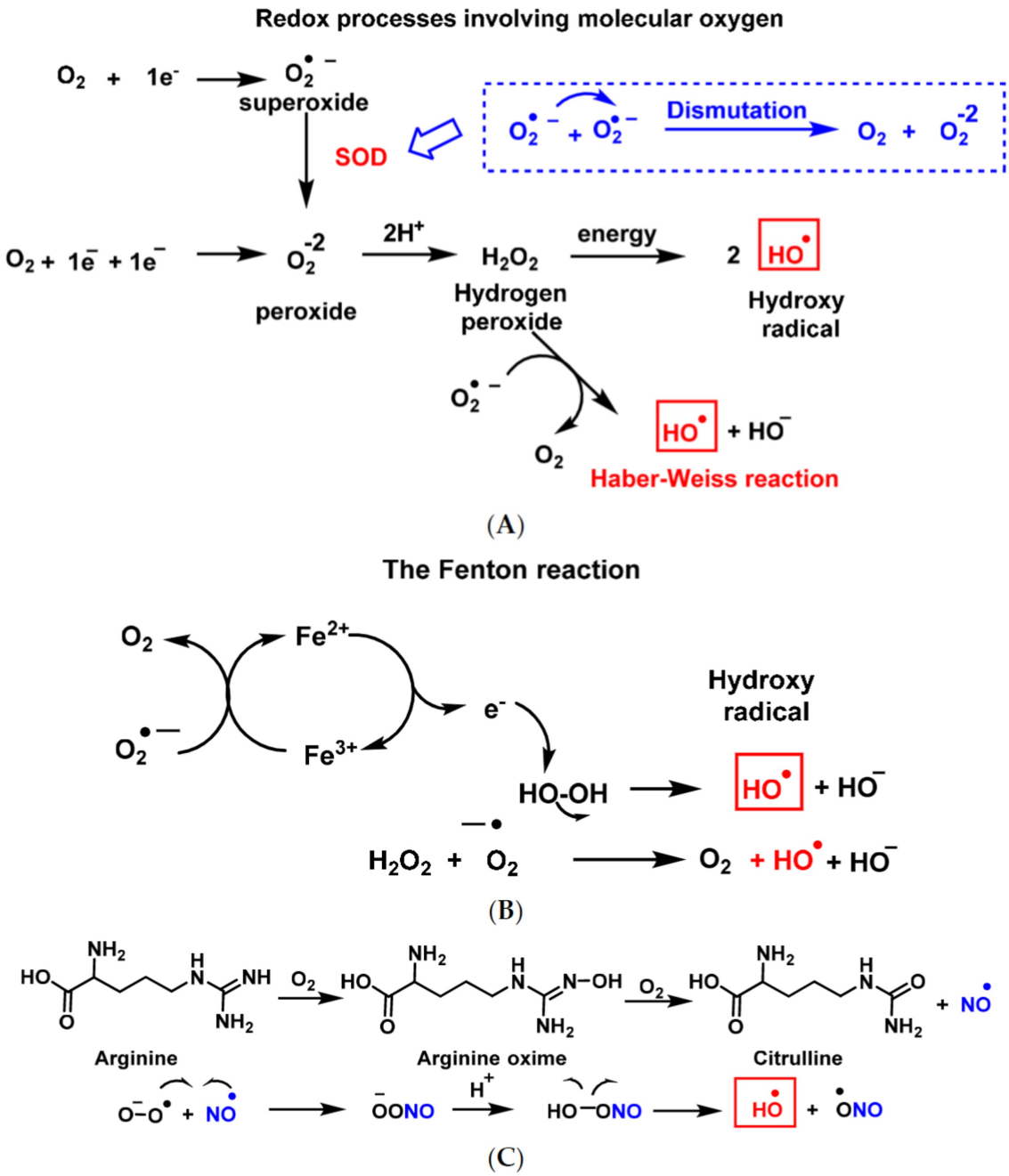

Figure 3.2 Some mechanisms of ROS formation through the reduction of oxygen [81]. Copyright © 2021 CC BY 4.0.

The $O_2^{\bullet -}$ is generated by the mitochondrial electron transport chain which is responsible for creating energy within the cell [84]. It is only moderately reactive on its own, but it participates in multiple reactions yielding a variety of ROS and reactive nitrogen species (RNS) such as hydrogen

peroxide (H_2O_2) and peroxynitrite ($ONOO^-$), from which many additional secondary radical species can be generated [83, 92, 93]. The organism produces an enzyme, superoxide dismutase (SOD), to control $O_2^{\bullet-}$ concentration by accelerating the reaction of $O_2^{\bullet-}$ with itself to form H_2O_2 and oxygen [83]. Another enzyme (glutathione peroxidase) catalyzes the degradation of H_2O_2.

$$2O_2^{\bullet-} + 2H^+ \rightarrow H_2O_2 + O_2$$

$$2H_2O_2 \rightarrow 2H_2O + O_2$$

Controlling $O_2^{\bullet-}$ the concentrations of these allows other radical species can be controlled.

$O_2^{\bullet-}$ is still potentially toxic despite not generally being considered a strong oxidizing agent. In particular, $O_2^{\bullet-}$ can oxidize iron-sulfur clusters in proteins, resulting in degradation and loss of the catalytic ion and therefore enzymatic activity [83]. Furthermore, the iron released from this process can directly reduce H_2O_2 via Fenton-type reactions, generating highly toxic hydroxyl radicals ($OH^{\bullet}$) which is a powerful oxidant that attacks DNA [83, 84, 91, 94].

$$O_2^- + Fe^{3+} \rightarrow O_2 + Fe^{2+}$$

$$H_2O_2 + Fe^{2+} \rightarrow OH^{\bullet} + OH^- + Fe^{3+} \text{(Fenton reaction)}$$

As previously stated, the formed $OH^{\bullet}$ is able to induce base oxidation in all nucleobases with non-sequence specificity [95]. It can also cause direct cleavage of the sugar-phosphate backbone. DNA damage can be induced in the absences of metal ions, but when metal ions are present the damage is enhanced through the secondary generation of H_2O_2 [95].

In the presence of copper ions, hydrogen peroxide can modify nucleic bases. Copper ions are associated with chromatin inside the cell to form stable complexes with DNA [95]. Individually

H_2O_2 is unable to cleave and oxidize DNA, however, incubation with DNA and Cu^{2+} causes base modifications at guanine, thymine, and cytosine residues. These base modification sites can be cleaved and the derived reactive species from H_2O_2 such as copper-peroxyl species (Cu(I)-OOH) are responsible for this DNA damage [95].

$$H_2O_2 + Cu^+ \rightarrow Cu(I)-OOH + H^+$$

Cu(I)-OOH is not greatly reactive compared to $OH^{\bullet}$, but its lifetime is relatively long to induce DNA damage [95]. Single-stranded DNA is easier to oxidize by these ROS.

Internal rearrangements of the unpaired electrons in O_2 produce singlet oxygen. Singlet oxygen ($^1O_2$) is in a quantum state where all electrons are spin paired [60, 95]. It is kinetically unstable at ambient temperature, but the rate of decay is slow. Singlet oxygen is the lowest excited state of the diatomic oxygen molecule [60]. Its physical properties only differ slightly from triplet ground state oxygen. However, its chemical reactivity is much higher toward organic compounds. The terms 'singlet oxygen' ($^1\Delta_g$) and 'triplet oxygen' ($^3\Sigma_g$) come from the number of possible arrangements of electron spins [60]. Singlet oxygen is very reactive and is significant in lipid peroxidation [92, 93]. Singlet oxygen in the gas phase is relatively long lived (54-86 milliseconds) and very reactive [60, 92, 93]. It is important in biological systems, specifically lipid peroxidation [92, 93].

3.4 Experimental and Theoretical Methods [1]

3.4.1 Plasma System

A dielectric barrier discharge plasma system was used for sterilization, AC, and biochar activation. A quartz tube was used as a vacuum chamber and was connected to a mechanical pump, pressure gauge, and a gas flow controller. A pair of electrodes was used to generate plasmas. One of the electrodes was connected to a radio frequency power generator through a matching network. The operation frequency was 13.56 MHz. The other electrode was grounded. If a magnetic field was used it was created by a permanent magnet assembly. The magnetic field in the plasma region was generated in a direction perpendicular to the electrical field. For the sterilization experiments, the sample was set at a downstream position right beyond the electrode (plasma) region, noted as the afterglow region.

The plasma setup used is shown in **Figure 3.3**. Before igniting a plasma, the quartz tube was evacuated with the vacuum pump to $< 1\times10^{-2}$ Torr and purged with the process gas 5 times to prevent cross contamination. The tube was subsequently filled with the process gas, e.g., a 10% O_2–90%Ar mixture. The gas flow was adjusted by a mass flow controller to achieve a test pressure. Then the radio frequency power was turned on and the matching network was adjusted to reach a zero-watt reflection power. The radio frequency power was then set maintained at 70 W for sterilization.

[1] Taken from [96] M. A. Mackinder, et al., "Magnetic field enhanced cold plasma sterilization," Clin. Plasma Med., (2020). Copyright © 2021 Elsevier

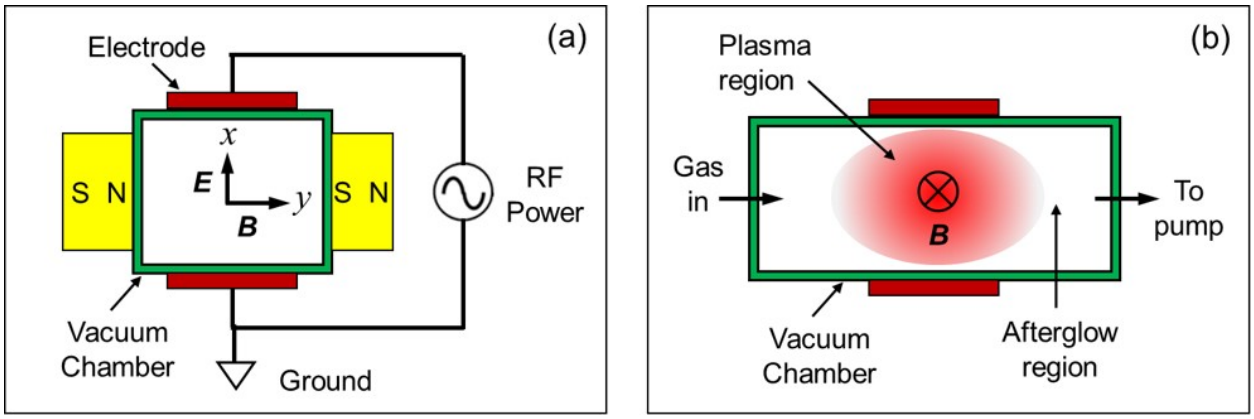

Figure 3.3 Schematic diagram of the plasma reactor setup. a) Profile view. b) Side.

3.4.2 Effects of Magnetic Field

High electron mobility makes plasmas generally very good conductors and thermal conductors [41]. Their high electrical conductivity does not allow them to support electrostatic fields except, somewhat, in a direction normal to a magnetic field, which inhibits the flow of charged particles in this direction [41]. Magnetized plasmas are anisotropic, meaning that their properties in the perpendicular to the magnetic field are different from those parallel to it. When a magnetic field is applied perpendicular to the electric field, this traps the electrons within the field, thus allowing the plasma density to be increased [14]. Particles in plasma diffuse from high density to lower density regions [41]. Electrons have a lower mass and tend to diffuse faster than ions [41]. The resulting charge separation generates a polarization electric field [41]. This field increases the diffusion of ions, while decreasing that of electrons, subsequently causing the ions and electrons to diffuse at approximately the same rate. This type of diffusion is known as ambipolar diffusion [41]. An externally applied magnetic field reduces the diffusion of charged particles across the field lines. Thus, strong magnetic field are effective in plasma confinement [41, 97]. In classical diffusion, the charged particles diffuse across magnetic field lines with a diffusion coefficient that is propor-

tional to $1/B^2$, where B denotes the magnetic field strength [41, 97]. It has been observed, many experimental plasma devices display non-classical diffusion, which is called Bohm diffusion. The so-called Bohm diffusion defines the diffusion coefficient as proportional to $1/B$ [41, 97]. Currently, there is no general consensus on which theory to use to describe electron cross-field diffusion [97].

The electromagnetic force F on a particle of charge q moving with a velocity v in an electric field E and a magnetic field B is described by the equation:

$$\mathbf{F} = \frac{d(m\boldsymbol{v})}{dt} = q\mathbf{E} + q\boldsymbol{v} \times \mathbf{B} \tag{3.5}$$

Both E and v can be split into components parallel and perpendicular to B.

$$v = v_{\parallel} + v_{\perp} \tag{3.6}$$

$$E = E_{\parallel} + E_{\perp} \tag{3.7}$$

Under the influence of a magnetic field the particle will gyrate in the plane perpendicular to B [10, 41, 45]. This is because the velocity parallel to the magnetic field, $v_{\parallel}$, is unaffected, and therefore, the magnetic field does no work on the particle [10, 41, 45]. Conversely, the velocity perpendicular to the magnetic field, $v_{\perp}$, is continually modified. In a uniform field, the motion of the particle in the plane normal to B is a cycloid with the constant velocity v_E which is called the plasma drift velocity [10, 41, 45]:

$$\boldsymbol{v_E} = \frac{\mathbf{E} \times \mathbf{B}}{\mathbf{B^2}} \tag{3.8}$$

The particle experiences a uniform acceleration along B. The electric force $qE_{\perp}$, acting

concurrently with the magnetic force, accelerates the particle causing it to increase or decrease velocity [10, 41, 45]. The change in velocity is dependent on the particle motion with respect to $E_{\perp}$ and the charge sign. This results in the charged particle gyrating around the magnetic field line with a guiding center moving with constant velocity along it [10, 41, 45]. All the charged particles drift in the same direction with the same velocity [10, 41, 45].

This, in turn, results in increased power efficiency due to an increase in collisions without needing to increase either power or pressure [14, 96]. Previous studies have shown that the reactive species and ions created in plasmas play an important role in applications such as sterilization [74]. Because of this, we hypothesize that the use of a magnetic field will (significantly) improve the sterilization capabilities of the plasma.

3.4.3 Plasma Sterilization Procedure

A dielectric barrier discharge plasma system was used for sterilization experiments (see **Chapter 2**). A quartz tube was used as a vacuum chamber and was connected to a mechanical pump, pressure gauge, and a gas flow controller. A pair of electrodes was used to generate plasmas. One of the electrodes was connected to a radio frequency power generator through a matching network. The operation frequency was 13.56 MHz. The other electrode was grounded. A magnetic field was created by a permanent magnet assembly (Figure 3.3). The magnetic field in the plasma region was generated in a direction perpendicular to the electrical field or in parallel to the electrode surface. A glass slide inoculated with the bacterial sample was placed on a boat and set at a downstream position right beyond the electrode (plasma) region, noted as the afterglow region. The magnetic field effectively confines energetic electrons from reaching the sample. Hence, using the afterglow region for sterilization is expected to further lower the process

temperature as compared to using the direct plasma region.

Before igniting a plasma, the quartz tube was evacuated with the vacuum pump to $< 1\times10^{-2}$ Torr and purged with the process gas 5 times to prevent cross contamination. The tube was subsequently filled with the process gas, e.g. a 10% O_2–90% Ar mixture. The gas flow was adjusted by a mass flow controller to achieve a test pressure. Then the radio frequency power was turned on and the matching network was adjusted to reach a zero-watt reflection power. The radio frequency power was maintained at 70 W through all experiments.

The temperature studies were performed for the direct and afterglow areas, and with and without a magnetic field. Temperature was measured using an infrared thermometer (Fluke 572-2 High Temperature Infrared Thermometer, Fluke Corporation, USA).

3.4.4 Preparation of Bacteria

The bacteria used for this study was *Escherichia coli* and was procured from a ThermoFischer Culti-loop. The bacterial sample was prepared following the given procedure for the indirect (broth) method. The broth used was a Luria-Bertani (LB) broth prepared in an autoclave. The cultures were grown and kept at 37 °C. After 24 hours a serial dilution and dilution plating on LB and agar media petri dishes were performed to calculate the number of bacteria present in each sample. The colonies were counted using Fiji ImageJ software and the Watershed segmentation function was performed to calculate the number of bacteria present in each sample. Then 50 μL of the bacterial cell suspension was deposited on sterile glass slides as a droplet using a pipette and a new sterile tip, then left to spread out and dry for no more than 10 min. After they were dry the inoculated glass slides were then placed on a boat inside the plasma tube for treatment.

Each bacterial slide was exposed to plasma treatment times of 10 sec, 30 sec, 1 min, 1.5

min, and 2.5 min. These treatments varied by pressure, location, and whether a magnetic field was present or not. All the plasma treatments for each round of testing were performed on the same day in order to make sure that the bacterial suspension was the same across each treatment. The experiments were repeated at least three times. For each round of tests, one sample was not exposed to the plasma and was kept as a control.

After the treatment was completed the boat with the inoculated glass slide was extracted. Each slide was swabbed with a new sterile swab. The swab was then mixed into a sterile vial with 10 mL sterilized phosphate-buffered saline (PBS). The swab was then discarded. The inoculated vial with PBS was then mixed and a 50 μL sample was taken using a pipette and new sterile tip. The 50 μL sample was placed on an agar media petri dish and a spread plate was made. The plates and vials were labeled accordingly and left to incubate for ~24 hours.

3.4.5 Optical Emission Spectroscopy

Optical emission spectroscopy (OES) studies were performed for the different pressures, and with and without a magnetic field to determine the primary plasma species and relative concentrations. OES was performed using an optical spectrometer (USB4000, Ocean Optics, Inc. USA).

3.4.6 Modeling of Magnetically Enhanced Plasma Discharges

A volume-averaged global model is developed to evaluate the magnetically enhanced dielectric barrier discharges, which can provide a description of plasmas with complex chemistry without the intensive computation required for spatially resolved models. The aim of using a global model here is to identify the main species generated in the plasma and quickly predict spatially

averaged plasma parameters such as densities of each species that would otherwise be difficult to simulate and diagnose. Since the qualitative change of the plasma parameters with the process parameters is the primary goal of this model research, the specific values of the plasma parameters are less important, this makes the global model the best choice here. The structure of the system is illustrated in Figure 3.3. The plasma generated in the quartz tube diffuses and loses isotropically to the inner walls of the tube. However, by applying a strong magnetic field in the y direction to the discharge system, the charged species and power losses perpendicular to the magnetic field are significantly suppressed. Due to the reduced effective loss area of mass and energy, the electron density as well as the number densities of reactive species are expected to be increased. In that case, the influence of magnetic field should be considered in the model, as described as follows.

First, consider the case of no magnetic field. The mass balance equation for heavy species is:

$$\frac{\partial n_k}{\partial t} = R_k + \frac{1}{V}\sum_s A_s \Gamma_{k,s} \tag{3.9}$$

where n_k is the number density of species k, t the time, $R_k = \sum_k k_{iz,k} n_k n_e$ the reaction rate, $k_{iz,k}$ the ionization rate coefficient of electron collisions with species k, n_e the electron density, $V = 7.8$ cm^3 the reactor volume, $A_s = 12.5$ cm^2 the surface area. The flux of ion species k at a surface s is $\Gamma_{k,s} = \frac{\gamma_k}{1-\gamma_k/2}\frac{1}{4} n_k \sqrt{\frac{8k_B T_k}{\pi m_k}}$, where k_B is the Boltzmann constant, $\sqrt{\frac{8k_B T_k}{\pi m_k}}$ the averaged thermal velocity, $\gamma_k = 1$ the sticking coefficient, $T_k = 400$ K the temperature and m_k the mass of heavy species k . Assuming the plasma is quasi-neutral, the electron density is:

$$n_e = \sum_k z_k n_k \tag{3.10}$$

where z_k is the charge number of species k. The energy balance equation is

$$e\frac{\partial n_\epsilon}{\partial t} = \frac{P_{abs}}{V} + R_\epsilon + \frac{1}{V}\sum_s \sum_{pi} eA_s\Gamma_{k,s}\left(\epsilon_e + \epsilon_i\right) \tag{3.11}$$

where e is the elementary charge, n_ϵ the electron energy density, P_{abs} = 70 W the absorbed power, $R_\epsilon = e\sum_K k_k n_k n_e \Delta\epsilon_k$ the electron energy variation due to polarization scattering and inelastic collisions, k_k and $\Delta\epsilon_k$ are the rate coefficient and the energy variation between electron and species k, $\epsilon_e = 2T_e$ and $\epsilon_i = \frac{1}{2}T_e + V_s$ are the mean kinetic energy lost per particle lost for electrons and ions, respectively [42]. T_e is the electron temperature and V_s is the potential drop across the sheath. The last term on the right-hand side of the above equation is summed over all surfaces and all positive ions.

Without an external magnetic field, the generated plasma contacts with the inner surface of the dielectric tube in the x and y directions and flows outward freely in the z direction. Assuming the center-to-edge density ratio of ions is h_s, the flux of ion species j can be expressed as $\Gamma_j = h_s n_j u_{B,j}$, where $u_{B,j}$ is the Bohm velocity of ion species j. From an intermediate pressure of 50 mTorr to a high pressure of 1 Torr, the center-to-edge ratio can be expressed as:

$$h_l \approx \frac{0.86}{\left[3 + l/2\lambda_i + (0.86lu_B/\pi D_a)^2\right]^{1/2}} \tag{3.12}$$

at the axial sheath edge and

$$h_R \approx \frac{0.8}{\left[4 + R/\lambda_i + (0.8Ru_B/\chi_{01}J_1(\chi_{01})D_a)^2\right]^{1/2}} \tag{3.13}$$

at the radial sheath edge, respectively [42]. l = 5 cm and R = 1.25 cm are the length and radius of the

cylindrical reactor, $\lambda_i = \frac{1}{n_g \sigma}$ is the mean free path of ions, n_g the number density of background gas and σ the cross section of ion-neutral collisions, $D_a \approx \mu_i T_e$ is the ambipolar diffusion coefficient, $\mu_i = z_i e / m_i \nu_m$ is the ion mobility, m_i is the ion mass and ν_m is the momentum transfer frequency, J_1 is the first-order Bessel function and χ_{01} is the first zero of the J_1 Bessel function. In the x direction, there are high-voltage sheaths on the dielectric surface, which we assume is about $V_s \approx 1000$ V. The neutral species α diffuses to the walls isotropically with a flux of $\Gamma_\alpha = 1/4 n_\alpha u_{T,\alpha}$, where $u_{T,\alpha}$ is the thermal velocity of α.

With a strong magnetic field B (e.g. 0.15 Tesla) parallel to the y direction, the charged species and power losses perpendicular to the magnetic field are significantly reduced. The diffusion coefficient of the plasma perpendicular to the magnetic field can be written as $D_{\perp a} \approx \mu_i T_e / (1 + (\omega_c \tau_e)^2)$, where $\omega_c = eB/m_e$ is the electron cyclotron frequency, m_e is the electron mass, $\tau_e = \lambda_e / \upsilon_{e,th}$ the mean time between interactions, λ_e is the electron mean free path, $\upsilon_{e,th} = \sqrt{8eT_e/\pi m_e}$ is the electron thermal velocity. The neutral species losses are not affected by the magnetic field.

The above model is established by the built-in plasma module of the commercial software COMSOL [98]. There are 12 primary species and 21 major reactions considered in the model. The 12 primary species considered are divided into neutral, positive, and negative species. The neutral species consist of Ar, Ar^m, O, O_2, O_3, and O_2(a). The positive and negative species considered are Ar^+, O^+, O_2^+, O^-, O_2^- , and e. The reactions included in the model are summarized in **Table 3.1**. Most of the heavy particle reactions are adopted from the reduced chemistry set provided by Gaens and Bogaerts [99]. In this reduction, only the reactions that contribute for more than 10% to the formation or destruction of a species were selected to reduce the number of reactions. The electron-impact reactions are characterized by the corresponding cross section data. For plasmas with a

relatively high pressure used in this model, the electron energy distribution function (EEDF) is assumed as Maxwellian. The processes considered are as follows: (1) elastic collisions, (2,6, & 8) ionization, (3 & 7) excitation, (4) deexcitation, (5) multistep/stepwise ionization, (9) dissociation, (10) dissociative attachment, (11, 15 & 18) charge exchange, (12) associative detachment, and (13, 14, 16, 17, 19, & 20) recombination.

Table 3.1 Principal rate coefficients used in this model [96].

	Reaction	Reaction coefficient (m^3/s)	Threshold (eV)	Reference
1	$e + Ar \rightarrow e + Ar$	$2.336 \times 10^{-14} T_e^{1.609} \times \exp(0.0618(\ln T_e)^2 - 0.1171\left((\ln T_e)^3\right)$		[42]
2	$e + Ar \rightarrow 2e + Ar^+$	$2.34 \times 10^{-14} T_e^{0.59} \exp(-17.44/T_e)$	15.76	[100]
3	$e + Ar \rightarrow e + Ar^m$	$2.5 \times 10^{-15} T_e^{0.74} \exp(-11.56/T_e)$	11.56	[101]
4	$e + Ar^m \rightarrow e + Ar$	$4.3 \times 10^{-16} T_e^{0.74}$	-11.56	[102]
5	$e + Ar^m \rightarrow 2e + Ar^+$	$6.8 \times 10^{-15} T_e^{0.67} \exp(-4.2/T_e)$	4.2	[103]
6	$e + O \rightarrow 2e + O^+$	cross section	13.61	[104]
7	$e + O_2 \rightarrow e + O_2(a)$	cross section	0.977	[105, 106]
8	$e + O_2 \rightarrow 2e + O_2^+$	cross section	12.06	[105]
9	$e + O_2 \rightarrow e + 2O$	cross section	13.5	[107]
10	$e + O_2 \rightarrow O^- + O$	cross section	4.3	[108]
11	$e + O_2(a) \rightarrow e + 2O$	cross section	12.523	[99]
12	$O + O^- \rightarrow e + O_2$	1.5×10^{-16}		[99]
13	$O + 2O_2 \rightarrow O_3 + O_2$	$6.4 \times 10^{-47} \exp(663/T_g)$		[99]
14	$O + O_2 + O_3 \rightarrow 2O_3$	$1.3 \times 10^{-46} \exp(663/T_g)$		[99]
15	$O + O_2^- \rightarrow O^- + O_2$	$1.5 \times 10^{-16} (T_g/300)^{0.5}$		[99]
16	$O + O_2^- \rightarrow e + O_3$	1.5×10^{-16}		[99]
17	$O + O_3 \rightarrow 2O_2$	$8 \times 10^{-18} \exp(-2060/T_g)$		[99]
18	$O^- + O_2 \rightarrow O + O_2^-$	1×10^{-16}		[99]
19	$O^- + O_2^+ + M \rightarrow O + O_2 + M$	$2 \times 10^{-37} (T_g/300)^{-2.5}$		[99]
20	$O_2(a) + O_3 \rightarrow 2O_2 + O$	1×10^{-20}		[99]

3.5 Results and Discussion [1]

3.5.1 Enhancement of Plasma Density by a Magnetic Field

Using the plasma model described above, the magnetic enhancement of the dielectric barrier discharges is verified and proven effective. The number densities of plasma species under different conditions are illustrated in **Figure 3.4**. With an absorbed power of 70 W and 90%-Ar + 10%-O_2 feeding gas, the external magnetic field leads to significantly increased number densities of all charged particles except O_2^-. However, with the magnetic field, the densities of the charged particles decrease as the pressure increases. This is because the magnetic confinement is weakened under the enhanced electron-neutral collisions. The number densities of neutral species tend to increase by applying an external magnetic field and by increasing the pressure.

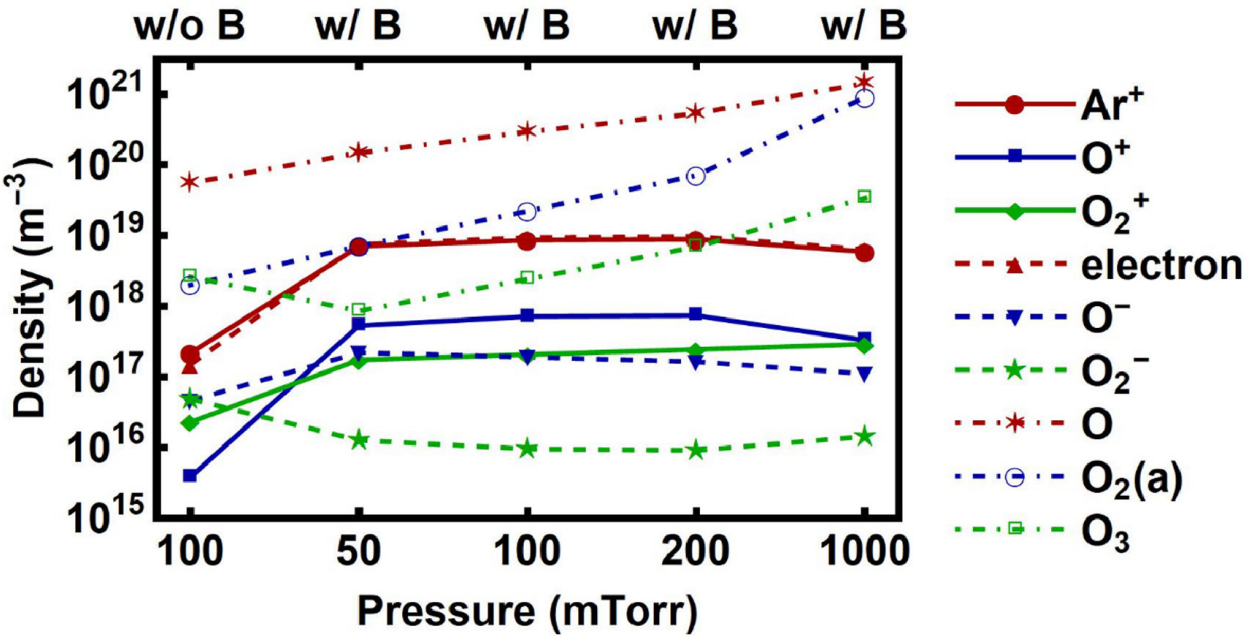

Figure 3.4 The number densities of plasma species under 100 mTorr without a magnetic field B, and under pressures from 50 mTorr to 1 Torr with an external magnetic field of 0.15 T. The absorbed power is 70 W in all cases.

3.5.2 Optical Emission Spectroscopy Study

Optical emission spectroscopy (OES) was used to confirm that the addition of the magnetic field increases plasma density and efficiency. A comparison of optical emission spectra in **Figure 3.5** shows the results of applying a magnetic field in regard to plasma intensity. The spectra clearly show that the addition of a magnetic field greatly increases the intensity (4-7 times) in the direct plasma region and by 2 times in the immediate afterglow region. compared to that of the plasma without a magnet. These findings are in good agreement with the modeled densities of the excited oxygen species (e.g., O_2(a)), which dominate the optical emissions. In a low density plasma, the neutral molecules surpass the Coulomb interactions of the charged molecules [10]. The charged particles then have a higher probability of colliding with the neutral particles than with other charged particles, which impedes plasma effects [10]. By applying a magnetic field perpendicular to the E-field, the electrons were trapped and the plasma density increased without the need to increase power and/or pressure. It is worth noting that the global plasma model only predicts the major species in the bulk plasmas rather than the species distributions in the reactor. The modeling results provide information on what species could play essential roles in the sterilization. The actual concentrations of the interested plasma species at the sample locations are determined from the optical emission measurements.

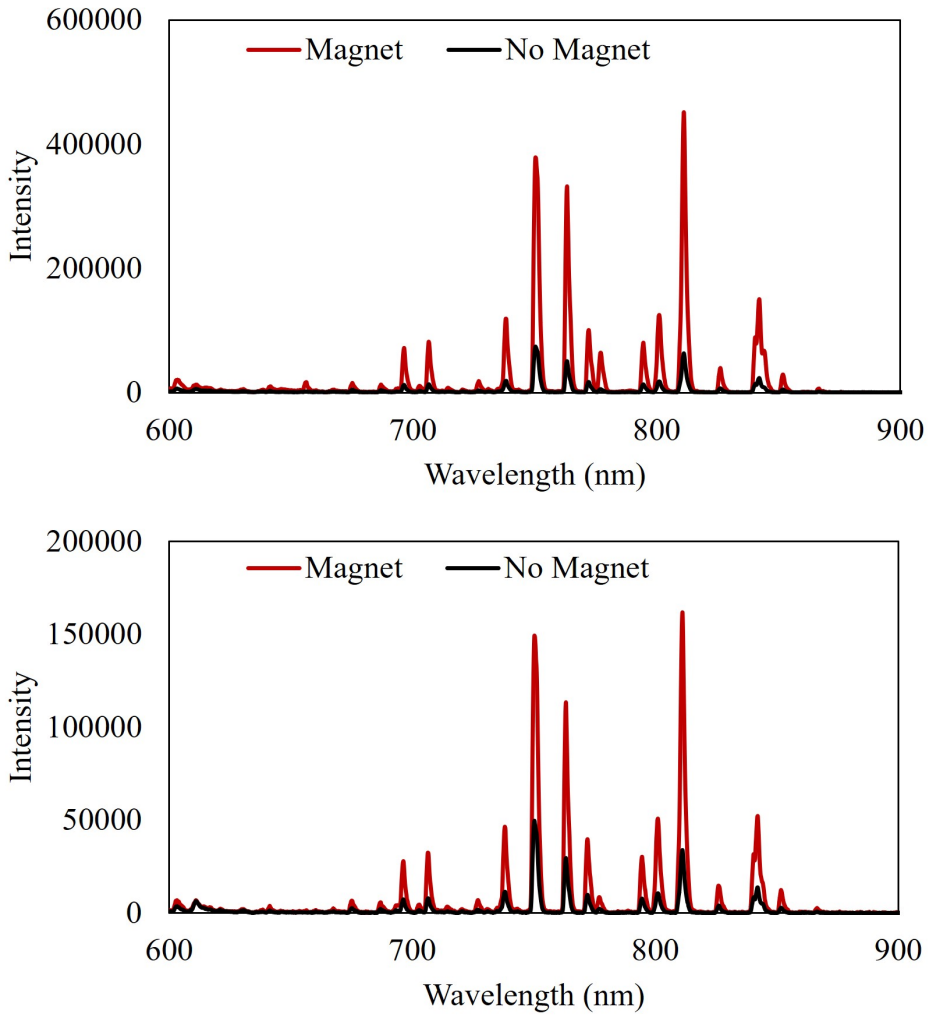

Figure 3.5 Top: Intensity of the direct area with and without magnet at 100 mTorr. Bottom: Intensity of the afterglow area with and without a magnet at 100 mTorr.

3.5.3 Temperature Study

Because increased plasma density leads to higher heating loads due to increased bombardment of charged particles onto the surface from the plasma, the bacterial samples were placed in the afterglow to minimize the effects of heat (see **Figure 3.6** and **Figure 3.7**).

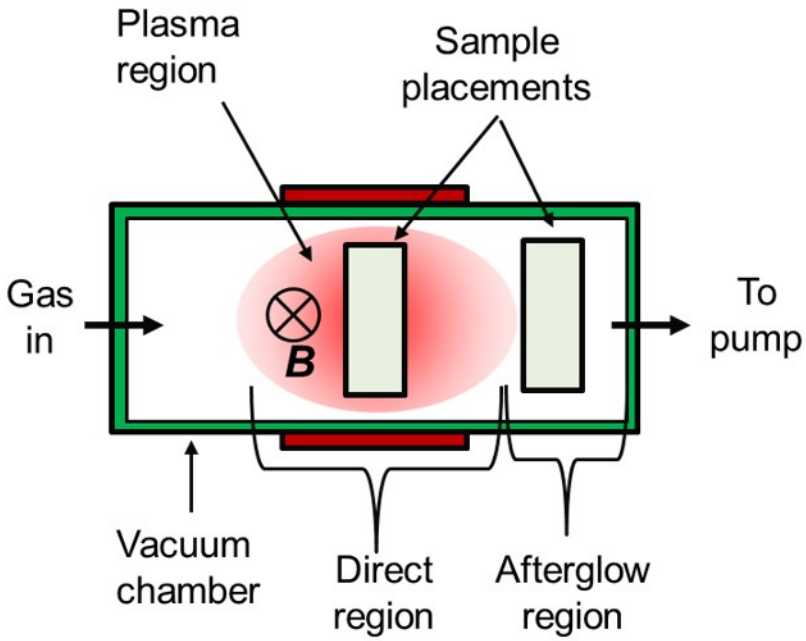

Figure 3.6 Schematic representation of the experimental setup and placement of samples within the direct and afterglow regions.

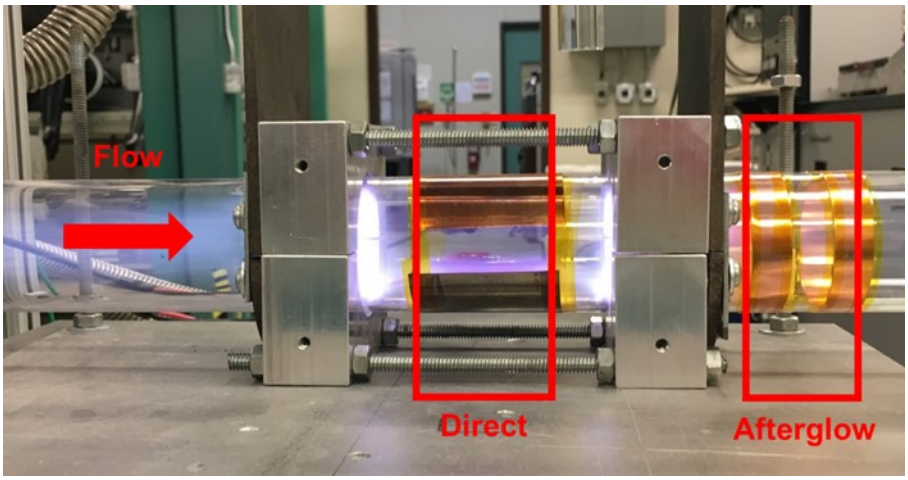

Figure 3.7 Experimental setup with the direct area and afterglow area labeled.

The known temperature threshold for *E.coli* death is 60 °C [100]. Keeping the temperature below this threshold ensures that heat is not the mechanism of sterilization and that there is little chance of polymer-based medical devices being heat damaged [101]. A temperature study was also conducted and repeated three times. The results are shown in **Figure 3.8**. The maximum uncertainty between the three recorded trials was ± 4 °C. This variation in temperature was mainly due to the measurement by the infrared thermometer and the pointing location in the sample surface. The graph clearly shows that the temperature within the direct plasma region is higher and increases faster than the afterglow region. After 5 minutes of treatment at 70 W and ~ 100 mTorr with a magnetic field, the direct region temperature exceeds the 60 °C threshold while the afterglow region stays below 40 °C. As will be shown in the next section, the plasma sterilization time needed to reach the sterilization assurance level (SAL) for the afterglow region is around 1 minute, implying that temperature would be well below the threshold for *E.coli* death. Although a less dramatic temperature disparity is seen between the treatments without a magnetic field, choosing the afterglow region is still more favorable in terms of localized heating by energetic charged particles to the sample. Comparing the OES and temperatures of the afterglow region between the treatments with and without a magnetic field highlight that the use of a magnetic field helps to further decrease the temperature of the treatment without compromising the plasma density. Hence, the magnetically enhanced plasma sterilization is expected to be more efficient.

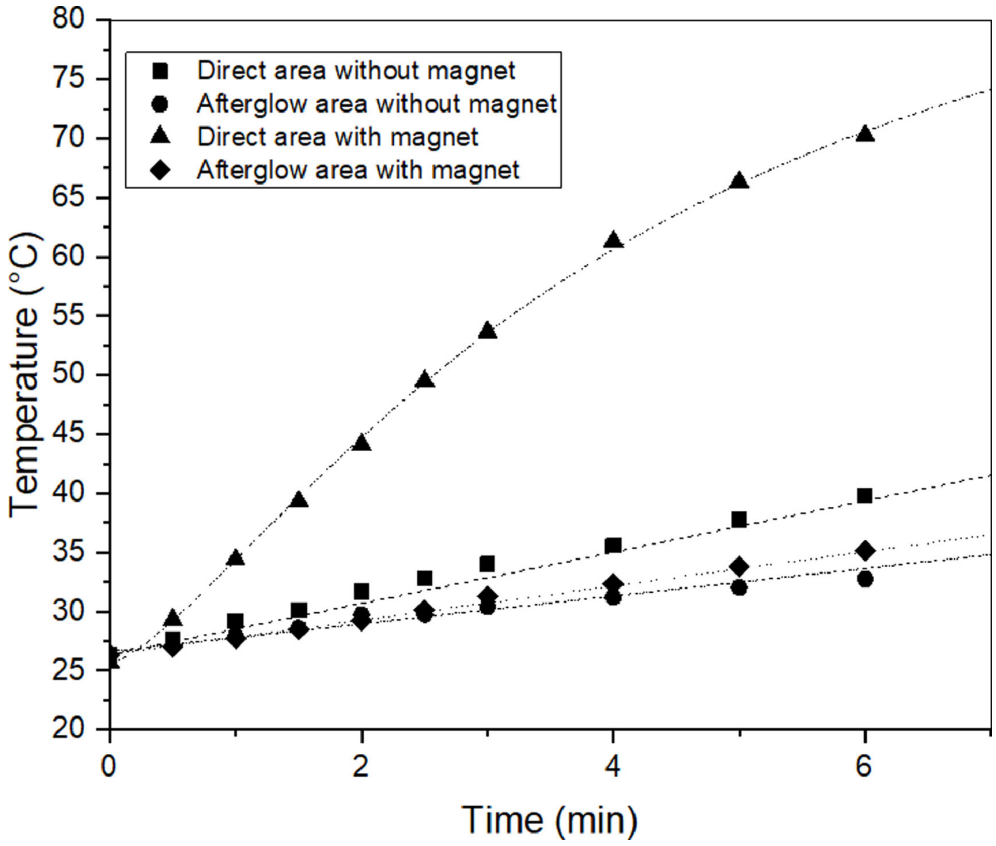

Figure 3.8 Temperature comparison between direct and afterglow areas with and without a magnetic field.

3.5.4 Effects of a Magnetic Field on Sterilization

Plasma sterilization experiments are first performed without the magnetic field for different time. The plasma discharges are generated at 70 W RF power and ~100 mTorr. **Figure 3.9** shows that there are no visible colonies at 1.5 minutes without a magnetic field. A D-value (decimal reduction time) of 0.113 min is deduced from the survival curve of the treatment. The D-value is the time required to kill 90% of a microorganism population. In order to determine a D-value, a "survivor curve" must be constructed. The survivor curve is created when a population of microorganisms of known number is treated. Samples are taken at different times and the number of surviving microorganisms is determined after incubation [102]. The "survivor curve" is then

constructed by plotting the log number of survivors vs. treatment time [102]. Fitting a line to the data allows for the D-value to be calculated from the time required for one logarithm reduction in survivor population or by taking the negative reciprocal of the slope [103]. The D-value is a logarithmic rate of killing and the SAL concept is based on the assumption that exponential first-order kinetics occurs for bacterial inactivation by physical or chemical processes, with a resulting linear inactivation graph on a semi-logarithmic plot [102]. To get SAL compatible sterilization the data needs to be extrapolated based on the results [102]. Using this D-value the estimated time needed to reach the SAL is 1.57 minutes, as illustrated in **Figure 3.10**.

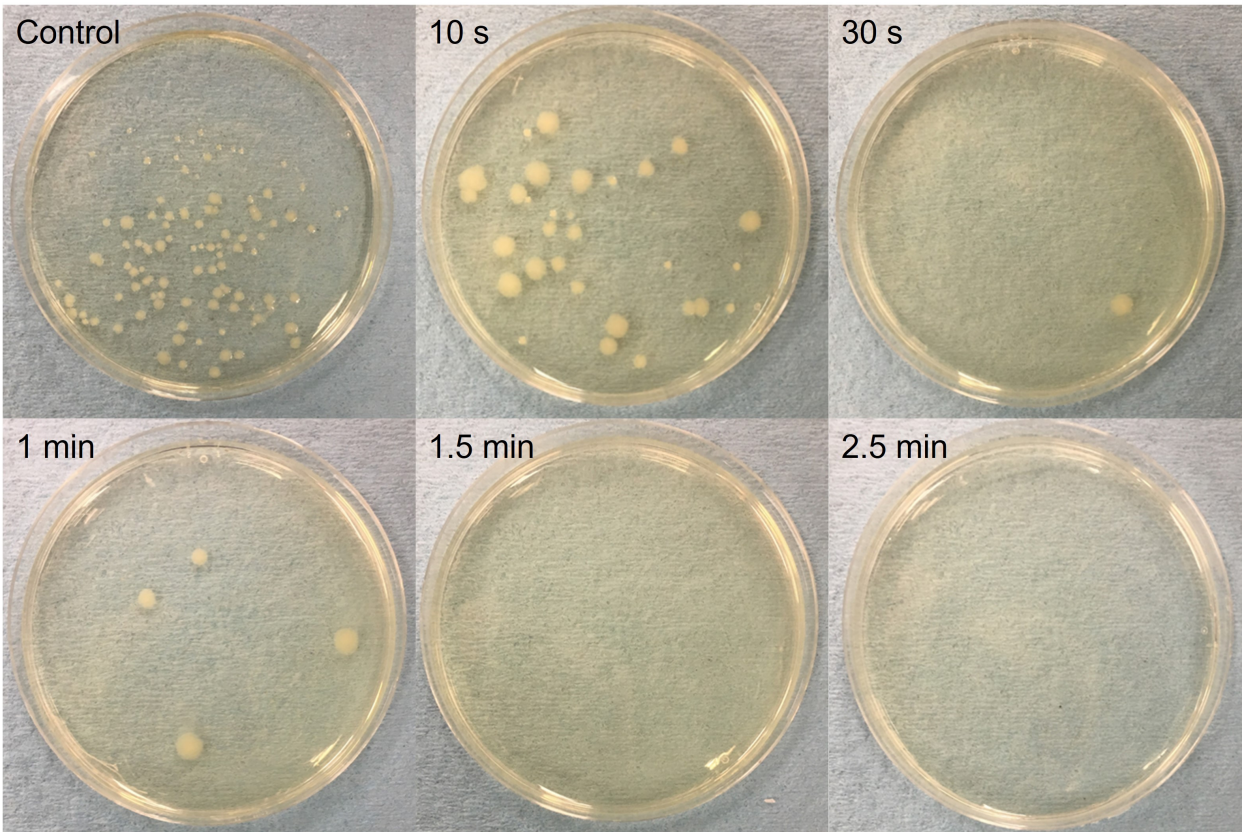

Figure 3.9 Growth after sample treatment without magnet. Top from left to right: control, 10 s, and 30 s. Bottom from left to right: 1 min, 1.5 min, and 2.5 min.

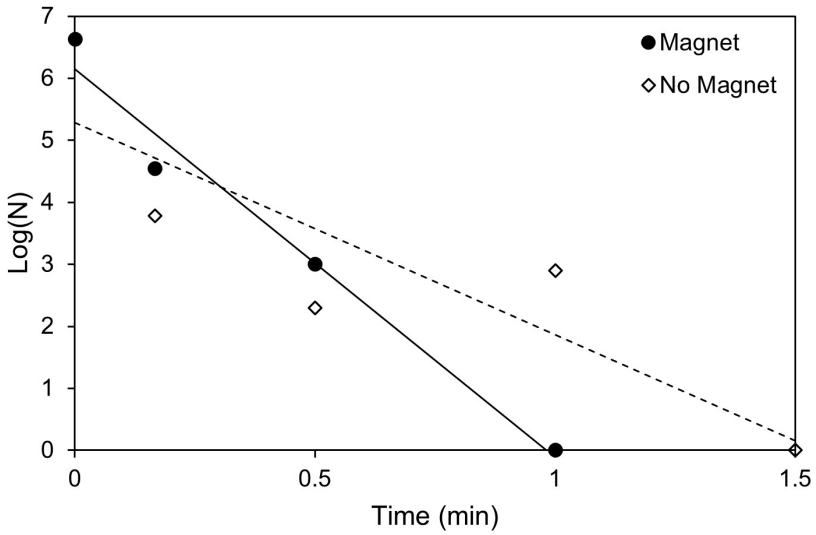

Figure 3.10 A comparison between the survival curves of the 100 mTorr treatment with and without a magnetic field (n=3).

Similar experiments are then performed using the same process parameters with an external magnetic field. As discussed before, the external magnetic field efficiently confines high-energy electrons and promote plasma densities and low-temperature treatments in the afterglow region. As shown in **Figure 3.11**, the addition of a magnetic field results in no visible colonies forming at 1 minute of treatment. Plotting and analyzing the survival curve of these results (Figure 3.10) gives a D-value of 0.069 minutes. The calculated time needed to reach the SAL is then 0.965 minutes. Comparing this to the time needed without the magnetic field, the magnetically enhanced plasma decreases treatment time by 61%.

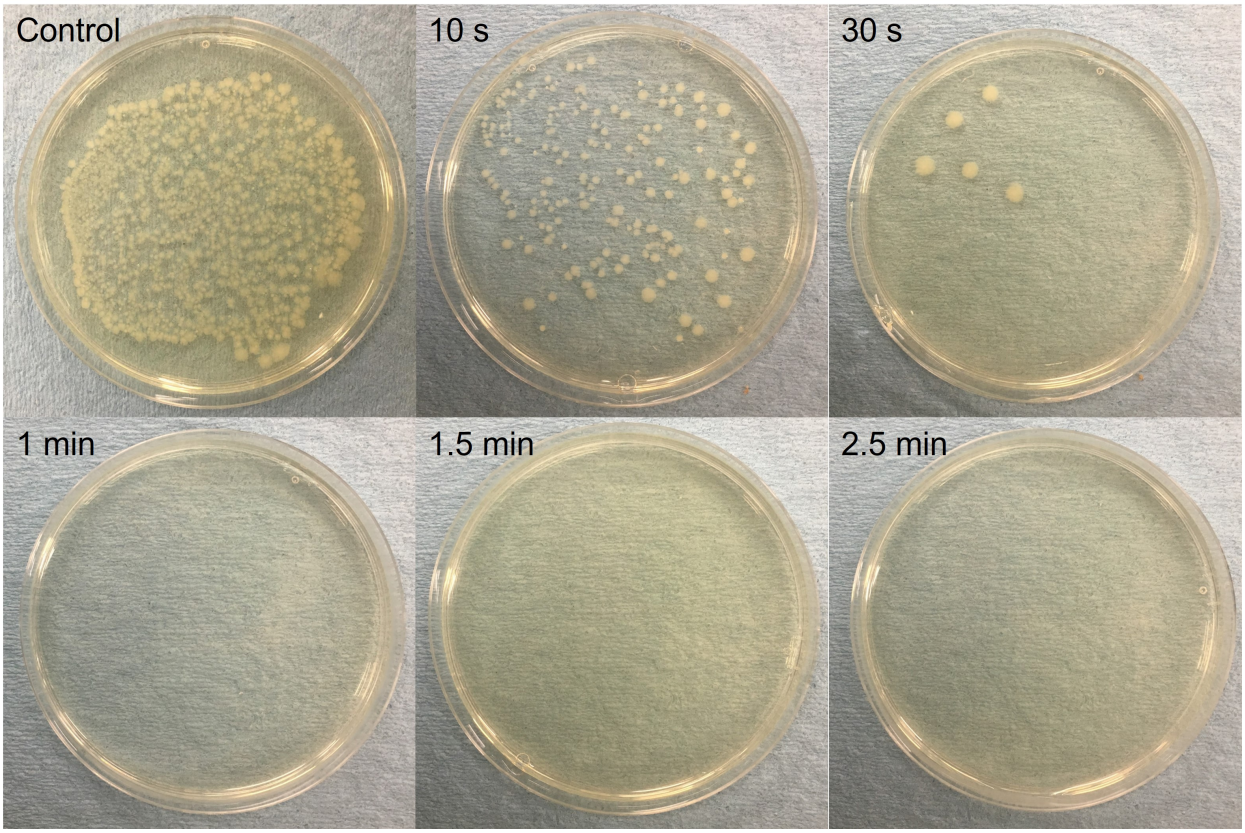

Figure 3.11 Growth after sample treatment with magnet. Top from left to right: control, 10 s, and 30 s. Bottom from left to right: 1 min, 1.5 min, and 2.5 min.

3.5.5 Effects of Pressure on Sterilization

As mentioned in the introduction and illustrated in **Figure 3.12**, the gas pressure has significant effects on the densities of the plasma species. Since the magnetic field promote the sterilization efficiency, the studies on the effects of gas pressure are performed with a magnetic field and the samples are placed in the afterglow region. From the previous experiments, the pressure of ~100 mTorr results in a D-value of 0.069 minutes and a SAL of 0.965 minutes. Subsequently, gas pressures below and above 100 mTorr are studied for comparison. The results are summarized in **Table 3.2**. The results indicate that there is an optimal gas pressure ~100 mTorr, which gives the most efficient sterilization. Increasing the gas pressure leads to a rapid increase in the D-value and sterilization time. This is due to the increased frequency of electron-neutral collisions that limit the

transfer of sufficient kinetic energy to ionize and excite the gas species. At a lower pressure (e.g. 50 mTorr), the electron-neutral collision probability decreases and subsequently the ionization and excitation are reduced.

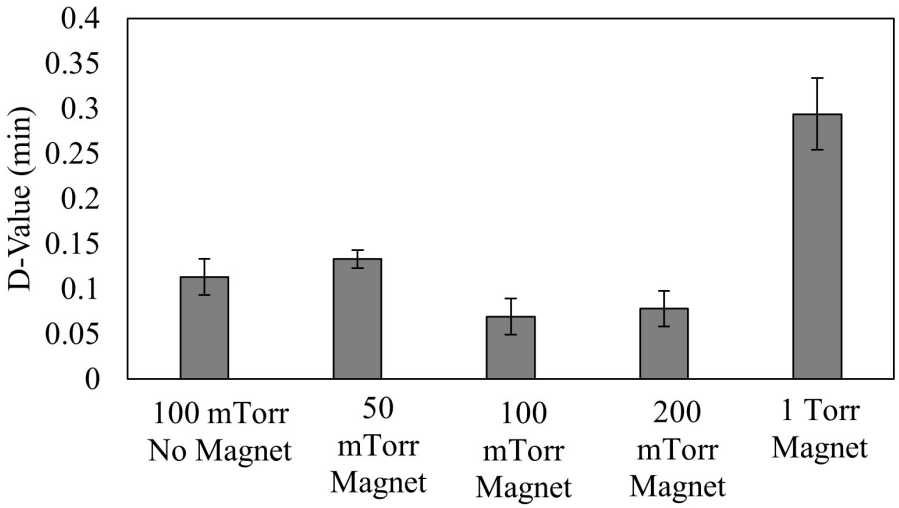

Figure 3.12 The effect of pressure on the calculated D-values for treatments with and without a magnetic field (n=3).

Table 3.2 D-value and SAL time at different gas pressures (n=3).

Magnetic field	**Yes**	**Yes**	**Yes**	**Yes**	**No**
Gas pressure (mTorr)	50	100	200	1000	100
D-value (min)	0.133±0.01	0.069±0.02	0.078±0.02	0.294±0.04	0.113±0.02
SAL time (min)	1.713±0.30	0.965±0.08	1.06±0.08	4.00±0.50	1.57±0.30

3.6 Discussion of Sterilization Mechanisms [1]

It has been known that reactive oxygen radicals damage the cells by either etching the outer membrane or diffusing through to cause damage to the inner membrane, proteins, and DNA by oxidation [6]. When micro-organisms undergo plasma treatment they are assaulted by the

oxygen radicals causing damage that the cell cannot repair [77]. This etching process happens due to the oxygen species being adsorbed onto the surface of the bacteria to react and form volatile compounds. Oxygen plasma has been previously shown to be effective for etching and oxidation [76]. The capability of the atomic oxygen species to oxidize is essential to their ability to sterilize [77].

To further understand the sterilization mechanisms, OES studies are performed for the magnetized O_2/Ar plasmas. **Figure 3.13** depicts the optical emission spectra for the afterglow area at four pressures: 50 mTorr, 100 mTorr, 200 mTorr, and 1 Torr. The major emission lines include 1) atomic oxygen transition lines at 777 nm and 844 nm, 2) O_2^* transition lines within the range of 480-580 nm, 3) Ar lines at 750 nm and 811 nm, and 4) OH lines at 287 and 308 nm. Except OH radicals, all the other species are predicted by the modeling to be dominant in the plasma.

The atomic oxygen transition lines at 777 nm and 844 nm have the greatest intensity at 100 mTorr [76]. The atomic oxygen line at 777 nm for 100 mTorr is ~4.5x greater than 50 mTorr, and ~2x greater than 200 mTorr and 1 Torr. The 100 mTorr atomic oxygen line at 844 nm is ~3.5x greater than 50 mTorr, and ~2.5x greater than 200 mTorr and 1 Torr. In the afterglow the optical emission intensities of the O_2^* species within the range of 480-580 nm are relatively constant at different pressures. As a result of the combined effect of the oxygen radicals, the sterilization is the most efficient at ~100 mTorr pressure. These findings are in good agreement with a previous study [79]. This mechanism is further reinforced by a study conducted by Liu et al. who find that, in the afterglow zone of an oxygen plasma, oxygen radicals are in high concentration and responsible for sterilization [104].

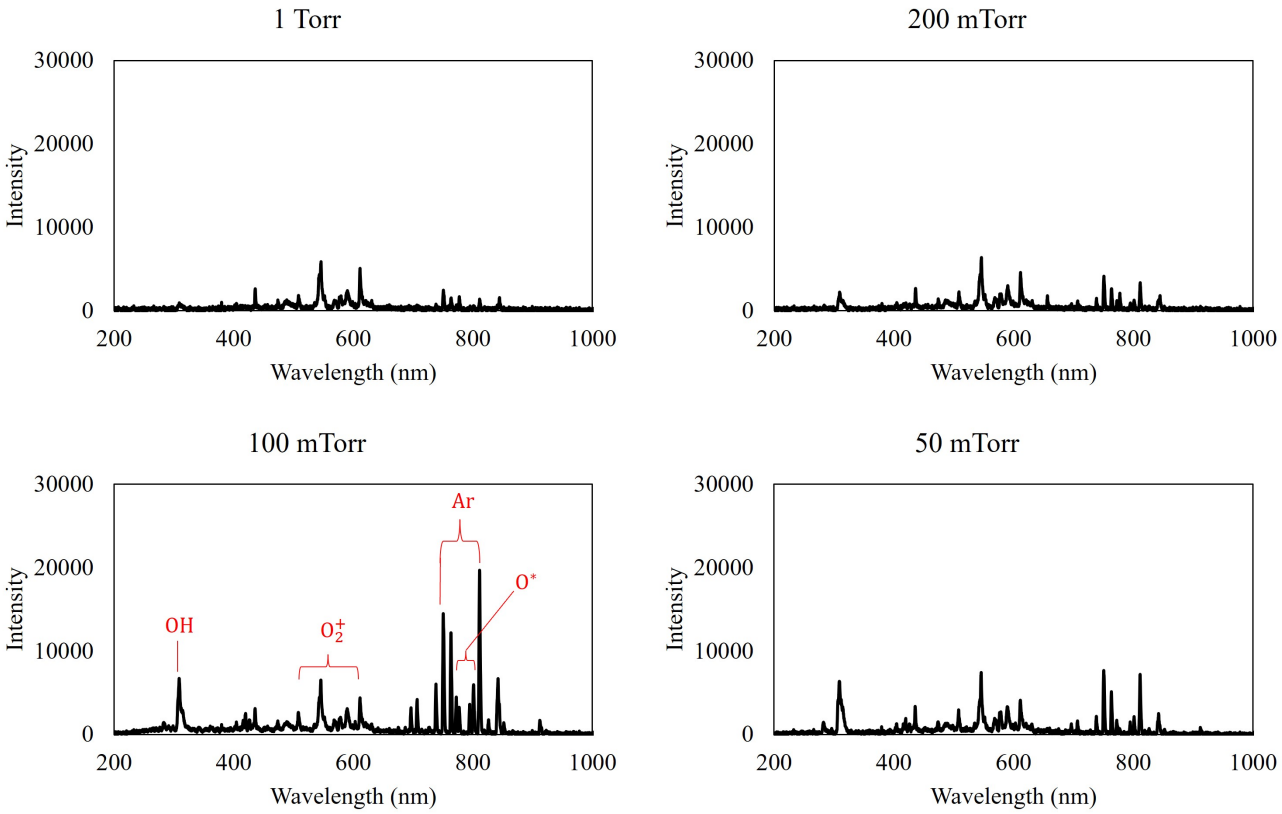

Figure 3.13 Optical emission spectrum of the afterglow at different pressures.

Yang et al. have studied the sterilization mechanisms of argon plasmas. They find that after treatment cells are eroded and their proteins and nucleic acid leak out [78]. The etching and rupturing of the cell membranes are due to argon ion bombardments [78]. These findings, along with the OES results showing that the argon emission peak at 750 nm has the greatest intensity at 100 mTorr, suggest that Ar ion etching also plays a significant role in plasma sterilization. Samples placed in the direct area run the risk of surface damage due to the impact of positive ions through a sheath of relatively high potential [79]. Hence, the afterglow area is a suitable choice for sterilization sample placement.

The UV emission lines at 287 and 308 nm are caused by the transitions of the OH band [105]. There are two possible reasons to form the OH species: 1) the reactions between the oxygen

species and the bacteria [106], and 2) the presence of residual H_2O [107]. Since the OH peaks are more intensive at 100 mTorr than at the other pressures in the afterglow, UV radiation highly likely plays a role in sterilization or is an indication of oxygen plasma etching of the bacteria.

3.7 Summary and Conclusions [1]

Plasmas, especially highly reactive plasmas like those of oxygen and argon mixture, have been shown to have the ability to sterilize surfaces. Their ability to kill microorganisms like *E. coli* depends strongly on the plasma characteristics and gas pressure. A magnetized plasma has the ability to greatly shorten sterilization time due to increased concentrations of reactive species. The direct discharge region of plasma has a greater density which leads to increased amounts of heating and intense etching, increasing the potential for damage to occur to fragile or heat-sensitive equipment. Therefore, the afterglow region with its lower temperature is a preferred location for the samples. It was found that atomic and molecular oxygen (ions and excited species) and argon ions were the plasma species that seemed to contribute most to the sterilization. The UV radiation of the plasma may also play a role in killing the bacteria and needs further evaluation to quantify its effects in sterilization.

CHAPTER 4

METHYLENE BLUE ADSORPTION BY PLASMA RE-ACTIVATED CARBON

4.1 Toxic Chemicals: Methylene Blue

Over 7×10^8 kg of dyestuff are produced annually in the textile industry alone [109–111]. The washing of dyed or printed textiles and fabrics generates 280,000 tons of dye laden effluent. This wastewater contains high levels of non-biodegradable organic compounds, especially dyes, and hazardous species which impact the aquatic flora, fauna, and human health [109–114].

These dyes are highly soluble in water, making them difficult to remove by conventional means [109, 114]. Due to their complex chemical structure, dyes are resistant to fading on exposure to light, water and many chemicals [109–111, 114]. It has been found that dyes in the water can have acute and/or chronic effects on exposed organisms depending on the exposure time and concentration [109]. The can act as toxic, mutagenic, and carcinogenic agents, persisting across entire food chains providing biomagnification [114]. Because dyes are highly visible, even minor concentrations an effect the color of surface waters, and their ability to absorb/reflect sunlight entering the water upsets bacterial growth and biological activity [109, 114]. There are many structural varieties, such as, acidic, basic, disperse, azo, diazo, anthraquinone based and meta complex dyes. These differences and complicated molecular structures make them difficult to treat and interfere with municipal waste treatment operations [109, 114]. Decolouration of textile dye effluent does not occur when treated aerobically my municipal sewage systems. Dyes in wastewater also undergo chemical and biological changes, consume dissolved oxygen from the water, and tend to sequester metal ions producing microtoxicity to fish and other organism, all of which harm

aquatic life [109, 114].

Basic dyes are historically important because they include the first synthetic textile dyes [109]. Basic or cationic dyes have cationic properties deriving from positively charged sulfur and nitrogen atoms [109]. The charge is generally delocalized throughout the chromophoric system, although it is probably more localized on the nitrogen atoms. They have components that dissociate into positively charged ions in an aqueous solution. Basic dyes are so named because the cations can interact with materials that have a net negative charge, forming salts which can be firmly attached [109]. In general, basic dyes are beautiful, shiny, crystalline compounds with outstanding brilliance. Their tinctorial value is exceptionally high with < 1 ppm of dye producing obvious coloration [109].

An important basic dye is methylene blue (MB) (**Figure 4.1**). Methylene blue is a dark green powder or crystalline solid. It dissociates in aqueous solution into a methlyene blue cation and a chloride ion [109]. Methylene blue is a cationic dye commonly found in industrial wastewater given its widespread use in material manufacturing, biological and medical applications, and the production of ink [15, 19–22, 29, 115–117]. While MB is not life-threatening in low doses, long-term MB exposure can cause vomiting, anemia, hypertension, cyanosis, and jaundice [20–22]. The MB cation is adsorbed preferentially by several adsorbents [109]. Because of this, and its widespread use, MB was selected as an adsorbate in this research.

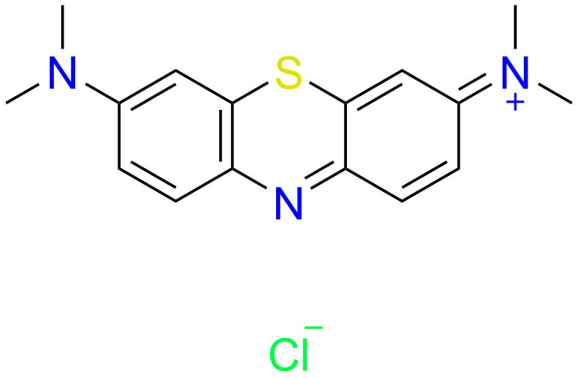

Figure 4.1 Basic chemical structure of the cationic dye methylene blue.

4.2 Wastewater Treatment

Industrial wastewater holds significant concentrations of toxic chemicals, posing a severe threat to both the environment and public health [15–17, 109, 114]. Furthermore, many of these pollutants are resistant to biodegradation and are thus require treatment to allow degradation (to occur). Two examples that will be discussed in this work are methylene blue (MB) and perfluorooctanoic acid (PFOA). Both chemicals are widely used, cause health problems, and are found in wastewater. Therefore, MB and PFOA need to be properly treated and removed from wastewater before returning the water to the environment.

Conventional methods for treating wastewater include chemical oxidation, membrane treatment, photo-degradation, chlorination, boiling, and adsorption [15, 16, 18, 118, 119]. A major limitation to these technologies is that they can only target specific chemicals, and thus cannot be used for the removal of a wide range of pollutants. Ion-exchange resins, for example, remove chemicals using van der Waals forces, but limited to treating ions that are oppositely charged [15, 16, 18, 118]. Reverse osmosis and nanofiltration can overcome this limitation and can be used to treat potable water on large scale, but are expensive due to the fouling and deterioration over time and require specialized treatments for proper disposal, thus increasing waste [118]. Elec-

trochemical oxidation is an alternative; however, these methods can generate toxic by-products [15, 16, 18, 119]. Chlorination is effective for killing biological contaminants (i.e., bacteria, viruses, microorganisms), but high doses may lead to carcinogenic by-products [120]. Boiling is also effective at removing biological contaminants only [120]. However, as the water evaporates chemical concentrations increase [120].

Activated carbon is probably the best-known adsorbent material. It is manufactured from charcoal produced from carbonaceous materials such as coals, petroleum coke, wood, and bones [121, 122]. There two different processes for the preparation of activated carbon are physical and chemical activation. In physical activations the charcoal is converted to activated carbon by activating it at high temperatures (800–1000 °C) in an oxidizing environment. The oxidizing gas is usually steam, CO_2, or air [122].

Recent investigations show adsorption by activated carbon (AC) can be utilized as an alternative method for removal of a wide range of toxic chemicals. It is a cost-effective and viable option for treating large volumes of waste water [23, 25, 117]. AC is both a versatile and effective adsorbent given its high microporosity, large surface area, and surface functional groups [16, 19, 25, 117]. The large adsorption capacity (for AC) is achieved by chemical activation. Conventional methods of chemical activation of carbon include mixing reactive chemicals (e.g. NaOH) with raw carbon materials application of temperatures of 500–900 °C. This process creates micropores of < 2 nm size, generating surface areas over 1,000 m^2/g [24].

Common granular activated carbon (GAC) materials are highly efficient adsorption dissolved contaminants due to being primarily composed of micropores (> 1 nm). The structure of GAC is heterogeneous and porous. Variation in pore size affects the adsorption capacity for molecules of different shapes and sizes. The IUPAC classifies porosity into three different groups of

pore sizes: micro, meso, and macropores (**Figure 4.2**) [123]. Typical ranges are given in **Table 4.1**.

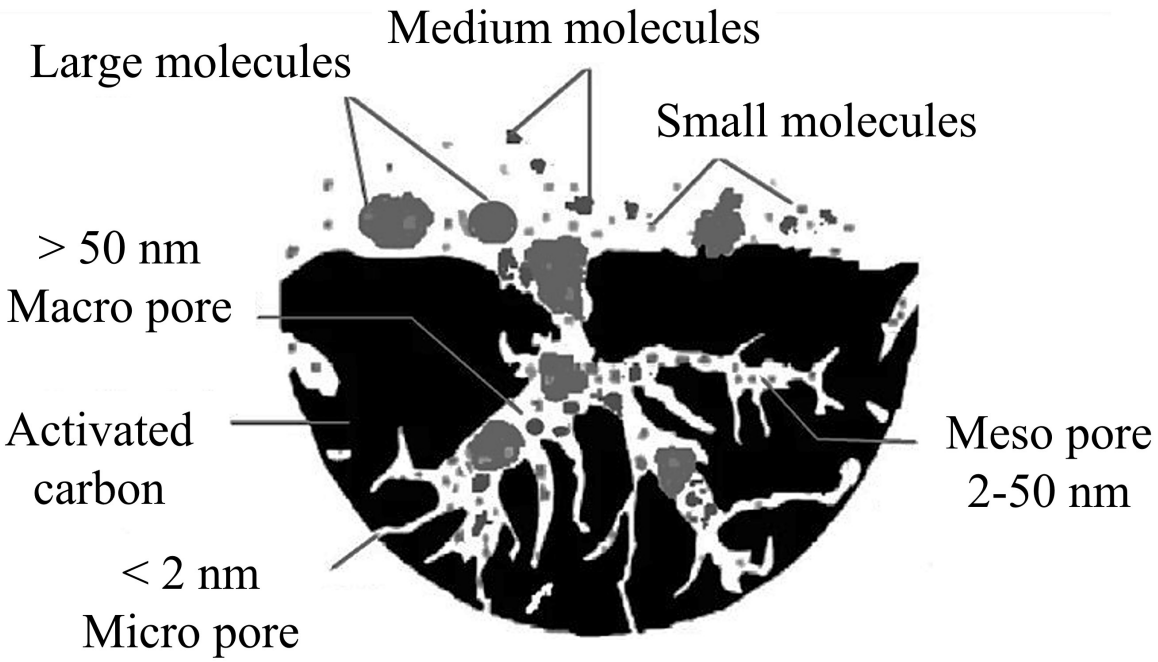

Figure 4.2 Schematic of different AC pore structures [124]. Copyright © 2021 Springer Nature.

Table 4.1 Classification of pore sizes.

	Diameter (nm)	**Pore volume(cm^3/g)**	**Surface area (m^2/g)**
Micropores	< 2	0.10	600–1900
Mesopores	2–50	0.02	20–70
Macropores	> 50	0.20–0.80	0.5–2

However, the micropores are easily blocked by suspended solids [125]. In a complex water environment micropores can become blocked by larger organic matter or biofilm, quickly losing its advantage if contaminants cannot reach the internal pore structure. Huggins et al. 2016, observed that carbon materials with higher microporosity increased adsorption capacity. The macroporosity avoids clogging and the blocking of smaller micropores thereby can result in higher overall adsorption capacities. The useful life span of GAC relies on the contaminant concentration,

adsorption capacity, and flowrate. Thus, selecting carbon material with the highest adsorption capacity for a targeted contaminant could aid in extending treatment capacity [125].

4.3 Adsorption Processes

Adsorption is defined as the adhesion of molecules to a solid surface, the adsorbent. Generally, in the laboratory, the adsorption process is carried out in a batch setup. The data gathered is then used to construct am adsorption kinetics curve describing the rate of retention or release of the solute from the aqueous environment to the solid surface as a given adsorbent does, temperature, or pH [126].

The primary parameter to consider when designing an adsorption system is adsorption kinetics. Adsorption kinetics describe the time-dependent progression of adsorption until equilibrium is achieved [121, 127]. The adsorption kinetics are influenced by the surface complexity of the absorbent and solute concentration [126]. At the solid-liquid interface, adsorption and adsorption site accessibility can be divided into four steps [121, 127]. The first is bulk transport, where adsorbate is transported from the fluid phase to the liquid film surrounding the adsorbent surface. Next, the adsorbate must diffuse across the surface liquid film surrounding the solid particles, which is termed external diffusion [121, 127]. Intraparticle diffusion (internal) of the adsorbate from the liquid film to the surface occurs either by pore diffusion or surface diffusion. Finally, the adsorbate interacts with surface sites, wither by chemical or physical adsorption [121, 127]. In the case of reversible adsorption, desorption of the adsorbate must also be considered.

Depending on the forces involved, adsorption processes may be classified as either physical or chemical [109, 121, 126]. These distinctions depend upon the interactions between the adsorbent matrix and the molecule being adsorbed. Physical adsorption “physisorption,” occurs without any

chemical reaction and is brought about as the result of weak attractive forces, Van der Waals (dipole-induced, dipole-dipole, and dispersion forces). It is commonly a reversible and rapid sorption process. These dispersion forces are electrostatic in origin and often account for a major part of the adsorbate-adsorbent potential [109]. Dispersion forces exist within all matter and are always present regardless of the nature of other interactions. Properties of the adsorbed material and of the surface of the adsorbent can affect the quality of physisorption. These include molecular size, boiling point, molecular mass, and polarity for the adsorbed material and polarity, pore size and spacing for the adsorbent surface [109]. If a chemical reaction occurs between the adsorbate and the adsorbent, the phenomena is referred to as chemical adsorption or "chemisorption" [109, 121, 126]. This process involves a sharing of electrons between the surface of the adsorbent and the adsorbate molecules. Chemisorption is restricted to a single layer of molecules on the surface, although an additional layer of molecules may be physically adsorbed after [109]. It involves a sharing of electrons between the adsorbate molecules and the surface of the adsorbent. It is restricted to just one layer of molecules on the surface, although it may be followed by additional layers of physically adsorbed molecules. Both processes can occur simultaneously or alternatively under favorable conditions [109].

During adsorption, atoms and molecules of the fluid phase (adsorptive) and the solid (adsorbent) interact [121]. The adsorbate surface may be regarded as a site with electronic and sterical properties inherent of the adsorbate matrix structure. These sites induce energetically heterogeneous energy levels based on the degree of interaction with the molecule being adsorbed [121]. Moreover, most adsorbents are characterized not only by their exterior surface, but also by their inner porous structure, which contributes to adsorption. Nonetheless, major differences in the interaction forces and the kinetics of adsorption exist between the exterior and inner surfaces [121].

4.4 Adsorption onto Carbon

The general adsorption process on a porous adsorbent like AC can be divided into three stages [127–129]. The first stage is external diffusion, where the adsorbates move from the bulk solution to the external surface of the adsorbent [127–129]. The second stage is intraparticle diffusion. During this stage the adsorbates diffuse further into the adsorbent to the adsorption sites [128, 129]. Finally, in the third stage, the adsorbates are adsorbed at the active sites on the adsorbent [128, 129]. This last step is a fast step and is usually considered negligible [127–129].

On a carbonaceous surface, chemical sorption of inorganic molecules occurs due to ion exchange with abundant surface functional groups, such as carboxylic, hydroxylic, of phenolic groups [130–132]. These groups can enhance cation exchange capacity (CEC). The chemisorption of cations relies on the release of protons and base cations (Na, K, Mg, or Ca) [130, 133]. Because chemical sorption is stoichiometric, the pH of the medium affects ion sorption efficiency [126, 130, 133]. Physical adsorption of inorganics onto carbon materials relies on electrostatic forces between positively charged ions in the water and the delocalized cloud of electrons associated with aromatic groups on the surface. This creates cation-π interactions with the C=C aromatic bonds [130, 134]. Differing from chemical sorption, physical adsorption of inorganics does not require stoichiometric release of protons and cations. Precipitation of inorganic pollutants, specifically metal cations, with insoluble salts occurs on the surface of high ash content carbonaceous materials [130, 135].

These physical and chemical characteristics of AC to adsorb MB from wastewater were investigated by Wang et al. 2005. They found that pore size distribution and surface charge of the adsorbent were the parameters that controlled the adsorption capacity [117]. Using mild acid treatment to modify the surface chemistry of AC resulted in decreased adsorption capacity [117]. It

was found that acid treatment reduced the hydroxide groups and produced acidic surface functional groups [117]. The acidic surface was not conducive to the adsorption of MB and gave evidence in support of surface chemistry being a primary component in adsorption capacity [117].

Chien et al. 2000, investigated the influence of mesopore volume and adsorbate size on the adsorption capacity of AC. They found that the adsorption capacity of AC with similar surface areas and micropore volumes increased directly with the increase in mesopore volume [25]. They concluded that the increase in mesopore volume enabled the adsorbates to adsorb to previously inaccessible adsorption sites [25]. An increase in mesopore volume reduced the length of diffusion path of micropores which would impact the diffusion of large molecule [25]. These findings reenforced the influence of pore structure on adsorption capacity.

The mechanisms of perchlorate adsorption on AC and ion exchange resin were investigated by Yoon et al. 2009. Their results showed that adsorption/desorption reached equilibrium within 30 minutes [136]. Raman spectra suggested that perchlorate was associated with functional groups on AC surface at neutral pH through interactions stronger than electrostatic forces [136]. Zeta potential showed that perchlorate was adsorbed on a negatively charged AC surface [136].

Many as-derived activated carbons exhibit an adsorption capacity inferior to that estimated from it surface area due to the inaccessibility of micropores and mesopores to the impurities. To rectify this, a high-temperature activation stage in combination with the use of excess amount of reactive chemicals is commonly used to increase mesopore volume allowing for access to the micropores. Saha et al., 2001, characterized AC after oxidation with nitric acid and air. They found that samples lost surface area and displayed signs of erosion after the oxidation process [137]. The combination of washing the acid oxidized samples with NaOH and heat treatment recovered some of the surface area by removing impurities blocking mesopores [137]. Overall,

they found that after modification the AC lost micropores and increased its mesoporosity [137]. A study by Chingombe et al., 2005, investigated the modification of commercial AC using multiple methods. They found that the oxidation process produced some by-products that would clog the micropores [26]. This led to a decrease in microporosity, which plays an important role in adsorption [26]. Washing the oxidized carbons with NaOH led to an increase in surface area due to the removal of humic substances which subsequently opened the mesopores [26]. The addition of nitric acid greatly increased sorption capacity for sodium compared to the AC before treatment, as well as gaining weakly acidic functional groups [26]. Overall, the study found that these different modes of modification, while lengthy and requiring high temperatures, lead to different chemical characteristics.

It has been shown that heat and chemical treatments of AC result in noticeable changes in surface morphology [129]. After the amination reaction, AC surface appeared eroded. It was theorized that this was due to nitric acid, which is a strong oxidizing agent, causing C−C bonds to split at the α-position of the benzylic carbon atoms [129]. Plasma also offers the ability to generate specific chemical species and functional surface groups using appropriate plasma gases, which allows the AC to be tailored for specific pollutants without high temperatures.

This study examined the adsorption capacity of plasma-treated AC, which was originally activated through conventional chemical activation. Due to its reactivity and etching capabilities oxygen plasma was studied. The treated AC samples were compared based on adsorption capacity. The material morphology and chemical structure characterization was performed to understand the differences in the adsorption capacity.

4.5 Experiment and Methods [1]

4.5.1 Plasma System and Process

A commercial activated carbon (AC R003) received from Oxbow Activated Carbon was used in this study. This chemically activated carbon was further treated through plasma generated by a capacitively coupled dielectric barrier discharge. A quartz tube connected to a mechanical pump was used as a vacuum chamber. A pair of copper electrodes were attached to the outside of the tube to generate plasma. One of the electrodes was connected to a radio frequency (RF) power generator (Kurt J. Lesker, Radio Frequency Power Supply R301) while the other electrode was grounded. The operation frequency was set at 13.56 MHz. Before the plasma was generated, the quartz tube was pumped down to < 1 x 10^{-2} Torr and purged with the process gas to prevent cross-contamination.

4.5.2 Plasma Activation Process

For plasma activation of the carbon, ~0.05 g of carbon powder was thinly spread across a ceramic plate. The ceramic plate was placed inside the tube between the two copper electrodes. The system was sealed and pumped down to low pressure. The tube was then filled with the process gas. The plasma pressure was kept constant for each treatment at 2 Torr (measured by a vacuum meter, Kurt J. Lesker). The RF power of the plasma was fixed at 75 W and adjusted to reach a zero-watt reflection power through all experiments. This process was repeated 5x for each test in order to reach a final mass of 0.250 g of treated AC. The plasma gas used was 10% O_2 - 90% Ar

[1] Taken from [138] M.A. Mackinder, K. Wang, Q.H. Fan, Methylene Blue Adsorption by Plasma Re-Activated Carbon, J. Water Resour. Prot. (2021).

mixture and treatment times were varied. The plasma treatment times for each gas were: 1 min, 2 min, 3 min, 4 min, 5 min, and 6 min. The setup of this process is shown in **Figure 4.3**.

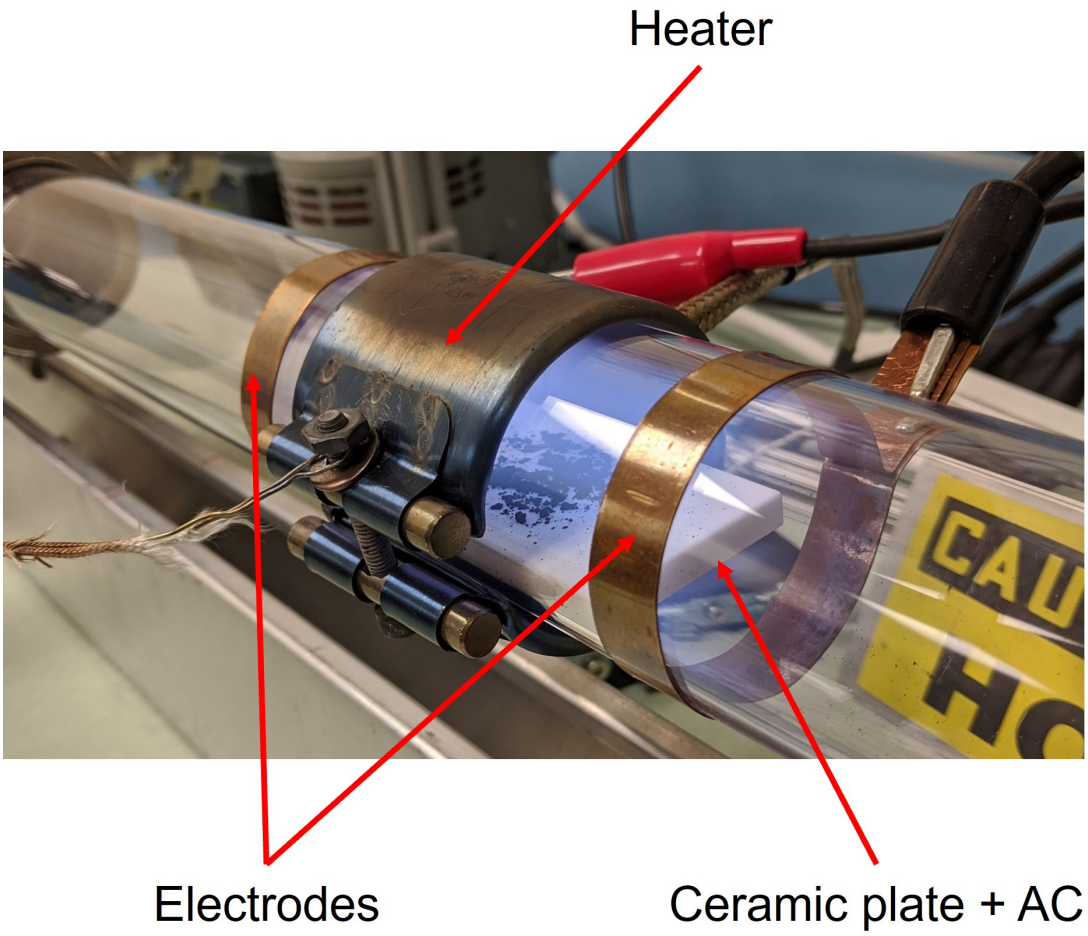

Figure 4.3 Setup for plasma treatment of activated carbon.

4.5.3 Methylene Blue Adsorption Methods

Methylene blue (MB) has an intrinsic adsorption at 664 nm wavelength. Therefore, the peak intensity at 664 nm of the UV-visible spectra of different methylene blue concentrations were used to construct a calibration curve of absorbance versus methylene blue concentration (mg/L). Next, batch adsorption tests were performed at room temperature. The experiments were used to

examine the effects of plasma treatment parameters on MB adsorption by AC. The experiments were conducted on samples of AC treated with O_2 plasma and different treatment times (1–20 min).

In each experiment, ~5 mg of AC was placed in a 50 mL centrifuge tube. Then 20 mL of 25 mg/L MB solution was added to the centrifuge tube. Then, the centrifuge tubes were spun in the centrifuge at 6000 rpm for 20 minutes. The supernatant was then collected and measured for the remaining MB concentration. The remaining concentration was found by measuring the absorbance of the solution by UV-visible spectroscopy at a wavelength of 664 nm. The adsorption capacities of MB on the AC samples, q_t (mg/mg), were calculated using the following equation:

$$q_t = \frac{V\,(C_0 - C_t)}{w} \tag{4.1}$$

where C_0 (mg/L) is the liquid-phase initial concentration of methylene blue, and C_t (mg/L) is the concentration of methylene blue at each time. The mass of dry AC is represented by w (g), and V (L) is the volume of methylene blue solution.

4.6 Results and Discussion [1]

4.6.1 UV-visible spectroscopy

To determine the amount of time needed for each adsorption experiment, the time it took for the AC to become saturated was investigated. The contact time between MB and AC was evaluated as a factor of adsorption efficiency. The UV-vis spectra for MB adsorption by AC from 5 to 30 minutes was collected. The results showed that the concentration of MB left in the solution reached a minimum between 10 and 20 minutes (shown in **Figure 4.4**), suggesting that the AC became saturated around this time. The concentration decreased ~89% after incubating MB with AC for 20

min and did not change from 20 to 30 minutes suggesting equilibrium was reached. These findings suggested that a soak time of 20 minutes was adequate for all subsequent studies. The adsorption capacity at equilibrium of the AC before plasma activation was 4.13 mg-g^{-1} ± 0.002 [139].

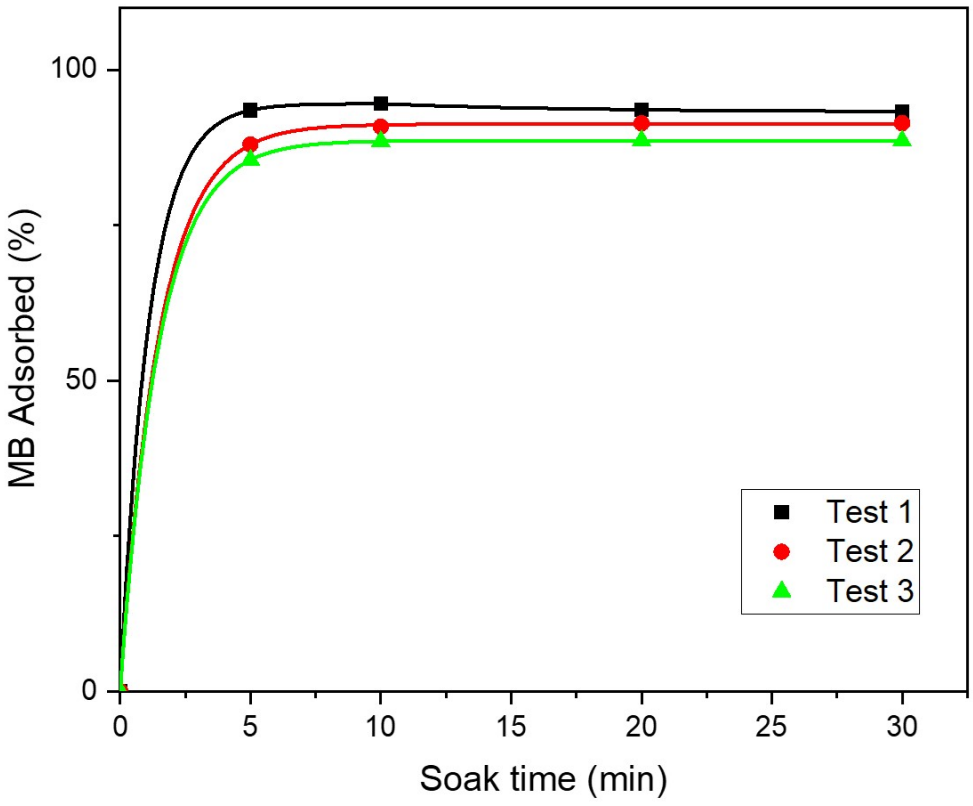

Figure 4.4 The percent of MB adsorbed by AC versus the amount of time that the AC was soaked in solution.

Next, the effect of different O_2 plasma treatment times was investigated. The adsorption capacity was found similar for a plasma treatment time in the range of 2–6 minutes but dramatically decreased for treatments longer than 10 minutes, as shown in **Figure 4.5**. This could be due to over etching of the AC causing the internal structure to collapse. All further studies were limited to a maximum plasma treatment of 6 minutes in order to avoid over etching.

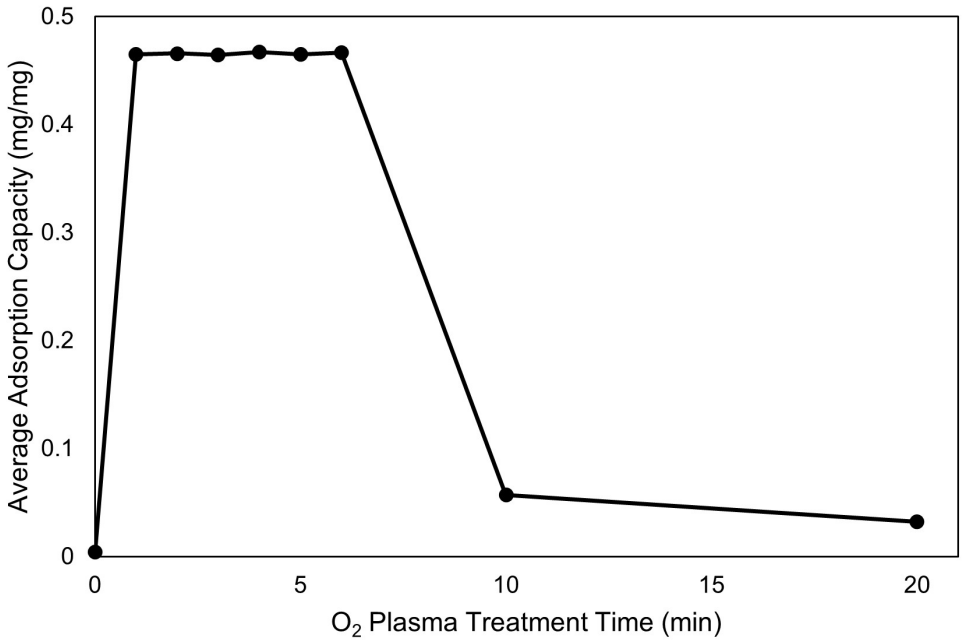

Figure 4.5 Average adsorption capacity of oxygen plasma treated samples with increasing treatment time (n=3).

The effects on adsorption capacity with different plasma treatment times were investigated and compared to non-plasma treated AC. The adsorption capacities of the plasma treated samples significantly increased as shown in Figure 4.5. The non-plasma treated sample had an adsorption capacity of $4.13(\pm 0.002)\times10^{-3}$ mg-mg^{-1}. As the O_2 plasma treatment was applied to the AC, the adsorption capacity of the samples increased up to 4 minutes. The adsorption capacity for the O_2 plasma treated samples reached its maximum adsorption capacity of 0.467 mg-mg^{-1} $\pm$ 0.0002 at 4 minutes of plasma treatment. After 4 minutes of treatment, the adsorption capacity decreased. After 10 minutes of O_2 plasma treatment, the adsorption capacity had decreased ~88% to 0.057 mg-mg^{-1} $\pm$ 0.0001, and after 20 minutes it had decreased ~93% to 0.032 mg-mg^{-1} $\pm$ 0.0003. Overall, the O_2 plasma treated samples had adsorption capacities higher than the non-plasma treated sample. Plasma treatment significantly improved the adsorption capacity when the treatment time was shorter than 6 minutes. The best adsorption capacity for the O_2 plasma treatment was found to be

0.467 mg-mg^{-1} ± 0.0002 at 4 minutes of plasma treatment which was over a one hundred times increase. The similarity in adsorption capacity for the plasma treated samples up to 6 minutes suggests that the treatment time does not significantly influence the adsorption capacity. This may be due to localized heating at the atomic level due to inelastic collisions of energy carriers such as electrons. The significant increase showed that plasma treatment of AC increases adsorption capacity.

A simple experiment was conducted to ensure that the increase in adsorption capacity was not due to the removal of residual water from vacuum and localized heating. The adsorption capacity of AC left in vacuum for 10 minutes and the adsorption capacity of AC left in a 110 °C oven for 10 minutes were compared to untreated AC (**Figure 4.6**). Figure 4.6 shows that the influence of heat and vacuum on the adsorption capacity of MB by the AC is insignificant.

To better explain how all the plasma treatments led to similar adsorption capacities, the original AC R003 from Oxbow was further examined. As shown in **Figure 4.7**, the combination of treatment factors, rather than individual ones, caused the most dramatic changes. The AC was heated to 300 °C for 30 minutes with and without being kept under vacuum. The treatments included in Figure 4.7 show that an increased temperature in concurrence with treatment under vacuum improved MB adsorption for the non-plasma treated samples. Then, the effect of treating AC with O_2 plasma at room temperature was compared with the non-plasma treated samples. The graph clearly shows that the 4-minute O_2 plasma treated sample had the highest adsorption capacity. The overall results suggest that the plasma treatment provided significant localized heating at atomic scale in addition to modifying the porous structure.

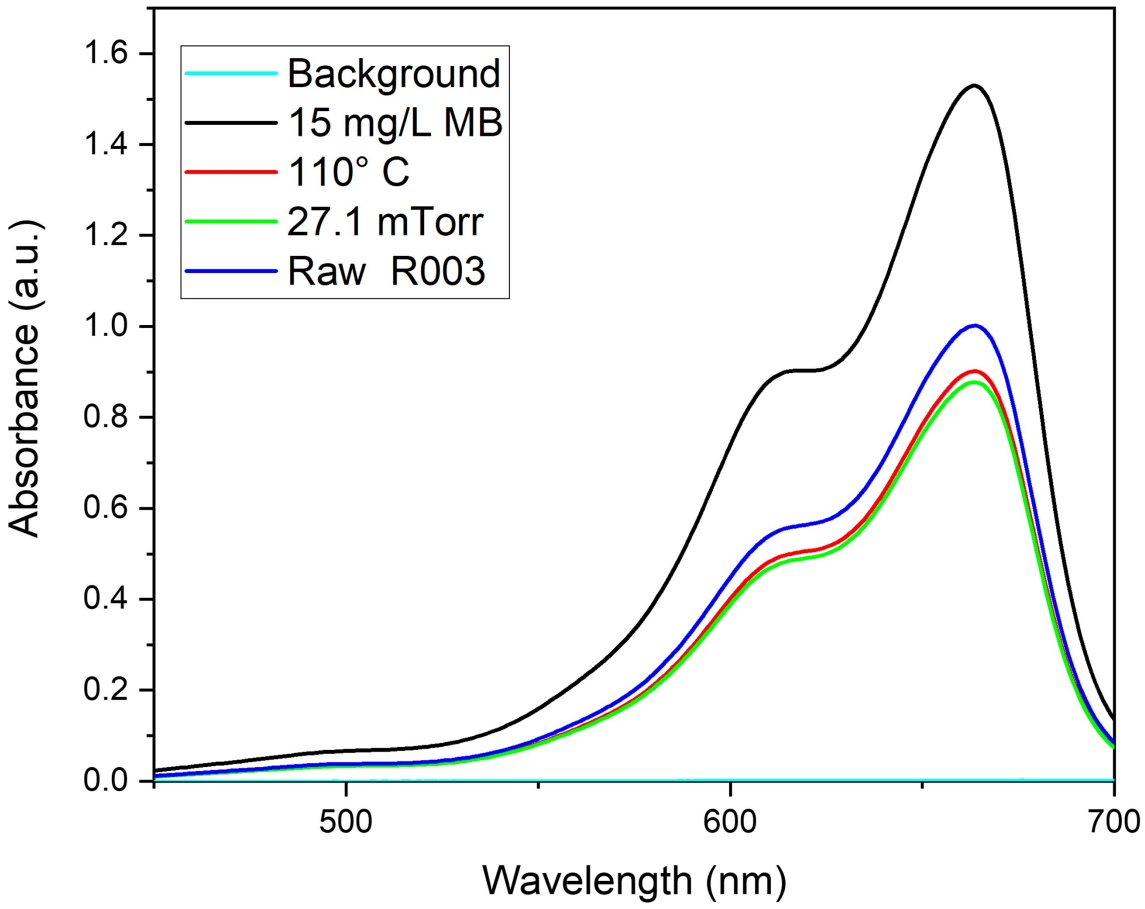

Figure 4.6 MB adsorption of AC that was heated left in vacuum, or raw.

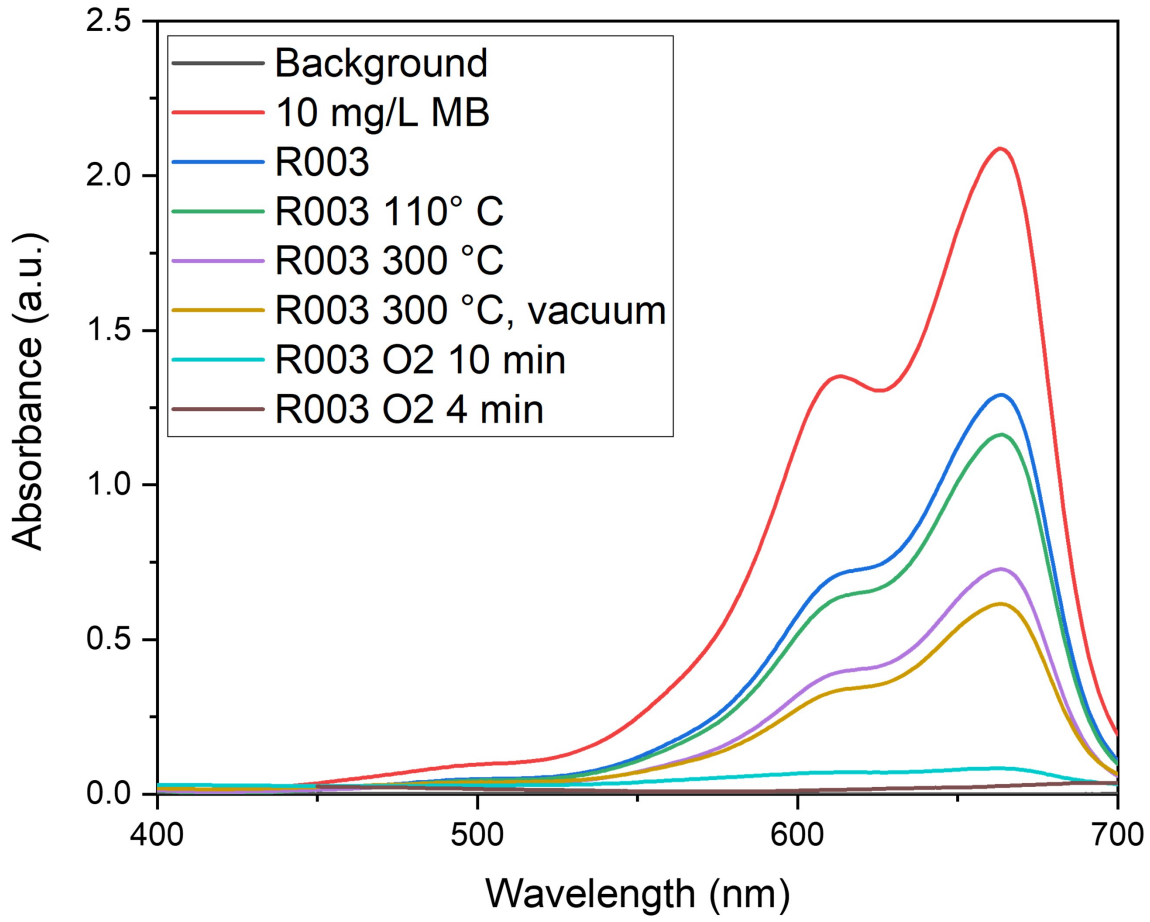

Figure 4.7 MB adsorption of AC under various experimental conditions.

4.6.2 Fourier-Transform Infrared Spectroscopy

Research has shown that atomic oxygen and ozone are highly effective in introducing oxygen groups to carbon surfaces [140]. We have previously shown that excited species like atomic oxygen are present in the 10% O_2-90% Ar plasma. The use of excited species within plasma is an effective way to introduce surface functionality to a carbon surface like activated carbon. When the oxygen species arrives on the carbon surface it may form a bond to the surface. This oxygen species may then react further or become a stable complex.

Chemical reactivity of surface functional groups plays a role in the adsorption capacity of AC. Identifying functional groups gives insight to the adsorption capacity and the influence of plasma treatment on the AC surface. FTIR spectra were generated for the characterization of AC surface groups. The assignment of observed bands in **Figure 4.8** are shown in **Table 4.2**. These bands were determined referencing papers studying the FTIR spectra of activated carbons having similar or the same wavelengths.

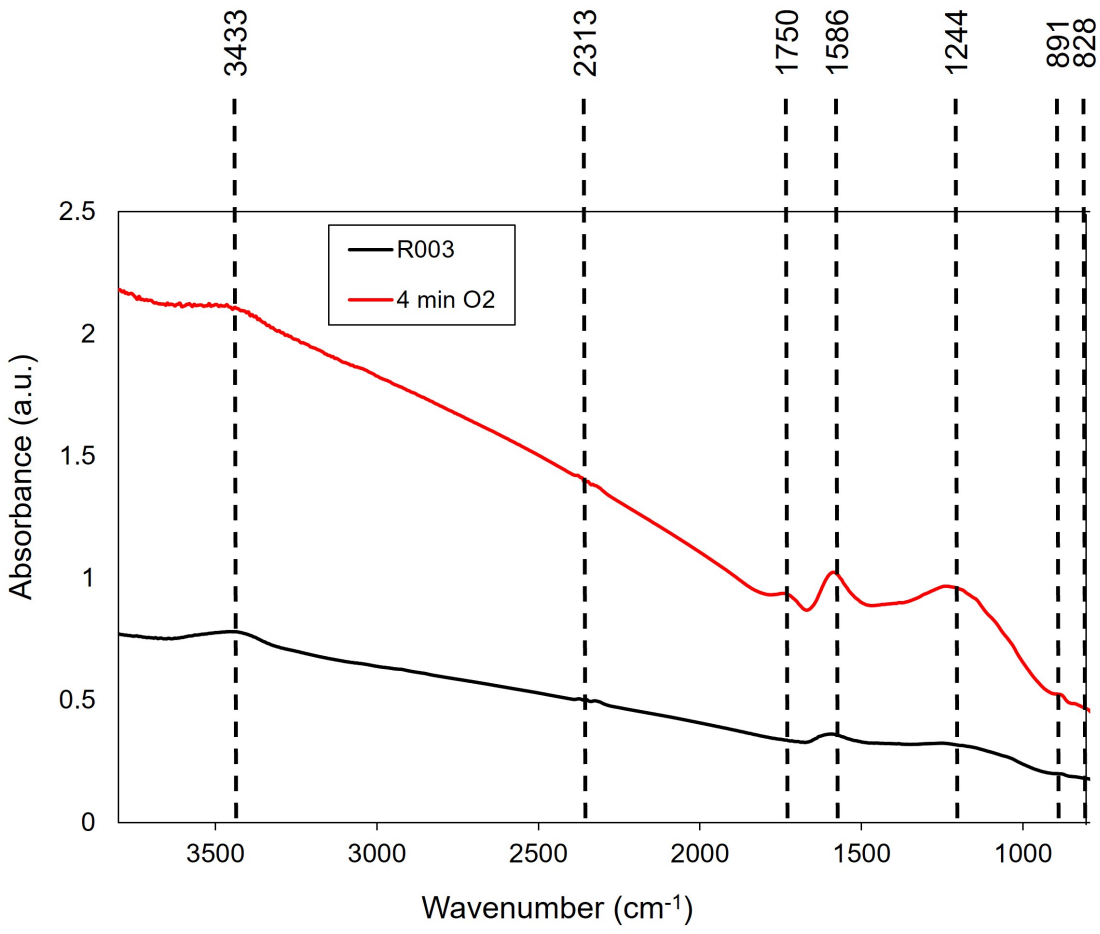

Figure 4.8 FTIR spectra of O_2 treated AC and untreated AC (R003).

Table 4.2 The assignment of FTIR vibrations found in Figure 4.8.

Peak (cm^{-1})	Surface group	Assignment	Reference
3500–3400	O−H	O−H stretching, presence of hydrogen bonds	[15, 19]
~ 2300	C=O	C=O stretching, ketones	[15, 17–20]
1770–1700	C=O	C=O stretching, ketones, carboxylic acid, aldehydes, or esters	[15, 17–20]
1600–1475	C=C	C=C stretching of aromatic compounds	[16, 21]
~1240		C−H stretching and OH deformation of COOH and C−O stretching of C−O−C in cellulose and hemicellulose	[17, 18]
900–700	Aromatic compound	Aromatic stretching	[18, 21]

Each individual spectrum had its baseline subtracted to find the peak heights. Both spectra show a peak between 3500–3400 cm^{-1} indicative of OH stretching, which presents possible hydrogen bonding sites [15–19]. The 4-minute O_2 treated AC has the higher measured absorbance for this OH stretching peak compared to the non-plasma treated AC (R003). That the peak is more prominent in the 4 minute O_2 treated sample suggests the presence of more −OH groups from increased carboxylic groups on the surface [26]. The peak at 2300 cm^{-1} indicates the C=O stretching of a ketone. The appearance of a peak between 1770–1700 cm^{-1} represents C=O stretching and is indicative of the presence of ketones, carboxylic acid, aldehydes, or esters [15, 17–20]. This suggests that O_2 plasma treatment was able to generate more oxygen functional groups on the AC surface. The peak between 1600–1475 cm^{-1} signifies C=C stretching of aromatic compounds, of which the O_2 sample had a much higher peak [16, 21]. The peak around 1240 cm^{-1} occurs because there was C−H stretching and OH deformation of COOH along with C−O stretching characteristic

of C−O−C in cellulose and hemicelluloses [17, 18]. The O_2 plasma treated AC had a much higher peak than R003. Peaks between 900–700 cm^{-1} indicate aromatic stretching and the presence of aromatic compounds [18, 21].

Overall, the FTIR further supports the results found previously. There was no significant difference in FTIR spectra between the different plasma treatments. There were more hydrogen bonding sites present for all plasma treatments, as depicted by the increase in the absorbance for the peak between 3500–3400 cm^{-1}. There was also a marked increase in the C−H bonds, along with C−O, C=C, and ketones after the AC underwent plasma treatment.

4.6.3 XPS

Compared to the untreated AC, XPS analysis (**Figure 4.9**) showed a decrease in carbon content. There was no discernable nitrogen found in the O_2 plasma treated sample, but there was an increase in oxygen. The increase in oxygen with a decrease in carbon indicates a change in polarity [18]. The samples with higher amounts of oxygen would be expected to be more polar and have less aromaticity leading to less hydrophobicity [18]. As the species within the plasma react with the carbon surface, there is a progressive removal of carbon atoms. This results in changes in the physical structure of the carbon surface such as changes in polarity and aromaticity [140]. There was no discernable nitrogen in the O_2 plasma treated or the non-plasma treated samples. XPS analysis further revealed a change in surface functional groups and atomic composition after plasma treatment.

The XPS analysis of AC is shown in Figure 4.9. XPS provides information about the surface functional species and composition. Carbon, oxygen, and nitrogen content were determined. The XPS analysis of AC that was not plasma treated gave the atomic concentrations 89.01% C 1s and

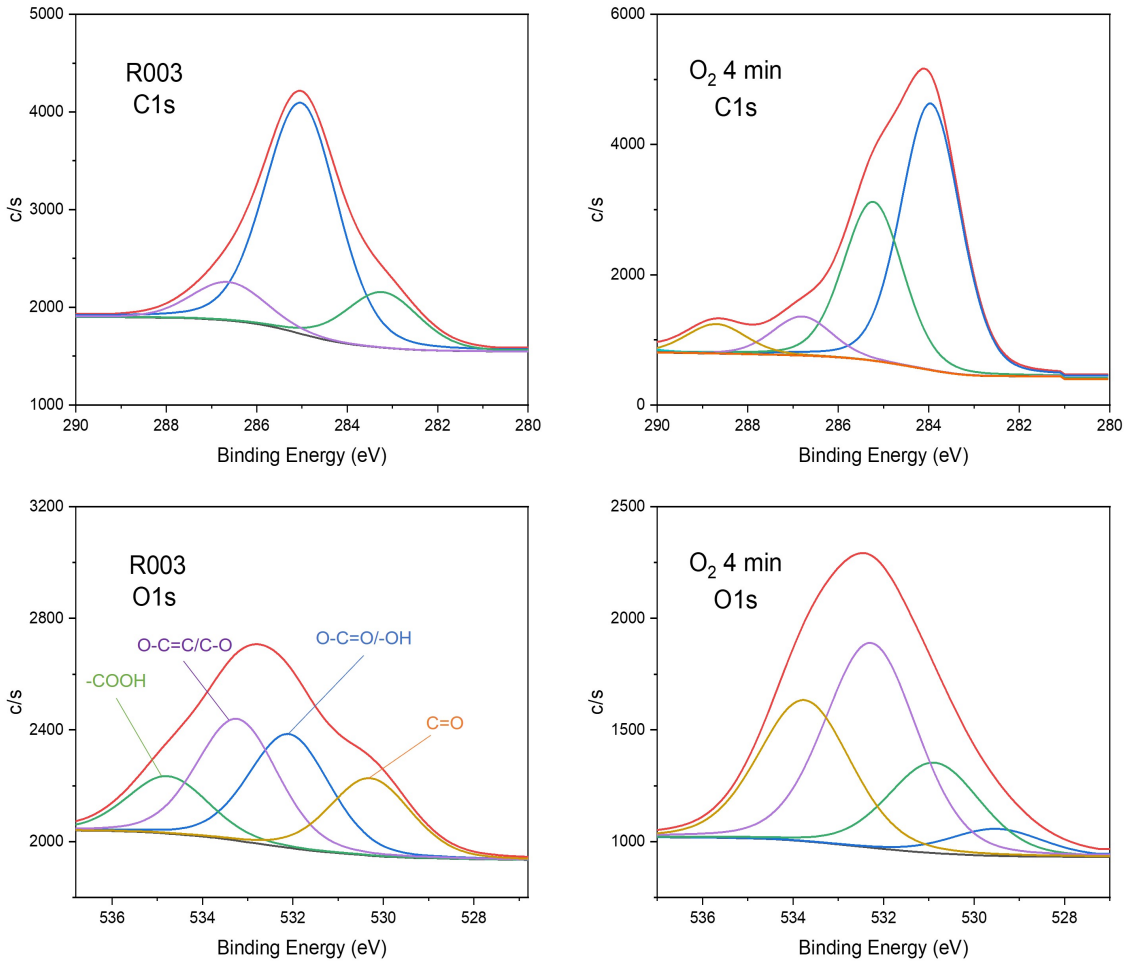

Figure 4.9 XPS data for non-plasma treated AC (top and bottom left) and AC that underwent oxygen plasma treatment for 4 minutes (top and bottom right).

10.99% O 1s. No N 1s was detected. The high-resolution spectrum of C 1s of untreated AC could be deconvoluted into 3 peaks: 282.97, 284.74, ad 286.35 eV. The O 1s region was made up of four peaks: 530.0, 531.59, 532.79, and 534.83 eV.

The XPS analysis of AC that was treated with O_2 plasma for 4 minutes gave the atomic concentrations 80.06% C 1s and 19.94% O 1s with no apparent N. The high-resolution spectrum of C 1s of AC that underwent O_2 plasma treatment for 4 minutes can be broken into 4 peaks: 284.37, 285.64, 287.22, and 289.11 eV. The O 1s region was split into 4 peaks: 530.1, 531.41, 532.80, and

533.95 eV.

Compared to the untreated AC, XPS analysis showed a decrease in carbon concentration in the O_2 plasma treated sample. There was no discernable nitrogen found in the O_2 plasma treated sample, but there was an increase in oxygen. The increase in oxygen with a decrease in carbon indicates a change in polarity [18]. The samples with higher amounts of oxygen would be expected to be more polar and have less aromaticity leading to less hydrophobicity [18]. There was no discernable nitrogen in the O_2 sample, or the non-plasma treated sample. XPS analysis further revealed a change in surface functional groups and atomic composition after plasma treatment.

The peak numbers and their interpretation are listed in **Table 4.3**. With plasma treatment, the C1s XPS spectra could be broken down into more peaks. Plasma treatment of AC resulted in an increase in C−O−C and C=O functional groups. In the O_2 plasma treated sample, a peak around 290 eV appeared. This peak corresponds to C=O/C=C (carbonate, occluded CO, π-electrons in aromatic rings) [24, 141–143]. With plasma treatment the O1s XPS spectra of the O_2 sample has four peaks with a higher intensity for the peak at 532.80 eV. The O_2 treated sample loses its O (oxide-like oxygen) and its C=O (quinone type carbonyl) peaks, and it gains a peak at 533.9 eV that corresponds with C-O (ester/amide/carboxylic anhydride) [141, 144–147]. This aligns with the typical oxygen complexes (phenolic, hydroxyl, quinonic, carboxylic acid and ethers) generated on carbon surfaces by reactions with species such as ozone [140].

Table 4.3 The assignment of the XPS peaks.

Peak (cm^{-1})	Surface group	Assignment	Reference
O1s			
528.6–529.3 eV	O	Oxide-like oxygen	[138, 148–151]
531–531.4 eV	C=O	Quinone/ketone/lactone/carbonyl	[138, 148–151]
532.3–532.6 eV	C=O/C−O	Ether/phenol/anhydride/lactone	[138, 148–151]
532.9–533.2 eV	C−O	Ester/amide/carboxylic anhydrides and oxygen atoms in hydroxyls or ethers	[138, 148–151]
534.2 eV	C−O	Carboxylic acid	[138, 148–151]
C1s			
284.2–284.9 eV	C	Graphite	[24, 138, 152, 153]
285.4–286.3 eV	C−O−	Ether/phenol/alcohol	[24, 138, 152, 153]
287.2–287.9 eV	C=O	Carbonyl/quinone	[24, 138, 152, 153]
288.7–289.3 eV	COO	Carboxyl/ester	[24, 138, 152, 153]
290.2–290.8 eV	C=O/C=C	Carbonate, occluded CO, π-electrons in aromatic ring	[24, 138, 152, 153]

4.6.4 Zeta Potential

The progressive reactions and removal of carbon atoms from the surface of activated carbon can influence the electric potential of the carbon surface [140]. Zeta potential measurements were performed on the O_2 and the non-plasma treated AC sample. **Figure 4.10** shows the comparison between each sample when the adsorption capacity was the highest. The O_2 plasma-treated AC has the most negative zeta potential compared to the non-plasma treated AC sample. The zeta potential

curve for O_2 plasma-treated AC shifts to the left of the non-plasma treated AC. The zeta potential of the O_2 plasma-treated AC is measured at -63 mV.

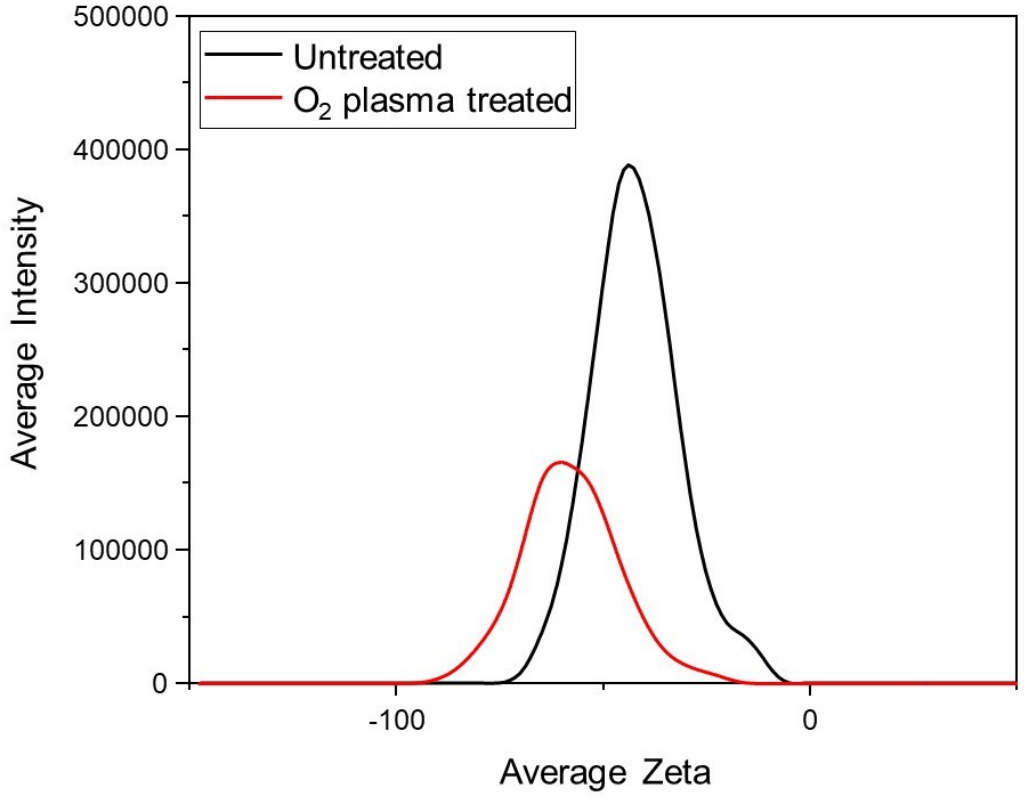

Figure 4.10 Zeta potential data of non-plasma and oxygen plasma treated AC samples (n=3).

Zeta potential is a measure of surface charge. It is the potential between the dispersed particle surface and the mobile dispersion medium [22]. It was observed that both adsorbents had large negative zeta potentials. This implies that the particles in suspension resist aggregation and are inclined to disperse homogeneously throughout the solution [22]. This opposition to aggregation and the ability to spread evenly throughout a solution is beneficial to adsorption. The magnitude of the zeta potential is indicative of colloidal stability [154]. Figure 4.10 clearly shows that the O_2 plasma treated sample has a zeta potential between -35 mV and -65 mV. Nanoparticles with zeta

potentials less than -30 mV are considered to have high degrees of stability [154].

4.6.5 Transmission Electron Microscopy

Transmission electron microscopy (TEM) is used to obtain information about morphology and nanostructure of materials [138, 152]. TEM images were taken of the best performing samples from the plasma treatment, along with the untreated AC. The samples appeared to be amorphous [152]. **Figure 4.11** shows TEM images of non-plasma treated AC (left) and O_2 plasma treated AC (right). The scale bars for each image differ due to the need for higher magnification to see the porous structure in the non-plasma treated sample. The image shows that the non-plasma treated AC contains mainly micropores. With plasma treatment, meso-pores with irregular shapes appear because the AC are etched by the plasma. The larger mesopores are easily visible under lower magnification. This combined meso-pores and micro-pores facilitate the transport of MB and promote the adsorption.

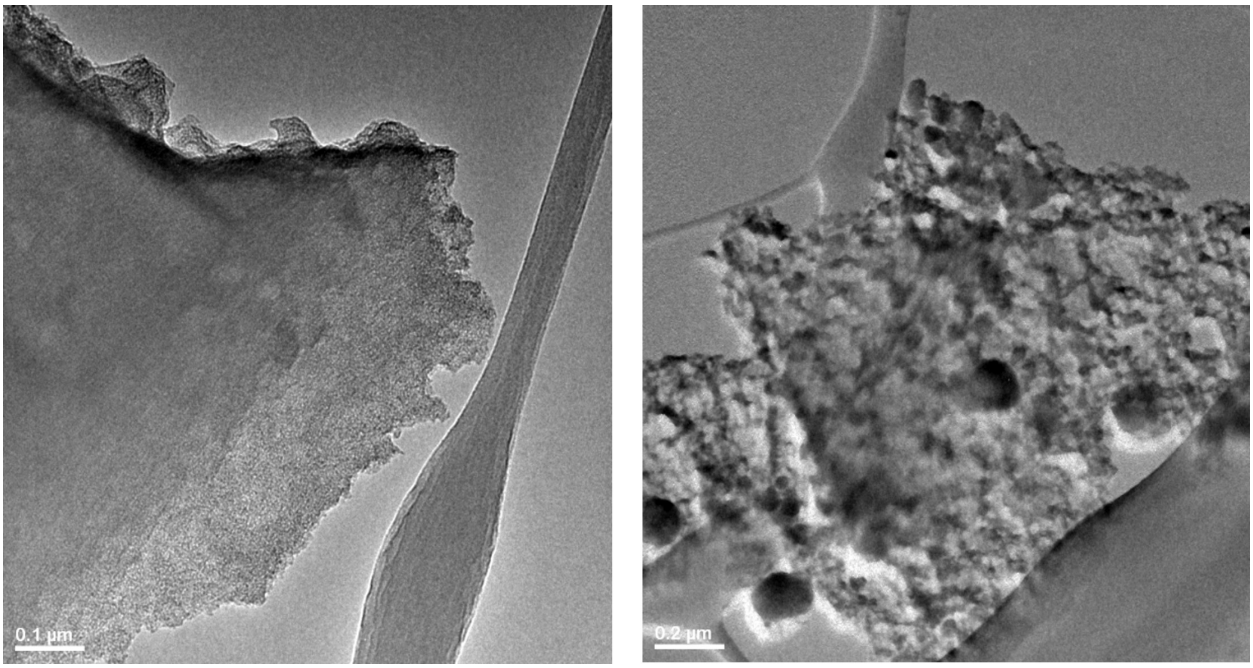

Figure 4.11 TEM images of non-plasma treated AC (left) and oxygen plasma treated AC (right).

4.6.6 Kinetics of Adsorption

Adsorption of dyes on AC may include chemical adsorption. To investigate the adsorption mechanism, the adsorption kinetics of MB onto AC that was not plasma treated was analyzed by using pseudo-first and pseudo-second order kinetic models. The pseudo-first-order equation can be written in the form:

$$\log(q_e - q_t) = \log(q_e) - \frac{k_1}{2.303}t \tag{4.2}$$

where q_e represents the amount of adsorption (mg/mg) at equilibrium, k_1 is the rate constant of the pseudo-first-order equation, and q_t is the amount of adsorption (mg/mg) at t, time (min) [115]. The rate constant, k_1, can be calculated by plotting $\log(q_e - q_t)$ versus t [115].

The pseudo-second-order kinetic equation is shown below:

$$\frac{t}{q_t} = \frac{1}{k_2 q_e^2} + \frac{1}{q_e}t \tag{4.3}$$

where k_2 is the pseudo-second-order rate constant. Plotting t/q_t versus t, a line of best fit can be found (**Figure 4.12**). This straight line can then be used to calculate k_2 [115]. The R^2 value for the pseud-second-order model was 0.99, where the R^2 value for the pseudo-first-order model was only 0.80. Therefore, the adsorption kinetics are adequately described by the pseudo-second-order model. Similar results have been found for the adsorption of MB onto rejected tea leaves, AC, and different carbonaceous materials [22, 115, 153].

The pseudo-second order model fit the kinetics data of MB adsorption onto AC. This suggests that chemisorption has a dominant role in the adsorption process [144, 153].

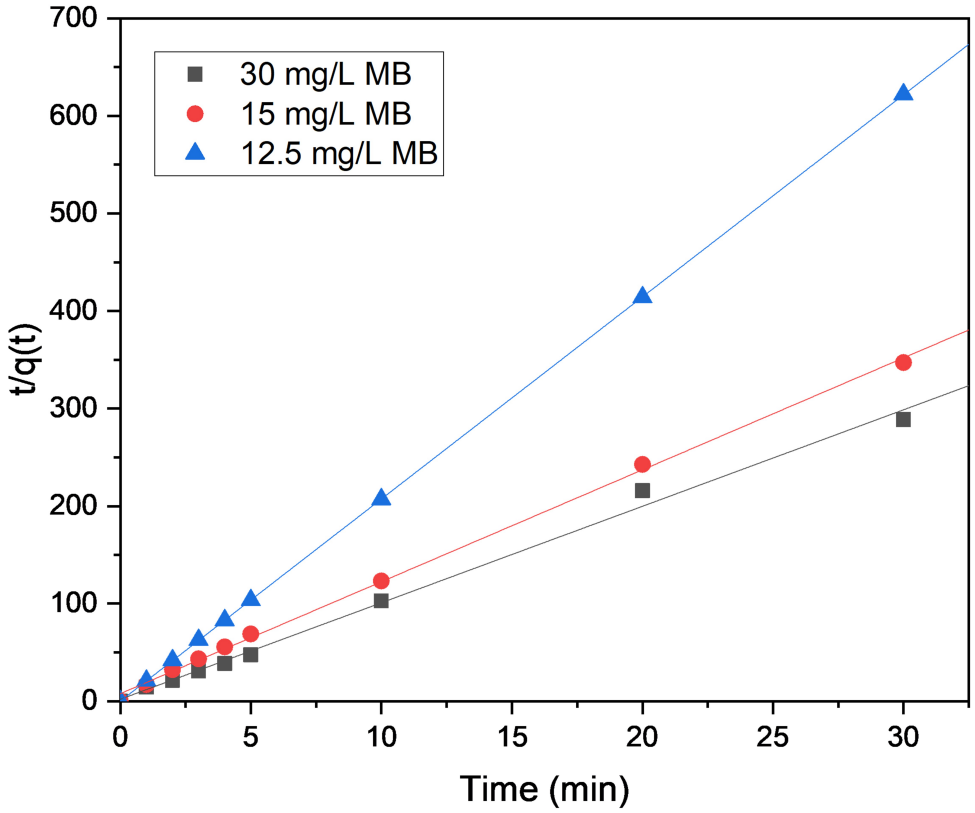

Figure 4.12 Plot showing a line of best fit for the pseudo-second order kinetic model (n=3).

4.6.7 Adsorption Isotherms

The relationship between the initial concentration of MB and the adsorbed amount of MB onto AC are investigated through adsorption isotherm models. The results show that the adsorption of MB increases with the increase of the equilibrium concentration of MB.

The two isotherms tested for their ability to describe the experimental results were the Langmuir and Freundlich adsorption isotherms [109, 148]. These models provide insight into the mechanism of adsorption and the surface properties [109, 148].

The Langmuir isotherm is based on the assumption of monolayer adsorption onto a ho-

mogeneous surface with a uniform distribution of adsorption [109, 115, 148]. It assumes that the adsorbent surface is composed of a series of distinct sites capable of binding the adsorbate. This is correlated with the chemisorption and the adsorbate binding is treated as a chemical reaction. The Langmuir isotherm is expressed by the following equation:

$$\frac{C_e}{q_e} = \frac{1}{q_{max}b} + \frac{1}{q_{max}}C_e \tag{4.4}$$

where C_e is the equilibrium concentration (mg/L), q_e is the adsorption capacity at equilibrium (mg/g), b is the Langmuir constant (L/g), q_{max} is the maximum adsorption capacity (mg/g). A linear plot of C_e/q_e versus C_e confirms the legitimacy of the Langmuir model.

The Freundlich isotherm is related to adsorption capacity and intensity [115]. The Freundlich isotherm assumes a heterogeneous surface with a non-uniform distribution of adsorption, and probably indicates multilayer adsorption [109, 115]. This model is correlated with physisorption. Mathematically it is characterized by the heterogeneity factor '$1/n$', which is related to the adsorption intensity [109]. It is expressed by the following equation:

$$q_e = K_f C_e^{1/n} \tag{4.5a}$$

$$\ln q_e = \ln K_f + \frac{1}{n}\ln C_e \tag{4.5b}$$

where C_e is the equilibrium concentration (mg/L), q_e is the adsorption capacity at equilibrium (mg/g), K_f is the Freundlich constant (L/mg), $1/n$ is the heterogeneity of the sorption sites and an indicator of isotherm nonlinearity [153]. A plot of $\ln q_e$ versus $\ln C_e$, gives a straight line with K_f and $1/n$ determined from the intercept and the slope, respectively [109, 115, 153].

The data was fit to the Langmuir and Freundlich isotherm adsorption models shown in **Figure 4.13**. The data fitting gave the regression coefficients Freundlich (R^2 > 0.996) and the Langmuir (R^2 > 0.977) models indicating that both models described the adsorption process adequately. This indicates that the adsorption of MB onto activated carbon occurred by single molecular adsorption (chemisorption) and physisorption [153].

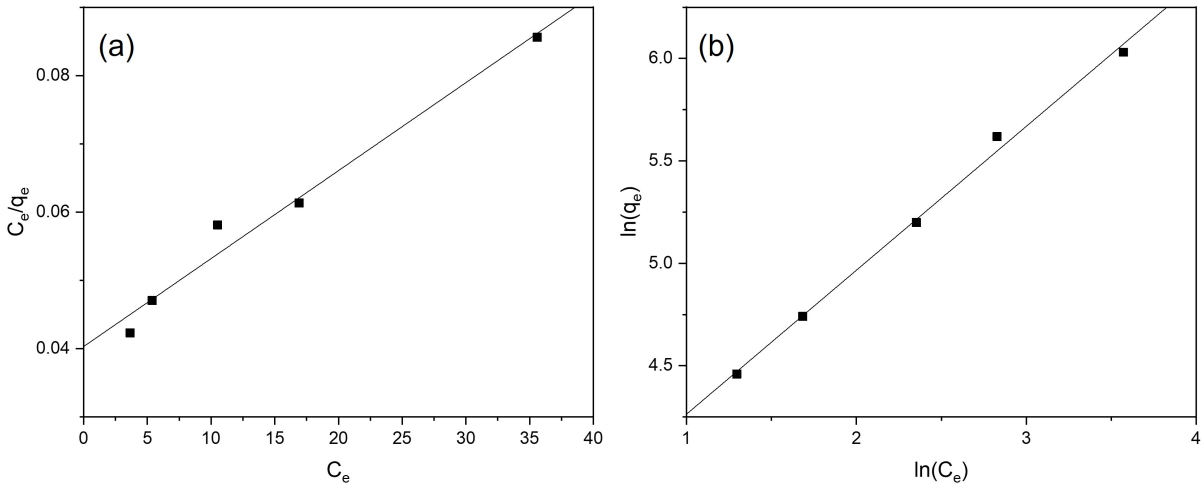

Figure 4.13 Langmuir (a) and Freundlich (b) isotherm adsorption models (n=3).

4.7 Conclusion[1]

The study shows that plasma treatment of AC can be used to increase the adsorption capacity by providing localized heating at atomic scale and completing the activation process. The overall results indicate that the AC as received contained some type of contamination that interfered with the adsorption of MB. The combination of heat, vacuum, and plasma-treatment effectively removed this contamination, causing the increased adsorption capacity. The maximum adsorption capacity of MB by O_2 plasma treated AC was 0.467 mg-mg^{-1} which was significantly higher than that of the untreated AC. The results of XPS analysis indicated a change in surface functional groups and

atomic composition after plasma treatment. The surface groups shown in both the O_2 plasma treated and non-plasma treated samples mainly consisted of carboxylic groups, phenols and/or ethers, and carbonyls. After plasma treatment C−O−C and C=O functional groups appeared. The adsorption kinetics and isotherm were also studied. Results showed that pseudo-second-order kinetics was the most suitable model for describing the adsorption of MB onto AC. Equilibrium data were well fitted to the Freundlich and Langmuir isotherm models.

CHAPTER 5

PLASMA ACTIVATION OF BIOCHAR

With increasing global population and environmental stressors (global climate change), access to potable water is expected to decrease in the coming years [28]. Anthropic activities such as agriculture, deforestation, and burning of fossil fuels exacerbate these issues, therefore solutions are needed [149]. Environmentally sustainable processes intend to maintain environmental resources by limiting the impact of anthropic activities and reducing the consumption of air, water, soils and sediments [149]. The new environmentally sustainable processes, such as wastewater treatment, seek to use renewable and clean energy sources. Current water treatments using AC traditionally use coal as the main carbon source, which is expensive, non-renewable, and energy intensive to produce, thus creating a need for an alternative water treatment [27, 28, 150].

The use of lignocellulosic materials to create biochar offers a renewable alternative. Annually, over 100 million tons of biomass are burnt in processing factories and fields, resulting in loss of carbon and nutrients from the soils, as well as a large increase in harmful atmospheric carbon emissions [151]. The vast quantities of biomass treated as waste could be converted into cost effective and sustainable biochar [151].

Biochar is porous carbon derived from biomass pyrolysis, the thermal degradation of organic matter in an oxygen poor environment [29–32]. Lignocellulosic materials have high carbon content and are composed of cellulose, hemicellulose, and lignin [27, 33]. These materials include agricultural wastes, providing a sustainable alternative to coal without compromising current agricultural production [33].

In 2016, Thompson et al. compared the environmental impact and cost of powdered

activated carbon (PAC) and biochar [150]. PAC has negative environmental impacts due to its generation from nonrenewable coal. PAC also requires energy-intensive thermal activation in order to develop its adsorption properties [150]. A potentially lower cost and environmentally friendly alternative is biochar. Biochar has demonstrated sorption capacity for a wide variety of contaminants including agrichemicals, pharmaceuticals, and endocrine disrupting compounds [150]. The global average price for biochar was \$2.56 kg^{-1} [155].

5.1 Influence of Feedstock on Chemical-Physical Characteristics of Biochar

5.1.1 Physical Carbon Structure of Biochar

Well known forms of carbon include the ordered structures of cubic diamond and hexagonal graphite. Each carbon atom in diamond has four covalent bonds (σ bonds) directed tetrahedrally to four other carbon atoms, making it sp^3 (**Figure 5.1**) [156]. There are no free electrons because all valence electrons are engaged in covalent bonds. Graphite is made so sp^2 hybridized carbon atoms where each has three covalent bones (σ bonds) directed to three other carbons in the same plane [156]. The fourth valence electron is not involved in sp^2 hybridization and is delocalized through π-π interactions, resulting in in-plane metallic bonding. As a result, within carbon the layer, the bonding is a mixture of covalent and metallic. Conversely, the adjacent layers are weakly bonded through van der Waals forces [156]. However, most carbonaceous materials are less ordered [157].

Coal, AC, and biochar are non-graphitic carbons, which is the most abundant class of sp^2-hybridized carbon materials [158]. The sp^2-hybridized carbons are structurally disordered comprised of both single and stacked graphene sheets called a "turbostratic" arrangement [158]. Non-graphitic carbons are further classified into graphitizable and non-graphitizable carbons. Biochar is an example of non-graphitizable carbon and possess a highly developed internal porosity and

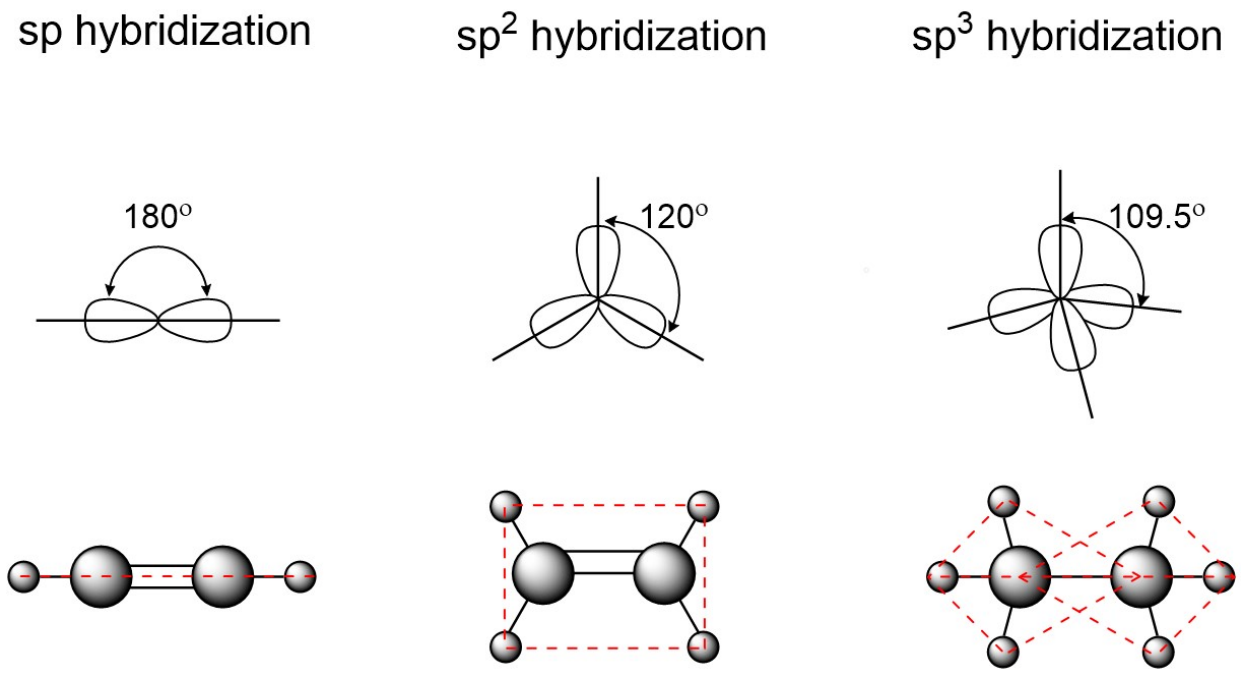

Figure 5.1 Carbon sp hybridized orbitals.

surface area [157, 158].

Biochar has a higher proportion of aromatic C and condensed aromatic structures compared to other organic matter [159]. The condensed aromatic structures vary in form, including amorphous C (dominates at lower pyrolysis temperatures), turbostratic C (formed at higher temperatures), and graphite C [159]. The effect of temperature on biochar structure and functional groups is depicted in **Figure 5.2**.

During thermal decomposition, biomass undergoes a series of phenomena including decomposition, transformation and rearrangement [160]. At low temperatures (100–200 °C) biomass remains almost unaltered and mainly undergoes dehydration [160]. As temperature increases, connections between cellulose, hemicellulose, and lignin decompose and consequently, isolated aromatic rings (transition biochar) begin to form [160]. When carbon atoms are transformed into rings with C=C double bonds, it is possible for the P-orbitals to overlap and π-electrons to be-

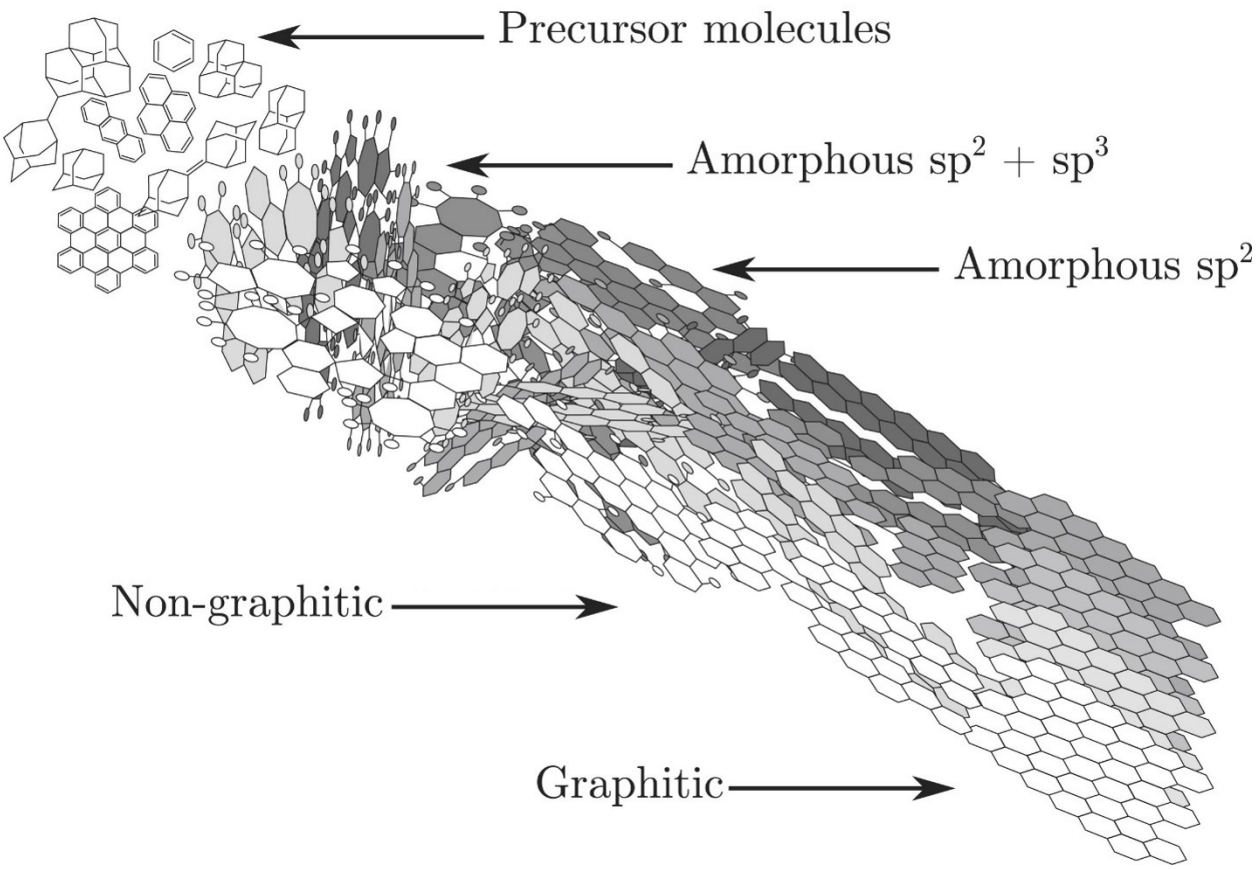

Figure 5.2 Example of different structures within biochar [158].

come delocalized, creating aromatic molecules [160]. This results in an increase in aromaticity and a decrease in polarity [160]. This process continues as the temperature increases until all biopolymers are degraded and substituted with isolated aromatic molecules with two to three rings (amorphous biochar) [160]. At higher temperatures, these small sheets of aromatic rings stack up to form small three-dimensional structures, consisting of three to five stacked C-sheets, termed turbostratic crystallites [160]. Both amorphous material and turbostratic crystallites are present in biochar structure (composite biochar). Biochar is considered "carbonized" or "turbostratic" when all amorphous organic carbon is either converted into aromatic rings or volatilized.

Thermal treatment removes hydrogen and heteroatoms like oxygen by releasing gases, ultimately reducing biochar yield. Two simultaneous processes reduce the carbonaceous material to

a more condensed structure: 1) loss of amorphous structure during gas release, and 2) transformation of the amorphous and disordered structures into aromatic ring systems [159, 160].

The well-organized C layers seen in biochar generated at higher temperatures (≥ 700 °C) is hydrophobic in nature [159, 160]. It is characterized by lower contents of O- and H-containing functional groups because of dehydration and deoxygenation of biomass. Surface functional groups on biochar can act as either electron donors or acceptors, leading to the formation of coexisting areas with opposing properties (acidic to basic and hydrophilic to hydrophobic) [159, 160]. This result causes biochar to exhibit a lower ion exchange capacity. Conversely, biochar produced at lower temperatures (300–400 °C) demonstrates more varied organic character as a result of aliphatic and cellulose type structures [159]. Overall, as pyrolysis temperature increases the structure of biochar appears to have more organized C layers (graphene like) and less surface functional groups [159]. However, biochar does not usually get to this point due to the requirement of either heating temperatures exceeding 700 °C or prolonged residence time [159, 160]. Therefore, most biochar have a highly disordered and heterogeneous carbon structure [160].

The current understanding of the transformation during the carbonization process begins with the precursor material. This material can range in composition. The general stages of atomic rearrangement during heat treatment begins with amorphous carbon exhibiting all three types of hybridization (sp, sp^2, and sp^3) without any crystalline structure is formed at temperatures above 700 °C [158, 161]. Around 1200 °C the mixed bonding turns into purely sp^2. Non-graphitic carbon is formed from further heating at temperatures from 1400 °C to 1700 °C, and above 1700 °C the crystallites transform into ordered stacks of graphene sheets (Figure 5.2) [158, 161]. Different precursor materials may not lead to the same transformations due to differences in bonding, networking capabilities and the types of defects in the non-graphitic and graphitic phase [158].

5.1.2 Composition of Lignocellulosic Biomass

The biomass used for biochar production influences the physical and chemical properties of biochar [149, 162, 163]. The three main components of lignocellulosic biomass are cellulose (40–50 wt %), hemicellulose (20–35 wt %), lignin (20–30 wt %) [149, 157, 162, 163].

5.1.2.1 Cellulose

Cellulose is a linear homopolymer of glucose consisting of β-D-glucose units linked via β-(1,4) glycosidic bonds, with cellobiose ($C_{12}H_{22}O_{11}$) as the fundamental repeating unit [157, 164–167]. Its chemical formula is $(C_6H_{10}O_5)_n$ (**Figure 5.3**) where n is the degree of polymerization (DP). The DP can vary significantly between materials, from a few hundreds to thousands (ex. DP value of wood cellulose is ~10,000 and plant cellulose ~15,000) [157, 165]. The DP refers to the number of monomer units in a polymer; in this case, the number of glucose units in one cellulose chain. Cellulose chains are rigid and arrange in parallel crystalline arrays held together by hydrogen bonds and van der Waals forces (**Figure 5.4**) [157, 164, 168]. Because of this, cellulose is difficult to hydrolyze contributing to its great resistance to chemical, biochemical, and biological conversions [164].

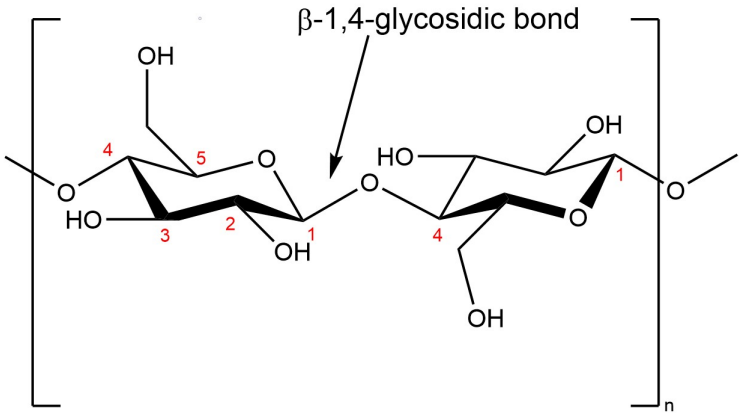

Figure 5.3 Two D-glucose units linked via β-(1,4)-linked D-glucose units.

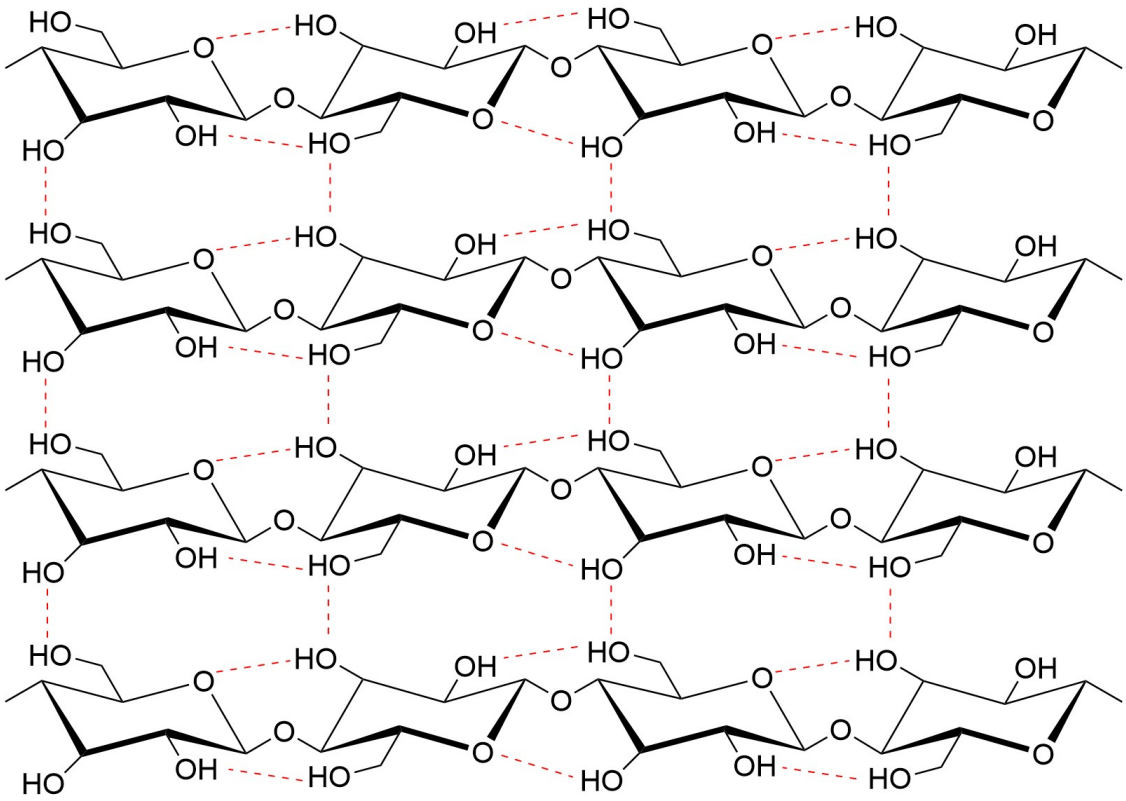

Figure 5.4 General structure of cellulose.

There are three hydroxyl groups (-OH) on each monomer which form hydrogen bonds with other cellulose chains [157, 165]. Long thread-like bundles of molecules called fibrils are laterally stabilized by these intermolecular hydrogen bonds [157, 165]. The groups of microfibrils make an array which is surrounded by a wall and are connecter by amorphous cellulose and hemicellulose (**Figure 5.5**) [157, 165].

The union of fibrils forms cellulose fiber. In plants, cellulose forms a microfibril composed of both highly ordered (crystalline) and less ordered (amorphous) regions [157, 165]. The main portion of cellulose is crystalline (native cellulose or cellulose I) with interspersed amorphous regions (cellulose II, III, and IV) [165]. There are two different crystalline structure of cellulose I: I_α which is a one-chain triclinic cell unit (mainly in bacterial cellulose), and I_β a two-chain

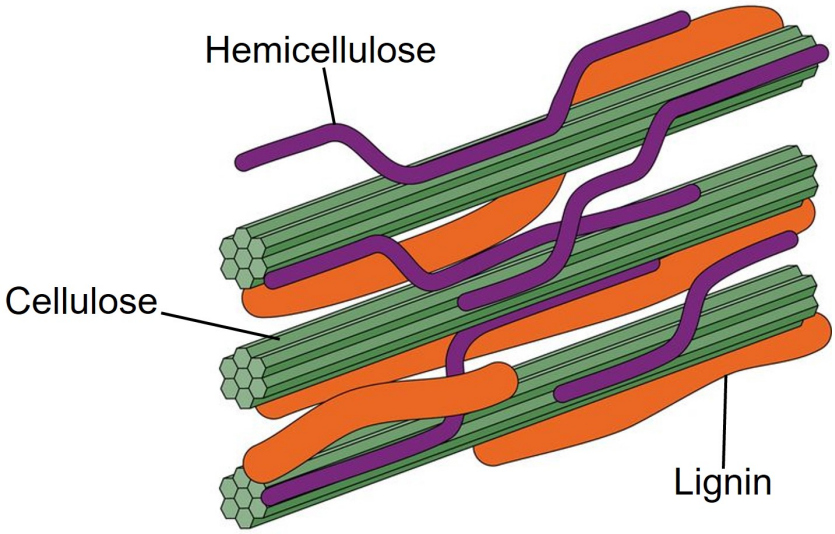

Figure 5.5 Simplified model of the main polysaccharides and lignin that form the plant cell wall structure [169].

monoclinic cell (plant cellulose) [165]. The chains of native cellulose (I) parallel to each other are held together through hydrogen bonds between O(6) and the adjacent intermolecular O(3) to form a layer [157, 165].

The arrays are associated with each other by lignin and hemicellulose. The few nm of space between microfibrils in an array is around the same size as micro- and mesopore diameters (2–50 nm) [157]. When heated during pyrolysis, cellulose, hemicellulose, and lignin are broken down into smaller monomers.

Cellulose is insoluble in water and most organic solvents. Only ionic liquids, like cadmium ethylenediamine, are known to solubilize the polymer. Cellulose is biodegradable. Some fungus and bacteria may be able to metabolize it, but this biological conversion can last several weeks.

5.1.2.2 Hemicellulose

Hemicellulose is a type of plant cell wall polysaccharide. Unlike cellulose, hemicellulose is branched and amorphous [164, 170]. Where cellulose is a homopolysaccharide with long linear chains, hemicellulose is a heteropolymer with short chains and lateral branches [164, 166, 167, 170, 171]. These lateral branches consist of monosaccharides and functional groups and prevent hemicellulose from forming a crystalline structure. Hemicellulose has a random amorphous structure that is easily hydrolyzed.

Generally, hemicellulose is composed of glucose, xylose, or mannose units linked via β-(1$\rightarrow$4) backbones (**Figure 5.6**) [164, 170]. Other possible components of hemicellulose include pentoses (xylose and arabinose), hexoses (glucose, galactose, mannose, and rhamnose), and carboxylic acids (acetic acid, glucuronic acid, and galacturonic acid). Their main role is to provide a linkage between cellulose and lignin in the plant cell wall [164, 170]. Non-covalent attractions on the surface of each cellulose microfibril tightly bind hemicellulose and cellulose together [164, 170]. The structure and composition of hemicellulose differs in different plant species and cell types [164, 170]. Examples include xylans that are characteristic of hardwoods, galactoglucomannans, that are predominant in soft woods, and arabinoglycuronoxylans, as well as many others. Because of this, hemicelluloses yield different sugars after hydrolysis treatment [164, 170]. For our experiments, biochar from bamboo was used.

Arabinose and xylose have been found to most likely be the main components in bamboo hemicellulose [172]. The primary hemicellulose of bamboo is thought to be glucuronoarabinoxylan which has a xylose backbone with arabinose, glucuronic acid, and acetyl side groups. Arabinoglucuronoxylan, another major hemicellulose component of bamboo and agricultural crops, contains

β-(1→4)-linked D-xylopyranose units along with some substitutions [164, 170, 172]. The common sidechains are 4-O-methyl-D-glucuronic acid attached by α-(1→2) bonds, and α-L-arabinofuranose units attached by α-(1→3) bonds [164, 170].

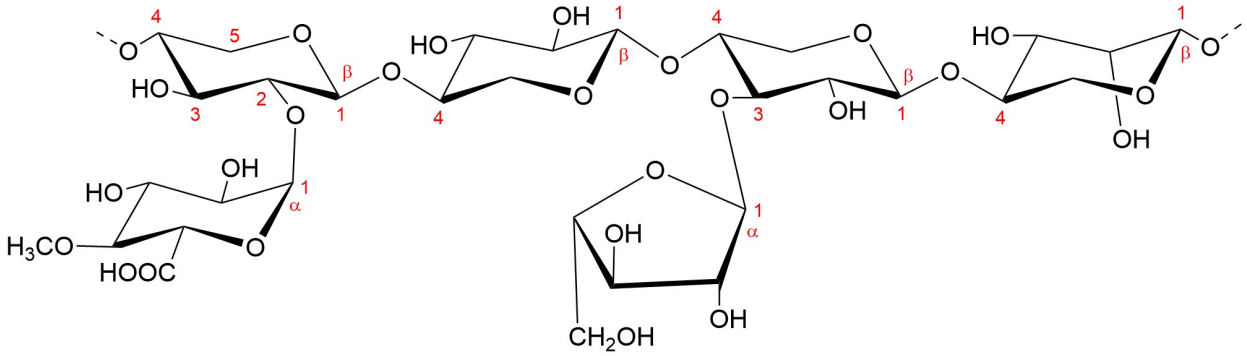

Figure 5.6 Structure of hemicellulose (xylan) consisting of a xylopyranose backbone, with glucuronic acid (1→2) and arabinofuranose (1→3) side branches.

5.1.2.3 Lignin

Lignin is an aromatic (phenolic), three-dimensional, macromolecule composed of phenylpropanoid units linked together through a complex network of ether and carbon-carbon bonds (**Figure 5.7**) [157, 164, 173]. Lignin is a hydrophobic amorphous polyphenol made up of the primary monolignols: coumaryl, coniferyl, and sinapyl alcohol [157, 164, 168, 173]. It gives strength and structural rigidity to the cell wall [157, 173]. Lignin is tightly bound to cellulose and hemicellulose through hydrogen bonds, lignin-carbohydrate complexes, and covalent bonds [164].

Lignin does not have a defined primary structure due to its heterogeneity. The main links between monolignols are C−O bonds of α- and β-arylalkyl ethers.

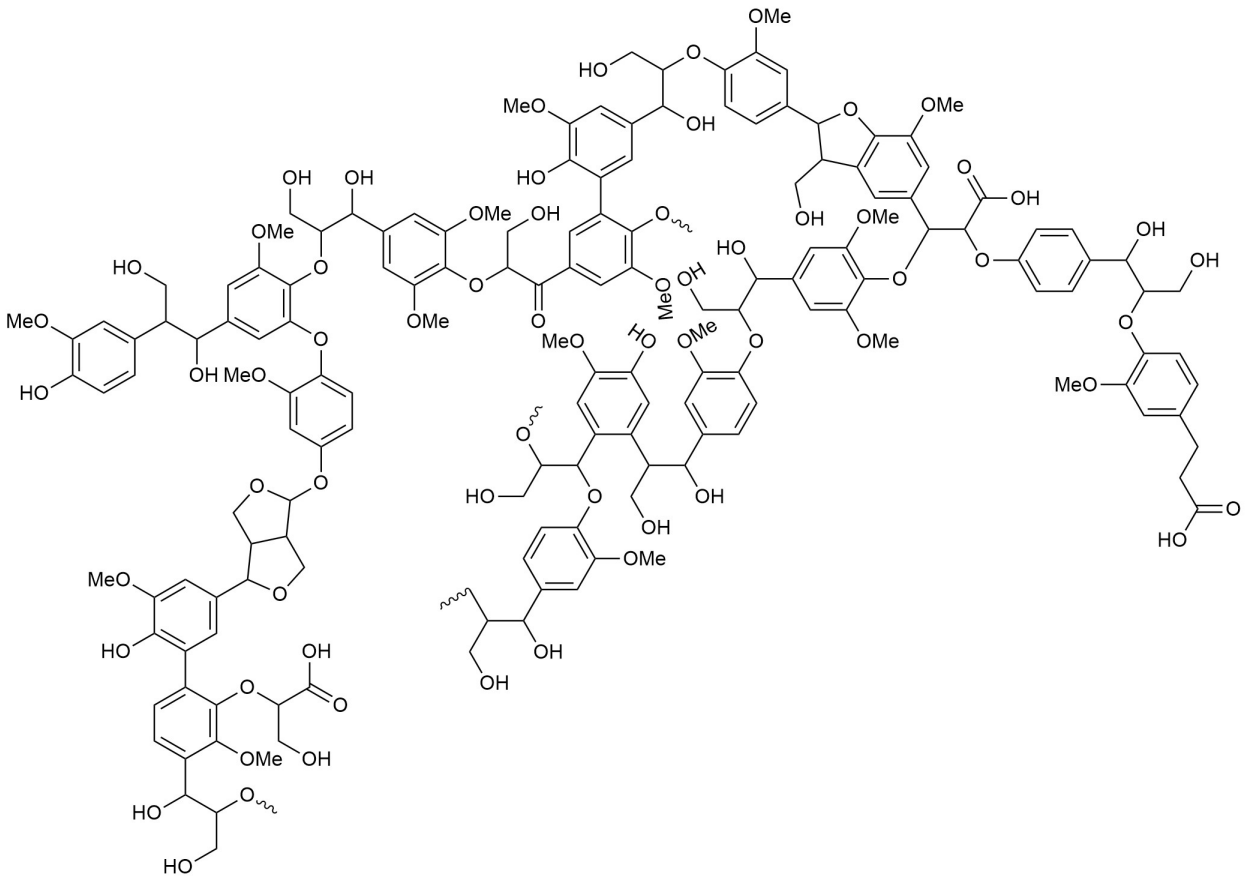

Figure 5.7 Example of lignin molecule structure.

5.1.3 Relationship Between Feedstock and Pyrolysis Products

The composition of cellulose, hemicellulose, and lignin varies between different feedstocks. These differences influence how the biomass behaves during thermal degradation [149, 162, 163]. Hemicellulose is the first to undergo decomposition at temperatures ranging between 200 and 260 °C [149, 157, 163]. However, cellulose and lignin break down at higher temperature ranges, 240–350 °C and 280–500 °C, respectively [149, 157, 163]. Pyrolysis of hemicellulose begins with depolymerization resulting in oligosaccharides, 3 to 10 unit carbohydrate chains [149]. Further cleavage of the xylan chain and molecular rearrangement produce xylopyranose, which is further degraded into small molecular weight compounds containing two or three carbon atoms. Simi-

larly, the first step in cellulose pyrolysis is its depolymerization into oligosaccharides [149]. The oligosaccharides are further broken down to produce D-glucopyranose which is intramolecularly rearranged producing levoglucosan. The latter ultimately decomposes to form small molecular weight compounds [149]. Pyrolysis of lignin generates phenolic compounds [149].

The amounts of cellulose, hemicellulose, and lignin in the biomass effect reactivity and yield, thereby affecting the ratios between biochar and volatile products (e.g., bio-oil and gas) [149]. For instance, feedstocks with low amounts of lignin, minerals, and nitrogen are primarily used for bio-oil and fuel-gas production [149]. Conversely, biochar is produced from feedstocks with more lignin. In general, woods produce biochars with low ash and high carbon content, whereas less rigid herbaceous biomasses, biosolids, and manures result in biochars with low carbon content and higher ash [149].

Feedstock biomass also influences the porosity, and therefore, the adsorptive properties of biochar. During thermal degradation, volatile organic compounds are lost resulting in a volume reduction [30, 32, 149, 174, 175]. The remaining mineral and carbon skeleton retains the rudimentary porosity and structure of the feedstock. This residual structure arising from the biological capillary structure of the biomass, contributes to the majority of the biochar macro-porosity [30, 149, 174, 175]. These larger pores serve as a feeder to smaller ones.

5.2 Biochar Fabrication

The pyrolysis of biomass produces a solid residue (biochar), a liquid product (bio-oil or tar), and a mixture of gases (syngas). The yield and physical characteristics of biochar depend on the biomass and the pyrolysis system used [18, 30, 174–179]. The original structure of the biochar's starting material is imprinted on the biochar product, influencing its physical and structural

characteristics [174]. During pyrolysis, the biomass shrinks and loses mass, but there is residual cellular structure and porosity [174]. The chemical composition of the original biomass also impacts the physical nature of the biochar formed [174]. Organic material begins to undergo some thermal decomposition at temperatures above 120 °C while also losing moisture. Plant cell wall components hemicellulose, cellulose, and lignin are degraded at 200 °C to 260 °C, 240 °C to 350 °C, and 280 °C to 500 °C respectively [174]. The proportions of these polymers will influence the degree of reactivity and the amount the physical structure is modified during pyrolysis [174].

The yield of biochar is linked to the lignin content of the feedstock biomass [180]. During pyrolysis the alkoxy groups (methoxy groups on the benzene ring) are decomposed and combine with free hydrogen, forming methanol [180]. This results in a significant difference in the surface chemical structure of biochar. Gong et al. studied the affect the types of lignin had on the ability of biochar to adsorb nitrogen gas [180]. They found that the samples with lignin composed of coniferyl alcohol and sinapyl alcohol units formed more oxygen-containing functional groups and hydroxyl groups. The sample with lignin composed of coniferyl alcohol formed a well-developed pore system and had the best adsorption performance.

5.2.1 Pyrolysis Methods

There are three main pyrolysis techniques, shown in **Table 5.1**, utilized to obtain the aforementioned by-products in the greatest yield: slow pyrolysis, fast pyrolysis, and gasification [18, 32, 176–179, 181]. Slow pyrolysis is characterized by heating in the absence of oxygen with relatively low temperatures, ranging from 300 to 700 °C, with heating rates around 5–7 K/min^{-1} (slow), and residence times ranging from minutes to days (long) [18, 32, 176–179, 182]. Residence time is the duration in which pyrolysis is kept at the highest treatment temperature. The

primary aim of slow pyrolysis is the production of char, a carbon rich solid residue. Similarly, fast pyrolysis is performed in in the absence of oxygen at lower temperatures from 400 to 600 °C. Conversely, fast pyrolysis is heated at a much faster rate, 600–1200 K/min, with residence times in seconds. The short residence times associated with fast pyrolysis yields bio-oil in high amounts [18, 32, 176–179, 181–183].

Table 5.1 The general parameters of different pyrolysis processes [18, 176–179].

	Slow	**Flash**	**Fast**	**Gasification**
Temperature (K)	300–800	400–1000	400–600	750–1000
Heating rate (K/min)	5–7	≥1000	600–1200	~1000
VRT	>60 min–1 day	2–3 s	1–10 s	10–20 s
Major products	Biochar	Bio-oil/bio-gas	Bio-oil	syngas
Biochar yield (wt %)	30–55	11–22	16–37	14–25

A significant difference between slow and fast pyrolysis is the primary by-products, biochar and bio-oil. This can be explained in theory by basic thermodynamics and kinetics. Slow pyrolysis is considered a thermodynamically controlled process because of the long residence time [18, 176–179]. The reactants and products are allowed adequate time to reach equilibrium, and the products are formed based on temperature and pressure, rather than reaction rate. Conversely, fast pyrolysis is kinetically controlled due to the rapid removal of vapor intermediates, thus preventing them from either condensing into secondary char or cracking into low molecular weight syngas [18, 176–179]. Therefore, fast pyrolysis is usually performed under vacuum, or a constant flow of inert gas, to remove the intermediates quickly to yield bio-oil in high quantities. Overall, the most promising biochar production strategy seems to be one that focuses on temperature and pressure, rather than

reaction rate.

Slow pyrolysis, or conventional carbonization, has a long vapor residence time and low heating rate [32, 182, 183]. An advantage is that stable biochar can retain up to 50% of the feedstock carbon [32]. This process has been used historically to generate charcoal [32]. Previous studies have focused on increasing charcoal yields during slow pyrolysis and have identified several critical variables: peak temperature, pressure, vapor residence time, and moisture content [32]. It has been shown that the charcoal yield decreases with an increase in temperature, but the fixed-carbon content of biochar will increase [32]. The increase in fixed-carbon content found in biochar is most pronounced in the temperature range from 300 to 500 °C [32]. The peak temperature also affects the pore size distribution and surface area, which are key factors in the adsorptive properties of biochar [32].

Understanding the pyrolytic behavior of cellulose, hemicellulose, and lignin is fundamental to the production of biochar. During pyrolysis, cellulose, hemicellulose, and lignin are broken down into smaller monomers through a series of complex reactions, as discussed in a previous section. Cellulose is mainly degraded into condensable organic vapors once the temperature of 400 °C is reached, but only if volatile compounds are simultaneously removed from the reaction medium [157]. At higher pressure if the process is not ventilated, the gases are more likely to react and form char at the expense of consuming condensable organic vapors [157]. Lignin decomposition occurs very slowly at a minor level in a wide range of temperatures (160–900 °C). The result of this gradual process is the yield of solid residue (known as char) up to almost 40% of the original sample weight [157].

Gasification is a partial combustion where biomass is reacted with steam or air, and the amount present is controlled [182]. It is carried out at high temperatures ranging from 750 to

1000 K. The primary by-product of gasification is syngas. During the process oxygen is restricted leading to the primary conversion of biomass into carbon monoxide (CO) and hydrogen gas (H_2) instead of complete oxidation/combustion into CO_2 and water [18, 176–179]. Gasification can be stoichiometrically controlled theoretically, but realistically, equilibrium is hard to achieve with current reactors, and thus, viscous tars are formed.

5.3 Biochar as an Adsorbent

Biochar has been considered as a sustainable means to remove pollutants from water due to its high surface area and resistance to degradation [30, 130, 175]. Biochar may remove pollutants from water by electrostatic attraction, ion exchange, or precipitation [130]. Therefore, most biochar treatments aim to either increase the surface area, modify or enhance surface properties [130]. The high surface area of biochars is due to the large quantity of micro and mesopores [130]. As the number of micropores increases, so does the surface area leading to more surface sites upon which pollutants can adsorb. Surface charge and functionality also influence the sorption capacity of biochar [130]. Functional groups on the surface of biochar influence the ion exchange of chemical sorption, which relies on base cations such as K, Na, Ca, and Mg [130]. These functional groups (i.e. carboxylic, hydroxylic, or phenolic groups) affect the cation exchange capacity of biochar due to the loss of oxygenated functional groups [130]. Electrostatic sorption occurs when ions in the water are attracted to the electrons associated with surface functional groups [130]. The loss of oxygenated functional groups effect the cation exchange capacity of biochar [130]. Electrostatic sorption occurs when ions in the water are attracted to the electrons associated with surface functional groups [130]. **Figure 5.8** shows the theoretical adsorption mechanisms for cations and anions for raw biochar and activated biochar [130]. Surface functional groups and area can be manipulated by activation or

modification of biochar to enhance its sorption capacities [130].

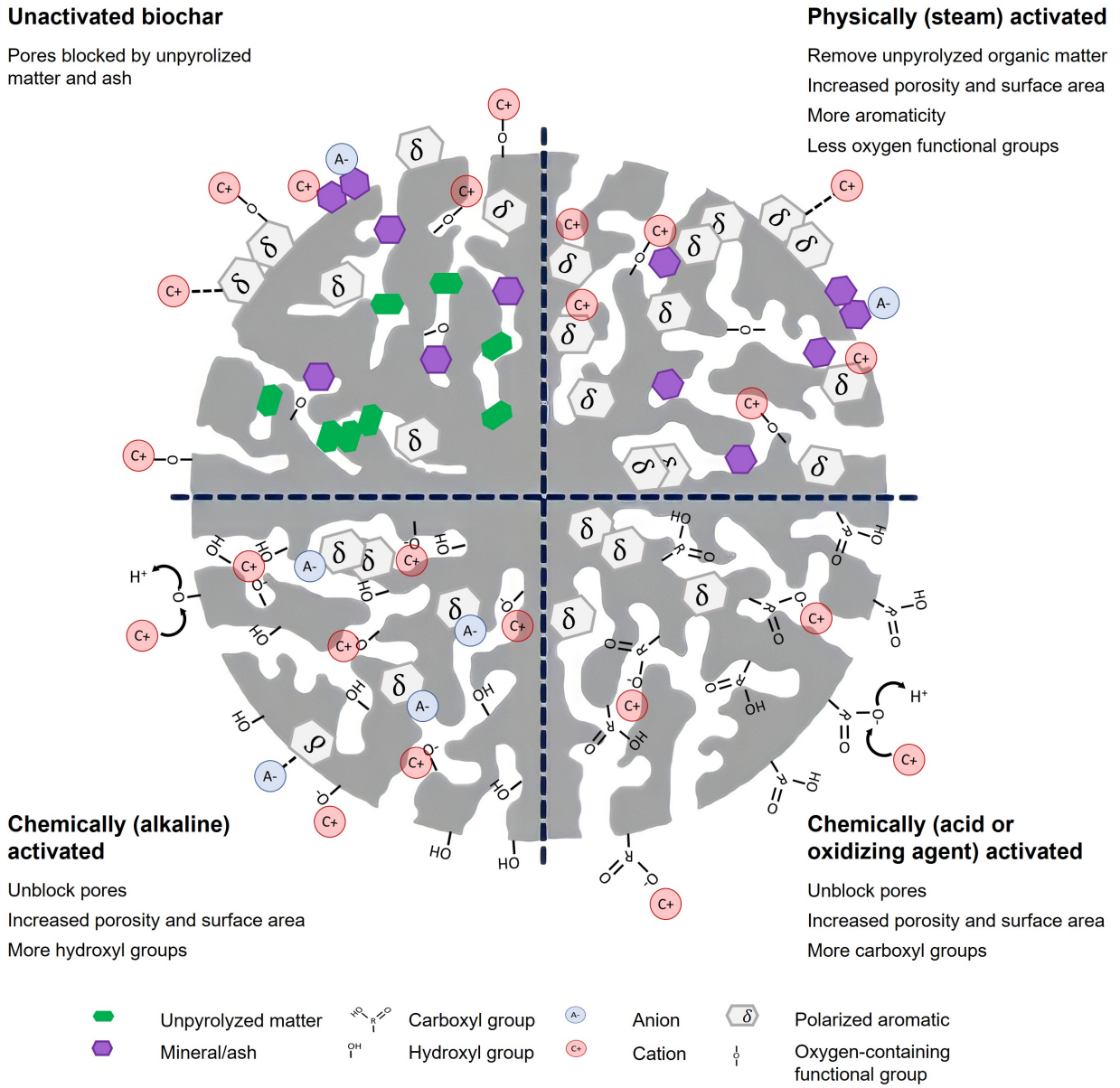

Figure 5.8 Theoretical adsorption mechanisms for metal cations and oxyanions onto unactivated biochar, physically activated biochar, or chemically activated biochar [130].

Surface area and porosity are key factors in the determination of adsorption capacity. A study by Chen et al. 2011, investigated the adsorption of Cu (II) and Zn (II) on two different biochars: hardwood and corn straw. They found that despite the hardwood biochar being more hydrophilic, its adsorption capacity was less than that of the corn biochar which had a greater

surface area [184]. The greater porosity and surface area were much more impactful and made the corn straw biochar better at adsorbing the heavy metals [184]. Sun et al. 2017, studied the effects of pyrolysis temperature on the properties of biochar. They found that the adsorption of iodine showed minimal change in relation to the increase in pyrolysis temperature, but what did change was the ash content and fixed-carbon content [185]. The yield, volatile matter, and the surface acid oxygen-containing functional groups decreased [185]. When the pyrolysis temperature increases, the biochar loses water and volatile matter [185]. As this occurs the chemical bonds break leading to an increase in ash content and pH [185]. Lower pyrolysis temperatures and shorter residence times improved the adsorption capacity of biochar [185]. It was found that at a temperature of 300 °C, carbon is consumed and micropores in the biochar open [185]. The larger micropores increased the specific surface area [185]. The lower temperature left more organics and active groups on the biochar surface, increasing iodine adsorption [185].

A study by Shen and Gu observed that the final mass of char at 800 °C increased with low heating rate [186]. This agreed with previous studies that had found the longer preheating (>1 hour) at low-temperature (370 °C) increased char production from cellulose pyrolysis [177, 187]. During the preheating treatment, internal rearrangement, such as, dehydration, bond breakage, formation of free radicals and carbonyl groups, reduction of the biomass molecular weight, and evolution of water, CO, and CO_2, occurs [177]. Next, at temperatures 200–300 °C biomass begins to depolymerize into anhydro-sugars (i.e., levoglucosan) and light volatiles such as furans, aldehydes, and acids. Once the pyrolysis process reaches temperatures > 300 °C, solid decomposition occurs and further cleavage of C-H and C-O bonds results increased carbon content [177].

5.4 Biochar Activation

Biochar is a stable carbonaceous solid that can be used in a wide variety of applications. The most common applications of biochar are adsorbents, soil amendments, and most recently in supercapacitors [157]. They have also been found useful for capturing carbon dioxide as a means to combat climate change [157]. However, biochar has limited porosity, surface area, and polar oxygenated surface groups before activation, negatively affecting its applications [155, 157]. This can be rectified through physical modification and chemical activation, offering a promising future for the synthesis of biochar with various desired properties.

Previous studies have demonstrated that biochar requires activation to achieve adsorption efficiencies similar to AC. The modification of biochar is achieved either through physical or chemical means. Physical modification changes the pore structure and surface area whereas chemical activation aims to increase active functional groups on the surface [188]. The study by Wang et al. 2018, showed that the chemical activation of biochar was 2–3 times more efficient than the physically activated biochar. This gives further evidence for the pseudo-second order kinetics of biochar found in previous works.

Physical activation of raw biochar is achieved by applying thermal treatment in a partial oxidizing medium, usually steam, CO_2, or a combination of the two [160, 189–192]. The biochar produced through pyrolysis has a high percentage of carbon, but the internal surface area is low due to blockage of pores by tar [190]. During the physical activation process the biochar is exposed to a desired volume of the activation gas. The process is usually performed at high temperatures 700–1000 °C [160, 189, 190]. These oxidizing agents penetrate the internal structure of the biochar and gasify the carbon atoms, thus removing them. This result in widening and opening of

previously inaccessible pores [160]. The mechanism of action in physical activation involves the physical agents (CO_2 or steam) removing the carbon atoms from the biochar structure according to the following Boudouard reactions [160, 192, 193]:

$$C + CO_2 \rightarrow 2CO, \Delta H = 159 \text{ kJ/mol} \tag{5.1a}$$

$$C + H_2O \rightarrow H_2, \Delta H = 117 \text{ kJ/mol} \tag{5.1b}$$

During this process, CO_2 forms a surface oxide and carbon monoxide through dissociative chemisorption on the carbon surface [160]. The surface oxide, C(O), is subsequently desorbed from the surface, further developing the pore structure [160]. CO in the gas may adsorb on the carbon active site, slowing further gasification [160]. Thermodynamically, Boudouard reaction is endothermic (large positive enthalpy), the equilibrium does not favor CO production until temperatures > 700 °C.

The smaller size of water molecules compared to CO_2 enables steam to be used for activation. Steam activation uses super-heated steam to develop porosity of biochar through its mild oxidation [160, 161]. At 800–900 °C, typically, H_2O reacts with carbon and produces CO + H_2 [160, 191]. Therefore, carbon is consumed, and pores are produced which progressively widen with time. The process is usually run between 30 minutes and 3 hours [160]. The overall reaction between steam and carbon and the reaction between CO_2 and carbon are endothermic and easy to control [160, 190].

It has been demonstrated that steam and CO_2 generate different pore size distributions due to side produced inhibitors, H_2 and CO respectively [191]. In CO_2 activation, CO enhances microporosity, whereas during steam activation H_2 enhances mesoporosity [191]. Each process

also forms different functional groups. Stable carbon-oxygen complexes are created and obstruct reaction sites, acting as a retardant [191]. Some of the complexes can decompose to CO, leaving a free carbon site for additional reactions to occur. Physical activation with steam creates C−H complexes, which are more stable than C−O complexes, leading to greater inhibition of the reaction [191]. These different surface interactions coincide to produce different activation results. The temperature impacts the gasification rate with lower reaction temperatures (~600 °C) favoring the production of CO_2 and higher temperatures (> 900 °C) favoring the production of CO [191].

Whereas, in chemical activation, different reactions occur simultaneously, based on the chemicals used [192]. Current activation of biochar with a base requires hours of high-temperature treatment (~960 °C) in an inert atmosphere using a strong base (KOH) or acid (H_3PO_4) mixed with biochar powder [31, 190, 192]. This activation is usually incorporated as part of the carbonization process. The acid H_3PO_4 may acts as a dehydration agent removing water from the biochar, while the base KOH can act as an oxidizing agent, transferring electrons between reactants [192]. In the thermal treatment of biochar, acids can be used as catalysts [192].

Various activators have been studied: KOH, H_3PO_4, $ZnCl_2$, and H_2, etc. KOH has the most promise due to its moderate activation temperature, higher biochar yields, highly developed microporous structure, and high specific surface area [157, 194, 195]. The first steps in KOH activation are soaking the biochar in the desired concentration of KOH at temperatures between 25 and 100 °C which may last hours or days [157]. This is then followed by a thermal treatment, usually around 760 °C. Alkalis, like KOH, under thermal treatment, can decompose to metallic compounds (metallic potassium) and be incorporated into the carbon structure, and react with CO_2

and CO to develop porosity as shown in Equations 5.2a–5.2d [192, 193, 196, 197]:

$$6KOH + 2C \rightarrow 2K + 3H_2 + 2K_2CO_3 \tag{5.2a}$$

$$K_2CO_3 \rightarrow K_2O + CO_2 \tag{5.2b}$$

$$K_2CO_3 + 2C \rightarrow 2K + 3CO \tag{5.2c}$$

$$K_2O + C \rightarrow 2K + CO \tag{5.2d}$$

The chemical reactions between KOH and carbon have been well studied and can be summarized in three steps: 1) KOH, K_2CO_3, and K_2O etch carbon via redox reactions; 2) gaseous products further react with carbon; and 3) metallic Potassium (K) intercalates into the carbon which results in a developed porosity [157, 194, 195].

The assumed mechanism is the reduction of KOH to metallic K and carbonate K_2CO_3 during the carbonization process. The alkaline metals and carbonate are then intercalated within the carbon matrix, subsequently widening and stabilizing the spaces between the carbon atomic layers [157, 196, 198]. Simultaneously, side chain reactions between the carbon surface and the active intermediates and the release of CO, CO_2, and H_2 may occur. Generally, KOH activation shifts mean pore diameter to a smaller range enhancing the volume of micropores [157, 199–202].

The chemical reactions between oxygen (or oxygen-containing species) and KOH was further elucidated by Chen et al. [194]. They found that the KOH was able to react with active O-containing species to remove the O-containing groups [194]. This formed vacancies which were filled by OH- (anions) from KOH entering and forming new O-containing species (i.e. C=O, −OH, C−O, −O−C=O, and −COOH) [194, 203]. KOH also etched carbon fragments to form vacancies, which OH− occupied to form new O-containing groups [194]. The potassium species formed

during activation, diffuse into the internal structure of the biochar creating new and widening existing pores [157]. Activation with KOH usually increases alcoholic or phenolic groups (−OH), carboxylic groups (C=O), aromatic groups (C−C), and alkenes (=C−H) (**Figure 5.9**). However, the surface oxygen groups on the carbon materials decompose upon heating, producing CO and CO_2 at different temperatures. Hence, C contents significantly increase while the quantities of O and H decreased due to the weight loss because of increasing the release of volatile products as a result of intensifying dehydration and elimination reactions [157, 204].

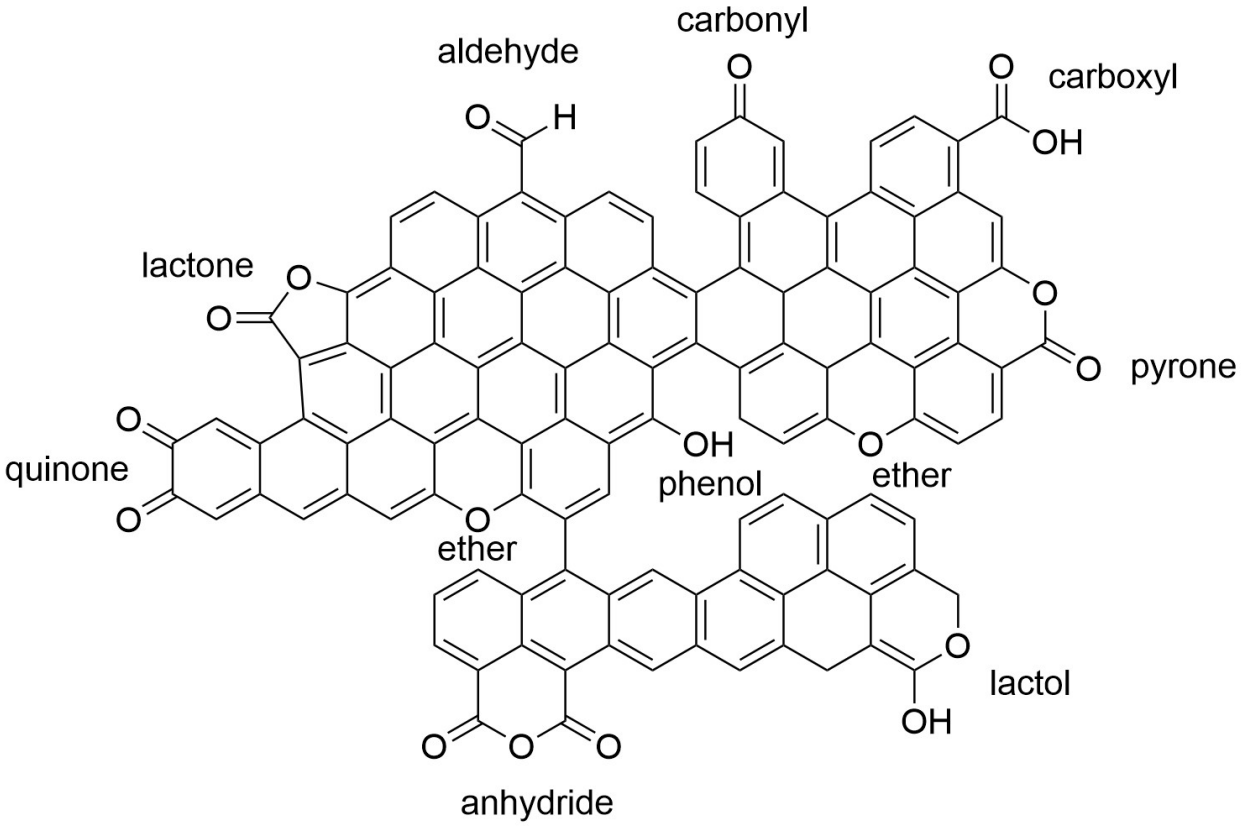

Figure 5.9 Example of oxygen enriched biochar with possible o-containing functional groups.

Feng et al. investigated the use of biochar for the adsorption of nitric oxides in the air due to flue gas emissions [205]. Flue gas is emitted from combustion plants when fossil fuels (i.e. coal, oil, natural gas) or wood are burned and contains residual substances and reaction products of fuel such

as sulfur oxides, nitrogen oxides, and carbon monoxide [206]. The chemical aspect of the activated biochar surface (e.g., functional groups and active sites) greatly influence the denitrification ability of biochar [180, 205, 207]. It has been found that oxygen-containing functional groups specifically enhance the denitrification efficiency [180, 205, 207]. Chemical activation by KOH is an effective method to improve flue gas denitrification [205]. KOH activation has been found to increase the number of oxygen-containing functional groups on the surface of biochar, as well as the adsorption abilities [194]. The alkali metal K has also been shown to effect reaction efficiency by acting as a catalyst in NO reduction [180, 205, 208].

Temperature and KOH concentration have been shown to influence this process. If the activation temperature exceeds 760 °C, the boiling point of potassium, the potassium diffuses into different layers of carbon and forms new pores [157, 204]. Therefore, it may be inferred that porosity could be further increased by more reactions between KOH and carbon, which may also enhance carbon burn-off [157, 201]. KOH modification could enhance porosity and surface area of biochar without extreme temperatures through removal of inorganic matter, unblocking of pores, and destruction of some micropore structure [157, 203, 209]. Aside from temperature, concentration of the activating chemical significantly affects pore size distribution. Higher KOH concentration typically generates carbon with higher surface area [201]. For example, the surface area of corncob derived biochar activated with KOH was almost 3–4 times higher for KOH/char ratios from 3–6 at 780 °C compared to those with a ratio of 0.5 to 2 [157, 200].

Current activation of biochar with a base requires hours of high-temperature treatment (~960 °C) in an inert atmosphere using a strong base (KOH) mixed with biochar powder [31]. This is an energy-intensive and time-consuming process that inhibits achieving cost-effective biochar. This work aims to establish a plasma treatment that effectively activates biochar at a low-temperature

and in less time. A study by Gupta et al., 2015, used low-temperature (< 150 °C) plasma treatment to activate yellow pine biochar [31]. The study focused on the effects of oxygen plasma on the biochar microstructure and supercapacitor characteristics like high capacitance [31]. They found that capacitance was enhanced with a 5 minute oxygen plasma treatment due to an increase in pore size distribution and surface area [31].

As discussed in plasma sterilization, biochar is an organic material made primarily of carbon. If it is treated with a plasma, for example oxygen plasma, then a microporous structure can be created. Plasma can also form specific functional groups on the surface of biochar. If an oxygen plasma is used to activate the biochar, the reactivity of carbon to oxygen would activate the biochar and increase its porosity and surface area, making it much more efficient in adsorption.

The ultimate goal of this study is to replace current water treatment methods with one low cost, universal method: biochar. Biochar requires chemical activation in order for its adsorption capacity to compete with commercial AC (> 100 mg/g) [29, 31, 34, 210]. Conventional chemical activation techniques utilize alkalis, like KOH, and require hours of high-temperature treatment (~960 °C) [31, 192]. This energy-intensive and time-consuming process inhibits achieving cost-effective biochar. Plasma activation offers a strategy that dramatically decreases energy costs of activation due to the decrease of treatment times from hours to minutes, and temperatures from higher than 900 °C to below 300 °C. This is possible due to the reactive species within the plasma gas. They collide and interact with the biochar surface, which ultimately etches the biochar and creates an improved porous structure without the need for high temperatures [37]. We aim to establish a plasma treatment that effectively activates biochar at a low-temperature and in less time. Additionally, the use of plasma improves pore structure and offers the ability to generate chemical species and functional surface groups using appropriate plasma gases, which allows the biochar to

be tailored for specific purposes [188].

5.5 Materials and Methods

A preliminary study was conducted in order to determine which activating agent and plasma gas combination was the most promising candidate for biochar activation. The 5 mg biochar samples were soaked in either KOH, H_3PO_4, or Na_2CO_3 (**Figure 5.10**). The chemically soaked samples were then treated with 1 of four plasma gases at 100 °C for 5 minutes: O_2, H_2, CH_4, and N_2. Next, 5 mg of the plasma treated biochar was place in 2 mL of 10 mg/L MB solution and soaked for 20 minutes. The solution was spun down and the supernatant was extracted for evaluation with UV-vis. The Adsorption capacity was then calculated from the concentration of MB remaining. The combination of KOH and O_2 plasma were the most promising, particularly because of O_2 reactivity.

The biochar was soaked in 1 of 3 KOH solutions: 0.1% KOH, 1% KOH, or 10% KOH. They were then left to dry at room temperature. Next, the samples of KOH treated biochar were placed in the plasma system and treated with oxygen plasma. An external heat source was used in the activation process and the temperature were varied.

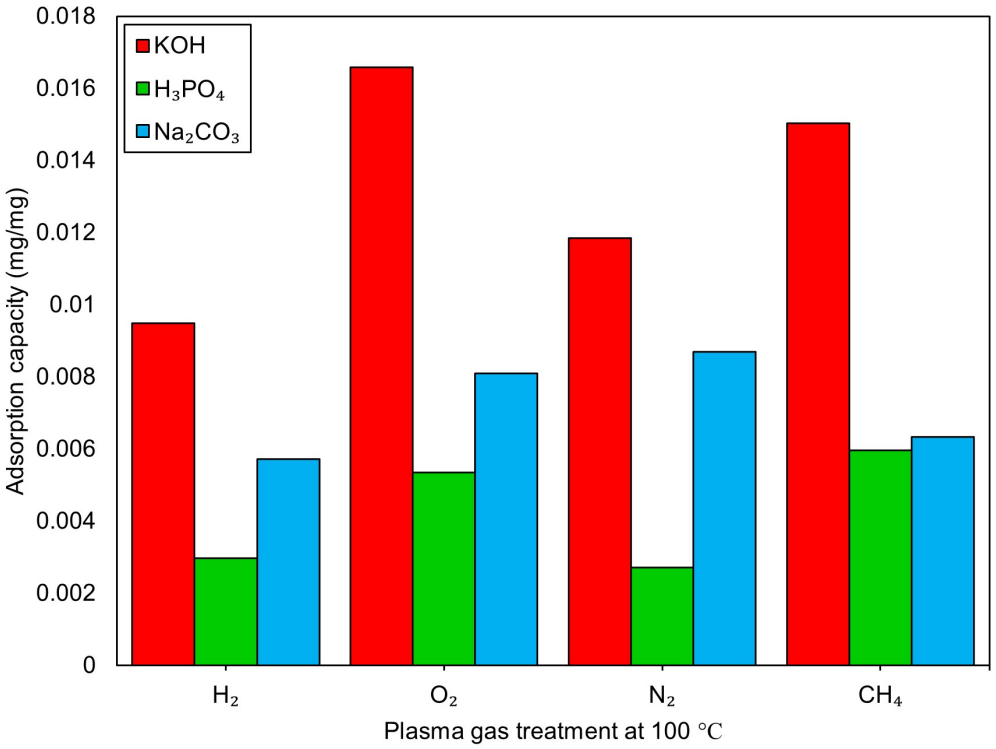

Figure 5.10 Preliminary study adsorption capacities of biochar soaked in one of three activating agents.

5.6 Results and Discussion

5.6.1 Mass Loss

The weight % lost was recorded for each of the samples. As shown in **Figure 5.11** at the lower temperature of 200 °C the % loss was around 15 % for all three concentrations of KOH. When the temperature was increased to 300 °C the % loss nearly tripled with the 10% KOH sample having the highest % loss. This is most likely due to the KOH decomposing to metallic potassium and reacting with CO_2 and CO in the carbon structure, causing increased porosity [192, 193, 196]. As the temperature increased, so did the reactivity, thus leading to increased wt % lost. The same can be said about the concentration of KOH increasing. Impregnating the biochar with higher concentrations of KOH, increased the rate of reaction which led to increased wt % lost up

to a point. Less mass reduction was found for samples treated with 30% KOH and 50% KOH with O_2 plasma at 300 °C for 5 min (**Figure 5.12**). This may be due to an excess of KOH after 10%. The overabundance of KOH can potentially plug pores of AC and prevent volatiles through pore channels, leading to a decrease in mass loss [198]. It has been shown that the amount of weight lost at higher mass ratios of KOH to biochar minimizes the weight loss. KOH acts as a dehydrating agent, influences pyrolytic decomposition, inhibits tar formation, and increases carbon yield [198, 211–213].

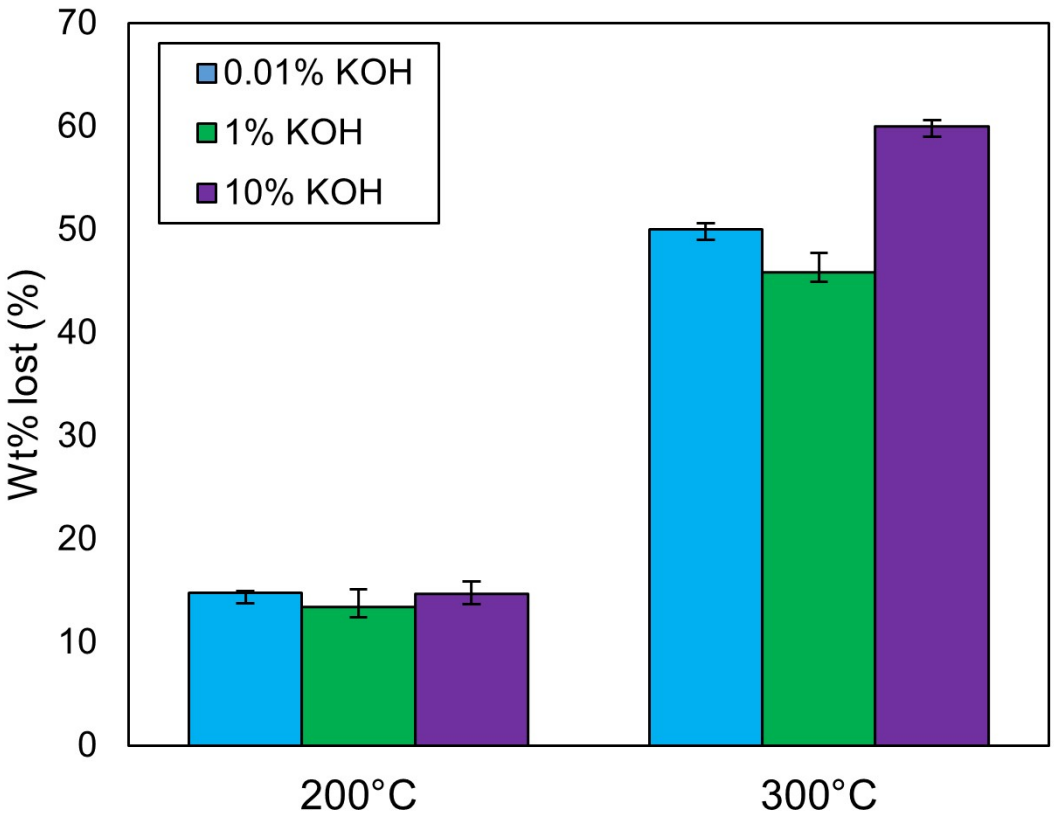

Figure 5.11 Average wt% loss after 5 minute oxygen plasma treatment for 0.01% KOH, 1% KOH, and 10% KOH biochar samples at either 200 °C (right) or 300 °C (left) (n=3).

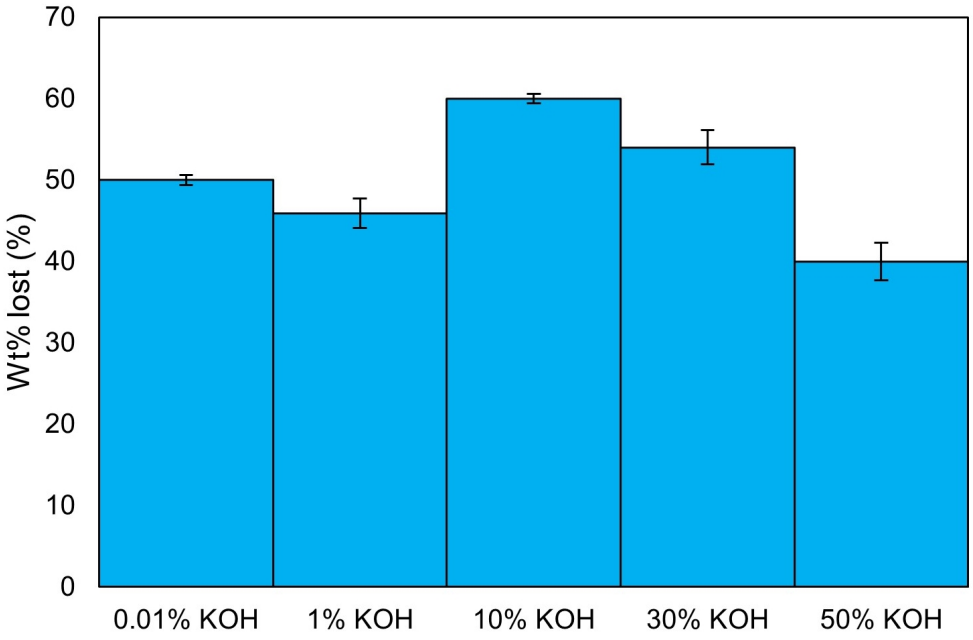

Figure 5.12 Average wt % lost for KOH treated biochar at 300 °C (n=3).

5.6.2 Methylene Blue Adsorption

As stated previously, porosity plays an influential role in the determination of adsorption capacity. We saw that with increased temperature and concentration of KOH, there was an increase in mass loss. The reaction of the base with the biochar leads to increased porosity, therefore we can theorize that the increased wt % lost correlates with an increase in porosity/ surface area. The MB adsorption capacity was found for each of the activation treatments. As shown in **Figure 5.13** and **Table 5.2**, the highest adsorption capacity, 0.0475 mg/mg, was obtained by the 10% KOH O_2 plasma treatment at 300 °C for 5 minutes, supporting the theory that increasing temperature and KOH concentration lead to more surface area. There is a risk of over etching the biochar and causing the internal pore structure to collapse. To combat this, we investigated increasing the plasma treatment time using a lower concentration KOH sample. Increasing the treatment time from 5 to 10 minutes saw an increase in adsorption capacity, although it still was not as high as the 10% KOH sample.

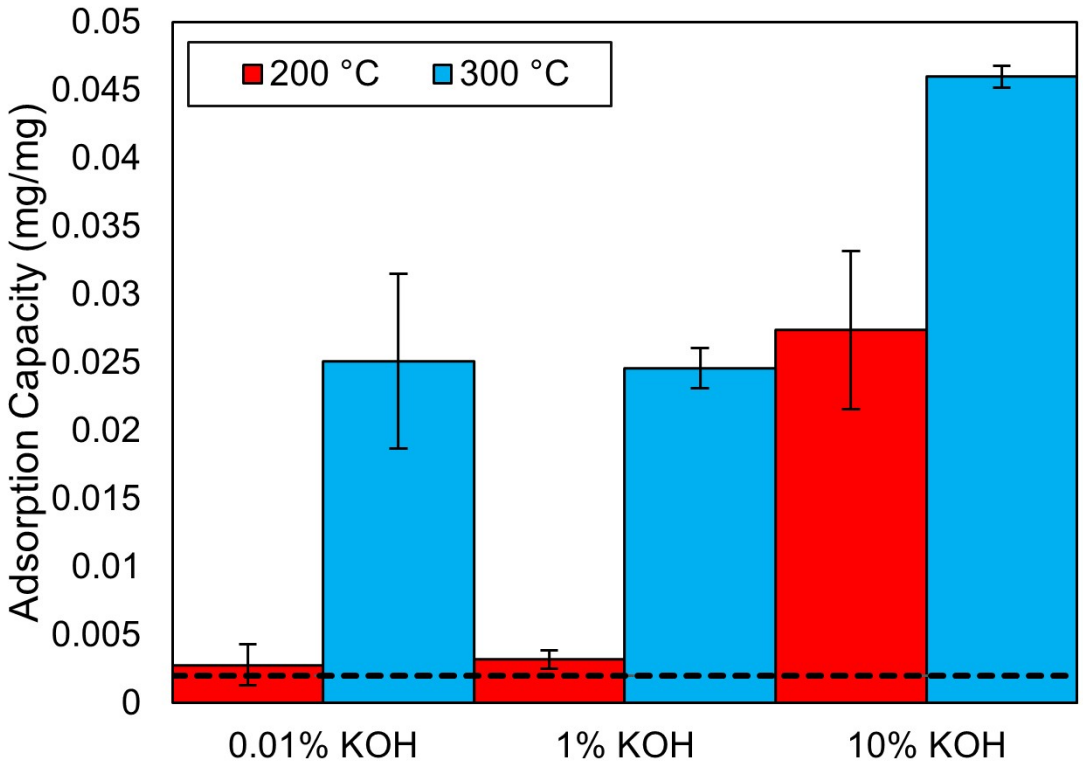

Figure 5.13 Average adsorption capacity of oxygen plasma treated biochar samples for 5 minutes. Dashed line represents the adsorption capacity of the untreated biochar (n=3).

Table 5.2 Calculated average adsorption capacities for oxygen + KOH activated biochar samples (n=3).

Biochar sample	Adsorption capacity (mg/mg)
Untreated	0.0020 ± 0.0008
0.01% KOH + O_2 at 200 °C for 5 min	0.0028 ± 0.0015
0.01% KOH + O_2 at 200 °C for 5 min	0.0251 ± 0.0064
1% KOH + O_2 at 200 °C for 5 min	0.0032 ± 0.0007
1% KOH + O_2 at 300 °C for 5 min	0.0246 ± 0.0015
1% KOH + O_2 at 300 °C for 10 min	0.0311 ± 0.0012
10% KOH + O_2 at 200 °C for 5 min	0.0274 ± 0.0058
10% KOH + O_2 at 300 °C for 5 min	0.0460 ± 0.0080

UV-vis was performed for samples using unreactive Ar plasma to determine whether the reactivity of the O_2 plasma was essential for activation. The spectra in **Figure 5.14** shows that treatment of 10% KOH soaked biochar with Ar-plasma at 300 °C for an hour did not improve adsorption to the extent that O_2 plasma did. Thus, the reactivity in O_2 plasma plays a larger role in activation besides etching.

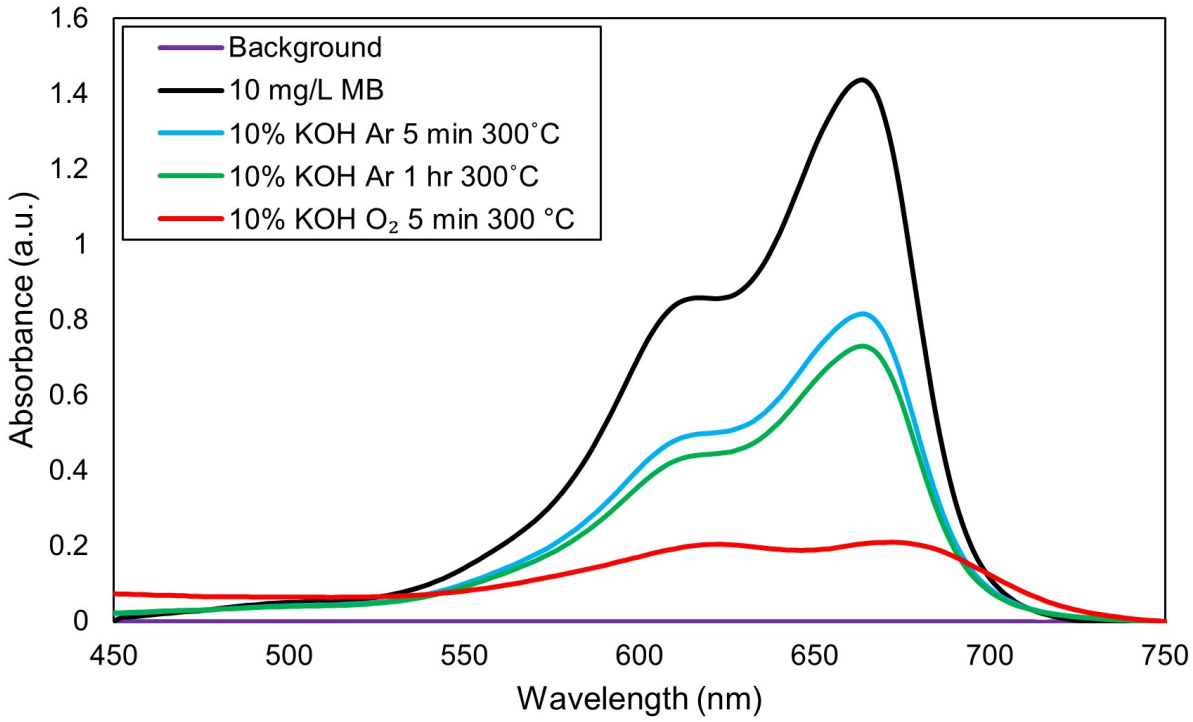

Figure 5.14 UV-vis spectra of biochar treated with argon plasma vs oxygen plasma.

Overall, biochar activation by O_2 plasma treatment combined with 10% KOH at 300 °C yielded the maximum adsorption capacity of MB at 0.460 ± 0.008 mg/mg. Other calculated average adsorption capacities are given in **Table 5.3**.

Table 5.3 Average adsorption capacity values for plasma activated biochar (n=3). (∗) denotes single trials.

Biochar sample	Adsorption capacity (mg/mg)
Untreated	0.0020 ± 0.0008
O_2	0.0030 ± 0.0019
300 °C	0.0133 ± 0.0014
0.01% KOH + O_2 at 200 °C for 5 min	0.0028 ± 0.0015
0.01% KOH + O_2 at 200 °C for 5 min	0.0251 ± 0.0064
1% KOH + O_2 at 200 °C for 5 min	0.0032 ± 0.0007
1% KOH + O_2 at 300 °C for 5 min	0.0246 ± 0.0015
1% KOH + O_2 at 300 °C for 10 min	0.0311 ± 0.0012
10% KOH + O_2 at 200 °C for 5 min	0.0274 ± 0.0058
10% KOH + O_2 at 260 °C for 5 min	0.0408 ∗
10% KOH + O_2 at 300 °C for 5 min	0.0460 ± 0.0080
30% KOH + O_2 at 300 °C for 5 min	0.0432 ± 0.0014
50% KOH + O_2 at 200 °C for 5 min	0.0322 ± 0.0030
50% KOH + O_2 at 300 °C for 5 min	0.0349 ± 0.0013

5.6.3 Adsorption Kinetics

Adsorption of dyes on biochar may include chemical adsorption. To investigate the adsorption mechanism, the adsorption kinetics of MB onto biochar that was not plasma treated was analyzed by using pseudo-first and pseudo-second order kinetic models. The pseudo-first-order

equation can be written in the form:

$$\log(q_e - q_t) = \log(q_e) - \frac{k_1}{2.303}t \tag{5.3}$$

where q_e represents the amount of adsorption (mg/g) at equilibrium, k_1 is the rate constant of the pseudo-first-order equation, and qt is the amount of adsorption (mg/g) at t, time (min) [115]. The rate constant, k_1, can be calculated by plotting $\log(q_e - q_t)$ versus t (**Figure 5.15**) [115].

The pseudo-second-order kinetic equation is shown below:

$$\frac{t}{q_t} = \frac{1}{k_2 q_e^2} + \frac{1}{q_e}t \tag{5.4}$$

where k_2 is the pseudo-second-order rate constant. Plotting t/q_t versus t, a line of best fit can be found (**Figure 5.16**). This straight line can then be used to calculate k_2 [115]. All the calculated kinetic values are shown in **Table 5.4**. The R^2 value for the pseud-second-order model was 0.99, where the R^2 value for the pseudo-first-order model was only 0.96. Therefore, the adsorption kinetics are adequately described by the pseudo-second-order model. Similar results have been found for the adsorption of MB onto rejected tea leaves, AC, and different carbonaceous materials [22, 115, 153].

The pseudo-second order model fit the kinetics data of MB adsorption onto biochar. This suggests that chemisorption has a dominant role in the adsorption process [144, 153].

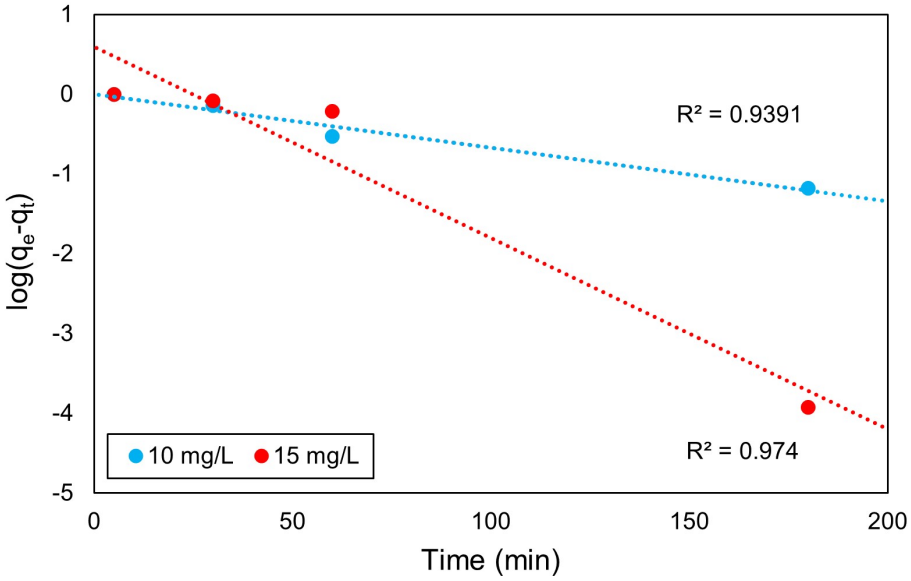

Figure 5.15 Pseudo-first order kinetic model for biochar (n=3).

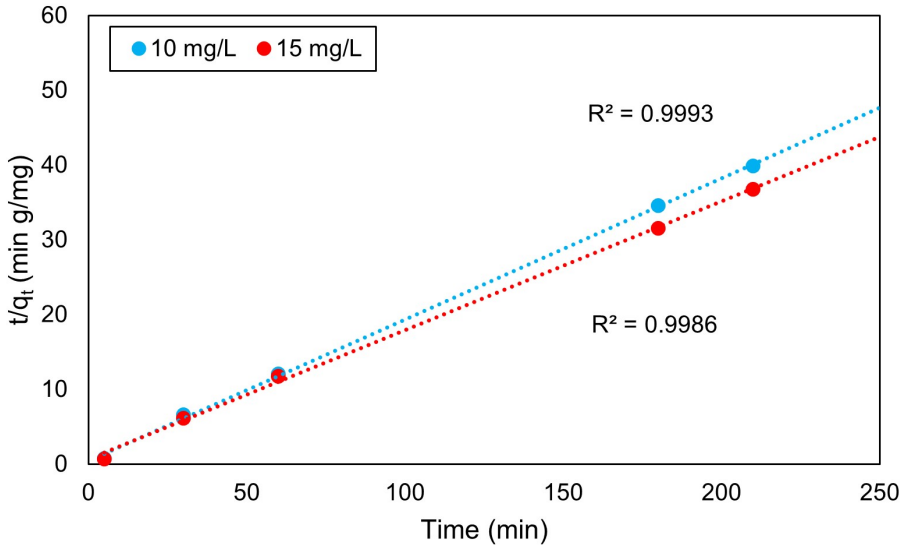

Figure 5.16 Pseudo-second order kinetic model for biochar (n=3).

Table 5.4 Calculated adsorption kinetics values (n=3).

	Initial concentrations (mg/L)			
	10.73		15.89	
Soak time (min)	**Biochar adsorption capacity (mg/g)**			
5	6.567	± 0.155	7.215	± 0.262
30	4.548	± 0.078	4.887	± 0.222
60	4.973	± 0.314	5.095	± 0.208
180	5.202	± 0.348	5.711	± 0.496
210	5.268	± 0.321	5.711	± 0.351
Kinetic models and its parameters				
Initial concentrations (mg/L)		10.73	15.89	
$q_{e,exp}$ (mg/g)		5.268	5.711	
Pseudo-first-order kinetic				
$q_{e,cal}$ (mg/g)		0.9251	6.8818	
k_1 (1/min)		0.0150	0.0516	
R^2		0.9647	0.9839	
Pseudo-second-order kinetic				
$q_{e,cal}$ (mg/g)		5.294	5.797	
k_2 (g/mg min)		0.9517	0.6388	
h (mg/g min)		2.190	1.538	
R^2		0.9993	0.9986	

5.6.4 Adsorption Isotherm

The relationship between the initial concentration of MB and the adsorbed amount of MB onto biochar are investigated. The graphs show that the adsorption of MB increases with the increase of the equilibrium concentration of MB.

The two isotherms tested for their ability to describe the experimental results were the Langmuir and Freundlich adsorption isotherms [109, 148]. These models provide insight into the mechanism of adsorption and the surface properties [109, 148].

The Langmuir isotherm is based on the assumption of monolayer adsorption onto a homogeneous surface with a uniform distribution of adsorption [109, 115, 148]. The Langmuir isotherm is expressed by the following equation:

$$\frac{C_e}{q_e} = \frac{1}{q_{max}b} + \frac{1}{q_{max}}C_e \tag{5.5}$$

where C_e is the equilibrium concentration (mg/L), q_e is the adsorption capacity at equilibrium (mg/g), b is the Langmuir constant (L/g), q_{max} is the maximum adsorption capacity (mg/g). A linear plot of C_e/q_e versus C_e confirms the legitimacy of the Langmuir model. The adsorption isotherm data was collected and the average concentrations and adsorption capacity were graphed, as shown in **Figure 5.17**. The values for this data can be found in the appendix.

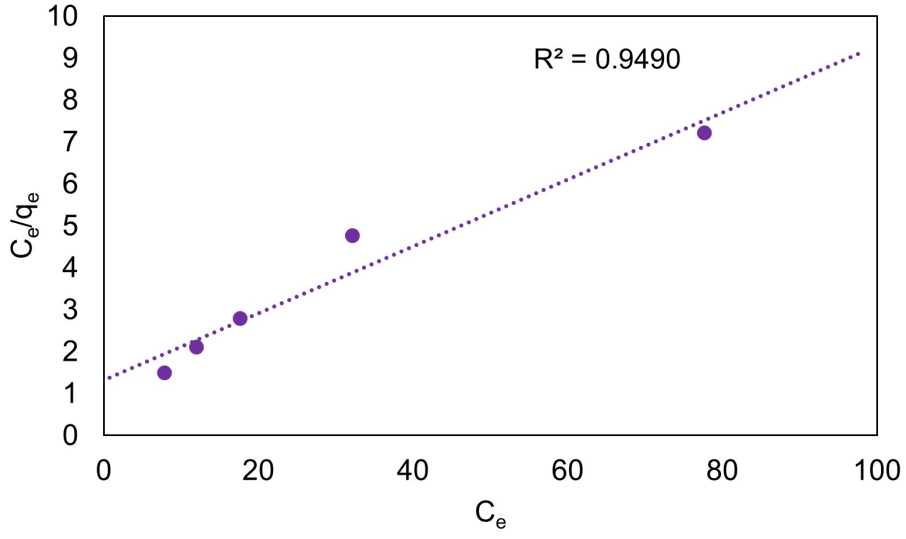

Figure 5.17 Langmuir isotherm model (n=3).

The Freundlich isotherm is related to adsorption capacity and intensity [115]. The Freundlich isotherm assumes a heterogeneous surface with a non-uniform distribution of adsorption, and probably indicates multilayer adsorption [109, 115]. Mathematically it is characterized by the heterogeneity factor '$1/n$', which is related to the adsorption intensity [109]. It is expressed by the following equation:

$$q_e = K_f C_e^{1/n}$$
$$\ln q_e = \ln K_f + \frac{1}{n} \ln C_e \tag{5.6}$$

where C_e is the equilibrium concentration (mg/L), q_e is the adsorption capacity at equilibrium (mg/g), K_f is the Freundlich constant (L/mg), $1/n$ is the heterogeneity of the sorption sites and an indicator of isotherm nonlinearity [153]. A plot of $\ln q_e$ versus $\ln C_e$, gives a straight line with K_f and $1/n$ determined from the intercept and the slope, respectively [109, 115, 153]. The adsorption isotherm data was collected and the average concentrations and adsorption capacity were graphed, as shown in **Figure 5.18**. The values for this data can be found in the appendix.

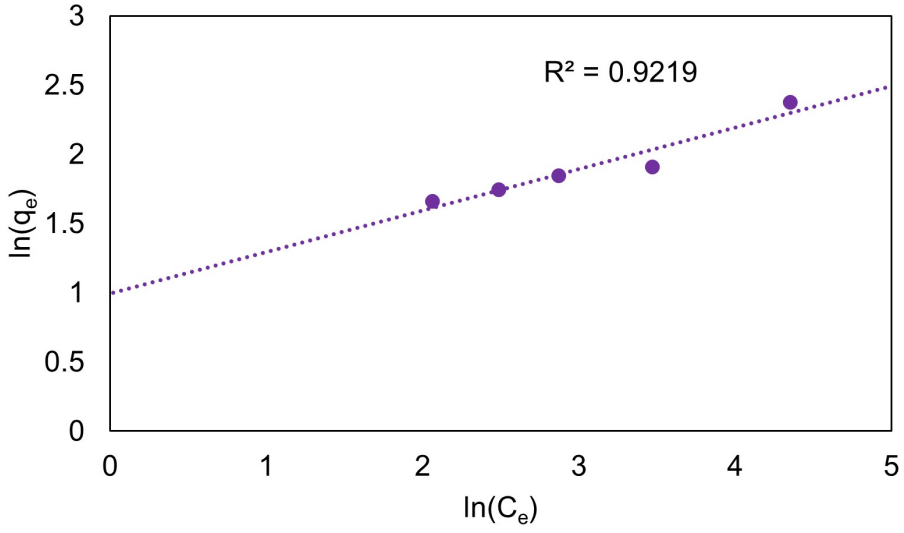

Figure 5.18 Freundlich isotherm model (n=3).

The data was fit to the Langmuir and Freundlich isotherm adsorption models. The data

fitting gave the regression coefficients of the Langmuir (R^2 >0.949) and the Freundlich (R^2> 0.9219) models indicating that the models described the adsorption process adequately. The essential characteristics of Langmuir isotherm are expressed thought the dimensionless equilibrium parameter R_L, indicates the type of isotherm model to be favorable (0<R_L<1), unfavorable (R_L>1), linear (R_L=1), or irreversible (R_L=0) [153]. The R_L values were calculated for all concentrations used and are shown in **Table 5.5**. The calculated parameters for the Freundlich isotherm model can be found in the appendix. All R_L values are between 0 and 1, indicating favorable adsorption. This indicates that the adsorption of MB onto biochar occurred primarily by chemisorption [153].

Table 5.5 Calculated values for the different intial concentrations (n=3).

Langmuir					
Slope	**Q_{max}**	**Intercept**	**b**	**C_O**	**R_L**
0.0798	12.53	1.321	0.0604	10.73	0.6068
				15.89	0.5102
				21.56	0.4343
				36.46	0.3123
				83.53	0.1654

5.7 Conclusion

We have shown the feasibility of a low temperature activation of biochar using O_2 plasma. The reactivity of O_2 plasma seems to play a larger role in activation than its etching ability. The kinetic data was well fit to pseudo-second order kinetics. The 10% KOH + O_2 plasma activation at 300 °C yielded the highest adsorption capacity of MB, 0.460 ± 0.008 mg/mg.

CHAPTER 6

ADSORPTION OF PFAS ONTO PLASMA ENHANCED BIOCHAR AND AC

6.1 Introduction to PFAS

6.1.1 Definition of PFAS

Per- and poly-fluoroalkyl substances (PFAS) are a family of chemicals which are hydrophobic, chemically stable, and resistant to biodegradation, oxidation, and hydrolysis [36, 38–40, 214–219]. PFAS are a subset of fluorinated substances that contain one or more C atoms on which F atoms have replaced all the H substituents (**Figure 6.1**) [38]. They contain the perfluoroalkyl moiety C_nF_{2n+1-} [36, 38, 216, 220]. The carbon chain is hydrophobic and lipophobic along with having strong C−F bonds. The carbon chain also has a carboxylic acid or sulfonic acid functional group which is hydrophilic [40, 219].

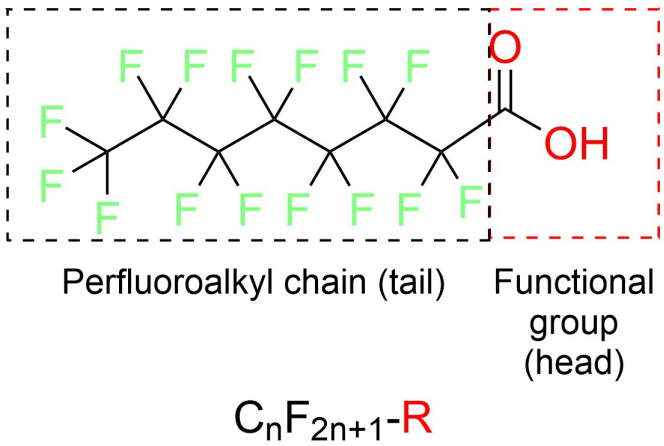

Figure 6.1 General structure of PFAS with a perfluoroalkyl chain tail and functional group head.

These characteristics make PFAS attractive for things like surface coatings on cookware, stain repellant carpet and fabric treatments, food contact paper, and fire-fighting foam [35, 38, 40,

214–217, 219, 221, 222]. The extensive use of PFAS has led to environmental contamination.

The PFAS family of chemicals have been produced since the late 1940s with more than 4000 known PFASs currently on the global market [215, 218]. They can be classified into two main categories: polymers and non-polymers [216, 220]. Polymers and non-polymers can be further divided into subclasses, groups, and subgroups as show in **Figure 6.2**. Non-polymer PFAS are the most commonly detected in the environment and in humans. They are divided into two major subclasses: perfluoroalkyl substances and polyfluoroalkyl substances. Perfluoroalkyl substances are made up of a perfluoroalkyl chain, meaning fluorine atoms replaced all their hydrogen atoms (perfluoro-) [36, 38–40, 214]. Conversely, polyfluoroalkyl substances have partially saturated alkyl chains, where fluorine has replaced all the H atoms attached to at least one, but not all, C atoms [38, 216].

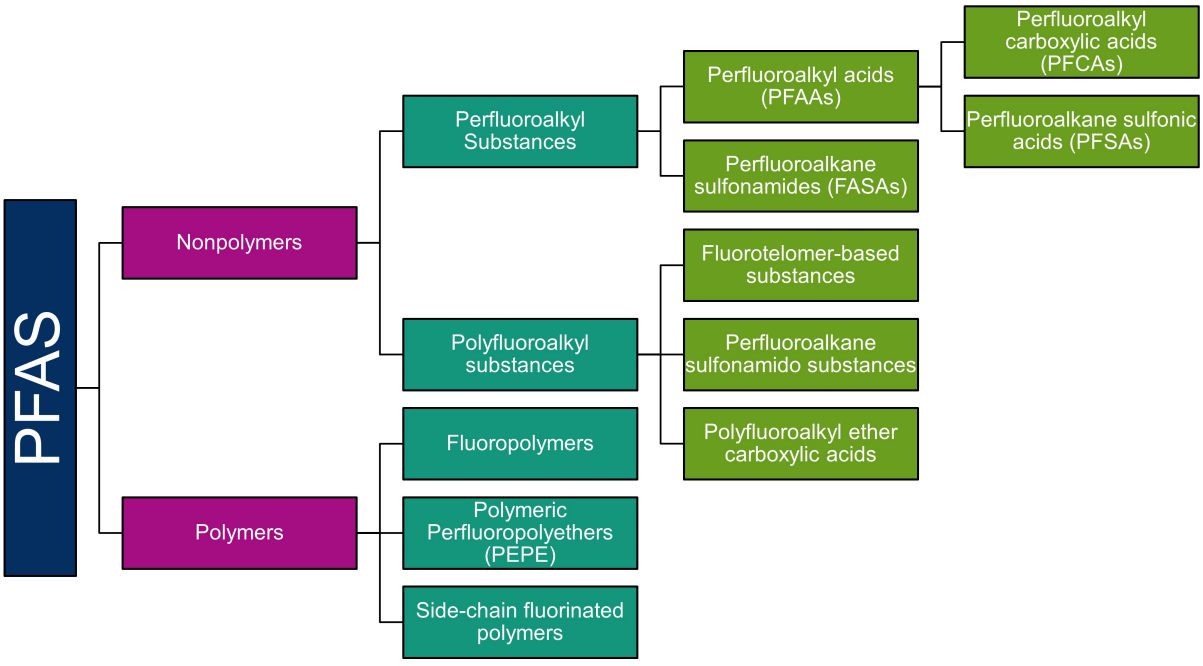

Figure 6.2 Summary of the PFAS family.

Within the subclass of perfluoroalkyl substances, the group perfluoroalkyl acids (PFAAs) are some of the least complex but most tested for PFAS molecules [216]. PFAAs are formed

as a result of biotic and abiotic degradation of many polyfluoroalkyl substances. Thus, PFAAs are sometimes referred to as "terminal PFAS" because they are non-degradable under normal environmental conditions [215, 216].

Two major subgroups of PFAAs are perfluoroalkyl carboxylic acids (PFCAs) and perfluoroalkane sulfonic acids (PFSAs), both of which are terminal degradation products of other polyfluoroalkyl. PFCAs can be generated through the transformation of fluorotelomer alcohols (FTOH). Similarly, PFSAs are terminal degradation products of perfluoroalkyl sulfonamido ethanols (PFSOEs) [38, 216]. Common examples of these subgroups are Perfluorooctanoic acid (PFOA) and perfluorooctane sulfonate (PFOS). PFCAs and PFSAs (especially PFOA and PFOS) are the most commonly tested for in the environment [216, 217].

PFAAS can also be described as either 'long-chain' or 'short-chain'. These delegations help to categorize PFCAs and PFSAs that may behave similarly in the environment, although other factors may affect bioaccumulation potential as well [216]. Long-chain PFAAs refer to PFCAS with 8 or more carbons and PFSAs with 6 or more. PFCAs with seven or less carbon and PFSAs with five or less carbons are called 'short-chain' [216, 220].

6.1.2 Physical and Chemical Properties of PFAS

The perfluoroalkyl moiety of PFAS (C_nF_{2n+1}) grants exceptional chemical and thermal stability [38, 39, 214]. This is due to the C−F bonds, which are considered the strongest chemical bond in organic chemistry. The C−F bonds possess a strong bonding energy up to 536 kJ/mol, which results in PFAS having a reported half-life of > 92 years [223, 224]. Their strong C−F bonds give them a high dissociation energy and make them extremely difficult to destroy and remove [39, 214]. The F-atoms are highly electronegative making the C−F bond polarized. High coulombic attraction

due to the charge separation between C and F creates a bond that is extremely short and strong. Additionally, the high electronegativity of F gives the bond a significant dipole moment where the electron density is concentrated around the fluorine. This along with the mall size of the F atom shields the carbon and enhances the chemical stability of the molecule. The low polarizability gives the molecule hydrophobic and lipophobic properties because less susceptible to the electric fields of other molecules. The partial charges of the C and F are attractive further enhancing the bond strength [216]. The culmination of the unique properties of fluorine provides the perfluoroalkyl moiety of PFAS (C_nF_{2n+1}) with enhanced properties such as: stain resistance (hydrophobic and lipophobic), strong acidity, chemical and thermal stability, and very low reactivity) [218, 225].

PFAS are often used as surfactants. Surfactants effectively lower surface tension of a liquid, the interfacial tension between two liquids, or between a liquid and a solid even at low concentrations [38, 40]. The efficiency of surfactants is related to selective adsorption of the surfactant at the interface which is a result of the amphiphilic nature of the surfactant [40]. Amphiphilic or amphipathic refers to the surfactant structure consisting of both a "solvent-soluble" lyophilic portion and a "solvent-insoluble" lyophobic part [40]. Conventional surfactants consist of a water-soluble hydrophilic part and a water-insoluble hydrophobic and lipophilic part [38, 40]. The hydrophobic part in PFAS contains fluorine which changes the properties of the surfactant resulting in the hydrophobic part repelling water as well as oil and fat [38, 40]. This water and oil repellency has been applied to exterior surface coatings. For example, when applied as a coating to the exterior of a textile, the perfluorinated tail of the molecule is projecting away from the surface, which then repels water and oil [226]. PFAS surfactants have superior aqueous surface tension, therefore, they excel as emulsifiers, dispersants, and foaming agents [38, 40]. The extent of fluorination and location of the F atoms affect the surface properties.

PFAS functional groups, such as carboxylates, sulfonates, sulfates, phosphates, and amines, control the transport properties of PFAS. Environmental transport is determined by ionic state of the molecule, which in turn determines its charge and physiochemical properties. The ionic state of environmental PFAS can alter its bioaccumulation potential [216]. Under appropriate pH conditions, functional groups of certain PFAS can dissociate into cations and anions in aqueous environments [216]. For example, PFOA has a low acid dissociation constant and dissociates into a perfluorooctanoate anion and hydrogen ion in water over a broad range of pH. PFAS can form cations, anions, or zwitterions. Therefore, PFAS may also be classified based on their functional groups [216, 227].

The polarity of PFAS can be exploited by creating electropositive functional groups on the biochar surface to promote electrostatic interaction between the biochar and PFAS. Many methods have been employed to remove them, the most utilized being activated carbon.

6.1.3 Synthesis of PFAS

PFAS is produced through two main manufacturing processes: electrochemical fluorination and telomerization [38].

During electrochemical fluorination, all the H atoms are replaced by F as a result of electrolysis of an organic precursor material in anhydrous HF [38]. A mixture of linear and branched perfluorinated isomers are produced, along with homologues of the starting material [228]. Typically, carbons in linear isomers are bonded to only 1 or 2 more C atoms, whereas carbons in branched isomers are bonded to many more [38, 226]. PFOA and PFOS are synthesized with a ratio of 7:3 or 8:2 linear to branched perfluorinated C chains, respectively [38].

The telomerization process creates perfluoroalkyl iodides with longer chains, called telom-

ere A. This happens through a reaction of perfluoroalkyl iodides and telofluoroethylene. Telomere A is further reacted with ethylene to produce telomere B, and both are used to produce fluorotelomer-based products. Telomerization primarily produces linear PFAS and materials for the manufacturing of surfactants, food contact packaging, and textile treatments [226].

6.1.4 Products and Uses

PFAS have been produced and used in a broad range of consumer products and applications since the 1940s [215, 218, 220, 223, 225, 226]. Currently, more than 4700 compounds have been classified as PFAS that are distributed on the global market [215, 218, 220, 223]. The remarkable characteristics of PFAS, due to its C−F bonds, have enabled a wide variety of uses in manufactured products designed to resist heat, stains, grease, water and friction [223, 229]. Some applications of PFAS include food packaging (heat and grease resistance), stain resistant fabrics, waterproof clothing, non-stick cookware, and fire-fighting foam [38, 40, 220, 223, 225, 226, 229].

6.1.5 Effects of PFAS in the Human Body

Paustenbach et al. 2007, conducted a retrospective exposure assessment for a population of ~50,000 people who resided near a facility where PFOA was used [230]. They used historical records of the facility emissions from 1951-2003 as the basis for the estimates of potential PFOA intake. The study estimated 1.7 million pounds of PFOA were released during this time. They analyzed numerous environmental concentrations and found that the primary exposure pathway was through drinking water [230]. The high mobility of PFAS and its disposal leads to the transport and proliferation through the environment, including, landfill leachate, surface water, groundwater, soil,

fresh water, marine water, and dust particle [224, 230]. Its widespread presence and persistence allows for the bioaccumulation of PFAS within organisms and humans [224].

Studies by Giesy and Kannan and Hansen et al. (2001) revealed the presence of PFOS and other PFAS species in human blood samples purchased from biological supply companies [38, 231, 232]. This study suggested that PFAS were responsible for a significant portion of the organic F detected in human serum in previous studies of people not occupationally exposed to PFAS [38, 231].

Extensive use and persistence of PFAS has led to accumulation in the environment. Evidence linked chronic exposure of PFAS in rats multiple health effects such as neurotoxicity, immunotoxicity, liver, pancreatic, and testicular tumors [224, 226, 233]. However, data is limited on the effects for acute toxicity in humans.

The concentrations of PFAS in wastewater treatment plants varies by compound. Phong Vo et al. 2020, conducted a comprehensive review of which PFAS compounds appear in highest concentration in wastewater treatment plants in various countries [223]. **Figure 6.3** depicts the influent and effluent concentrations (ng/L) found in these wastewater treatment plants. The PFAS concentrations range from 0.02 to 106 ng/L [223]. The concentration of short chain PFAS was at least 50-fold larger than that of long chain PFAS in all instances. wastewater treatment plants receive influent streams from landfill leachate that is discharged to sewer infrastructure [234]. Some PFAS, such as PFOA and PFOS, may be resistant to wastewater treatment. Precursor compounds can transform during biological treatment resulting in effluent concentrations exceeding influent levels [234]. Long-chain PFAS can break down and degrade into short-chain PFAAs (C4-C7). These short-chain PFAS are predominant in leachates because they are highly soluble and mobile in water and soil [224, 234, 235]. They are also extremely persistent due to being final degradation

products. This high mobility results in a fast distribution to water sources, and ultimately drinking water [235]. A deficit in appropriate water treatment technologies for short-chain PFAS results in a constant background concentration in the environment and exposure [235].

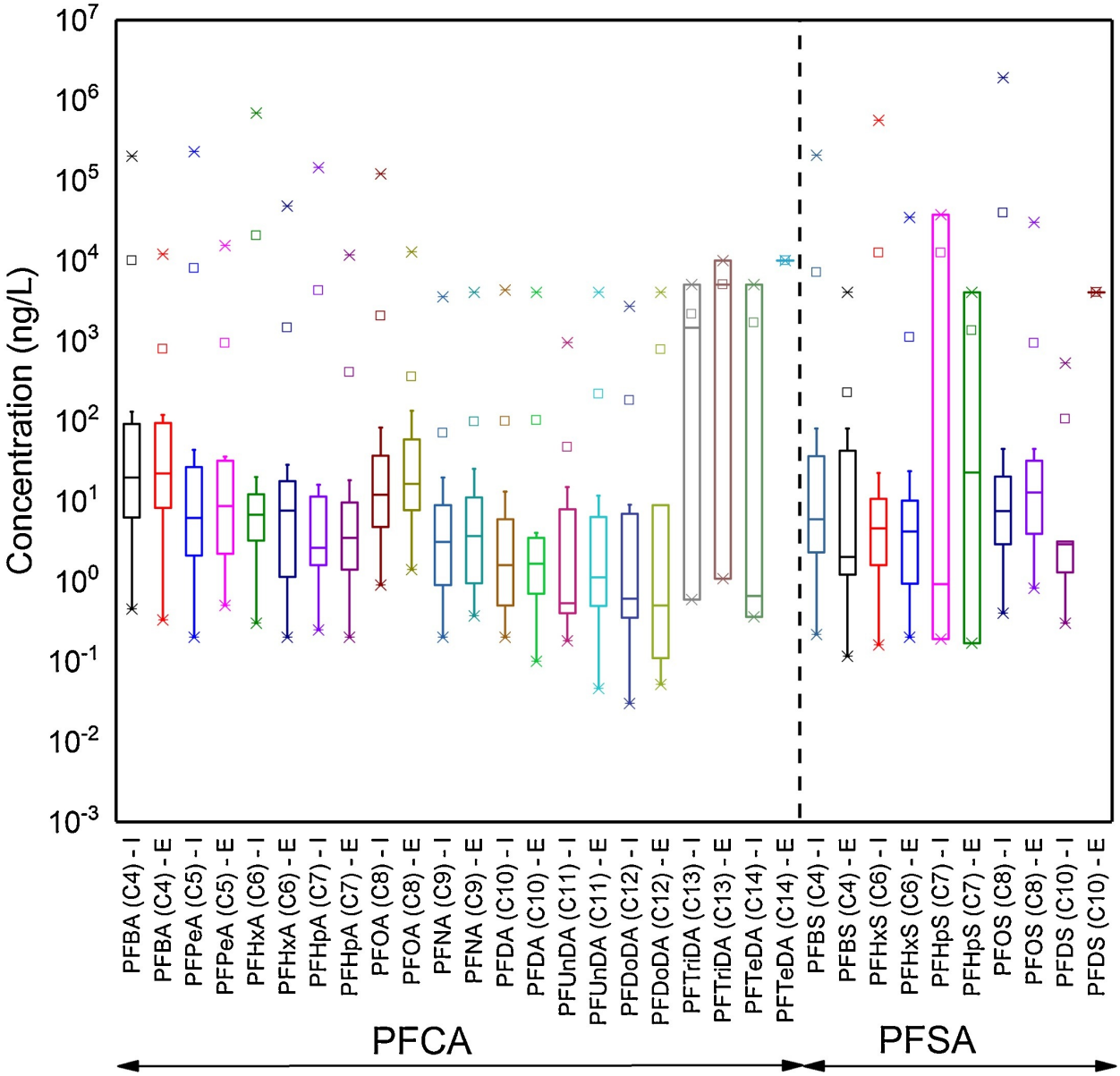

Figure 6.3 The Influent and effluent concentrations (ng/L) of selected PFAS compounds in wastewater treatment plants [223]. © Copyright 2020 Elsevier.

There are two species of PFAS that are most investigated: PFOA (perfluorooctanoic acid) and PFOS (perfluorooctanesulfonic acid) (**Figure 6.4**) [236]. These species are found in human

milk and dust, leading to direct exposure of newborns and toddlers [233]. Johansson et al. had previously reported that PFOA and PFOS can cause neuro-behavioral defects and changes in the cholinergic system of adult mice [233]. When PFOA and PFOS were directly given to neonatal mice, they found that a single oral dose of 21 μmol PFOA or PFOS/kg body weight significantly increased the level of important proteins for normal brain development which could be a mechanism of behavioral defects [233].

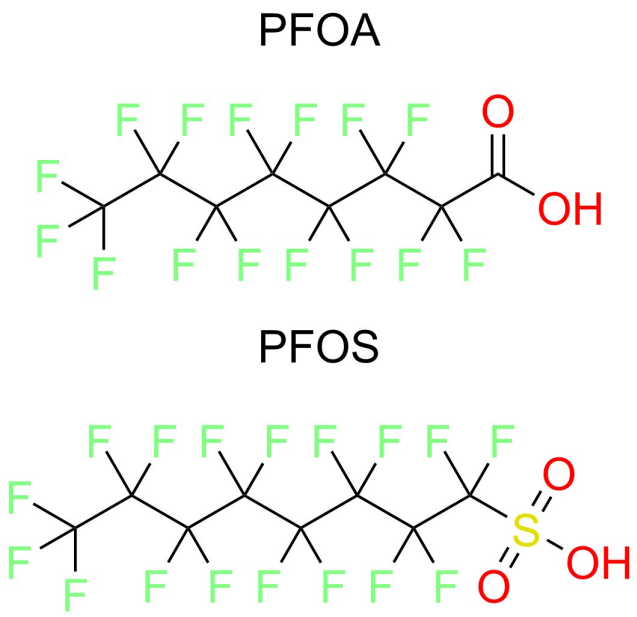

Figure 6.4 Chemical structure of PFOA and PFOS.

Dietary intake is theorized to be the main route of exposure to PFOA and PFOS [236]. In humans, they do not usually accumulate in lipids, but in blood [236]. Concentrations of several PFAS in human blood have been measured from multiple countries [236]. It is unknown whether the route of exposure to these compounds plays an important part in their toxicity [236]. Recent studies have shown that the indoor environment (dust, coated food contact materials, impregnation sprays, and carpet treatments) along with the intake of contaminated foods and drinking water, may be an important contributor to chronic human exposure [236].

The existence of PFAS, like PFOA and PFOS, in the environment stems from the industrial and commercial use and disposal of these substances and products that contain them [38, 237, 238].

6.1.6 PFAS Regulations

Lilienthal et al. looked into the detection of PFAS in drinking water and the regulations implemented in various countries [219]. PFOA and PFOS were focused on due to their wide-spread past use. Numerous institutions revised regulations or decreased the maximum recommended maximum concentrations in drinking water and food [219]. The U.S. Environmental Protection Agency (EPA) issued a water health advisory for PFOA and PFOS [239]. Health advisories are not regulated or enforced. Instead, they provide technical information to state governments and public health officials so that they may be informed about the health effects, current treatments, and analysis methods [239]. The EPA instituted a health advisory level of PFOA and PFOS at 70 parts per trillion in drinking water [239].

Perfluoroalkyl acids (PFAA), such as perfluoroalkyl carboxylic and sulfonic acids, are another species of PFAS that have been increasingly detected in U.S. drinking water [240]. In the environment PFAA are biologically stable and exist primarily as anions [240]. A study by Inyang and Dickenson looked at the use of carbon adsorbents to remove PFAA from potable reuse systems [240]. They used granular activated carbon in their study. They found that PFAA removal was influenced by the alkyl chain length, functional groups, and solution chemistry [240]. The adsorption of PFOS on activated carbon was found to increase with increasing alkyl chain length, with a removal of 182 mg g^{-1} [240].

Although, PFAS have been produced since the 1940s, they did not garner large scale attention until the early 2000s [226]. Previously, companies had conducted evaluations of potential

health effects, but there were in the form of internal reports and not published [226]. The possible risks PFAS continued to be broadly unrecognized until research efforts documented two groups of long-chain PFASs to be present worldwide in the environment and in human blood serum [226, 235, 241].

The 3M Company was a major producer of PFAS starting in 1949, with a total production estimated at approximately 96,000 metric tons of PFAS between the years 1907 and 2002 [226]. The EPA worked with 3M to voluntarily phased out the production and use of PFOS and related compounds between 2000 and 2002 [226, 229]. However, to meet market demands, other companies began producing an estimated 1000 metric tons per year starting in 2002 [226, 229]. The U.S. began to restrict the production and use of PFAS. In 2006, the EPA worked with 8 major chemical companies in the U.S. that joined the 2010/2015 PFOA Stewardship Program to reduce emissions and stop production of long-chain PFAAs by 2015 [226, 229].

PFOS, its derivatives, and perfluorooctane sulfonyl fluoride (PFOSF) were added to Annex B of the Stockholm Convention on Persistent Organic Chemicals in 2009, which restricts production and use to a few particular applications [224, 226]. Consequently, multiple PFAS are being evaluated for listing and both PFOS and PFOA are banned or being phased out in many countries [224, 226]. Concerns about PFAS toxicity have led to strict regulation, however, a lack of detailed information and understanding of their environmental impact have resulted in differing guidelines between countries [224].

In 2016, the U.S. Environmental Protection Agency established a health advisory level of 0.07 μg/L for the combined concentration of PFOS and PFOA in drinking water [239, 242, 243]. Many states have set drinking water standards for PFOS, PFOA, or both, but the uncertainty in the understanding of health protective levels has led to a wide range of variability in state standards

that can be greater or less than the EPA advisory level [229].

6.1.7 Adsorption by AC

Adsorption using anion exchange resins and AC has been a key technologies for PFAS remediation [223]. The mechanisms for PFAS adsorption are complex and co-contaminants such as anions and organics compromise the performance of these adsorbents. Consequently, strategies have been developed to modify adsorbents to increase PFAS adsorption capacity based on the affinity and porosity of adsorbent [223].

Adsorption on AC is the most commonly applied treatment for PFOA and PFOS removal from water [244]. However, variations in performance among AC types highlights the need for a better understanding of structure-property correlations in order to modify AC for selective PFAS adsorption [244].

Adsorbents adsorb PFAS via hydrophobicity, ligand exchange, electrostatic interaction, formation of hydrogen bond, and the nature of PFAS [223]. Electrostatic interaction and the hydrophobic effect are considered to be two main driving forces for adsorption of PFOA and PFOS on AC [223, 244]. PFOA and PFOA have low pKa values and thus, primarily exist as anions in environmentally relevant scenarios (pH of 5–8) [216, 244, 245]. As discussed in a previous section, PFOA dissociates into an anion and hydrogen ion in water [216]. With low pKa values, it is to be expected that they fully dissociate in water and the electrostatic interaction between the anionic head group and charged surface groups of AC influence their adsorption [244]. Hydrophobicity also plays a role in PFOA and PFOS adsorption, although it is more pronounced with the longer chained PFOS [244]. The surface chemistry of AC is crucial to determining the adsorption affinity of PFOA and PFOS [223, 244, 245].

PFAS adsorption also relies on the pore size distribution. The pore size range of 1-2 nm has been correlated with efficient PFAS adsorption. Conversely, pores smaller than 1 nm do not show such a correlation [223, 246].

Zhi and Liu, 2015, found that sorbent surface chemistry overwhelmed physical properties in controlling the extent of uptake [245]. Carbon surface basicity showed the strongest positive effect on affinity of PFOA and PFOS, suggesting high anion exchange capacity/anion exchange sites were important for PFOS and PFOA uptake [223, 245]. However, carbon polarity had an insignificant impact on adsorption [245].

PFAS is present in water and wastewater matrix together with various minerals, humic acid, and dissolved organic matter [223]. These other molecules interfere with PFAS adsorption by dominating the adsorption sites and create a negative charge on the adsorbent surface. **Figure 6.5** shows the mechanism of competitive adsorption of long-chain, short-chain PFAS, and organic matter. The negative charge initiates electrostatic repulsion with the anion head of PFAS and the adsorbent [223]. Organic matter may also attract the hydrophobic tail of long-chain PFAS. These hydrophobic interactions may enable long-chain PFAS adsorption due to the charged head being far enough away from the negatively charged surface [223, 247]. Due to stronger hydrophobic interactions, PFOA and PFOS have been shown to have higher sorption than short-chain PFAS [240, 247].

Short-chain and long-chain PFAS are adsorbed in different ways, due to their structure and hydrophobicity [223, 248]. Short-chain PFAS tend to be adsorbed less because they are more hydrophilic than long-chain PFAS [223, 247]. The steric hinderance of the sulfonate group in PFSAs compared to the carboxyl group in PFCAs results in slower and less adsorption [223, 249]. Increasing PFAS concentration may cause the long-chain PFAS to block the pores on the AC,

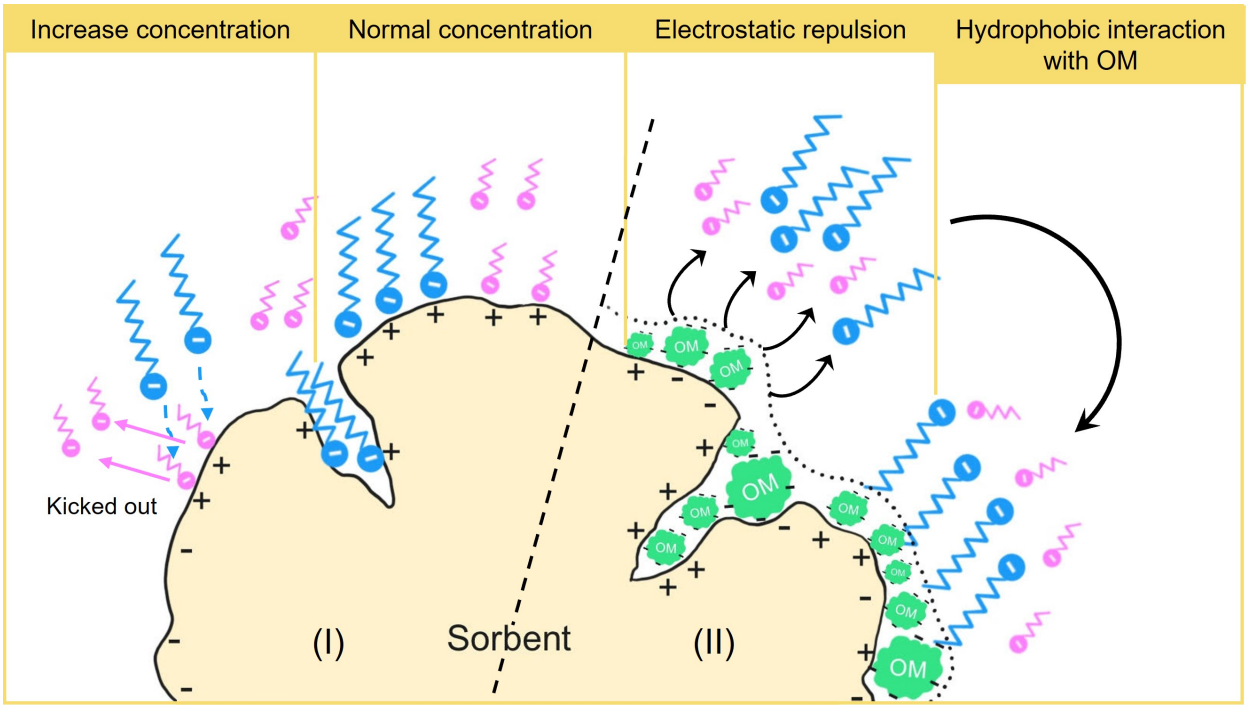

Figure 6.5 Mechanism of competitive adsorption of long chain, short chain PFAS and organic matter (OM) [223].

preventing adsorption and diffusion of other PFAS [223, 247, 248]. The long-chain PFAS can also desorb short-chain PFAS by replacing the adsorption site [223, 248, 249]. This desorption and their hydrophilic character results in the deteriorating removal efficiency of short-chain PFAS overtime [249]. AC has been shown to efficiently adsorb long-chain PFAS but are not selective for short-chain PFAS.

Yu et al. 2009, investigated the adsorption kinetics of PFOS and PFOA onto AC. They found that the sorption kinetics of PFOS and PFOA on granular activated carbon (GAC) in the initial stage followed an intraparticle diffusion-controlled adsorption, except the sorption of PFOA on the GAC at pH 3 [128]. Solution pH 3 is very close to the pKa of PFOA, therefore some PFOA may exist in the form of neutral molecules, but all PFOS molecules are still in anionic form because of its negative pKa (-3.27) [128]. This resulted in enhanced adsorption of PFOS at pH

3 due to increased protonated groups on the GAC [128]. The adsorption of PFOA was expected to decrease at pH 3 given that there was decreased anionic PFOA. However, there was actually increased PFOA adsorption from pH 7 to pH 3, indicating that hydrophobic interactions must play a role in the sorption at pH 3 [128]. Concurrently, hydrophobic neutral PFOA may adsorb on the adsorbent via hydrophobic interactions, while anionic PFOA is adsorbed through electrostatic interactions [128]. Comparing the adsorption of PFOS and PFOA on anion-exchange resin, GAC, and powdered activated carbon (PAC), it was found that PAC was the best for adsorption of PFOS. The adsorption of PFOA was high onto PAC compared to GAC. The sorption kinetics revealed that the sorption of PFOS and PFOA onto GAC and anion-exchange resin was extremely slow, with sorption equilibrium achieved after at least 168 h [128]. Conversely, the sorption equilibrium for PAC was only 4 h showing that adsorbent size affected the sorption velocity [128].

6.1.8 Adsorption by Biochar

One of the chemicals in this group is perfluorooctane sulfonate (PFOS). PFOS is a persistent organic pollutant used in metal plating processes and fire-fighting foam [250]. There is a need to develop an efficient and cost-effective way to not only remove PFOS from the water, but also to dispose of it. Guo et al. 2017 researched how the pyrolytic temperature affected the adsorption of PFOS on biochar. Results showed that a high temperature increased the surface area, fine-pore structures, and the aromaticity of the biochar [250].

Guo et al. studied the adsorption of PFOS in DI water by corn biochar that was pyrolyzed under different temperatures [250]. They found that the difference in adsorption of aromatic contaminants relied heavily on the structure and the functional groups of the biochar [250]. It was found in SEM images that as the pyrolysis temperature increased, the surface of the biochar

became smoother. The ash content also increased with temperature. It was seen that at 250 °C, −OH, aliphatic C−O, and ester C=O groups were removed from the surface of the biochar [250]. As the temperature increased, surface area increased because of the complete removal of aliphatic alkyl and ester C=O groups that were shielding the aromatic core [250]. At the highest temperature in the study, 700 °C, phenolic-OH linked to the aromatic cores were removed [250]. The results showed a large surface area at 297.58 m^2/g with the indication of fine pore structures [250]. The study determined that biochar had a higher capacity for PFOS adsorption as pyrolytic temperature increased, possibly due to more aromatic groups in the biochar [250]. The pseudo-second order adsorption model was again shown to describe the adsorption process on biochar. It was speculated that PFOS was adsorbed via hydrophobic interactions [250].

The paper also investigated the effects of pH on the adsorption. The pH of the PFOS solution was increased from 3.0 to 10, resulting in a decrease in the amount of PFOS adsorbed by biochar [250]. PFOS is negatively charged at a pH above 3.0, whereas the biochar was positively charged, suggesting a strong electrostatic interaction occurred between PFOS and the biochar which resulted in a high adsorption rate [250].

6.2 Materials and Methods

6.2.1 Plasma System and Process

Commercial activated carbon purchased from Oxbow Activated Carbon was used in this study. The chemically activated carbon was further treated through plasma generated by a capacitively coupled dielectric barrier discharge. A quartz tube connected to a mechanical pump was used as a vacuum chamber. A pair of copper electrodes were attached to the outside of the tube to generate plasma. One of the electrodes was connected to a radio frequency (RF) power generator

(Kurt J. Lesker, Radio Frequency Power Supply R301) while the other electrode was grounded. The operation frequency was set at 13.56 MHz. Before the plasma was generated, the quartz tube was pumped down to < 1×10^{-2} Torr and purged with the process gas to prevent cross-contamination.

6.2.2 Plasma Activation Process

For plasma activation of the biochar and AC, ~0.05 g of carbon powder was thinly spread ceramic plate. The ceramic plate was placed inside the tube between the two copper electrodes. The system was sealed and pumped down to low pressure. The tube was then filled with the process gas. The plasma pressure was kept constant for each treatment at 2 Torr (measured by a vacuum meter, Kurt J. Lesker). The RF power of the plasma was fixed at 75 W and adjusted to reach a zero-watt reflection power through all experiments. This process was repeated 5x for each test in order to reach a final mass of 0.250 g of treated AC. The plasma gas and treatment times were varied. The gases used were: 10% O_2–90% Ar mixture, H_2, N_2, and CH_4. The plasma treatment times for each gas were: 1 min, 2 min, 3 min, 4 min, 5 min, and 6 min.

6.2.3 PFOA Preparation and LC-MS/MS Measurement

Batch adsorption tests were performed at room temperature. The experiments were used to examine the effects of plasma treatment parameters on MB adsorption by AC. The experiments were conducted on samples of AC treated with different plasma gases (O_2, H_2, N_2, and CH_4) and treatment times (1, 2, 3, 4, 5, and 6 min).

Perfluorooctanoic acid (PFOA, > 97%) was purchased from Sigma Aldrich. A 2 ppb PFOA stock solution was prepared with HPLC water. A sample of the stock solution before the addition of biochar was taken as a control. Then 5 mg of biochar/AC was added to 20 mL of the PFOA solution

in a 50 mL polypropylene centrifuge tube. The sample was left to soak at room temperature for 20 minutes. After 20 minutes the sample was extracted. A labeled standard (13C8-PFOA) was then added to the final samples. The PFOA concentrations were determined using LC-MS/MS. The adsorbed amount of PFOA by the biochar was calculated as the difference between the initial and final PFOA solution concentrations.

The adsorption capacity, q_t (μg/mg), of biochar to adsorb PFOA was calculated using the following equation:

$$q_t = \frac{V(C_0 - C_t)}{w} \tag{6.1}$$

where C_0 (μg/L) is the liquid-phase initial concentration of PFOA, and C_t (μg/L) is the concentration of PFOA after treatment. The mass of dry biochar is represented by w (mg), and V (L) is the volume of PFOA solution.

6.2.4 LC-MS/MS

The concentration of PFOA was measured with liquid chromatography (Waters Acquity I-class Plus UPLC) coupled with a Waters TQ-XS mass spectrometer. The PFOA separation was performed on an Acquity UPLC BEH C18 (2.1 × 50 mm, 1.7 μm) column. 10 mM ammonium acetate in water (A) and acetonitrile (B) (A:B= 99:1) were used for the mobile phase. Negative ESI multiple reaction monitoring (MRM) mode was used by the TQ-XS mass spectrometer operated in negative ESI multiple reaction monitoring (MRM) mode. The parameters used for quantification of PFOA were precursor mass m/z of 413, daughter ion mass m/z of 369, dwell time of 163 ms, cone voltage of 20 V, and collision energy of 10 V. The gradient elution was: 0 min (A=99%, B=1%), then ramp to (A=1%, B= 99%) at 4 min, next ramp to (A=99%, B=1%) at 5 min and kept

until 7 min. An internal standard 13C8 PFOA was used for mass loss correction (precursor mass m/z of 421, daughter ion mass m/z of 376). The desolvation temperature, desolvation gas flow, and ion spray voltage were maintained at 400 °C, 800 L/h, and 1000 V, respectively. The cone gas flow was 150 L/h and the nebulizer gas flow was 7 psi.

For the quality assurance, isotope dilution analyte carbon-13 labeled analog was used for correction for analytical bias. C-13 PFOA was spiked into the samples at the time of extraction.

6.3 Results and Discussion

6.3.1 PFOA Adsorption on AC

We theorized that electropositive or neutral gas discharges would create an adsorbent surface more suitable to PFOA adsorption than electronegative O_2 plasma. This is because PFOA dissociates into an perfluorooctanoate anion and hydrogen ion in water [216, 244, 245]. Its pKa value has been reports as > 4, and thus will exist in aqueous solutions at neutral pH (7) almost entirely as the dissociated acid [216]. When the pH of a solution and the pKa are equal, half of the PFAS molecules will be dissociated, therefore, it is assumed for our experiment of PFOA in HPLC water with a pH 7 that PFOA will exist primarily in its anionic form [216, 244, 245]. It is important to note that pKa, unlike pH, is unaffected by concentration. Because anionic and undissociated PFOA differ in physical and chemical properties, it is essential to distinguish between forms and select an appropriate adsorbent [216].

Surface chemistry has been found to have a greater influence on adsorption of PFOS and PFOA compared to physical properties [245]. Adsorption of organic compounds by AC is controlled by physical and chemical interactions. Physical interactions include size exclusion and porosity, specifically microporosity effects [251]. Chemical interactions encompass the chemical nature

of the AC surface, adsorbate, and the solvent. Hydrophobic interactions are important for the compatibility between the adsorbate and solvent, as well as, adsorption by dispersive forces [251]. The adsorbate can specifically interact with the AC surface through functional groups and unpaired electrons. Surface chemistry has been found to have a greater influence on adsorption of PFOS and PFOA compared to physical properties [245, 251].

The effects on adsorption capacity of PFOA on AC with different plasma gases was investigated and compared. The adsorption capacities of the plasma treated samples increased the adsorption capacity with time in all samples but the oxygen sample. It should be noted that a base-line adsorption capacity for AC (R003) was not accurately deduced due to concentrations of PFOA increasing past stock solution concentrations.

Within the first two minutes of plasma treatment, adsorption capacity increased for all samples as shown in **Figure 6.6**. There was no significant difference between the samples. After 2 minutes of plasma treatment the upward trend continued for H_2, N_2, and CH_4 adsorption capacities, but significantly decreased for O_2 (see **Figure 6.7**). The calculated adsorption capacities are reported in the appendix. The best adsorption capacities for the H_2, N_2, and CH_4 plasma treated AC samples were after 4 minutes of treatment. The values are given in **Table 6.1**. Conversely, 4 minutes of treatment with O_2 plasma produced the worst adsorption capacity for that sample group. This may be due to new generation of oxygen functional groups on the surface leading to a more negative surface charge. Because PFOA is almost completely dissociated, the like charges of the perfluorooctanoate anion and the negative oxygen groups will repel each other, leading to decreased adsorption on the O_2 treated AC.

The maximum adsorption capacity was found for the H_2 treated AC as shown in Figure 6.7. Although no significant difference was seen between H_2, N_2, and CH_4. H_2 is a strong reducing

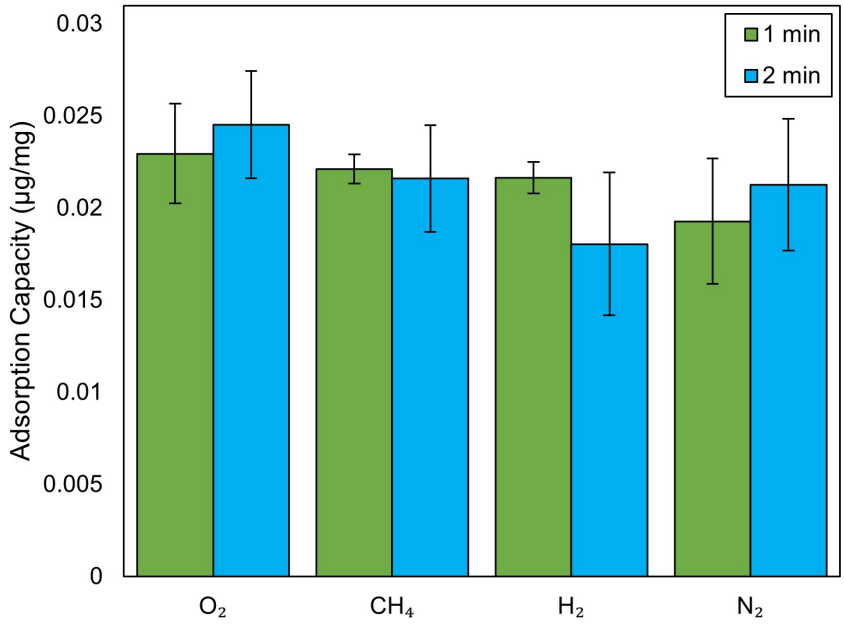

Figure 6.6 Average adsorption capacity for PFOA onto plasma treated AC at 1 and 2 minutes (n=3).

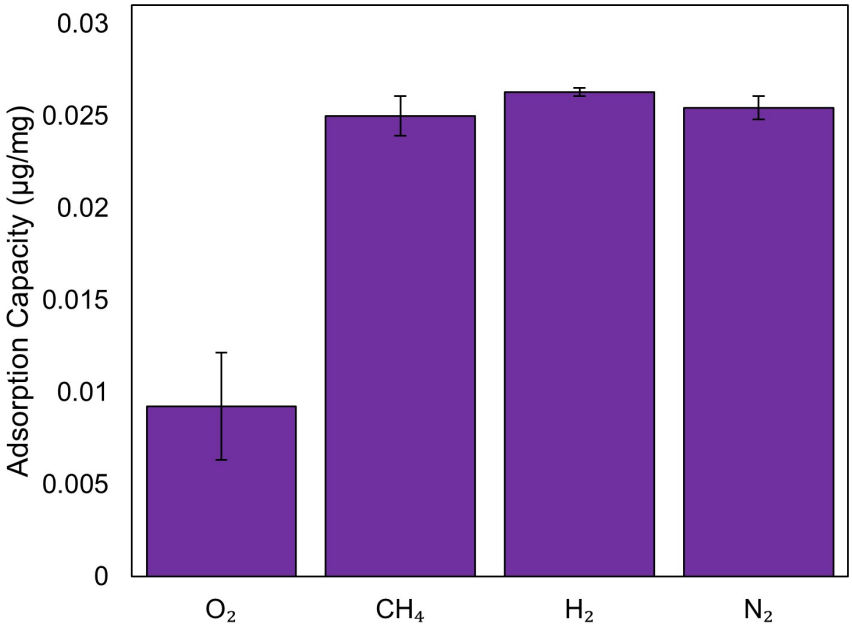

Figure 6.7 Average adsorption capacity of PFOA on plasma treated AC at 4 min (n=3).

Table 6.1 Average adsorption capacity of PFOA onto AC treated with various plasmas for 4 minutes (n=3).

Plasma treatment	Adsorption capacity (μg/mg)
O_2	0.0092 ± 0.003
CH_4	0.0250 ± 0.001
H_2	0.0263 ± 0.0002
N_2	0.0254 ± 0.0006

agent, giving the surface more electrons and reducing oxides. H_2 plasmas have been shown to remove surface contaminants for carbon material surfaces [252]. Highly energetic ions may etch the carbon. Along with etching, H_2 plasma has been used to dope graphene and enhance electrical conductivity.

Adsorption capacity decreased after 4 minutes. **Figure 6.8** depicts the average adsorption capacities after 6 minutes of treatment, the values of which are found in the appendix. The decrease in adsorption capacity for CH_4, N_2, and H_2 as well as the slight increase in O_2 may be attributed to over etching. For O_2 over estching of the surface may result in less oxygen functional groups on the surface and thus, less negative charge. In all samples over etching would also lead to a destruction of internal pore structure. More work would need to be done to visualize structure changes and evaluate pore volume.

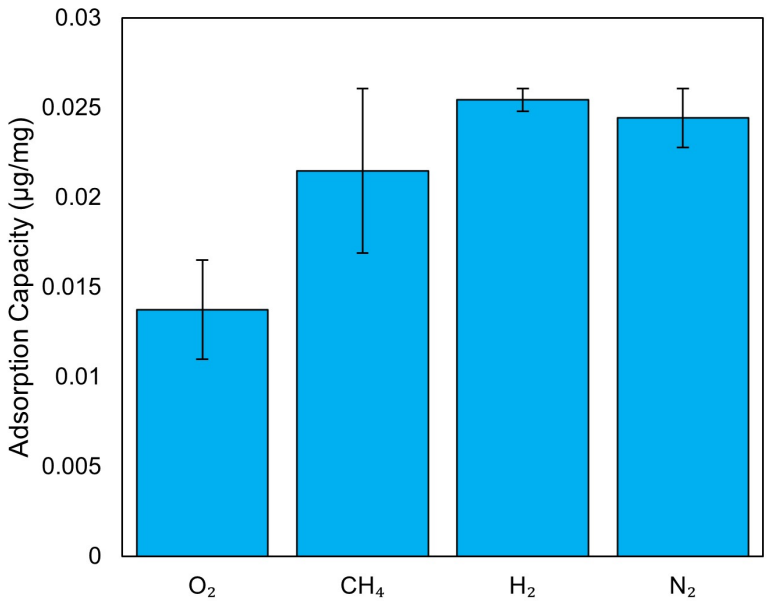

Figure 6.8 Average adsorption capacity of PFOA on plasma treated AC at 6 min (n=3).

6.3.2 Zeta Potential of AC

Zeta potential measurements were performed on the O_2, H_2, N_2, and CH_4 plasma-treated AC samples as well as the non-plasma treated AC sample. **Figure 6.9** shows the average zeta potentials between each sample. The O_2 plasma-treated AC has the most negative zeta potential compared to the other plasma-treated AC samples and the non-plasma treated AC sample. The zeta potential of the O_2 plasma-treated AC is measured at -63 mV around 4 minutes. H_2, CH_4, and N_2 were much more positive than the O_2 sample. It can be seen that the oxygen sample reached a minimum for zeta potential at 4 minutes which coincides with its lower adsorption capacity. The three other samples had average zeta potentials ~-35 mV with around 4 minutes of treatment.

Surface basicity has been shown to enhance PFOA adsorption on GAC [245, 251]. Zeta potential. The enhanced adsorption of PFOA onto H_2 plasma treated AC may be due to a combination of increased positive surface charge and removal of contaminants by etching. Conversely, the negative surface charge of the oxygen treated AC hindered the adsorption of PFOA.

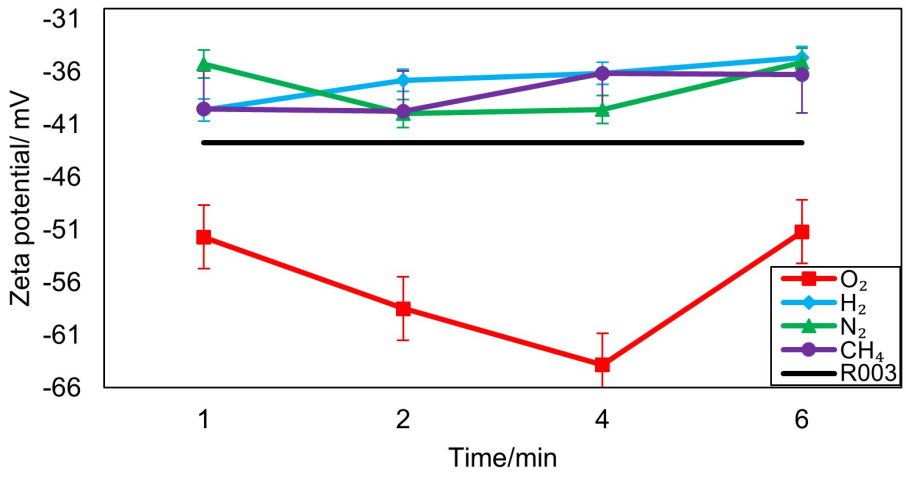

Figure 6.9 Average zeta potential of plasma treated AC at 1, 2, 4, and 6 minutes (n=3).

The overall results suggest that the AC as received had some type of contamination that interfered with the adsorption of PFOA. Heating in vacuum was able to remove this contamination, but high temperature and extended time was required. The addition of plasma treatment provided localized heating at atomic scale and efficiently further remove contamination. The increased adsorption capacity arises from the already present pore structure and the more positive surface charge.

6.3.3 PFOA Adsorption on Biochar

As a green alternative to AC, biochar should be able to adequately adsorb a wide range of chemicals. Using the same general procedure as for AC, we investigated the adsorption capacity of PFOA onto biochar. The biochar sample chosen was the most efficient at adsorption of MB in the previous chapter, 10% KOH at 300 °C treated with O_2 plasma for 5 minutes. We compared the adsorption capacity to that of raw biochar (NREL) and the industry favored AC Calgon F400. Shown in **Figure 6.10** are the results. The plasma activation process significantly enhanced the

adsorption of PFOA onto biochar compared to raw biochar. However, the adsorption capacity was still significantly less than that of F400. The average adsorption values are given in **Table 6.2**.

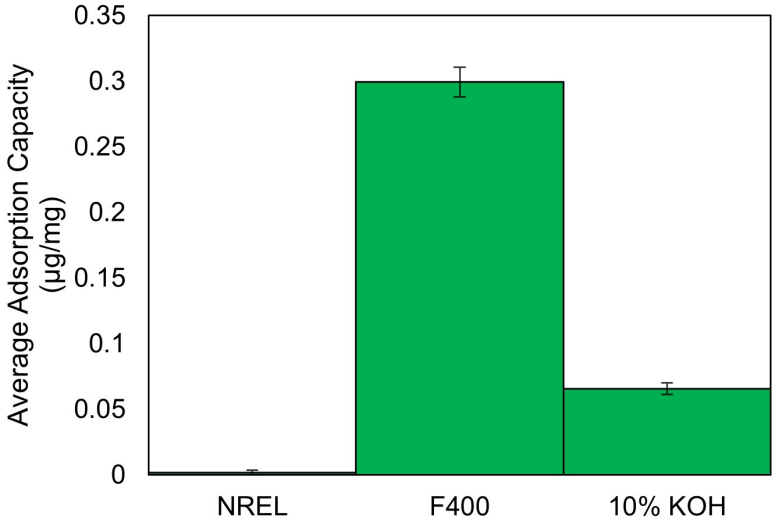

Figure 6.10 Average adsorption capacities of PFOA onto raw biochar (NREL), commercial AC (F400), and plasma activated biochar (10% KOH) (n=3).

Table 6.2 Average adsorption capacity for PFOA onto raw biochar (NREL), commercial AC (F400), and plasma activated biochar (10% KOH) (n=3).

Sample	Average Adsorption capacity (μg/mg)
NREL	0.0017 ± 0.0019
F400	0.2992 ± 0.0114
10% KOH	0.0656 ± 0.0044

FTIR spectra of AC (R003) was compared to that of R003 soaked for 30 minutes in a 20 mg/L MB solution and on R003 soaked for 30 minutes in a 2 ppb PFOA solution **Figure 6.11**. Peaks at 2908 and 2888 cm^{-1} appear after adsorption of both MB and PFOA. This peak is indicative of aliphatic C−H stretching. The peak at 2360 cm^{-1} becomes more prominent which may be attributed to C=O stretching and the presence of ketones, carboxylic acids, aldehydes, or esters.

After adsorption peaks at 1387 and 1156 cm^{-1} appear for both soaking samples which represent acyl and phenyl C−O. There were also peak increases at 1570 and 1251 cm^{-1}. The peak at 1570 cm^{-1} indicates C=C stretching of aromatic compounds. The peak at 1251 cm^{-1} occurs due to C−H stretching and OH deformation of COOH along with C−O stretching characteristic of C−O−C in cellulose.

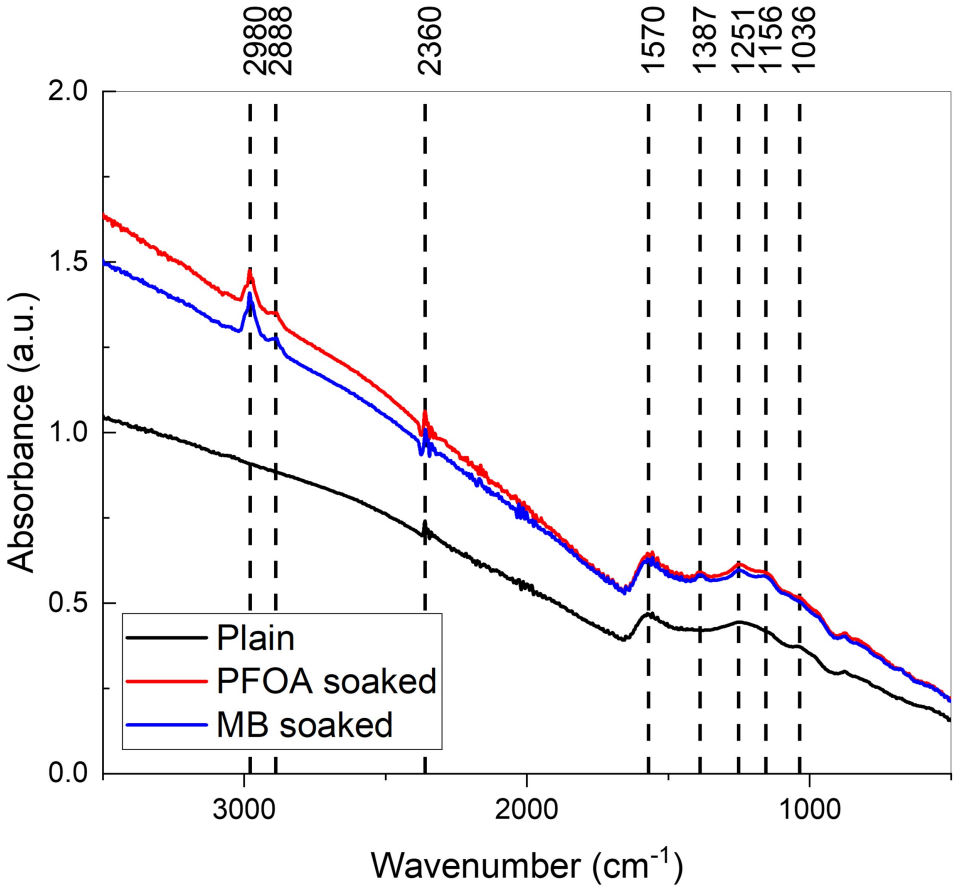

Figure 6.11 FTIR spectrum of plain AC (R003), AC soaked in PFOA, and AC soaked in MB.

Chemical reactivity of surface functional groups plays a role in the adsorption capacity of AC. Identifying functional groups gives insight to the adsorption capacity and the influence of plasma treatment on the AC surface. FTIR spectra were generated for the characterization of AC surface groups. The assignment of observed bands in **Figure 6.12** are shown in **Table 6.3**. These

bands were determined referencing papers studying the FTIR spectra of activated carbons having similar or the same wavelengths.

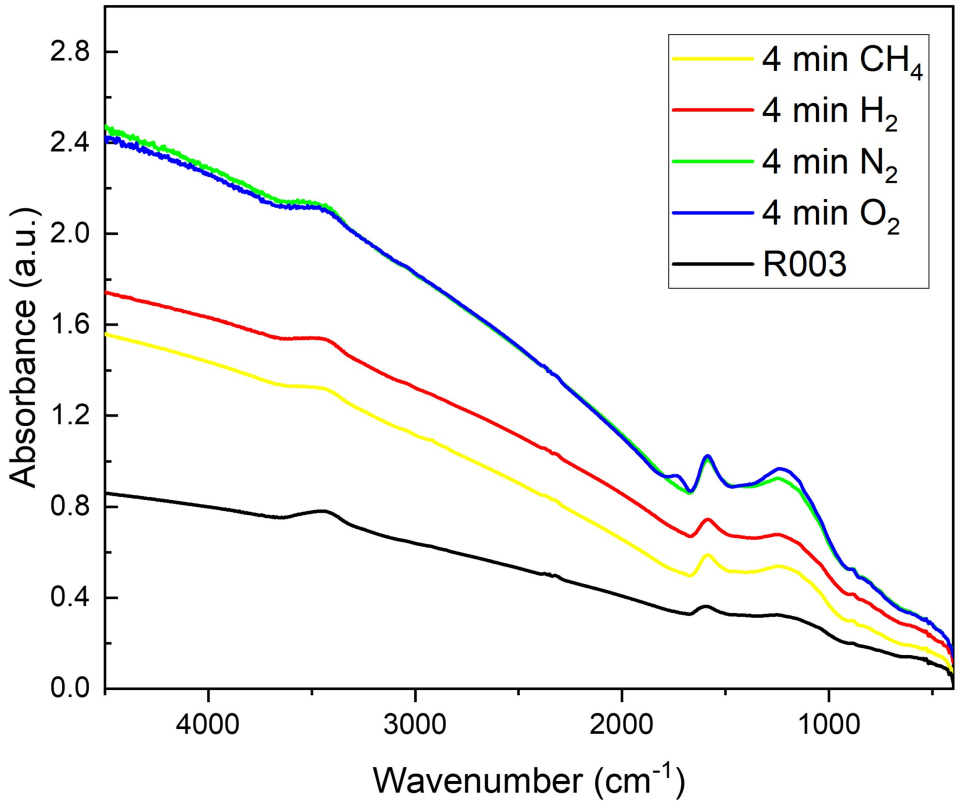

Figure 6.12 FTIR data for non-plasma treated and plasma treated AC.

FTIR was performed on each of the best samples from each group. The non-plasma treated AC had peaks at 3454 cm^{-1}, 2327 cm^{-1}, 1592 cm^{-1}, 1251 cm^{-1}, and 886.1 cm^{-1}. The AC that underwent O_2 plasma activation for 4 minutes had peaks at 3433 cm^{-1}, 2313 cm^{-1}, 1750 cm^{-1}, 1586 cm^{-1}, 1244 cm^{-1}, 891.9 cm^{-1}, and 828.3 cm^{-1}. The AC that underwent N_2 plasma activation for 4 minutes had peaks at 3433 cm^{-1}, 1586 cm^{-1}, 1245 cm^{-1}, 883.2 cm^{-1}, and 814.8 cm^{-1}. The AC that underwent H_2 plasma activation for 4 minutes had peaks at 3434 cm^{-1}, 2322 cm^{-1}, 1586 cm^{-1}, 1249 cm^{-1}, 885.2 cm^{-1}, and 837.9 cm^{-1}. The AC that underwent CH_4 plasma activation for

Table 6.3 The assignment of FTIR vibrations found in Figure 6.12.

Peak (cm^{-1})	**Surface group**	**Assignment**	**Plasma treatment**	**Reference**
3500–3400	O−H	O−H stretching, presence of hydrogen bonds	O_2, N_2, H_2, CH_4	[15, 19]
2920–2850	C−H	C−H stretching	CH_4	[16, 19, 20]
∼ 2300	C=O	C=O stretching, ketones	O_2, H_2, CH_4	[15, 17–20]
1770–1700	C=O	C=O stretching, ketones, carboxylic acid, aldehydes, or esters	O_2	[15, 17–20]
1640–1550	N−H	N−H stretching in amides	N_2	[18]
1600–1475	C=C	C=C stretching of aromatic compounds	O_2, N_2, H_2, CH_4	[16, 21]
∼1240		C−H stretching and OH deformation of COOH and C−O stretching of C−O−C in cellulose and hemicellulose	O_2, N_2, H_2, CH_4	[17, 18]
900–700	Aromatic compound	Aromatic stretching	O_2, N_2, H_2, CH_4	[18, 21]

4 minutes had peaks at 3440 cm^{-1}, 2926 cm^{-1}, 2355 cm^{-1}, 1585 cm^{-1}, 1245 cm^{-1}, 877.5 cm^{-1}, and 823.5 cm^{-1}.

The FTIR spectra for plasma treated AC and non-plasma treated AC are presented in Figure 6.12. Each individual spectrum had its baseline subtracted to find the peak heights. The similarities between the spectra suggest that the plasma-treated AC possessed similar surface functional groups regardless of the gas used [26]. Each spectrum shows a peak between 3500–3400 cm^{-1} indicative of OH stretching, which presents possible hydrogen bonding sites [15–19]. The 4-minute O_2 treated AC has the highest measured absorbance for this OH stretching peak, while the

non-plasma treated AC (R003) had the lowest. That the peak is more prominent in the 4 minute O_2 treated sample suggests the presence of more $-$OH groups from increased carboxylic groups on the surface [26]. The peak at ~2920 cm^{-1} is indicative of aliphatic C$-$H stretching RN_{16},RN_{19},RN_{20}. The peak at 2300 cm^{-1} indicates the C=O stretching of a ketone. Peaks between 1770–1700 cm^{-1} also indicates C=O stretching and is indicative of the presence of ketones, carboxylic acid, aldehydes, or esters [15, 17–20]. The peak between 1600-1475 cm^{-1} signifies C=C stretching of aromatic compounds [16, 21]. The spectra for the 4-minute O_2 had the highest absorbance with R003 having the lowest. The peak around 1240 cm^{-1} occurs because there was C$-$H stretching and OH deformation of COOH along with C$-$O stretching characteristic of C$-$O$-$C in cellulose and hemicelluloses [17, 18]. The 4-minute oxygen treatment has the greatest absorbance and the R003 has the lowest. Peaks between 900–700 cm^{-1} indicate aromatic stretching and the presence of aromatic compounds [18, 20]. O_2 has the largest absorbance, R003 has the lowest, and CH_4 is very close. Overall, the plasma treatment can add a variety of functional groups to the surface of AC. There were more hydrogen bonding sites present, as depicted by the increase in the absorbance for the peak between 3500–3400 cm^{-1}. There was also a marked increase in the C$-$H bonds, along with C$-$O, C=C, and ketones after the AC underwent plasma treatment.

6.4 Conclusion and Future Work

Overall, it has been demonstrated that plasma treatment can improve PFOA adsorption. However, the exact mechanism remains unclear. The negative surface charge was shown to negatively impact PFOA adsorption which aligns with the hypothesis that PFOA would preferentially adsorb onto more positive surfaces due to its anionic state in water. Future studies should focus on elucidation of the exact PFOA adsorption mechanisms to AC and biochar. Additionally, pore

volume distribution should be investigated using BET and imaging (TEM).

CHAPTER 7

SUMMARY AND FUTURE WORK

Oxygen based plasmas have been shown to possess the ability to kill *E. coli*. We have shown that the effectiveness of plasma sterilization depends strongly on the plasma characteristics and gas pressure. A magnetized plasma, one with an introduced external magnetic field, greatly shortens the sterilization time due to the increased concentrations of the reactive species. We demonstrated that the direct discharge region possesses higher plasma density which leads to more intensive etching and heating. This could potentially damage the surfaces of medical devices, specifically heat sensitive equipment, under sterilization. Therefore, the afterglow is a preferred location for samples, as it was shown that the temperature remained under 60 °C for the duration of treatment. The plasma species found to contribute to sterilization include atomic and molecular oxygen radicals (ions and excited species), as well as argon ions.

The UV emission lines present in the OES spectra were caused by the transition of the OH band. The OH peaks were more intensive at 100 mTorr in the afterglow compared to other pressures. Therefore, UV radiation most likely plays a role in sterilization or is indicative of oxygen plasma etching. Previous works have demonstrated the sensitivity of *E. coli* to certain UV light is influence by the specific growth rate [253]. Future research should measure and evaluate the specific growth rate the bacteria to quantify its effects in sterilization and better evaluate the role of UV radiation.

It would also be beneficial to study the magnetically enhanced RF cold plasma sterilization of multiple microorganisms. Future work should evaluate whether plasma sterilization can successfully sterilize surfaces inoculated with spore forming bacteria such as *Bacillus* and *Clostridium*,

antibiotic resistant strains, as well as biofilms. Spore forming produce highly resistant dormant structures, spores, with durable protein coats. These bacteria are generally resistant to sterilization. As shown in **Figure 7.1**, reactive species within oxygen based plasmas possess the ability to impact microorganisms by (1) damaging DNA or RNA, (2) degrade lipids within cell membranes, and (3) oxidation of proteins causing numerous detrimental effects [81–84]. Gram-positive bacteria are common causes of nosocomial hospital infections, specifically antibiotic resistant strains [254]. Comparing the sterilization efficiency of magnetic plasma on gram-positive bacteria (i.e., *Bacillus subtilis*) vs. gram-negative (i.e., *Escherichia coli*) would illuminate the ability of high energy plasma species, such as oxygen radicals, to penetrate the thick peptidoglycan wall to etch the bacteria. Gram-negative bacteria possess an outer lipid membrane and a thin peptidoglycan layer. A specific concern is the mechanism of resistance in bacteria such as vancomycin resistant *S. aureus*, which is linked to cell wall thickening [254]. Biofilms, may be involved in 65% of nosocomial infections, particularly those related to indwelling medical devices and endoscope tubing [255]. Biofilms are a community of bacteria growing on a surface and is enclosed in an extracellular polymeric substance. These biofilms are protected and resistant to many forms of sterilization. Prolonged exposure to energetic species within magnetic oxygen plasma may allow for the ROS to penetrate these biofilms and provide a method for sterilization within the risk of antibiotic resistance. Overall, low-temperature RF plasma enhanced with a magnetic field shows promising sterilization abilities that should be further investigated.

The ultimate goal of this study is to replace current water treatment methods with one low cost, universal method: biochar. Biochar requires activation in order for its adsorption capacity to compete with commercial AC (> 100 mg/g) [29, 31, 34, 210]. We established a time-efficient, low-temperature, plasma activation strategy for biochar. We have demonstrated the feasibility of

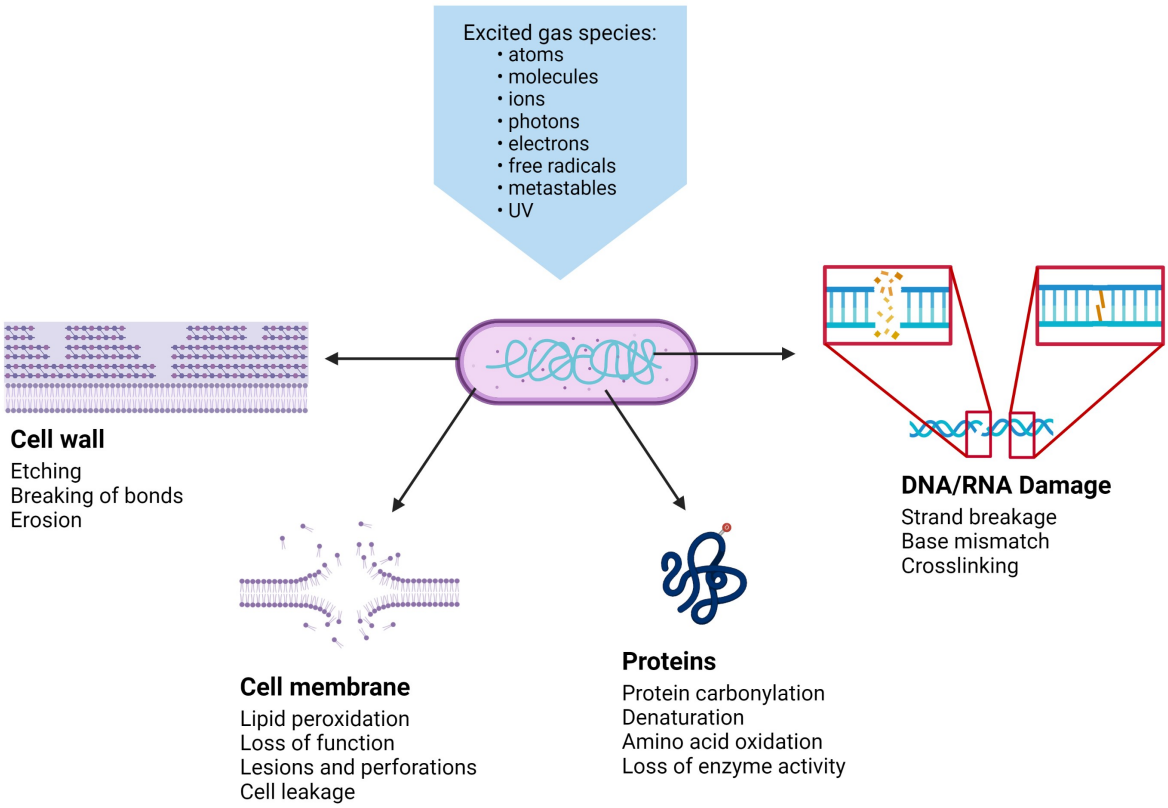

Figure 7.1 Reactive species within oxygen plasma and their effects on bacteria.

plasma activation of biochar at temperatures well below the conventional chemical activation.

Activating biochar surface with reactive plasma after pre-treatment with various concentrations of KOH improves adsorption. The temperature was kept at 300 °C or below, and the plasma treatment time wase less than 20 minutes. The optimal concentration of KOH seems to lie somewhere between 10 and 30%. Further studies should be conducted to find the optimal concentration.

The adsorption capacity was evaluated using MB adsorption. Future work should focus on the manipulation of temperature and time of treatment. Additionally, determining the active species concentrations present in the plasma and better elucidating the surface functional groups and properties would be beneficial to advancing plasma activation of biochar. We have shown

that the adsorption capacity can be increased using plasma activation, although the process is not fine-tuned to produce biochar with adsorption capabilities higher than most commercial carbons.

The pore volume distribution as well as surface area should be determined in order to better understand the role physical characteristics play in adsorption of MB and PFOA. Plasma improves pore structure and offers the ability to generate chemical species and functional surface groups using appropriate plasma gases, which allows the biochar to be tailored for specific purposes. Additional work should focus on the biochar activation with different plasma gases. Oxygen and CH_4 plasmas are expected to create two types of distinct surface functional groups: an electronegative oxygen atom in C−O and an electropositive C−H, respectively. We expect the biochar samples to exhibit different adsorption behaviors. We have shown that the surface chemistry does impact the adsorption of PFOA onto AC. This should be further validated through intensive characterization. The proposed studies will establish a new method of biochar activation that will overcome current limitations and provide a strategy that utilizes plasma to efficiently treat and generate specific surface functional groups.

APPENDIX

Table A1 Average adsorption capacity of MB by oxygen plasma treated AC with increasing treatment time from Section 4.6.1 (n=3).

O_2 Plasma	
Treatment time (min)	**Average adsorption capacity (mg/mg)**
0	0.00413 ± 2E-06
1	0.465 ± 0.0008
2	0.466 ± 0.0007
3	0.464 ± 0.0008
4	0.467 ± 0.0002
5	0.467 ± 0.0009
6	0.467 ± 0.0004
10	0.0572 ± 0.0001
20	0.0323 ± 0.0003

Table A2 Average mass loss with different oxygen plasma treatments and KOH concentrations from Section 5.6.1.

Mass % lost						
	200°C			**Average**	**Std Dev**	**Error**
0.01% KOH	15.1	14.3	14.9	14.8	0.4	0.2
1% KOH	10.8	12.8	16.6	13.4	2.9	1.7
10% KOH	13.0	17.0	14.0	14.7	2.1	1.2
	300°C			**Average**	**Std Dev**	**Error**
0.01% KOH	46.4	52.0	51.7	50.0	1.1	0.6
1% KOH	45.0	43.4	49.3	45.9	3.1	1.8
10% KOH	59.0	60.0	61.0	60.0	1.0	0.6
30% KOH	50.0	55.0	57.0	54.0	3.6	2.1
50% KOH	34.0	35.0	42.1			
50% KOH	47.0	35.0	44.0	39.5	5.5	2.3

Table A3 The calculated Langmuir and Fruendlich isotherm data for biochar from experiments in Section 5.6.4.

			Langmuir		**Freundlich**	
C_0	C_e	q_e	C_e	C_e/q_e	$\ln C_e$	$\ln q_e$
10.73	7.858	5.268	7.858	1.491	2.061	1.662
15.89	12.02	5.711	12.02	2.104	2.486	1.742
21.56	17.65	6.338	17.65	2.785	2.871	1.847
36.46	32.11	6.743	32.11	4.762	3.469	1.909
83.53	77.66	10.77	77.66	7.214	4.352	2.376

Table A4 The calculated Fruendlich isotherm parameters from Section 5.6.4.

Freundlich				
Slope	**n**	**Intercept**	**KF**	**1/n=slope**
0.2995	3.339	0.9942	2.703	0.2995

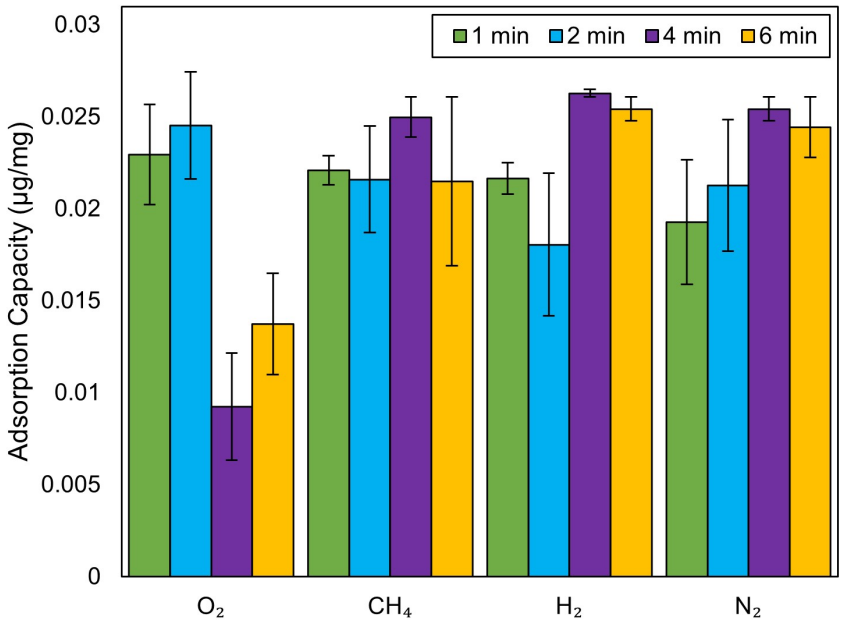

Figure S1 Average adsorption capacity for PFOA onto plasma treated AC from Section 6.3.1 (n=3).

Table A5 Average adsorption capacity for PFOA onto plasma treated AC from Section 6.3.1 (n=3).

Plasma treated AC	Average adsorption capacity (μg/mg)	Error
O_2 1 min	0.0230	0.0027
O_2 2 min	0.0245	0.0029
O_2 4 min	0.0092	0.0029
O_2 6 min	0.0137	0.0028
CH_4 1 min	0.0221	0.0008
CH_4 2 min	0.0216	0.0029
CH_4 4 min	0.0250	0.0011
CH_4 6 min	0.0215	0.0046
H_2 1 min	0.0217	0.0009
H_2 2 min	0.0181	0.0039
H_2 4 min	0.0263	0.0002
H_2 6 min	0.0254	0.0006
N_2 1 min	0.0193	0.0034
N_2 2 min	0.0213	0.0036
N_2 4 min	0.0254	0.0006
N_2 6 min	0.0244	0.0016

BIBLIOGRAPHY

BIBLIOGRAPHY

[1] Imran Ali. The quest for active carbon adsorbent substitutes: Inexpensive adsorbents for toxic metal ions removal from wastewater. *Separation and Purification Reviews*, 39(3-4): 95–171, nov 2010. ISSN 15422119. doi: 10.1080/15422119.2010.527802. URL http://www.tandfonline.com/doi/abs/10.1080/15422119.2010.527802.

[2] Salman Khazaei, Somayeh Khazaei, and Erfan Ayubi. Importance of prevention and control of nosocomial infections in Iran. *Iranian Journal of Public Health*, 47(2):307–308, feb 2018. ISSN 22516093. URL http://www.ncbi.nlm.nih.gov/pubmed/29445648http://www.pubmedcentral.nih.gov/articlerender.fcgi?artid=PMC5810401.

[3] François Rossi, Ondřej Kylián, and Marina Hasiwa. Decontamination of surfaces by low pressure plasma discharges. *Plasma Processes and Polymers*, 3(6-7):431–442, 2006. ISSN 16128850. doi: 10.1002/ppap.200600011. URL http://doi.wiley.com/10.1002/ppap.200600011.

[4] P. M. Olaechea, J. Insausti, A. Blanco, and P. Luque. Epidemiología e impacto de las infecciones nosocomiales. Technical Report 4, 2010. URL http://www.who.int/emc{%}0Ahttp://www.who.int/emc{%}0Ahttp://www.who.int/emc{%}0Ahttp://www.who.int/emc{%}0Ahttp://www.who.int/emc{%}0Ahttp://www.who.int/emc{%}0Ahttp://www.who.int/emc{%}0Ahttp://apps.who.int/medicinedocs/documents/s16355e/s16355e.pdf.

[5] William A. Rutala, Maria F. Gergen, and David J. Weber. Sporicidal Activity of a New Low-Temperature Sterilization Technology: The Sterrad 50 Sterilizer. *Infection Control & Hospital Epidemiology*, 20(7):514–516, 1999. ISSN 0899-823X. doi: 10.1086/501662. URL https://www.cambridge.org/core/journals/infection-control-and-hospital-epidemiology/article/sporicidal-activity-of-a-new-lowtemperature-sterilization-technology-the-sterrad-50-sterilizer/3A9B12DCAC9ABE1DC68383A2368F8D4C.

[6] A. Sureshkumar, R. Sankar, Mahitosh Mandal, and Sudarsan Neogi. Effective bacterial inactivation using low temperature radio frequency plasma. *International Journal of Pharmaceutics*, 396(1-2):17–22, aug 2010. ISSN 03785173. doi: 10.1016/j.ijpharm.2010.05.045. URL https://www.sciencedirect.com/science/article/pii/S0378517310004072.

[7] Michel Moisan, Karim Boudam, Denis Carignan, Danielle Kéroack, Pierre Levif, Jean Barbeau, Jacynthe Séguin, Kinga Kutasi, Benaïssa Elmoualij, Olivier Thellin, and Willy Zorzi. Sterilization/disinfection of medical devices using plasma: The flowing afterglow of the reduced-pressure N2-O2 discharge as the inactivating medium. *EPJ Applied Physics*, 63(1):10001–p1–10001–p46, jul 2013. ISSN 12860050. doi: 10.1051/epjap/2013120510. URL http://www.epjap.org/10.1051/epjap/2013120510.

[8] M. S. Kyi, J. Holton, and G. L. Ridgway. Assessment of the efficacy of a low temperature hydrogen peroxide gas plasma sterilization system. *Journal of Hospital Infection*, 31(4): 275–284, 1995. ISSN 01956701. doi: 10.1016/0195-6701(95)90206-6. URL https://www.sciencedirect.com/science/article/pii/0195670195902066.

[9] Hideharu Shintani, Akikazu Sakudo, Peter Burke, and Gerald McDonnell. Gas plasma sterilization of microorganisms and mechanisms of action. *Experimental and Therapeutic Medicine*, 1(5):731–738, 2010. ISSN 17920981. doi: 10.3892/etm.2010.136. URL https://www.spandidos-publications.com/etm/1/5/731?text=abstract.

[10] Umran Inan and Marek Gołkowski. Principles of plasma physics for engineers and scientists. *Principles of Plasma Physics for Engineers and Scientists*, 9780521193:1–270, 2010. doi: 10.1017/CBO9780511761621.

[11] I. E. Kieft, J. L.V. Broers, V. Caubet-Hilloutou, D. W. Slaaf, F. C.S. Ramaekers, and E. Stoffels. Electric discharge plasmas influence attachment of cultured CHO K1 cells. *Bioelectromagnetics*, 25(5):362–368, 2004. ISSN 01978462. doi: 10.1002/bem.20005.

[12] S. A. Ermolaeva, O. F. Petrov, B. S. Naroditsky, V. E. Fortov, G. E. Morfill, and A. L. Gintsburg. Cold Plasma Therapy. In *Comprehensive Biomedical Physics*, volume 10, pages 343–369. Elsevier, jul 2014. ISBN 9780444536327. doi: 10.1016/B978-0-444-53632-7.01021-2.

[13] A. A. Bol'shakov, B. A. Cruden, R. Mogul, M. V.V.S. Rao, S. P. Sharma, B. N. Khare, and M. Meyyappan. Radio-Frequency Oxygen Plasma as a Sterilization Source. *AIAA Journal*, 42(4):823–832, apr 2004. ISSN 00011452. doi: 10.2514/1.9562. URL http://arc.aiaa.org/doi/10.2514/1.9562.

[14] Keliang Wang, Bocong Zheng, Maheshwar Shrestha, Thomas Schuelke, and Qi Hua Fan. Magnetically enhanced plasma exfoliation of polyaniline-modified graphene for flexible solid-state supercapacitors. *Energy Storage Materials*, 14:230–237, 2018. ISSN 24058297. doi: 10.1016/j.ensm.2018.04.004. URL https://www.sciencedirect.com/science/article/pii/S240582971830062X.

[15] Ehsan Behazin, Emmanuel Ogunsona, Arturo Rodriguez-Uribe, Amar K. Mohanty, Manjusri Misra, and Anthony O. Anyia. Mechanical, chemical, and physical properties of wood and perennial grass biochars for possible composite application. *BioResources*, 11(1): 1334–1348, dec 2016. ISSN 19302126. doi: 10.15376/biores.11.1.1334-1348. URL http://ojs.cnr.ncsu.edu/index.php/BioRes/article/view/7804.

[16] Leônidas C.A. Melo, Aline R. Coscione, Cleide A. Abreu, Aline P. Puga, and Otávio A. Camargo. Influence of pyrolysis temperature on cadmium and zinc sorption capacity of sugar cane straw-derived biochar. *BioResources*, 8(4):4992–5004, aug 2013. ISSN 19302126. doi: 10.15376/biores.8.4.4992-5004. URL http://ojs.cnr.ncsu.edu/index.php/BioRes/article/view/4370.

[17] Natália Aragão de Figueredo, Liovando Marciano da Costa, Leônidas Carrijo Azevedo Melo, Evair Antônio Siebeneichlerd, and Jairo Tronto. Characterization of biochars from different sources and evaluation of release of nutrients and contaminants. *Revista Ciencia Agronomica*, 48(3):395–403, 2017. ISSN 18066690. doi: 10.5935/1806-6690.20170046. URL http://www.gnresearch.org/doi/10.5935/1806-6690.20170046.

[18] Keri B. Cantrell, Patrick G. Hunt, Minori Uchimiya, Jeffrey M. Novak, and Kyoung S. Ro. Impact of pyrolysis temperature and manure source on physicochemical characteristics of biochar. *Bioresource Technology*, 107:419–428, mar 2012. ISSN 09608524. doi: 10.1016/j.biortech.2011.11.084. URL https://www.sciencedirect.com/science/article/pii/S0960852411016956.

[19] Fanghua Hao, Xuchen Zhao, Wei Ouyang, Chunye Lin, Siyang Chen, Yushu Shan, and Xuehui Lai. Molecular structure of corncob-derived Biochars and the mechanism of Atrazine sorption. *Agronomy Journal*, 105(3):773–782, 2013. ISSN 00021962. doi: 10.2134/agronj2012.0311. URL https://www.agronomy.org/publications/aj/abstracts/105/3/773.

[20] Yingmei Lou, Stephen Joseph, Lianqing Li, Ellen R. Graber, Xiaoyu Liu, and Genxing Pan. Water extract from straw biochar used for plant growth promotion: An initial test. *BioResources*, 11(1):249–266, nov 2016. ISSN 19302126. doi: 10.15376/biores.11.1.249-266. URL http://ojs.cnr.ncsu.edu/index.php/BioRes/article/view/7293.

[21] A. Ben Hassen-Trabelsi, T. Kraiem, S. Naoui, and H. Belayouni. Pyrolysis of waste animal fats in a fixed-bed reactor: Production and characterization of bio-oil and bio-char. *Waste Management*, 34(1):210–218, jan 2014. ISSN 0956053X. doi: 10.1016/j.wasman.2013.09.019. URL https://www.sciencedirect.com/science/article/pii/S0956053X13004534.

[22] Yanhui Li, Qiuju Du, Tonghao Liu, Xianjia Peng, Junjie Wang, Jiankun Sun, Yonghao Wang, Shaoling Wu, Zonghua Wang, Yanzhi Xia, and Linhua Xia. Comparative study of methylene blue dye adsorption onto activated carbon, graphene oxide, and carbon nanotubes. *Chemical Engineering Research and Design*, 91(2):361–368, feb 2013. ISSN 02638762. doi: 10.1016/j.cherd.2012.07.007.

[23] Dilek Angin, Esra Altintig, and Tijen Ennil Köse. Influence of process parameters on the surface and chemical properties of activated carbon obtained from biochar by chemical activation. *Bioresource Technology*, 148:542–549, nov 2013. ISSN 18732976. doi: 10.1016/j.biortech.2013.08.164. URL https://www.sciencedirect.com/science/article/pii/S0960852413014223.

[24] Qing Song Liu, Tong Zheng, Peng Wang, and Liang Guo. Preparation and characterization of activated carbon from bamboo by microwave-induced phosphoric acid activation. *Industrial Crops and Products*, 31(2):233–238, mar 2010. ISSN 09266690. doi: 10.1016/j.indcrop.2009.10.011.

[25] Chien To Hsieh and Hsisheng Teng. Influence of mesopore volume and adsorbate size on

adsorption capacities of activated carbons in aqueous solutions. *Carbon*, 38(6):863–869, jan 2000. ISSN 00086223. doi: 10.1016/S0008-6223(99)00180-3.

[26] P. Chingombe, B. Saha, and R. J. Wakeman. Surface modification and characterisation of a coal-based activated carbon. *Carbon*, 43(15):3132–3143, dec 2005. ISSN 00086223. doi: 10.1016/j.carbon.2005.06.021. URL https://www.sciencedirect.com/science/article/pii/S000862230500360X.

[27] F. Marrakchi, M. J. Ahmed, W. A. Khanday, M. Asif, and B. H. Hameed. Mesoporous-activated carbon prepared from chitosan flakes via single-step sodium hydroxide activation for the adsorption of methylene blue. *International Journal of Biological Macromolecules*, 98:233–239, may 2017. ISSN 18790003. doi: 10.1016/j.ijbiomac.2017.01.119.

[28] Mark A. Shannon, Paul W. Bohn, Menachem Elimelech, John G. Georgiadis, Benito J. Marĩas, and Anne M. Mayes. Science and technology for water purification in the coming decades. *Nature*, 452(7185):301–310, 2008. ISSN 14764687. doi: 10.1038/nature06599.

[29] Mandu Inyang, Bin Gao, Andrew Zimmerman, Ming Zhang, and Hao Chen. Synthesis, characterization, and dye sorption ability of carbon nanotube-biochar nanocomposites. *Chemical Engineering Journal*, 236:39–46, jan 2014. ISSN 13858947. doi: 10.1016/j.cej.2013.09.074. URL https://www.sciencedirect.com/science/article/pii/S1385894713012679.

[30] Jingchun Tang, Wenying Zhu, Rai Kookana, and Arata Katayama. Characteristics of biochar and its application in remediation of contaminated soil. *Journal of Bioscience and Bioengineering*, 116(6):653–659, dec 2013. ISSN 13891723. doi: 10.1016/j.jbiosc.2013.05.035. URL https://www.sciencedirect.com/science/article/pii/S138917231300217X.

[31] Rakesh Kumar Gupta, Mukul Dubey, Parashu Kharel, Zhengrong Gu, and Qi Hua Fan. Biochar activated by oxygen plasma for supercapacitors. *Journal of Power Sources*, 274:1300–1305, jan 2015. ISSN 03787753. doi: 10.1016/j.jpowsour.2014.10.169. URL https://www.sciencedirect.com/science/article/pii/S0378775314017881.

[32] Joan J. Manyà. Pyrolysis for biochar purposes: A review to establish current knowledge gaps and research needs. *Environmental Science and Technology*, 46(15):7939–7954, 2012. ISSN 0013936X. doi: 10.1021/es301029g. URL https://pubs.acs.org/sharingguidelines.

[33] Aya Zoghlami and Gabriel Paës. Lignocellulosic Biomass: Understanding Recalcitrance and Predicting Hydrolysis. *Frontiers in Chemistry*, 7, 2019. ISSN 22962646. doi: 10.3389/fchem.2019.00874.

[34] Lei Sun, Shungang Wan, and Wensui Luo. Biochars prepared from anaerobic digestion residue, palm bark, and eucalyptus for adsorption of cationic methylene blue dye: Characterization, equilibrium, and kinetic studies. *Bioresource Technology*, 140:406–413, jul 2013. ISSN 18732976. doi: 10.1016/j.biortech.2013.04.116. URL https://www.sciencedirect.com/science/article/pii/S0960852413007499.

[35] Susan A. Beach, John L. Newsted, Katie Coady, and John P. Giesy. Ecotoxicological evaluation of perfluorooctanesulfonate (PFOS). Technical report, 2006. URL http://www.epa.gov/epahome/dockets.htm.

[36] Antonia M. Calafat, Kayoko Kato, Kendra Hubbard, Tao Jia, Julianne Cook Botelho, and Lee Yang Wong. Legacy and alternative per- and polyfluoroalkyl substances in the U.S. general population: Paired serum-urine data from the 2013–2014 National Health and Nutrition Examination Survey. *Environment International*, 131:105048, oct 2019. ISSN 18736750. doi: 10.1016/j.envint.2019.105048.

[37] Ludovica Silvani, Gerard Cornelissen, Andreas Botnen Smebye, Y. Zhang, G. Okkenhaug, Andrew R. Zimmerman, Gorm Thune, Hilmar Sævarsson, and Sarah E. Hale. Can biochar and designer biochar be used to remediate per- and polyfluorinated alkyl substances (PFAS) and lead and antimony contaminated soils? *Science of the Total Environment*, 694:133693, jul 2019. ISSN 18791026. doi: 10.1016/j.scitotenv.2019.133693. URL https://www.sciencedirect.com/science/article/pii/S0048969719336253.

[38] Robert C. Buck, James Franklin, Urs Berger, Jason M. Conder, Ian T. Cousins, Pim De Voogt, Allan Astrup Jensen, Kurunthachalam Kannan, Scott A. Mabury, and Stefan P.J. van Leeuwen. Perfluoroalkyl and polyfluoroalkyl substances in the environment: Terminology, classification, and origins. *Integrated Environmental Assessment and Management*, 7(4):513–541, oct 2011. ISSN 15513793. doi: 10.1002/ieam.258. URL https://setac.onlinelibrary.wiley.com/doi/full/10.1002/ieam.258{%}4010.1002/{%}28ISSN{%}291551-3793.PFASHttps://onlinelibrary.wiley.com/doi/full/10.1002/ieam.258https://onlinelibrary.wiley.com/doi/abs/10.1002/ieam.258https://setac.onlinelibrary.wiley.com/doi.

[39] Darya Kupryianchyk, Sarah E. Hale, Gijs D. Breedveld, and Gerard Cornelissen. Treatment of sites contaminated with perfluorinated compounds using biochar amendment. *Chemosphere*, 142:35–40, jan 2016. ISSN 18791298. doi: 10.1016/j.chemosphere.2015.04.085. URL https://www.sciencedirect.com/science/article/pii/S0045653515004312.

[40] E. Kissa. *Fluorinated Surfactants and Repellents*, volume 71. Marcel Dekker, Inc., New York, NY, second edition, 2001. ISBN 0-8247-0472-X. doi: 10.1177/004051750107100823. URL https://books.google.com/books?hl=en{&}lr={&}id=iAmE8v3bFnUC{&}oi=fnd{&}pg=PR3{&}dq=Kissa+E+(2001)+Fluorinated+surfactants+and+repellents,+vol+97,+2nd+edn.+Marcel+Dekker,+New+York{&}ots=D7Yu17haCw{&}sig=mepKELSfcRNIbcUVqyUTTzhTIvo{#}v=onepage{&}q=KissaE(2001)Fluor.

[41] J. A. Bittencourt. *Introduction*, pages 1–32. Springer New York, New York, NY, 2004. ISBN 978-1-4757-4030-1. doi: 10.1007/978-1-4757-4030-1_1. URL https://doi.org/10.1007/978-1-4757-4030-1{_}1.

[42] Michael A. Lieberman and Allan J. Lichtenberg. *Principles of Plasma Discharges and Materials Processing: Second Edition*. Number June. Wiley-Interscience, 2005. ISBN

0471720011. doi: 10.1002/0471724254. URL http://home.zcu.cz/{~}kozakt/MPPL/literatura/Lieberman-PrinciplesofPlasmaDischargesandMaterialsProcessing-2ndedition.pdf.

[43] Alexander Fridman. *Plasma chemistry*, volume 9780521847. Cambridge University Press, Cambridge, 2008. ISBN 9780511546075. doi: 10.1017/CBO9780511546075. URL https://www.cambridge.org/core/product/identifier/9780511546075/type/book.

[44] H. Conrads and M. Schmidt. Plasma generation and plasma sources. *Plasma Sources Science and Technology*, 9(4):441–454, 2000. ISSN 09630252. doi: 10.1088/0963-0252/9/4/301. URL http://iopscience.iop.org/article/10.1088/0963-0252/9/4/301/meta.

[45] K. Wiesemann. A short introduction to plasma physics. *CAS-CERN Accelerator School: Ion Sources - Proceedings*, pages 85–122, 2013. doi: 10.5170/CERN--2013--007.85.

[46] Annemie Bogaerts, Erik Neyts, Renaat Gijbels, and Joost Van der Mullen. Gas discharge plasmas and their applications. *Spectrochimica Acta - Part B Atomic Spectroscopy*, 57(4):609–658, 2002. ISSN 05848547. doi: 10.1016/S0584-8547(01)00406-2.

[47] J.L. Shohet. Plasma Science and Engineering. *Encyclopedia of Physical Science and Technology*, pages 401–423, 2003. doi: 10.1016/b0-12-227410-5/00584-6.

[48] Yury Gorbanev, Angela Privat-Maldonado, and Annemie Bogaerts. Analysis of Short-Lived Reactive Species in Plasma-Air-Water Systems: The Dos and the Do Nots. *Analytical Chemistry*, 90(22):13151–13158, nov 2018. ISSN 15206882. doi: 10.1021/acs.analchem.8b03336. URL https://pubs.acs.org/sharingguidelines.

[49] National Research Council. *Plasma Science*. The National Academies Press, Washington, DC, 1995. ISBN 978-0-309-05231-3. doi: 10.17226/4936. URL https://www.nap.edu/catalog/4936/plasma-science-from-fundamental-research-to-technological-applications.

[50] Vladimir Kolobov and Valery Godyak. Electron kinetics in low-temperature plasmas. *Physics of Plasmas*, 26(6):60601, 2019. ISSN 10897674. doi: 10.1063/1.5093199. URL https://aip.scitation.org/doi/abs/10.1063/1.5093199.

[51] Francis F. Chen. Radiofrequency Plasma Sources for Semiconductor Processing. In *Advanced Plasma Technology*, pages 99–115. Wiley-VCH Verlag GmbH & Co. KGaA, 2008. ISBN 9783527405916. doi: 10.1002/9783527622184.ch6.

[52] J. Ehlbeck, U. Schnabel, M. Polak, J. Winter, Th Von Woedtke, R. Brandenburg, T. Von Dem Hagen, and K. D. Weltmann. Low temperature atmospheric pressure plasma sources for microbial decontamination, jan 2011. ISSN 00223727. URL http://stacks.iop.org/0022-3727/44/i=1/a=013002?key=crossref.0390e970db31e45f99a7ac0921a7d924.

[53] P. Gibbon. Introduction to plasma physics. *CAS-CERN Accelerator School: Plasma Wake*

Acceleration 2014, Proceedings, pages 51–65, 2014. doi: 10.5170/CERN-2016-001.51. URL https://arxiv.org/abs/2007.04783v1.

[54] Michael A. Lieberman and Allan J. Lichtenberg. *Basic Plasma Equations and Equilibrium*, chapter 2, pages 23–42. John Wiley & Sons, Ltd, 2005. ISBN 9780471724254. doi: 10.1002/0471724254.ch2.

[55] R Fitzpatrick. *Plasma physics: an introduction*. Crc Press, 2014. URL https://books.google.com/books?hl=en{&}lr={&}id=0RwbBAAAQBAJ{&}oi=fnd{&}pg=PP1{&}dq=Plasma+Physics++++++++Richard+Fitzpatrick{&}ots=n{_}PgCUY3jr{&}sig=DVODX8xfFFRbJWokBQXVIJP1X{_}Q.

[56] A. Formenti, A. Maffini, and M. Passoni. Non-equilibrium effects in a relativistic plasma sheath model. *New Journal of Physics*, 22(5), 2020. ISSN 13672630. doi: 10.1088/1367-2630/ab83cf. URL https://doi.org/10.1088/1367-2630/ab83cf.

[57] Luis Conde. The elementary plasma processes. *An Introduction to Plasma Physics and its Space Applications, Volume 1: Fundamentals and elementary processes*, 2018. doi: 10.1088/2053-2571/aae132ch6.

[58] N. St J. Braithwaite. Introduction to gas discharges. *Plasma Sources Science and Technology*, 9(4):517–527, 2000. ISSN 09630252. doi: 10.1088/0963-0252/9/4/307. URL https://iopscience.iop.org/article/10.1088/0963-0252/9/4/307https://iopscience.iop.org/article/10.1088/0963-0252/9/4/307/meta.

[59] Raluca Ilie. Theoretical description. In Vania K Jordanova, Raluca Ilie, and Margaret W Chen, editors, *Ring Current Investigations*, pages 53–98. Elsevier, 2020. ISBN 978-0-12-815571-4. doi: 10.1016/b978-0-12-815571-4.00003-2. URL https://www.sciencedirect.com/science/article/pii/B9780128155714000032.

[60] R. M. Harris. *Physical chemistry for the life sciences*, volume 284. Oxford University Press, USA, 1980. ISBN 0-7167-8759-8. doi: 10.1038/284084b0.

[61] J. A. Krommes. An introduction to the physics of the Coulomb logarithm, with emphasis on quantum-mechanical effects. *Journal of Plasma Physics*, 85(1), 2019. ISSN 0022-3778. doi: 10.1017/s0022377818001319. URL https://www.cambridge.org/core/journals/journal-of-plasma-physics/article/abs/an-introduction-to-the-physics-of-the-coulomb-logarithm-with-emphasis-on-quantummechanical-effects/59E2266BDFC8E73A36709181A43D3D57.

[62] C. Dimopoulou, N. Haag, R. Moshammer, P. D. Fainstein, A. Dorn, M. Dürr, D. Fischer, and J. Ullrich. Fragmentation of molecules by fast ion impact. *Journal of Physics: Conference Series*, 58(1):49–54, 2007. ISSN 17426596. doi: 10.1088/1742-6596/58/1/007. URL https://scholarsmine.mst.edu/phys{_}facworkThedefinitiveversionisavailableathttps://doi.org/10.1088/1742-6596/58/1/007.

[63] Boris M. Smirnov. *Properties of Gas Discharge Plasma*. Cham: Spring International Publishing, 2015. doi: 10.1007/978-3-319-11065-3_2. URL https://link.springer.com/content/pdf/10.1007/978-3-319-11065-3.pdf.

[64] A. J. Appleby. Chemistry, Electrochemistry, and Electrochemical Applications | Oxygen. In Jürgen Garche, editor, *Encyclopedia of Electrochemical Power Sources*, pages 810–852. Elsevier, Amsterdam, 2009. ISBN 9780444527455. doi: 10.1016/B978-044452745-5.00067-8. URL https://www.sciencedirect.com/science/article/pii/B9780444527455000678.

[65] Kwan Chi Kao. Optical and Electro-Optic Processes. In Kwan Chi Kao, editor, *Dielectric Phenomena in Solids*, pages 115–212. Academic Press, San Diego, 2004. ISBN 978-0-12-396561-5. doi: 10.1016/b978-012396561-5/50013-x. URL https://www.sciencedirect.com/science/article/pii/B978012396561550013X.

[66] Konrad Dennerl. Charge transfer reactions. *Space Science Reviews*, 157(1-4):57–91, 2010. ISSN 00386308. doi: 10.1007/s11214-010-9720-5. URL https://link.springer.com/article/10.1007/s11214-010-9720-5.

[67] S. Lerouge and A. Simmons. Sterilisation of biomaterials and medical devices. *Sterilisation of Biomaterials and Medical Devices*, pages 1–330, 2012. doi: 10.1533/9780857096265. URL https://books.google.com/books?hl=en{&}lr={&}id=xVtEAgAAQBAJ{&}oi=fnd{&}pg=PP1{&}ots=AEZnRWR3q-{&}sig=jC8kCOdriZGGeNcxM5X73oLAVHY.

[68] Jun-Ichi Sasaki and Satoshi Imazato. Autoclave sterilization of dental handpieces: A literature review. *Journal of Prosthodontic Research*, 64:239–242, 2020. doi: 10.1016/j.jpor.2019.07.013. URL https://doi.org/10.1016/j.jpor.2019.07.013.

[69] Giridhar ReddyY and Nikhilanand Hegde. Sterilization Methods in Orthodontics -A Review. *International Journal of Dental Clinics*, 3(1):44–47, 2011. ISSN 0975-8437. URL https://go-gale-com.proxy2.cl.msu.edu/ps/i.do?p=HRCA{&}sw=w{&}issn=09758437{&}v=2.1{&}it=r{&}id=GALE{%}7CA346926656{&}sid=googleScholar{&}linkaccess=fulltexthttps://go-gale-com.proxy2.cl.msu.edu/ps/i.do?p=HRCA{&}sw=w{&}issn=09758437{&}v=2.1{&}it=r{&}id=GALE{%}7CA346926656{&}sid=googl.

[70] Q. Q. Qiu, W. Q. Sun, and J. Connor. Sterilization of biomaterials of synthetic and biological origin. *Comprehensive Biomaterials*, 4:127–144, 2011. doi: 10.1016/b978-0-08-055294-1.00248-8.

[71] David E. Freeman and Jörg A. Auer. Instrument Preparation, Sterilization, and Antiseptics. *Equine Surgery*, pages 98–111, 2012. doi: 10.1016/B978-1-4377-0867-7.00009-0.

[72] OSHA. OSHA Fact Sheet. pages 1–2, 2002. URL https://www.osha.gov/OshDoc/data{_}General{_}Facts/ethylene-oxide-factsheet.pdf.

[73] Wanwisa Sudprasert, Panida Navasumrit, and Mathuros Ruchirawat. Effects of low-dose

gamma radiation on DNA damage, chromosomal aberration and expression of repair genes in human blood cells. *International Journal of Hygiene and Environmental Health*, 209(6): 503–511, 2006. ISSN 1618131X. doi: 10.1016/j.ijheh.2006.06.004.

[74] Pervin Basaran, Nese Basaran-Akgul, and Lutfi Oksuz. Elimination of Aspergillus parasiticus from nut surface with low pressure cold plasma (LPCP) treatment. *Food Microbiology*, 25(4):626–632, jun 2008. ISSN 07400020. doi: 10.1016/j.fm.2007.12.005.

[75] S. Hury, D. R. Vidal, F. Desor, J. Pelletier, and T. Lagarde. A parametric study of the destruction efficiency of Bacillus spores in low pressure oxygen-based plasmas. Technical Report 6, 1998. URL https://onlinelibrary.wiley.com/doi/pdf/10.1046/j.1472-765X.1998.00365.x.

[76] Uroš Cvelbar, Nikša Krstulović, Slobodan Milošević, and Miran Mozetič. Inductively coupled RF oxygen plasma characterization by optical emission spectroscopy. *Vacuum*, 82 (2 SPEC. ISS.):224–227, oct 2007. ISSN 0042207X. doi: 10.1016/j.vacuum.2007.07.016. URL https://www.sciencedirect.com/science/article/pii/S0042207X07002321.

[77] M. Moreau, N. Orange, and M. G.J. Feuilloley. Non-thermal plasma technologies: New tools for bio-decontamination. *Biotechnology Advances*, 26(6):610–617, 2008. ISSN 07349750. doi: 10.1016/j.biotechadv.2008.08.001.

[78] Liqing Yang, Jierong Chen, and Junling Gao. Low temperature argon plasma sterilization effect on Pseudomonas aeruginosa and its mechanisms. *Journal of Electrostatics*, 67(4):646–651, jul 2009. ISSN 03043886. doi: 10.1016/j.elstat.2009.01.060. URL https://www.sciencedirect.com/science/article/pii/S0304388609000709http://linkinghub.elsevier.com/retrieve/pii/S0304388609000709.

[79] M. Moisan, J. Barbeau, S. Moreau, J. Pelletier, M. Tabrizian, and L'H Yahia. Low-temperature sterilization using gas plasmas: A review of the experiments and an analysis of the inactivation mechanisms. *International Journal of Pharmaceutics*, 226(1-2):1–21, sep 2001. ISSN 03785173. doi: 10.1016/S0378-5173(01)00752-9. URL https://www.sciencedirect.com/science/article/pii/S0378517301007529.

[80] S. Moreau, M. Moisan, M. Tabrizian, J. Barbeau, J. Pelletier, A. Ricard, and L'H Yahia. Using the flowing afterglow of a plasma to inactivate Bacillus subtilis spores: Influence of the operating conditions. *Journal of Applied Physics*, 88(2):1166–1174, 2000. ISSN 00218979. doi: 10.1063/1.373792. URL https://aip.scitation.org/doi/abs/10.1063/1.373792.

[81] Celia Andrés Juan, José Manuel Pérez de la Lastra, Francisco J. Plou, and Eduardo Pérez-Lebeña. The chemistry of reactive oxygen species (Ros) revisited: Outlining their role in biological macromolecules (dna, lipids and proteins) and induced pathologies. *International Journal of Molecular Sciences*, 22(9):4642, 2021. ISSN 14220067. doi: 10.3390/ijms22094642. URL https://www.mdpi.com/1422-0067/22/9/4642/htmhttps://www.mdpi.com/1422-0067/22/9/4642.

[82] Lian Jiu Su, Jia Hao Zhang, Hernando Gomez, Raghavan Murugan, Xing Hong, Dongxue Xu, Fan Jiang, and Zhi Yong Peng. Reactive Oxygen Species-Induced Lipid Peroxidation in Apoptosis, Autophagy, and Ferroptosis. *Oxidative Medicine and Cellular Longevity*, 2019, 2019. ISSN 19420994. doi: 10.1155/2019/5080843.

[83] Ying Wang, Robyn Branicky, Alycia Noë, and Siegfried Hekimi. Superoxide dismutases: Dual roles in controlling ROS damage and regulating ROS signaling. *Journal of Cell Biology*, 217(6):1915–1928, 2018. ISSN 15408140. doi: 10.1083/jcb.201708007. URL https://doi.org/10.1083/jcb.201708007.

[84] Rodrigo M. Cordeiro. Reactive oxygen species at phospholipid bilayers: Distribution, mobility and permeation. *Biochimica et Biophysica Acta - Biomembranes*, 1838(1 PARTB): 438–444, 2014. ISSN 00052736. doi: 10.1016/j.bbamem.2013.09.016.

[85] Kateryna D. Makova and Ross C. Hardison. The effects of chromatin organization on variation in mutation rates in the genome. *Nature Reviews Genetics*, 16(4):213–223, 2015. ISSN 14710064. doi: 10.1038/nrg3890. URL /pmc/articles/PMC4500049//pmc/articles/PMC4500049/?report=abstracthttps://www.ncbi.nlm.nih.gov/pmc/articles/PMC4500049/.

[86] Da Peng Dai, Wei Gan, Hiroshi Hayakawa, Jia Lou Zhu, Xiu Qing Zhang, Guo Xin Hu, Tao Xu, Zhe Li Jiang, Li Qun Zhang, Xue Da Hu, Ben Nie, Yue Zhou, Jin Li, Xiao Yang Zhou, Jian Li, Tie Mei Zhang, Qing He, Dong Ge Liu, Hai Bo Chen, Nan Yang, Ping Ping Zuo, Zhi Xin Zhang, Huan Ming Yang, Yao Wang, Samuel H. Wilson, Yi Xin Zeng, Jian Ye Wang, Mutsuo Sekiguchi, and Jian Ping Cai. Transcriptional mutagenesis mediated by 8-oxoG induces translational errors in mammalian cells. *Proceedings of the National Academy of Sciences of the United States of America*, 115(16):4218–4222, 2018. ISSN 10916490. doi: 10.1073/pnas.1718363115. URL www.pnas.org/cgi/doi/10.1073/pnas.1718363115.

[87] Mizuki Ohno, Kunihiko Sakumi, Ryutaro Fukumura, Masato Furuichi, Yuki Iwasaki, Masaaki Hokama, Toshimichi Ikemura, Teruhisa Tsuzuki, Yoichi Gondo, and Yusaku Nakabeppu. 8-Oxoguanine causes spontaneous de novo germline mutations in mice. *Scientific Reports*, 4(1):1–9, 2014. ISSN 20452322. doi: 10.1038/srep04689. URL https://www.nature.com/articles/srep04689.

[88] Marcus S. Cooke, Mark D. Evans, Miral Dizdaroglu, and Joseph Lunec. Oxidative DNA damage: mechanisms, mutation, and disease. *The FASEB Journal*, 17(10):1195–1214, 2003. ISSN 0892-6638. doi: 10.1096/fj.02-0752rev. URL https://onlinelibrary.wiley.com/doi/full/10.1096/fj.02-0752revhttps://onlinelibrary.wiley.com/doi/abs/10.1096/fj.02-0752revhttps://faseb.onlinelibrary.wiley.com/doi/10.1096/fj.02-0752rev.

[89] Pawan Kumar Maurya. Animal Biotechnology as a Tool to Understand and Fight Aging. *Animal Biotechnology: Models in Discovery and Translation*, pages 177–191, 2013. doi: 10.1016/B978-0-12-416002-6.00010-9.

[90] Bruce Alberts and Julian Lewis. The Lipid Bilayer. *Molecular Biology of the Cell*, pages

6–11, 2013. URL https://www.ncbi.nlm.nih.gov/books/NBK26871/.

[91] M. Laroussi and F. Leipold. Evaluation of the roles of reactive species, heat, and UV radiation in the inactivation of bacterial cells by air plasmas at atmospheric pressure. *International Journal of Mass Spectrometry*, 233(1-3):81–86, 2004. ISSN 13873806. doi: 10.1016/j.ijms.2003.11.016.

[92] A B Lumb and C R Thomas. *Nunn's applied respiratory physiology eBook*. Elsevier Health Sciences, 9th edition, 2020. ISBN 978-0-7020-7933-7. URL https://books.google.com/books?hl=en{&}lr={&}id=k0XpDwAAQBAJ{&}oi=fnd{&}pg=PP1{&}dq=e+book{&}ots=-qw5eVwvoj{&}sig=xdLUAvjx--UyIbKOLGuYO{_}kwmeE.

[93] N. R. Webster and J. F. Nunn. Molecular structure of free radicals and their importance in biological reactions. *British Journal of Anaesthesia*, 60(1):98–108, 1988. ISSN 00070912. doi: 10.1093/bja/60.1.98.

[94] Kay Keyer and James A. Imlay. Superoxide accelerates DNA damage by elevating free-iron levels. *Proceedings of the National Academy of Sciences of the United States of America*, 93(24):13635–13640, 1996. ISSN 00278424. doi: 10.1073/pnas.93.24.13635. URL /pmc/articles/PMC19375//pmc/articles/PMC19375/?report=abstracthttps://www.ncbi.nlm.nih.gov/pmc/articles/PMC19375/.

[95] Kazutaka Hirakawa. Biomolecules Oxidation by Hydrogen Peroxide and Singlet Oxygen. *Reactive Oxygen Species (ROS) in Living Cells*, 2018. doi: 10.5772/intechopen.71465. URL https://www.intechopen.com/chapters/57450.

[96] Madeline A. Mackinder, Keliang Wang, Bocong Zheng, Maheshwar Shrestha, and Qi Hua Fan. Magnetic field enhanced cold plasma sterilization. *Clinical Plasma Medicine*, 17-18:100092, 2020. ISSN 22128166. doi: 10.1016/j.cpme.2019.100092.

[97] Davide Curreli and Francis F Chen. Cross-field diffusion in low-temperature plasma discharges of finite length *. *Plasma Sources Science and Technology Plasma Sources Sci. Technol*, 23:9, 2014. doi: 10.1088/0963-0252/23/6/064001. URL http://iopscience.iop.org/0963-0252/23/4.

[98] Multiphysics COMSOL. Plasma Module User's Guide, 2013. URL https://doc.comsol.com/5.6/docserver/{#}!/com.comsol.help.comsol/helpdesk/helpdesk.html.

[99] W. Van Gaens and A. Bogaerts. Kinetic modelling for an atmospheric pressure argon plasma jet in humid air. *Journal of Physics D: Applied Physics*, 46(27), 2013. ISSN 00223727. doi: 10.1088/0022-3727/46/27/275201.

[100] Takayuki Ohshima, Kanako Okuyama, and Masayuki Sato. Effect of culture temperature on high-voltage pulse sterilization of Escherichia coli. *Journal of Electrostatics*, 55(3-4):227–235, jul 2002. ISSN 03043886. doi: 10.1016/S0304-3886(01)00206-6. URL

https://www.sciencedirect.com/science/article/pii/S0304388601002066.

[101] Min Hyong Lee and Chin Wook Chung. Self-consistent global model with multi-step ionizations in inductively coupled plasmas. *Physics of Plasmas*, 12(7):1–5, jul 2005. ISSN 1070664X. doi: 10.1063/1.1935407. URL http://aip.scitation.org/doi/10.1063/1.1935407.

[102] Thomas von Woedtke, Axel Kramer, and Klaus Dieter Weltmann. Plasma sterilization: What are the conditions to meet this claim? *Plasma Processes and Polymers*, 5(6):534–539, aug 2008. ISSN 16128850. doi: 10.1002/ppap.200800013. URL http://doi.wiley.com/10.1002/ppap.200800013.

[103] Erin R. Sanders. Aseptic laboratory techniques: Plating methods. *Journal of Visualized Experiments*, (63):1–18, may 2012. ISSN 1940087X. doi: 10.3791/3064. URL http://www.ncbi.nlm.nih.gov/pubmed/22617405http://www.pubmedcentral.nih.gov/articlerender.fcgi?artid=PMC4846335.

[104] Russ R. Laher and Forrest R. Gilmore. Updated Excitation and Ionization Cross Sections for Electron Impact on Atomic Oxygen. *Journal of Physical and Chemical Reference Data*, 19(1):277–305, jan 1990. ISSN 15297845. doi: 10.1063/1.555872. URL http://aip.scitation.org/doi/10.1063/1.555872.

[105] Y. Itikawa, A. Ichimura, K. Onda, K. Sakimoto, K. Takayanagi, Y. Hatano, M. Hayashi, H. Nishimura, and S. Tsurubuchi. Cross Sections for Collisions of Electrons and Photons with Oxygen Molecules. *Journal of Physical and Chemical Reference Data*, 18(1):23–42, jan 1989. ISSN 15297845. doi: 10.1063/1.555841. URL http://aip.scitation.org/doi/10.1063/1.555841.

[106] Annemie Bogaerts. Effects of oxygen addition to argon glow discharges: A hybrid Monte Carlo-fluid modeling investigation. *Spectrochimica Acta - Part B Atomic Spectroscopy*, 64 (11-12):1266–1279, nov 2009. ISSN 05848547. doi: 10.1016/j.sab.2009.10.003. URL https://www.sciencedirect.com/science/article/pii/S0584854709003243.

[107] P. C. Cosby. Electron-impact dissociation of oxygen. *The Journal of Chemical Physics*, 98(12):9560–9569, jun 1993. ISSN 00219606. doi: 10.1063/1.464387. URL http://aip.scitation.org/doi/10.1063/1.464387.

[108] Yukikazu Itikawa. Cross sections for electron collisions with oxygen molecules. *Journal of Physical and Chemical Reference Data*, 38(1):1–20, mar 2009. ISSN 00472689. doi: 10.1063/1.3025886. URL http://aip.scitation.org/doi/10.1063/1.3025886.

[109] Emad N. El Qada, Stephen J. Allen, and Gavin M. Walker. Adsorption of Methylene Blue onto activated carbon produced from steam activated bituminous coal: A study of equilibrium adsorption isotherm. *Chemical Engineering Journal*, 124(1-3):103–110, nov 2006. ISSN 13858947. doi: 10.1016/j.cej.2006.08.015.

[110] Mohamed Berradi, Rachid Hsissou, Mohammed Khudhair, Mohammed Assouag, Omar Cherkaoui, Abderrahim El Bachiri, and Ahmed El Harfi. Textile finishing dyes and their impact on aquatic environs. *Heliyon*, 5(11):e02711, 2019. ISSN 24058440. doi: 10.1016/j.heliyon.2019.e02711.

[111] Tim Robinson, Geoff McMullan, Roger Marchant, and Poonam Nigam. Remediation of dyes in textile effluent: A critical review on current treatment technologies with a proposed alternative. *Bioresource Technology*, 77(3):247–255, 2001. ISSN 09608524. doi: 10.1016/S0960-8524(00)00080-8.

[112] Betina Royer, Natali F. Cardoso, Eder C. Lima, Vanusa S.O. Ruiz, Thaís R. Macedo, and Claudio Airoldi. Organofunctionalized kenyaite for dye removal from aqueous solution. *Journal of Colloid and Interface Science*, 336(2):398–405, 2009. ISSN 00219797. doi: 10.1016/j.jcis.2009.04.025.

[113] M. Berradi, R. Hsissou, M. Khudhair, T. Lakdioui, A. Bekhta, M. El Gouri, M. Rafik, A. El Bachiri, and A. El Harfi. Ultrafiltration of wastewater-models loaded with indigo blue by membranes composed of organic polymers at different percentages: Comparative study. *Moroccan Journal of Chemistry*, 7(2):230–235, 2019. ISSN 2351812X. doi: 10.48317/IMIST.PRSM/MORJCHEM-V7I2.13841. URL https://revues.imist.ma/index.php/morjchem/article/view/13841.

[114] Bruno Lellis, Cíntia Zani Fávaro-Polonio, João Alencar Pamphile, and Julio Cesar Polonio. Effects of textile dyes on health and the environment and bioremediation potential of living organisms. *Biotechnology Research and Innovation*, 3(2):275–290, 2019. ISSN 24520721. doi: 10.1016/j.biori.2019.09.001.

[115] N. Nasuha, B. H. Hameed, and Azam T.Mohd Din. Rejected tea as a potential low-cost adsorbent for the removal of methylene blue. *Journal of Hazardous Materials*, 175(1-3):126–132, mar 2010. ISSN 03043894. doi: 10.1016/j.jhazmat.2009.09.138.

[116] Deepak Pathania, Shikha Sharma, and Pardeep Singh. Removal of methylene blue by adsorption onto activated carbon developed from Ficus carica bast. *Arabian Journal of Chemistry*, 10:S1445–S1451, feb 2017. ISSN 18785352. doi: 10.1016/j.arabjc.2013.04.021. URL https://www.sciencedirect.com/science/article/pii/S187853521300110X.

[117] Shaobin Wang, Z. H. Zhu, Anthony Coomes, F. Haghseresht, and G. Q. Lu. The physical and surface chemical characteristics of activated carbons and the adsorption of methylene blue from wastewater. *Journal of Colloid and Interface Science*, 284(2):440–446, apr 2005. ISSN 00219797. doi: 10.1016/j.jcis.2004.10.050.

[118] Sunil J. Wimalawansa. Purification of Contaminated Water with Reverse Osmosis: Effective Solution of Providing Clean Water for Human Needs in Developing Countries. *International Journal of Emerging Technology and Advanced Engineering*, 3(12):15, 2013. URL www.ijetae.com.

[119] A. Hassani and A. R. Khataee. Activated carbon fiber for environmental protection. In *Activated Carbon Fiber and Textiles*, pages 245–280. Elsevier Inc., 2017. ISBN 9780081006788. doi: 10.1016/B978-0-08-100660-3.00010-9.

[120] Willis Gwenzi, Nhamo Chaukura, Chicgoua Noubactep, and Fungai N.D. Mukome. Biochar-based water treatment systems as a potential low-cost and sustainable technology for clean water provision, jul 2017. ISSN 10958630.

[121] Judith Kammerer, Reinhold Carle, and Dietmar R. Kammerer. Adsorption and ion exchange: Basic principles and their application in food processing. *Journal of Agricultural and Food Chemistry*, 59(1):22–42, jan 2011. ISSN 00218561. doi: 10.1021/jf1032203. URL https://pubs.acs.org/sharingguidelineshttps://pubs.acs.org/doi/full/10.1021/jf1032203.

[122] Dilek Cuhadaroglu and Oznur Aydemir Uygun. Production and characterization of activated carbon from a bituminous coal by chemical activation. *African Journal of Biotechnology*, 7(20):3706–3713, 2008. ISSN 16845315. doi: 10.4314/ajb.v7i20.59416. URL https://www.ajol.info/index.php/ajb/article/view/59416.

[123] Kenneth S.W. Sing. Characterization Of Porous Solids: An Introductory Survey. *Studies in Surface Science and Catalysis*, 62(C):1–9, 1991. ISSN 01672991. doi: 10.1016/S0167-2991(08)61303-8.

[124] Mohamed Nouri. Potentials and challenges of date pits as alternative environmental clean-up ingredients. *Biomass Conversion and Biorefinery*, pages 1–28, 2021. ISSN 21906823. doi: 10.1007/s13399-020-01215-w. URL https://link.springer.com/article/10.1007/s13399-020-01215-w.

[125] Tyler M. Huggins, Alexander Haeger, Justin C. Biffinger, and Zhiyong Jason Ren. Granular biochar compared with activated carbon for wastewater treatment and resource recovery. *Water Research*, 94:225–232, 2016. ISSN 18792448. doi: 10.1016/j.watres.2016.02.059.

[126] George William Kajjumba, Serkan Emik, Atakan Öngen, H. Kurtulus Özcan, and Serdar Aydın. Modelling of Adsorption Kinetic Processes—Errors, Theory and Application. In Serpil Edebali, editor, *Advanced Sorption Process Applications*, chapter 10. IntechOpen, Rijeka, 2019. doi: 10.5772/intechopen.80495. URL https://doi.org/10.5772/intechopen.80495.

[127] Tapas Ranjan Sahoo and Benedicte Prelot. Adsorption processes for the removal of contaminants from wastewater: The perspective role of nanomaterials and nanotechnology. *Nanomaterials for the Detection and Removal of Wastewater Pollutants*, pages 161–222, 2020. doi: 10.1016/B978-0-12-818489-9.00007-4.

[128] Qiang Yu, Ruiqi Zhang, Shubo Deng, Jun Huang, and Gang Yu. Sorption of perfluorooctane sulfonate and perfluorooctanoate on activated carbons and resin: Kinetic and isotherm study. *Water Research*, 43(4):1150–1158, 2009. ISSN 00431354. doi: 10.1016/j.watres.2008.12.

001.

[129] P. Chingombe, B. Saha, and R. J. Wakeman. Sorption of atrazine on conventional and surface modified activated carbons. *Journal of Colloid and Interface Science*, 302(2):408–416, 2006. ISSN 00219797. doi: 10.1016/j.jcis.2006.06.065.

[130] Tom Sizmur, Teresa Fresno, Gökçen Akgül, Harrison Frost, and Eduardo Moreno-Jiménez. Biochar modification to enhance sorption of inorganics from water. *Bioresource Technology*, 246:34–47, dec 2017. ISSN 18732976. doi: 10.1016/j.biortech.2017.07.082. URL https://www.sciencedirect.com/science/article/pii/S0960852417311987.

[131] James W. Lee, Michelle Kidder, Barbara R. Evans, Sokwon Paik, A. C. Buchanan, Charles T. Garten, and Robert C. Brown. Characterization of biochars produced from cornstovers for soil amendment. *Environmental Science and Technology*, 44(20):7970–7974, 2010. ISSN 0013936X. doi: 10.1021/es101337x. URL https://pubs.acs.org/doi/abs/10.1021/es101337x.

[132] B. Liang, J. Lehmann, D. Solomon, J. Kinyangi, J. Grossman, B. O'Neill, J. O. Skjemstad, J. Thies, F. J. Luizão, J. Petersen, and E. G. Neves. Black Carbon Increases Cation Exchange Capacity in Soils. *Soil Science Society of America Journal*, 70(5):1719–1730, 2006. ISSN 03615995. doi: 10.2136/sssaj2005.0383. URL https://onlinelibrary.wiley.com/doi/full/10.2136/sssaj2005.0383https://onlinelibrary.wiley.com/doi/abs/10.2136/sssaj2005.0383https://acsess.onlinelibrary.wiley.com/doi/10.2136/sssaj2005.0383.

[133] Minori Uchimiya, Isabel M. Lima, K. Thomas Klasson, Sechin Chang, Lynda H. Wartelle, and James E. Rodgers. Immobilization of heavy metal ions (CuII, CdII, NiII, and PbII) by broiler litter-derived biochars in water and soil. *Journal of Agricultural and Food Chemistry*, 58(9):5538–5544, 2010. ISSN 00218561. doi: 10.1021/jf9044217. URL https://pubs.acs.org/doi/abs/10.1021/jf9044217.

[134] Omar R. Harvey, Bruce E. Herbert, Roy D. Rhue, and Li Jung Kuo. Metal interactions at the biochar-water interface: Energetics and structure-sorption relationships elucidated by flow adsorption microcalorimetry. *Environmental Science and Technology*, 45(13):5550–5556, 2011. ISSN 0013936X. doi: 10.1021/es104401h. URL https://pubs.acs.org/doi/abs/10.1021/es104401h.

[135] Xinde Cao, Lena Ma, Bin Gao, and Willie Harris. Dairy-manure derived biochar effectively sorbs lead and atrazine. *Environmental Science and Technology*, 43(9):3285–3291, 2009. ISSN 0013936X. doi: 10.1021/es803092k. URL https://pubs.acs.org/doi/abs/10.1021/es803092k.

[136] In Ho Yoon, Xiaoguang Meng, Chao Wang, Kyoung Woong Kim, Sunbaek Bang, Eunyoung Choe, and Lee Lippincott. Perchlorate adsorption and desorption on activated carbon and anion exchange resin. *Journal of Hazardous Materials*, 164(1):87–94, may 2009. ISSN 03043894. doi: 10.1016/j.jhazmat.2008.07.123.

[137] B. Saha, M. H. Tai, and M. Streat. Study of activated carbon after oxidation and subsequent treatment: Characterization. *Process Safety and Environmental Protection*, 79(4):211–217, 2001. ISSN 09575820. doi: 10.1205/095758201750362253.

[138] Prakash R Somani and Masayoshi Umeno. Importance of Transmission Electron Microscopy for Carbon Nanomaterials Importance of Transmission Electron Microscopy for Carbon Nanomaterials Research. *Modern Research and Educational Topics in Microscopy*, (July): 634–642, 2007. URL https://www.researchgate.net/publication/228758446.

[139] Madeline A. Mackinder, Keliang Wang, and Qi Hua Fan. Methylene Blue Adsorption by Plasma Re-Activated Carbon. *Journal of Water Resource and Protection*, 13(10):778–793, 2021. ISSN 1945-3094. doi: 10.4236/jwarp.2021.1310041. URL http://www.scirp.org/journal/PaperInformation.aspx?PaperID=112498http://www.scirp.org/Journal/Paperabs.aspx?paperid=112498.

[140] Harry Marsh and Francisco Rodríguez-Reinoso. Characterization of Activated Carbon. *Activated Carbon*, pages 143–242, 2006. doi: 10.1016/B978-008044463-5/50018-2.

[141] John F Moulder, William F Stickle, Peter E Sobol, and Kenneth D Bomben. *Handbook of X-ray photoelectron spectroscopy: a reference book of standard spectra for identification and interpretation of XPS data*. 1992. ISBN 978-0-9627026-2-4. URL https://www.cnyn.unam.mx/{~}wencel/XPS/MANXPS.pdf.

[142] Artur P. Terzyk. The influence of activated carbon surface chemical composition on the adsorption of acetaminophen (paracetamol) in vitro. Part II. TG, FTIR, and XPS analysis of carbons and the temperature dependence of adsorption kinetics at the neutral pH. *Colloids and Surfaces A: Physicochemical and Engineering Aspects*, 177(1):23–45, feb 2001. ISSN 09277757. doi: 10.1016/S0927-7757(00)00594-X.

[143] Zhenyu Ryu, Haiqin Rong, Jingtang Zheng, Maozhang Wang, and Bijiang Zhang. Microstructure and chemical analysis of PAN-based activated carbon fibers prepared by different activation methods, 2002. ISSN 00086223.

[144] Li Liu, Shisuo Fan, and Yang Li. Removal behavior of methylene blue from aqueous solution by tea waste: Kinetics, isotherms and mechanism. *International Journal of Environmental Research and Public Health*, 15(7), jul 2018. ISSN 16604601. doi: 10.3390/ijerph15071321.

[145] Lidia Armelao, Davide Barreca, Gregorio Bottaro, Silvia Gross, Alberto Gasparotto, Cinzia Maragno, Eugenio Tondello, and Andrea Zattin. Introduction to XPS Studies of Metal and Metal-oxide Nanosystems. *Surface Science Spectra*, 10(1):137–142, 2003. ISSN 1055-5269. doi: 10.1116/11.20050199. URL https://doi.org/10.1116/11.20050199.

[146] Travis E. Jones, Tulio C.R. Rocha, Axel Knop-Gericke, Catherine Stampfl, Robert Schlögl, and Simone Piccinin. Insights into the Electronic Structure of the Oxygen Species Active in Alkene Epoxidation on Silver. *ACS Catalysis*, 5(10):5846–5850, 2015. ISSN 21555435.

doi: 10.1021/acscatal.5b01543. URL https://pubs.acs.org/sharingguidelines.

[147] D. Lennon, D. T. Lundie, S. D. Jackson, G. J. Kelly, and S. F. Parker. Characterization of activated carbon using X-ray photoelectron spectroscopy and inelastic neutron scattering spectroscopy. *Langmuir*, 18(12):4667–4673, 2002. ISSN 07437463. doi: 10.1021/la011324j. URL https://pubs.acs.org/sharingguidelines.

[148] Lihua Chen, Anas Ramadan, Lili Lü, Wenjing Shao, Fang Luo, and Ji Chen. Biosorption of methylene blue from aqueous solution using lawny grass modified with citric acid. *Journal of Chemical and Engineering Data*, 56(8):3392–3399, aug 2011. ISSN 00219568. doi: 10.1021/je200366n.

[149] Pellegrino Conte, Roberta Bertani, Paolo Sgarbossa, Paola Bambina, Hans Peter Schmidt, Roberto Raga, Giuseppe Lo Papa, Delia Francesca Chillura Martino, and Paolo Lo Meo. Recent developments in understanding biochar's physical–chemistry. *Agronomy*, 11(4):615, 2021. ISSN 20734395. doi: 10.3390/agronomy11040615. URL https://www.mdpi.com/2073-4395/11/4/615/htmhttps://www.mdpi.com/2073-4395/11/4/615.

[150] Kyle A Thompson, Kyle K Shimabuku, Joshua P Kearns, Detlef R U Knappe, R Scott Summers, and Sherri M Cook. Environmental Comparison of Biochar and Activated Carbon for Tertiary Wastewater Treatment. *Environmental Science and Technology*, 50(20): 11253–11262, 2016. ISSN 15205851. doi: 10.1021/ACS.EST.6B03239/SUPPL_FILE/ES6B03239_SI_001.PDF. URL https://pubs.acs.org/doi/full/10.1021/acs.est.6b03239.

[151] Aditya Rawal, Stephen D. Joseph, James M. Hook, Chee H. Chia, Paul R. Munroe, Scott Donne, Yun Lin, David Phelan, David R.G. Mitchell, Ben Pace, Joseph Horvat, and J. Beau W. Webber. Mineral-Biochar Composites: Molecular Structure and Porosity. *Environmental Science and Technology*, 50(14):7706–7714, 2016. ISSN 15205851. doi: 10.1021/acs.est.6b00685. URL https://ro.uow.edu.au/aiimpapershttps://ro.uow.edu.au/aiimpapers/2177.

[152] Karolina Jurkiewicz, Mirosława Pawlyta, and Andrzej Burian. Structure of Carbon Materials Explored by Local Transmission Electron Microscopy and Global Powder Diffraction Probes. *C, Journal of Carbon Research*, 4(4):68, dec 2018. ISSN 2311-5629. doi: 10.3390/c4040068. URL http://www.mdpi.com/2311-5629/4/4/68.

[153] Shisuo Fan, Jie Tang, Yi Wang, Hui Li, Hao Zhang, Jun Tang, Zhen Wang, and Xuede Li. Biochar prepared from co-pyrolysis of municipal sewage sludge and tea waste for the adsorption of methylene blue from aqueous solutions: Kinetics, isotherm, thermodynamic and mechanism. *Journal of Molecular Liquids*, 220:432–441, aug 2016. ISSN 01677322. doi: 10.1016/j.molliq.2016.04.107.

[154] Ajeet Kumar and Chandra Kumar Dixit. Methods for characterization of nanoparticles. In *Advances in Nanomedicine for the Delivery of Therapeutic Nucleic Acids*, pages 44–58. Elsevier, 2017. ISBN 9780081005637. doi: 10.1016/B978-0-08-100557-6.00003-1. URL

https://linkinghub.elsevier.com/retrieve/pii/B9780081005576000031.

[155] Xiao fei Tan, Shao bo Liu, Yun guo Liu, Yan ling Gu, Guang ming Zeng, Xin jiang Hu, Xin Wang, Shao heng Liu, and Lu hua Jiang. Biochar as potential sustainable precursors for activated carbon production: Multiple applications in environmental protection and energy storage. *Bioresource Technology*, 227:359–372, 2017. ISSN 18732976. doi: 10.1016/j.biortech.2016.12.083.

[156] Michio Inagaki and Feiyu Kang. *Materials Science and Engineering of Carbon*. Butterworth-Heinemann, 2016. doi: 10.1016/c2014-0-03769-0. URL https://books.google.com/books?hl=en{&}lr={&}id=j3UYAwAAQBAJ{&}oi=fnd{&}pg=PP1{&}dq=Carbon+Materials:+Science+and+Applications{&}ots=fvAjMEm08G{&}sig=WTRF5wF09L{_}7DfQBu4b-PpMdfOs.

[157] Baharak Sajjadi, Wei Yin Chen, and Nosa O. Egiebor. A comprehensive review on physical activation of biochar for energy and environmental applications. *Reviews in Chemical Engineering*, 35(6):735–776, 2019. ISSN 01678299. doi: 10.1515/revce-2017-0113. URL https://www.degruyter.com/document/doi/10.1515/revce-2018-0003/html.

[158] Dominique B. Schuepfer, Felix Badaczewski, Juan Manuel Guerra-Castro, Detlev M. Hofmann, Christian Heiliger, Bernd Smarsly, and Peter J. Klar. Assessing the structural properties of graphitic and non-graphitic carbons by Raman spectroscopy. *Carbon*, 161:359–372, 2020. ISSN 00086223. doi: 10.1016/j.carbon.2019.12.094.

[159] Agnieszka Tomczyk, Zofia Sokołowska, and Patrycja Boguta. Biochar physicochemical properties: pyrolysis temperature and feedstock kind effects. *Reviews in Environmental Science and Biotechnology*, 19(1):191–215, mar 2020. ISSN 15729826. doi: 10.1007/s11157-020-09523-3. URL https://doi.org/10.1007/s11157-020-09523-3https://link.springer.com/article/10.1007/s11157-020-09523-3.

[160] Baharak Sajjadi, Wei Yin Chen, and Nosa O. Egiebor. A comprehensive review on physical activation of biochar for energy and environmental applications. *Reviews in Chemical Engineering*, 35(6):735–776, 2019. ISSN 01678299. doi: 10.1515/revce-2017-0113. URL https://www.degruyter.com/document/doi/10.1515/revce-2017-0113/html.

[161] G. C. Loh and D. Baillargeat. Graphitization of amorphous carbon and its transformation pathways. *Journal of Applied Physics*, 114(3):33534, 2013. ISSN 00218979. doi: 10.1063/1.4816313. URL https://aip.scitation.org/doi/abs/10.1063/1.4816313.

[162] Xiaoxiao Yang, Zewu Fu, Duoduo Han, Yuying Zhao, Rui Li, and Yulong Wu. Unveiling the pyrolysis mechanisms of cellulose: Experimental and theoretical studies. *Renewable Energy*, 147(5):1120–1130, 2020. ISSN 18790682. doi: 10.1016/j.renene.2019.09.069. URL https://pubs.acs.org/doi/full/10.1021/acs.energyfuels.9b00482.

[163] Haiping Yang, Rong Yan, Hanping Chen, Dong Ho Lee, and Chuguang Zheng. Character-

istics of hemicellulose, cellulose and lignin pyrolysis. *Fuel*, 86(12-13):1781–1788, 2007. ISSN 00162361. doi: 10.1016/j.fuel.2006.12.013.

[164] Hector A. Ruiz, Mette Hedegaard Thomsen, and Heather L. Trajano. Hydrothermal Processing in Biorefineries: Production of Bioethanol and High Added-Value Compounds of Second and Third Generation Biomass. *Hydrothermal Processing in Biorefineries: Production of Bioethanol and High Added-Value Compounds of Second and Third Generation Biomass*, pages 1–511, 2017. doi: 10.1007/978-3-319-56457-9.

[165] Angeles Blanco, M. Concepcion Monte, Cristina Campano, Ana Balea, Noemi Merayo, and Carlos Negro. Nanocellulose for industrial use: Cellulose nanofibers (CNF), cellulose nanocrystals (CNC), and bacterial cellulose (BC). *Handbook of Nanomaterials for Industrial Applications*, pages 74–126, 2018. doi: 10.1016/B978-0-12-813351-4.00005-5.

[166] Heather L. Trajano, Jingqian Chen, Zhaoyang Yuan, and Elisa Zanuso. Response of biomass species to hydrothermal pretreatment. *Hydrothermal Processing in Biorefineries: Production of Bioethanol and High Added-Value Compounds of Second and Third Generation Biomass*, pages 95–140, 2017. doi: 10.1007/978-3-319-56457-9_4. URL https://link.springer.com/chapter/10.1007/978-3-319-56457-9{_}4.

[167] Michael R. Ladisch, Eduardo Ximenes, Cristiane S. Farinas, and Youngmi Kim. Hydrothermal pretreatment of lignocellulosic biomass for bioethanol production. *Hydrothermal Processing in Biorefineries: Production of Bioethanol and High Added-Value Compounds of Second and Third Generation Biomass*, pages 181–205, 2017. doi: 10.1007/978-3-319-56457-9_7. URL https://link.springer.com/chapter/10.1007/978-3-319-56457-9{_}7.

[168] M. Misra, S. Vivekanandhan, A. K. Mohanty, and J. Denault. Nanotechnologies for Agricultural Bioproducts. *Comprehensive Biotechnology, Second Edition*, 4:111–119, 2011. doi: 10.1016/B978-0-08-088504-9.00260-9.

[169] Johanna Rytioja, Kristiina Hildén, Jennifer Yuzon, Annele Hatakka, Ronald P. de Vries, and Miia R. Mäkelä. Plant-Polysaccharide-Degrading Enzymes from Basidiomycetes. *Microbiology and Molecular Biology Reviews*, 78(4):614–649, 2014. ISSN 1092-2172. doi: 10.1128/mmbr.00035-14. URL /pmc/articles/PMC4248655//pmc/articles/PMC4248655/?report=abstracthttps://www.ncbi.nlm.nih.gov/pmc/articles/PMC4248655/.

[170] Hector A. Ruiz, Mette Hedegaard Thomsen, and Heather L. Trajano. Hydrothermal Processing in Biorefineries: Production of Bioethanol and High Added-Value Compounds of Second and Third Generation Biomass, 2017.

[171] Oussama Benaimeche, Nadhir Toubal Seghir, Łukasz Sadowski, and Mekki Mellas. The Utilization of Vegetable Fibers in Cementitious Materials. *Encyclopedia of Renewable and Sustainable Materials*, pages 649–662, 2020. doi: 10.1016/b978-0-12-803581-8.11596-6.

[172] Hong Peng, Na Wang, Zhengrong Hu, Ziping Yu, Yuhuan Liu, Jinsheng Zhang, and Roger Ruan. Physicochemical characterization of hemicelluloses from bamboo (Phyllostachys pubescens Mazel) stem. *Industrial Crops and Products*, 37(1):41–50, 2012. ISSN 09266690. doi: 10.1016/j.indcrop.2011.11.031.

[173] I. Kögel-Knabner and W. Amelung. Dynamics, Chemistry, and Preservation of Organic Matter in Soils. *Treatise on Geochemistry: Second Edition*, 12:157–215, 2013. doi: 10.1016/B978-0-08-095975-7.01012-3.

[174] Johannes Lehmann and Stephen Joseph. *Biochar for environmental management: Science and technology*. Earthscan, 2012. ISBN 9781849770552. doi: 10.4324/9781849770552. URL https://books.google.com/books?id=w-CUty{_}JIfcC{&}dq=biochar{&}lr={&}source=gbs{_}navlinks{_}s.

[175] Mandu Inyang and Eric Dickenson. The potential role of biochar in the removal of organic and microbial contaminants from potable and reuse water: A review. *Chemosphere*, 134:232–240, sep 2015. ISSN 18791298. doi: 10.1016/j.chemosphere.2015.03.072. URL https://www.sciencedirect.com/science/article/pii/S0045653515003161.

[176] Gajanan Sampatrao Ghodake, Surendra Krushna Shinde, Avinash Ashok Kadam, Rijuta Ganesh Saratale, Ganesh Dattatraya Saratale, Manu Kumar, Ramasubba Reddy Palem, Hind A. AL-Shwaiman, Abdallah M. Elgorban, Asad Syed, and Dae Young Kim. Review on biomass feedstocks, pyrolysis mechanism and physicochemical properties of biochar: State-of-the-art framework to speed up vision of circular bioeconomy. *Journal of Cleaner Production*, 297:126645, 2021. ISSN 09596526. doi: 10.1016/j.jclepro.2021.126645.

[177] G. Maschio, C. Koufopanos, and A. Lucchesi. Pyrolysis, a promising route for biomass utilization. *Bioresource Technology*, 42(3):219–231, 1992. ISSN 09608524. doi: 10.1016/0960-8524(92)90025-S.

[178] Jordan L. Klinger, Tyler L. Westover, Rachel M. Emerson, C. Luke Williams, Sergio Hernandez, Glen D. Monson, and J. Chadron Ryan. Effect of biomass type, heating rate, and sample size on microwave-enhanced fast pyrolysis product yields and qualities. *Applied Energy*, 228:535–545, 2018. ISSN 03062619. doi: 10.1016/j.apenergy.2018.06.107.

[179] P. R. Yaashikaa, P. Senthil Kumar, Sunita Varjani, and A. Saravanan. A critical review on the biochar production techniques, characterization, stability and applications for circular bioeconomy. *Biotechnology Reports*, 28:e00570, 2020. ISSN 2215017X. doi: 10.1016/j.btre.2020.e00570.

[180] Qing Chao Gong, Liu Qing He, Li Hui Zhang, and Feng Duan. Comparison of the NO heterogeneous reduction characteristics using biochars derived from three biomass with different lignin types. *Journal of Environmental Chemical Engineering*, 9(1):105020, 2021. ISSN 22133437. doi: 10.1016/j.jece.2020.105020.

[181] Riya Chatterjee, Baharak Sajjadi, Wei Yin Chen, Daniell L. Mattern, Nathan Hammer, Vijayasankar Raman, and Austin Dorris. Effect of Pyrolysis Temperature on PhysicoChemical Properties and Acoustic-Based Amination of Biochar for Efficient CO2 Adsorption. *Frontiers in Energy Research*, 8:85, 2020. ISSN 2296598X. doi: 10.3389/fenrg.2020.00085.

[182] Dinesh Mohan, Ankur Sarswat, Yong Sik Ok, and Charles U. Pittman. Organic and inorganic contaminants removal from water with biochar, a renewable, low cost and sustainable adsorbent - A critical review. *Bioresource Technology*, 160:191–202, may 2014. ISSN 18732976. doi: 10.1016/j.biortech.2014.01.120. URL https://www.sciencedirect.com/science/article/pii/S096085241400145X.

[183] Jessica A. Allen and Adriana E. Downie. Predicting Slow Pyrolysis Process Outcomes with Simplified Empirical Correlations for a Consistent Higher Heating Temperature: Biochar Yield and Ash Content. *Energy and Fuels*, 34(11):14223–14231, nov 2020. ISSN 15205029. doi: 10.1021/acs.energyfuels.0c02597. URL https://pubs.acs.org/doi/10.1021/acs.energyfuels.0c02597.

[184] Xincai Chen, Guangcun Chen, Linggui Chen, Yingxu Chen, Johannes Lehmann, Murray B. McBride, and Anthony G. Hay. Adsorption of copper and zinc by biochars produced from pyrolysis of hardwood and corn straw in aqueous solution. *Bioresource Technology*, 102 (19):8877–8884, oct 2011. ISSN 09608524. doi: 10.1016/j.biortech.2011.06.078. URL https://www.sciencedirect.com/science/article/pii/S0960852411009059.

[185] Kaifeng Wang, Na Peng, Guining Lu, and Zhi Dang. Effects of Pyrolysis Temperature and Holding Time on Physicochemical Properties of Swine-Manure-Derived Biochar. *Waste and Biomass Valorization*, 11(2):613–624, 2020. ISSN 1877265X. doi: 10.1007/s12649-018-0435-2. URL http://www.tandfonline.com/action/journalInformation?journalCode=sagb20.

[186] D. K. Shen and S. Gu. The mechanism for thermal decomposition of cellulose and its main products. *Bioresource Technology*, 100(24):6496–6504, 2009. ISSN 09608524. doi: 10.1016/j.biortech.2009.06.095.

[187] A Broido and Maxine A Nelson. Char yield on pyrolysis of cellulose. *Combustion and Flame*, 24(C):263–268, 1975. ISSN 0010-2180. doi: 10.1016/0010-2180(75)90156-X.

[188] Tao Wang, Jun Liu, Yongsheng Zhang, Huicong Zhang, Wei Yin Chen, Pauline Norris, and Wei Ping Pan. Use of a non-thermal plasma technique to increase the number of chlorine active sites on biochar for improved mercury removal. *Chemical Engineering Journal*, 331:536–544, jan 2018. ISSN 13858947. doi: 10.1016/j.cej.2017.09.017. URL https://www.sciencedirect.com/science/article/pii/S138589471731505X.

[189] Virpi Siipola, Tarja Tamminen, Anssi Källi, Riikka Lahti, Henrik Romar, Kimmo Rasa, Riikka Keskinen, Jari Hyväluoma, Markus Hannula, and Hanne Wikberg. Effects of biomass type, carbonization process, and activation method on the properties of bio-based

activated carbons. *BioResources*, 13(3):5976–6002, 2019. ISSN 19302126. doi: 10.15376/biores.13.3.5976-6002. URL http://ojs.cnr.ncsu.edu/index.php/BioRes/article/view/BioRes{_}13{_}3{_}5976{_}Siipola{_}Biomass{_}Type{_}Carbonization{_}Process{_}Activation{_}M

[190] Ajay K. Dalai and Ramin Azargohar. Production of activated carbon from biochar using chemical and physical activation: Mechanism and modeling. *ACS Symposium Series*, 954: 463–476, 2007. ISSN 00976156. doi: 10.1021/bk-2007-0954.ch029. URL https://pubs.acs.org/doi/abs/10.1021/bk-2007-0954.ch029.

[191] D. Bergna, T. Hu, H. Prokkola, H. Romar, and U. Lassi. Effect of Some Process Parameters on the Main Properties of Activated Carbon Produced from Peat in a Lab-Scale Process. *Waste and Biomass Valorization*, 11(6):2837–2848, 2020. ISSN 1877265X. doi: 10.1007/s12649-019-00584-2. URL https://link.springer.com/article/10.1007/s12649-019-00584-2.

[192] Flavia Lega Braghiroli, Hassine Bouafif, Carmen Mihaela Neculita, and Ahmed Koubaa. Activated Biochar as an Effective Sorbent for Organic and Inorganic Contaminants in Water. *Water, Air, and Soil Pollution*, 229(7):1–22, jul 2018. ISSN 15732932. doi: 10.1007/s11270-018-3889-8. URL https://doi.org/10.1007/s11270-018-3889-8.

[193] Yupeng Guo, Shaofeng Yang, Kaifeng Yu, Jingzhe Zhao, Zichen Wang, and Hongding Xu. The preparation and mechanism studies of rice husk based porous carbon. *Materials Chemistry and Physics*, 74(3):320–323, 2002. ISSN 02540584. doi: 10.1016/S0254-0584(01)00473-4.

[194] Wei Chen, Meng Gong, Kaixu Li, Mingwei Xia, Zhiqun Chen, Haoyu Xiao, Yang Fang, Yingquan Chen, Haiping Yang, and Hanping Chen. Insight into KOH activation mechanism during biomass pyrolysis: Chemical reactions between O-containing groups and KOH. *Applied Energy*, 278:115730, 2020. ISSN 03062619. doi: 10.1016/j.apenergy.2020.115730.

[195] Jiacheng Wang and Stefan Kaskel. KOH activation of carbon-based materials for energy storage. *Journal of Materials Chemistry*, 22(45):23710–23725, 2012. ISSN 09599428. doi: 10.1039/c2jm34066f. URL https://pubs.rsc.org/en/content/articlehtml/2012/jm/c2jm34066fhttps://pubs.rsc.org/en/content/articlelanding/2012/jm/c2jm34066f.

[196] D. Lozano-Castelló, J. M. Calo, D. Cazorla-Amorós, and A. Linares-Solano. Carbon activation with KOH as explored by temperature programmed techniques, and the effects of hydrogen. *Carbon*, 45(13):2529–2536, 2007. ISSN 00086223. doi: 10.1016/j.carbon.2007.08.021.

[197] Haiyan Mao, Dingguo Zhou, Zaher Hashisho, Sunguo Wang, Heng Chen, and Haiyan Wang. Preparation of pinewood- and wheat straw-based activated carbon via a microwave-assisted potassium hydroxide treatment and an analysis of the effects of the microwave activation conditions. *BioResources*, 10(1):809–821, 2015. ISSN 19302126. doi: 10.15376/biores.10.1.809-821.

[198] M. A. Lillo-Ródenas, D. Cazorla-Amorós, and A. Linares-Solano. Understanding chemical reactions between carbons and NaOH and KOH: An insight into the chemical activation mechanism. *Carbon*, 41(2):267–275, 2003. ISSN 00086223. doi: 10.1016/S0008-6223(02)00279-8.

[199] Feng Chin Wu, Ru Ling Tseng, and Ruey Shin Juang. Comparisons of porous and adsorption properties of carbons activated by steam and KOH. *Journal of Colloid and Interface Science*, 283(1):49–56, 2005. ISSN 00219797. doi: 10.1016/j.jcis.2004.08.037.

[200] Ru Ling Tseng and Szu Kung Tseng. Pore structure and adsorption performance of the KOH-activated carbons prepared from corncob. *Journal of Colloid and Interface Science*, 287(2):428–437, 2005. ISSN 00219797. doi: 10.1016/j.jcis.2005.02.033.

[201] Julio J. Lado, Rafael L. Zornitta, Felipe A. Calvi, Mariana Martins, Marc A. Anderson, Francisco G.E. Nogueira, and Luís A.M. Ruotolo. Enhanced capacitive deionization desalination provided by chemical activation of sugar cane bagasse fly ash electrodes. *Journal of Analytical and Applied Pyrolysis*, 126:143–153, 2017. ISSN 01652370. doi: 10.1016/j.jaap.2017.06.014.

[202] R. Hilton, P. Bick, A. Tekeei, E. Leimkuehler, P. Pfeifer, and G. J. Suppes. Mass balance and performance analysis of potassium hydroxide activated carbon. *Industrial and Engineering Chemistry Research*, 51(26):9129–9135, 2012. ISSN 15205045. doi: 10.1021/ie301293t. URL https://pubs.acs.org/doi/abs/10.1021/ie301293t.

[203] Pei Liu, Wu Jun Liu, Hong Jiang, Jie Jie Chen, Wen Wei Li, and Han Qing Yu. Modification of bio-char derived from fast pyrolysis of biomass and its application in removal of tetracycline from aqueous solution. *Bioresource Technology*, 121:235–240, 2012. ISSN 09608524. doi: 10.1016/j.biortech.2012.06.085.

[204] R. Rostamian, M. Heidarpour, S. F. Mousavi, and M. Afyuni. Characterization and sodium sorption capacity of biochar and activated carbon prepared from rice husk. *Journal of Agricultural Science and Technology*, 17(4):1057–1069, 2015. ISSN 23453737.

[205] Kaixuan Feng, Yuyan Hu, and Tongcheng Cao. Mechanism of Fuel Gas Denitration on the KOH-Activated Biochar Surface. *Journal of Physical Chemistry A*, 126(2):296–305, 2022. ISSN 15205215. doi: 10.1021/acs.jpca.1c09518. URL https://pubs.acs.org/doi/full/10.1021/acs.jpca.1c09518.

[206] Samantha Hepburn. Unconventional gas regulation. *Mining and Energy Law*, pages 175–238, 2018. doi: 10.1017/cbo9781107480025.006. URL https://linkinghub.elsevier.com/retrieve/pii/B9780128095706000035.

[207] Yali Wang, Nannan Qin, Suping Cui, Xiaoyu Ma, and Siyu Peng. Influence of biochar composition and micro-structure on the denitration of flue gases at high temperature. *Applied Sciences (Switzerland)*, 10(6):1920, 2020. ISSN 20763417. doi: 10.3390/app10061920.

URL https://www.mdpi.com/2076-3417/10/6/1920/htmhttps://www.mdpi.com/2076-3417/10/6/1920.

[208] Qiaoyan Li, Yaqin Hou, Jiancheng Wang, Yongjin Liu, Ning Xiang, and Zhanggen Huang. Superiority of Raw Biomass and Potassium Hydroxide in Preparation of Ultrahigh Nitrogen Doping of Carbon for NH3-SCR Reaction. *ACS Sustainable Chemistry and Engineering*, 8(30):11308–11316, 2020. ISSN 21680485. doi: 10.1021/acssuschemeng.0c03193. URL https://pubs.acs.org/doi/abs/10.1021/acssuschemeng.0c03193.

[209] Hongmei Jin, Sergio Capareda, Zhizhou Chang, Jun Gao, Yueding Xu, and Jianying Zhang. Biochar pyrolytically produced from municipal solid wastes for aqueous As(V) removal: Adsorption property and its improvement with KOH activation. *Bioresource Technology*, 169:622–629, 2014. ISSN 18732976. doi: 10.1016/j.biortech.2014.06.103.

[210] E. Santoso, R. Ediati, Y. Kusumawati, H. Bahruji, D. O. Sulistiono, and D. Prasetyoko. Review on recent advances of carbon based adsorbent for methylene blue removal from waste water, jun 2020. ISSN 24685194.

[211] J. M. Rosas, J. Bedia, J. Rodríguez-Mirasol, and T. Cordero. HEMP-derived activated carbon fibers by chemical activation with phosphoric acid. *Fuel*, 88(1):19–26, 2009. ISSN 00162361. doi: 10.1016/j.fuel.2008.08.004.

[212] R. Azargohar and A. K. Dalai. Biochar as a precursor of activated carbon. *Applied Biochemistry and Biotechnology*, 131(1-3):762–773, 2006. ISSN 02732289. doi: 10.1385/ABAB:131:1:762.

[213] J L Figueiredo, M F R Pereira, M M A Freitas, and J J M Órfão. Modification of the surface chemistry of activated carbons. *Carbon*, 37(9):1379–1389, 1999. ISSN 0008-6223. doi: 10.1016/S0008-6223(98)00333-9.

[214] Wendy D'Hollander, Luc De Bruyn, An Hagenaars, Pim de Voogt, and Lieven Bervoets. Characterisation of perfluorooctane sulfonate (PFOS) in a terrestrial ecosystem near a fluorochemical plant in Flanders, Belgium. *Environmental Science and Pollution Research*, 21(20):11856–11866, oct 2014. ISSN 16147499. doi: 10.1007/s11356-013-2449-4. URL http://link.springer.com/10.1007/s11356-013-2449-4.

[215] Shoji F. Nakayama, Mitsuha Yoshikane, Yu Onoda, Yukiko Nishihama, Miyuki Iwai-Shimada, Mai Takagi, Yayoi Kobayashi, and Tomohiko Isobe. Worldwide trends in tracing poly- and perfluoroalkyl substances (PFAS) in the environment. *TrAC - Trends in Analytical Chemistry*, 121:115410, 2019. ISSN 18793142. doi: 10.1016/j.trac.2019.02.011.

[216] ITRC (Interstate Technology & Regulatory Council). PFAS Technical and Regulatory Guidance Document and Fact Sheets PFAS-1. Washington, D.C.: Interstate Technology & Regulatory Council, PFAS Team., 2020. URL https://pfas-1.itrcweb.org/.

[217] Oscar Quiñones and Shane A. Snyder. Occurrence of perfluoroalkyl carboxylates and sulfonates in drinking water utilities and related waters from the United States. *Environmental Science and Technology*, 43(24):9089–9095, 2009. ISSN 0013936X. doi: 10.1021/es9024707. URL https://pubs.acs.org/doi/abs/10.1021/es9024707.

[218] Zhanyun Wang, Jamie C. Dewitt, Christopher P. Higgins, and Ian T. Cousins. A Never-Ending Story of Per- and Polyfluoroalkyl Substances (PFASs)? *Environmental Science and Technology*, 51(5):2508–2518, 2017. ISSN 15205851. doi: 10.1021/acs.est.6b04806. URL https://pubs.acs.org/doi/abs/10.1021/acs.est.6b04806.

[219] Hellmuth Lilienthal, Hermann H. Dieter, Jürgen Hölzer, and Michael Wilhelm. Recent experimental results of effects of perfluoroalkyl substances in laboratory animals – Relation to current regulations and guidance values. *International Journal of Hygiene and Environmental Health*, 220(4):766–775, jun 2017. ISSN 1618131X. doi: 10.1016/j.ijheh.2017.03.001. URL https://www.sciencedirect.com/science/article/pii/S1438463917301347.

[220] UNEP/OECD. Synthesis paper on per- and polyfluorinated chemicals (PFCs), 2013. URL https://www.oecd.org/env/ehs/risk-management/PFC{_}FINAL-Web.pdf.

[221] J. T. Gudmundsson and E. G. Thorsteinsson. Oxygen discharges diluted with argon: Dissociation processes. *Plasma Sources Science and Technology*, 16(2):399–412, may 2007. ISSN 09630252. doi: 10.1088/0963-0252/16/2/025. URL http://stacks.iop.org/0963-0252/16/i=2/a=025?key=crossref.6a20a646b0a6f8f877167084776339f9.

[222] Xiaona Li, Shuo Chen, Xie Quan, and Yaobin Zhang. Enhanced adsorption of PFOA and PFOS on multiwalled carbon nanotubes under electrochemical assistance. *Environmental Science and Technology*, 45(19):8498–8505, 2011. ISSN 0013936X. doi: 10.1021/es202026v. URL https://pubs.acs.org/sharingguidelines.

[223] Hoang Nhat Phong Vo, Huu Hao Ngo, Wenshan Guo, Thi Minh Hong Nguyen, Jianxin Li, Heng Liang, Lijuan Deng, Zhuo Chen, and Thi An Hang Nguyen. Poly-and perfluoroalkyl substances in water and wastewater: A comprehensive review from sources to remediation. *Journal of Water Process Engineering*, 36:101393, 2020. ISSN 22147144. doi: 10.1016/j.jwpe.2020.101393.

[224] Georgia M. Sinclair, Sara M. Long, and Oliver A.H. Jones. What are the effects of PFAS exposure at environmentally relevant concentrations? *Chemosphere*, 258:127340, 2020. ISSN 18791298. doi: 10.1016/j.chemosphere.2020.127340.

[225] Juliane Glüge, Martin Scheringer, Ian T. Cousins, Jamie C. Dewitt, Gretta Goldenman, Dorte Herzke, Rainer Lohmann, Carla A. Ng, Xenia Trier, and Zhanyun Wang. An overview of the uses of per- And polyfluoroalkyl substances (PFAS). *Environmental Science: Processes and Impacts*, 22(12):2345–2373, 2020. ISSN 20507895. doi: 10.1039/d0em00291g. URL https://pubs.rsc.org/en/content/articlehtml/2020/em/d0em00291ghttps://pubs.rsc.org/en/content/articlelanding/2020/em/d0em00291g.

[226] Andrew B. Lindstrom, Mark J. Strynar, and E. Laurence Libelo. Polyfluorinated compounds: Past, present, and future. *Environmental Science and Technology*, 45(19):7954–7961, 2011. ISSN 0013936X. doi: 10.1021/es2011622. URL https://pubs.acs.org/doi/full/10.1021/es2011622.

[227] Krista A Barzen-Hanson, Simon C Roberts, Sarah Choyke, Karl Oetjen, Alan McAlees, Nicole Riddell, Robert McCrindle, P Lee Ferguson, Christopher P Higgins, and Jennifer A Field. Discovery of 40 Classes of Per- and Polyfluoroalkyl Substances in Historical Aqueous Film-Forming Foams (AFFFs) and AFFF-Impacted Groundwater. *Environmental Science and Technology*, 51(4):2047–2057, 2017. ISSN 15205851. doi: 10.1021/ACS.EST.6B05843/SUPPL_FILE/ES6B05843_SI_002.XLSX. URL https://pubs.acs.org/doi/full/10.1021/acs.est.6b05843.

[228] Y. W. Alsmeyer, W. V. Childs, R. M. Flynn, G. G. I. Moore, and J. C. Smeltzer. Electrochemical Fluorination and Its Applications. *Organofluorine Chemistry*, pages 121–143, 1994. doi: 10.1007/978-1-4899-1202-2_5. URL https://link.springer.com/chapter/10.1007/978-1-4899-1202-2{_}5.

[229] Lydia R. Dorrance, Seth Kellogg, and Adam H. Love. What you should know about per- and polyfluoroalkyl substances (PFAS) for environmental claims. *Environmental Claims Journal*, 29(4):290–304, 2017. ISSN 1547657X. doi: 10.1080/10406026.2017.1377015. URL https://www.tandfonline.com/doi/abs/10.1080/10406026.2017.1377015.

[230] Dennis J. Paustenbach, Julie M. Panko, Paul K. Scott, and Kenneth M. Unice. A methodology for estimating human exposure to perfluorooctanoic acid (PFOA): A retrospective exposure assessment of a community (1951-2003). *Journal of Toxicology and Environmental Health - Part A: Current Issues*, 70(1):28–57, 2007. ISSN 15287394. doi: 10.1080/15287390600748815. URL https://www.tandfonline.com/doi/abs/10.1080/15287390600748815.

[231] John P. Giesy and Kurunthachalam Kannan. Global distribution of perfluorooctane sulfonate in wildlife. *Environmental Science and Technology*, 35(7):1339–1342, 2001. ISSN 0013936X. doi: 10.1021/es001834k. URL https://pubs.acs.org/doi/abs/10.1021/es001834k.

[232] K. J. Hansen, L. A. Clemen, M. E. Ellefson, and H. O. Johnson. Compound-specific, quantitative characterization of organic fluorochemicals in biological matrices. *Environmental Science and Technology*, 35(4):766–770, 2001. ISSN 0013936X. doi: 10.1021/es001489z. URL https://pubs.acs.org/doi/abs/10.1021/es001489z.

[233] Niclas Johansson, Per Eriksson, and Henrik Viberg. Neonatal exposure to PFOS and PFOA in mice results in changes in proteins which are important for neuronal growth and synaptogenesis in the developing brain. *Toxicological Sciences*, 108(2):412–418, apr 2009. ISSN 10966080. doi: 10.1093/toxsci/kfp029. URL https://academic.oup.com/toxsci/article/1668308/Neonatal.

[234] Jason R. Masoner, Dana W. Kolpin, Isabelle M. Cozzarelli, Kelly L. Smalling, Stephanie C. Bolyard, Jennifer A. Field, Edward T. Furlong, James L. Gray, Duncan Lozinski, Debra Reinhart, Alix Rodowa, and Paul M. Bradley. Landfill leachate contributes per-/poly-fluoroalkyl substances (PFAS) and pharmaceuticals to municipal wastewater. *Environmental Science: Water Research and Technology*, 6(5):1300–1311, 2020. ISSN 20531419. doi: 10.1039/d0ew00045k. URL https://pubs.rsc.org/en/content/articlehtml/2020/ew/d0ew00045khttps://pubs.rsc.org/en/content/articlelanding/2020/ew/d0ew00045k.

[235] Stephan Brendel, Éva Fetter, Claudia Staude, Lena Vierke, and Annegret Biegel-Engler. Short-chain perfluoroalkyl acids: environmental concerns and a regulatory strategy under REACH. *Environmental Sciences Europe*, 30(1), 2018. ISSN 21904715. doi: 10.1186/s12302-018-0134-4. URL /pmc/articles/PMC5834591//pmc/articles/PMC5834591/?report=abstracthttps://www.ncbi.nlm.nih.gov/pmc/articles/PMC5834591/.

[236] José L. Domingo. Health risks of dietary exposure to perfluorinated compounds. *Environment International*, 40(1):187–195, apr 2012. ISSN 18736750. doi: 10.1016/j.envint.2011.08.001. URL https://www.sciencedirect.com/science/article/pii/S0160412011002157.

[237] Alexander G. Paul, Kevin C. Jones, and Andrew J. Sweetman. A first global production, emission, and environmental inventory for perfluorooctane sulfonate. *Environmental Science and Technology*, 43(2):386–392, jan 2009. ISSN 0013936X. doi: 10.1021/es802216n. URL https://pubs.acs.org/doi/10.1021/es802216n.

[238] Konstantinos Prevedouros, Ian T. Cousins, Robert C. Buck, and Stephen H. Korzeniowski. Sources, fate and transport of perfluorocarboxylates. *Environmental Science and Technology*, 40(1):32–44, 2006. ISSN 0013936X. doi: 10.1021/es0512475. URL https://pubs.acs.org/doi/abs/10.1021/es0512475.

[239] US Environmental Protection Agency. Drinking Water Health Advisories for PFOA and PFOS: Questions and Answers. 2016. URL https://www.epa.gov/ground-water-and-drinking-water/drinking-water-health-advisories-pfoa-and-pfos-questions-and.

[240] Mandu Inyang and Eric R.V. Dickenson. The use of carbon adsorbents for the removal of perfluoroalkyl acids from potable reuse systems. *Chemosphere*, 184:168–175, oct 2017. ISSN 18791298. doi: 10.1016/j.chemosphere.2017.05.161. URL https://www.sciencedirect.com/science/article/pii/S0045653517308755.

[241] Magali Houde, Jonathan W. Martin, Robert J. Letcher, Keith R. Solomon, and Derek C.G. Muir. Biological monitoring of polyfluoroalkyl substances: A review. *Environmental Science and Technology*, 40(11):3463–3473, 2006. ISSN 0013936X. doi: 10.1021/es052580b. URL https://pubs.acs.org/doi/abs/10.1021/es052580b.

[242] US Environmental Protection Agency. Drinking Water Health Advisory for Perfluorooctane Sulfonate (PFOS), Office of Water Health and Ecological Criteria Division. (May):1–88,

2016.

[243] USEPA. Drinking water health advisory for perfluorooctanoic acid (PFOA). (May 2016 EPA 822-R-16-005). *United States Environmental Protection Agency*, (May):1–103, 2016. URL https://www.epa.gov/sites/production/files/2016-05/documents/pfoa{_}health{_}advisory{_}final{_}508.pdf.

[244] Navid Saeidi, Frank Dieter Kopinke, and Anett Georgi. Understanding the effect of carbon surface chemistry on adsorption of perfluorinated alkyl substances. *Chemical Engineering Journal*, 381:122689, 2020. ISSN 13858947. doi: 10.1016/j.cej.2019.122689.

[245] Yue Zhi and Jinxia Liu. Adsorption of perfluoroalkyl acids by carbonaceous adsorbents: Effect of carbon surface chemistry. *Environmental Pollution*, 202:168–176, 2015. ISSN 18736424. doi: 10.1016/j.envpol.2015.03.019.

[246] Longfei Liu, Yanli Liu, Bin Gao, Rong Ji, Chengliang Li, and Shengsen Wang. Removal of perfluorooctanoic acid (PFOA) and perfluorooctane sulfonate (PFOS) from water by carbonaceous nanomaterials: A review. *Critical Reviews in Environmental Science and Technology*, 50(22):2379–2414, 2020. ISSN 15476537. doi: 10.1080/10643389.2019.1700751. URL https://www.tandfonline.com/doi/abs/10.1080/10643389.2019.1700751.

[247] Fei Wang, Kaimin Shih, and James O. Leckie. Effect of humic acid on the sorption of perfluorooctane sulfonate (PFOS) and perfluorobutane sulfonate (PFBS) on boehmite. *Chemosphere*, 118(1):213–218, 2015. ISSN 18791298. doi: 10.1016/j.chemosphere.2014.08.080.

[248] Wei Wang, Xin Mi, Ziming Zhou, Shuangxi Zhou, Chunli Li, Xue Hu, Delin Qi, and Shubo Deng. Novel insights into the competitive adsorption behavior and mechanism of per- and polyfluoroalkyl substances on the anion-exchange resin. *Journal of Colloid and Interface Science*, 557:655–663, 2019. ISSN 10957103. doi: 10.1016/j.jcis.2019.09.066.

[249] Philip McCleaf, Sophie Englund, Anna Östlund, Klara Lindegren, Karin Wiberg, and Lutz Ahrens. Removal efficiency of multiple poly- and perfluoroalkyl substances (PFASs) in drinking water using granular activated carbon (GAC) and anion exchange (AE) column tests. *Water Research*, 120:77–87, 2017. ISSN 18792448. doi: 10.1016/j.watres.2017.04.057.

[250] Wei Guo, Shouliang Huo, Jinglan Feng, and Xiaofei Lu. Adsorption of perfluorooctane sulfonate (PFOS) on corn straw-derived biochar prepared at different pyrolytic temperatures. *Journal of the Taiwan Institute of Chemical Engineers*, 78:265–271, sep 2017. ISSN 18761070. doi: 10.1016/j.jtice.2017.06.013. URL https://www.sciencedirect.com/science/article/pii/S1876107017303085.

[251] Tanju Karanfil and James E. Kilduff. Role of granular activated carbon surface chemistry on the adsorption of organic compounds. 1. Priority pollutants. *Environmental Science and Technology*, 33(18):3217–3224, 1999. ISSN 0013936X. doi: 10.1021/es981016g. URL https://pubs.acs.org/doi/full/10.1021/es981016g.

[252] Swati Achra, Tomoki Akimoto, Jean François de Marneffe, Stefanie Sergeant, Xiangyu Wu, Thomas Nuytten, Steven Brems, Inge Asselberghs, Zsolt Tokei, Kazuyoshi Ueno, and Marc Heyns. Enhancing interface doping in graphene-metal hybrid devices using H2 plasma clean. *Applied Surface Science*, 538:148046, 2021. ISSN 01694332. doi: 10.1016/j.apsusc.2020.148046.

[253] Michael Berney, Hans Ulrich Weilenmann, Julian Ihssen, Claudio Bassin, and Thomas Egli. Specific growth rate determines the sensitivity of Escherichia coli to thermal, UVA, and solar disinfection. *Applied and Environmental Microbiology*, 72 (4):2586–2593, apr 2006. ISSN 00992240. doi: 10.1128/AEM.72.4.2586-2593.2006. URL http://www.ncbi.nlm.nih.gov/pubmed/16597961http://www.pubmedcentral.nih.gov/articlerender.fcgi?artid=PMC1449012.

[254] Louis B. Rice. Antimicrobial resistance in gram-positive bacteria. *American Journal of Infection Control*, 34(5 SUPPL.):S11–S19, 2006. ISSN 01966553. doi: 10.1016/j.ajic.2006.05.220.

[255] J. A. Otter, K. Vickery, J. T. Walker, E. deLancey Pulcini, P. Stoodley, S. D. Goldenberg, J. A.G. Salkeld, J. Chewins, S. Yezli, and J. D. Edgeworth. Surface-attached cells, biofilms and biocide susceptibility: Implications for hospital cleaning anddisinfection. *Journal of Hospital Infection*, 89(1):16–27, 2015. ISSN 15322939. doi: 10.1016/j.jhin.2014.09.008.